Masaaki Okubo

# Electrical Sustainable Energy for Mechanical Engineering

Springer

# Electrical Sustainable Energy for Mechanical Engineering

Masaaki Okubo

# Electrical Sustainable Energy for Mechanical Engineering

Springer

Masaaki Okubo
Department of Mechanical Engineering
Graduate School of Engineering
Osaka Metropolitan University
Sakai, Osaka, Japan

ISBN 978-981-96-5169-6 ISBN 978-981-96-5170-2 (eBook)
https://doi.org/10.1007/978-981-96-5170-2



This Springer imprint is published by the registered company Springer Nature Singapore Pte Ltd.
The registered company address is: 152 Beach Road, #21-01/04 Gateway East, Singapore 189721, Singapore

# Preface

This book describes the fundamentals and applications of sustainable electrical energy in mechanical engineering. The main objective of this book is to provide readers with an easy-to-understand resource for the foundations and applications of sustainable electrical energy. The book is among first publications to address these topics. Furthermore, this book aims to bridge the gap between the fundamental and technical aspects of industrial applications in sustainable electrical energy engineering.

Recently, sustainable energy technologies have attracted considerable attention in advanced energy engineering. This textbook was specifically crafted to serve as a resource for undergraduate and graduate school students, particularly in departments other than electrical engineering, such as mechanical engineering departments at universities. The aim is to provide foundational knowledge on sustainable electrical energy and energy conversion principles. The topics covered in this work are those the author found valuable for pursuing research in mechanical engineering and its connection to sustainable electrical engineering. This book does not introduce the specifics of renewable energy systems such as solar battery, wind turbine, and biomass fuels but is intended to equip readers with the basic skills to read technical books that deal with such topics. The content is designed to span a 15-week semester (90 min per week) and is organized into nine chapters. Specifically, it is recommended that Chap. 1 be covered over two weeks, Chaps. 2–6 over five weeks, Chap. 7 over two weeks, and Chaps. 8 and 9 over six weeks. Note that Chaps. 8 and 9 treat advanced application topics. Additionally, the chapters include comprehensive exercise problems. These exercises can be utilized either as in-class integrative activities or as weekly homework assignments, aimed at enhancing students' problem-solving skills. Upon request, sample answers will be sent to instructors who have adopted this book as a textbook.

The author is affiliated with the Department of Mechanical Engineering at the university and has been involved in mentoring students and professionals in the fields of environmental and energy engineering for many years. The author has been particularly dedicated to educational research at the intersection of electrical and mechanical engineering with a focus on plasma processing and electrostatic precipitation. A

significant gap in the electrical engineering knowledge of students undertaking final-year projects has been observed. This course was specifically designed to address this gap, providing insights into topics such as electrical circuits and sustainable energy conversion—areas often overlooked in conventional electrical engineering curricula. The course covers techniques related to energy principles and circuit matching. This book is intended to serve as both a foundational guide and bridge to advanced applications for graduate students and engineers exploring plasma circuitry. Additionally, it includes a wide range of specific problems with detailed solutions. The content has been carefully curated to emphasize the fundamental aspects of sustainable electrical engineering, drawing on the author's extensive research experiences and collaborative industrial projects

The contents of this book are summarized as follows:

Chapter 1 outlines the basic laws of electrical circuits, Maxwell's equations, and the law of charge conservation. Kirchhoff's current law, Ohm's Law, DC circuits, power supply, DC and AC circuits, and transient phenomena calculations are described. Chapter 2 discusses the fundamentals of AC electrical circuits (1); complex notation, AC circuits, and mechanical-electrical system analogy are covered. Chapter 3 discusses the fundamentals of AC electrical circuits (2); resonant circuits and various AC circuits are covered. Chapter 4 covers impedance matching and energy conversion (1); power calculation and impedance matching apparatus are explained. Chapter 5 covers impedance matching and energy conversion (2); Smith chart and matching circuit design method are explained. Chapter 6 covers impedance matching and energy conversion (3); example problems on Smith chart, transformers, and induction motors are mainly covered. Chapter 7 discusses the energy principle and approximated solution of energy systems. The principles of least action, variational theory, energy principles, and approximate solutions using variational methods in electrical and mechanical engineering are discussed. Chapter 8 addresses the fundamentals of continuum thermal-energy fluid science and electrical circuits. The basic equation system for plasma–fluid heat transfer, characteristics of plasma–fluid heat transfer, and examples of the analysis of the basic equation system related with electrical circuits are described. Chapter 9 discusses gas turbine combined-energy systems and renewable energy technologies. Especially, plasma technologies for renewable energy are discussed. All chapters compile comprehensive exercise problems. Appendix covers the background of this book's descriptions and formulas on vectors and tensors.

The unique elements of this book can be expressed as follows:

1. **Covers**… Principles, fundamentals, apparatus, methods, and industry application examples of electrical sustainable energy technologies are covered.
2. **Explains**… Principles and methods of sustainable electrical energy technologies are explained in detail. In particular, basic knowledge on how to utilize electrically sustainable energy can be obtained.
3. **Demonstrates**… Successful industrial application technologies for electrical sustainable energy are demonstrated.

4. **Introduces**… Principles and methods of electrical sustainable energy technologies are introduced for beginner engineers and graduate students.
5. **Readers**... This book should be read by engineering students and all technicians working on electrical sustainable energy.

Although phenomena in electrical circuits can be fundamentally explained by the principles of electromagnetism, standard textbooks often do not treat the derivation of circuit laws based on these principles. Considering the possibility that electromagnetism courses may not be extensively covered in mechanical engineering curricula, this book includes explanations derived from the laws of electromagnetism as foundational knowledge of electrical circuits. In writing this textbook, numerous domestic and international references were consulted and gratitude is expressed. We hope that this textbook will serve as a foundational resource for a broad spectrum of mechanical engineers, enabling them to understand and apply their knowledge of electrical and energy engineering to their professional endeavors.

Our research group has more than 20 years of research projects on environmental plasma and electrical energy engineering for many companies toward the development of new machines. These projects provided us with a wide range of exciting experiences. We aim to share our fascination with this technology in this book, enabling scientists and engineers to successfully engage with it. We believe that our research work should be documented and that it is vital that these technologies are passed on to future generations. Most of these projects were conducted at Osaka Metropolitan University (formerly Osaka Prefecture University) in Sakai City, Japan. Sakai City has prospered maritime trade for centuries. In the 16th century, it was called "Oriental Venice" or "Saccai" by Europeans, and it has been a prosperous international trade port and home to many industries. Sakai City is an important industrial city in Japan with a large industrial zone in the coastal area. Sakai has a long tradition of using metals. I would like to publish this book on sustainable electrical energy engineering from Osaka Metropolitan University, which is located in this traditional Japanese city. This book covers the recent developments in energy technologies and their fundamental aspects. Selected applications of sustainable electrical energy technologies are also described. Although some of these technologies have reached the commercial stage, others are still in the early stages of development. This book provides technical details of sustainable electrical energy engineering.

The author first wrote each chapter separately based on materials that had been published previously as scientific papers, reviews, and book chapters, and then knit the contents together to maintain comprehensive unity. I am grateful to many individuals who assisted in the preparation of this book. We are grateful to Ms. Ayako Yoden for meticulously typing handwritten manuscripts. Furthermore, it has been a pleasure to work with the editors of this book, Mr. Smith Ahram Chae and Ms. Vinothini Elango, in Springer Nature. Collaboration with colleagues over the years has been enriched and enjoyable. I discussed the future prospects of various electrical energy plasma treatment systems with Dr. Tomoyuki Kuroki and Dr. Haruhiko Yamasaki of Osaka Metropolitan University, Prof. Toshiaki Yamamoto and Dr. Hidekatsu Fujishima of Osaka Prefecture University. Research studies performed with students

over 20 years of age at Osaka Prefecture University and Osaka Metropolitan University have been enriching and enjoyable, and most of these are credited in this book through citations of their published work. I truly enjoyed studying and conducting experiments on sustainable energy. I hope that this book proves beneficial not only to mechanical engineers and students but also to professionals in other fields such as electrical, chemical, and environmental engineering, who wish to gain essential knowledge of the emerging electrical sustainable energy system technologies.

Sakai, Japan Masaaki Okubo

**Competing Interests** The author has no competing interests to declare that are relevant to the content of this manuscript.

# Contents

# About the Author

**Dr. Masaaki Okubo** received his B.Eng., M.Eng., and Ph.D. in Mechanical Engineering from the Tokyo Institute of Technology, Tokyo, Japan, in 1985, 1987, and 1990, respectively. He is Professor at the Department of Mechanical Engineering, Osaka Metropolitan University, Sakai, Japan. In April 2022, Osaka Prefecture University and Osaka City University merged to form Osaka Metropolitan University. His previous positions included Associate Professor at Osaka Prefecture University, Assistant Professor at Tokyo Institute of Technology, and Assistant Professor at Tohoku University. He also served as an Invited Professor at Tohoku University, Japan, in 2015.

His current research interests include the environmental applications of nonthermal plasmas, particularly nanoparticle control, electrostatic precipitators, aftertreatment of clean diesel engines and combustors, and surface treatment of materials and their biomedical applications. His work spans multidisciplinary fields, including electrical, chemical, and mechanical engineering. Dr. Okubo has published more than 230 peer-reviewed and invited papers in scientific journals and has authored 33 books.

Dr. Okubo is Fellow of the Institute of Electrical and Electronics Engineers (IEEE) and Japan Society of Mechanical Engineers (JSME). He was Chairman of the Environmental Engineering Division of the JSME in 2007. He served as Chairman of the Electrostatic Process Committee of the IEEE Industry Application Society from 2016 to 2018. He is Associate Editor of the *IEEE Transactions on Industry Applications*, Kansai Branch Chair of the Institute of Electrostatics Japan, and Editorial Board Member of *Journal of Electrostatics and Plasma Chemistry and Plasma Processing*. He received the Environmental Engineering Achievement Award from the Environmental Engineering Division of the Japan Society of Mechanical Engineers in 2013.

# Chapter 1
# Basic Laws of Electrical Circuits


**Abstract** This chapter outlines the basic law of electrical circuits, Maxwell's equations and the law of conservation of charge, Kirchhoff's current law, Ohm's law and linear circuit element, Kirchhoff's voltage law, and displacement current are explained. Following these, DC and AC circuits and calculations, and Transient phenomena in DC and AC circuits are explained. The chapter is concluded by the conclusions and exercise problems.

## 1.1 Introduction

Electric circuits form the foundation of modern technology, from the simplest electronic devices to complex power distribution systems. Understanding how these circuits operate requires a thorough grasp of the fundamental laws that govern the behavior of electrical currents and voltages. This chapter introduces these essential principles, laying the groundwork for more advanced studies in sustainable electrical engineering, based on textbook and Refs. [1–5].

We begin with Maxwell's equations, which encapsulate the core concepts of electromagnetism, linking electric fields, magnetic fields, and charge distributions. These equations are not only central to understanding electromagnetism but also provide the theoretical basis for many of the laws that govern circuit behavior. The law of conservation of charge, one of the consequences of Maxwell's equations, is described as it plays a crucial role in the operation of electric circuits.

Following this, we treat Kirchhoff's laws, which are indispensable tools for analyzing circuits. Kirchhoff's current law and Kirchhoff's voltage law are derived from the fundamental principles of electromagnetism and energy conservation, respectively. Kirchhoff's current law deals with the flow of current at junctions within a circuit, while Kirchhoff's current law addresses the sum of potential differences around a closed loop. These laws provide a framework for understanding how currents and voltages distribute themselves within a circuit.

Ohm's law, another cornerstone of circuit theory, relates the voltage across a linear circuit element to the current flowing through it, with the proportionality constant



M. Okubo, *Electrical Sustainable Energy for Mechanical Engineering*,
https://doi.org/10.1007/978-981-96-5170-2_1

being the resistance. This simple yet powerful relationship allows for the analysis of linear circuit elements, which include resistors, capacitors, and inductors. Each of these elements behaves predictably under the influence of an applied voltage, and their combined behavior can be systematically analyzed using the principles outlined in this chapter.

We also explore the concept of displacement current, which extends the applicability of Maxwell's equations to circuits involving changing electric fields. This concept is particularly relevant in alternating current (AC) circuits, where time-varying currents and voltages are common.

The chapter then guides you through the analysis of both direct current (DC) and AC circuits. DC circuits, which involve constant currents and voltages, serve as the simplest context for applying Kirchhoff's laws and Ohm's law. AC circuits, however, introduce complexities due to the time-varying nature of their currents and voltages. Understanding these types of circuits requires additional concepts such as impedance and phase angles, which are covered in detail. Finally, we address transient phenomena in both DC and AC circuits. Transients occur when circuits switch states, such as when a switch is opened or closed. These phenomena are characterized by temporary deviations from the steady-state behavior of the circuit, and understanding them is crucial for the accurate analysis and design of electrical systems.

In summary, this chapter equips you with the knowledge of fundamental laws and techniques necessary for analyzing both simple and complex electrical circuits. By mastering these concepts, you are prepared to tackle a wide range of challenges in electrical engineering and related fields. Note that textbooks of electromagnetics, electrical circuits [6–12], mechanical vibration [13] and field theory and vector and tensor [14–17] are listed in references.

## 1.2 Maxwell's Equations and Law of Conservation of Charge

Maxwell's equations and law of conservation of charge are explained based on Ref. [1]. Electromagnetic properties are well described using Maxwell's equations:

(Gauss's law for electric charges)

$$\nabla \cdot \boldsymbol{D} = \rho \tag{1.1}$$

(Gauss's law for magnetic charges)

$$\nabla \cdot \boldsymbol{B} = 0 \tag{1.2}$$

(Faraday's law)

$$\nabla \times \boldsymbol{E} = -\frac{\partial \boldsymbol{B}}{\partial t} \tag{1.3}$$

(Maxwell–Ampere's law)

$$\nabla \times \boldsymbol{H} = \boldsymbol{J} + \frac{\partial \boldsymbol{D}}{\partial t} \tag{1.4}$$

where $\boldsymbol{D}$ represents the electric flux density vector, $\boldsymbol{B}$ represents the magnetic flux density vector, $\boldsymbol{E}$ represents the electric field vector, $\boldsymbol{H}$ represents the magnetic field vector, and $\rho$ represents the charge density. Maxwell's equations are four cornerstone equations that unify electric and magnetic fields. They provide a complete description of electromagnetic fields.

By calculating the divergence of both sides of Faraday's law given by Eq. (1.3), Gauss's law for magnetic charges, Eq. (1.2), can be derived from the vector formula $\nabla \cdot \nabla \times \boldsymbol{A} = \boldsymbol{0}$, where $\boldsymbol{A}$ is an arbitrary vector. Similarly, by calculating the divergence $\nabla \cdot$ of both sides of Maxwell–Ampere's law of Eq. (1.4), we obtain:

$$\nabla \cdot \boldsymbol{J} + \frac{\partial}{\partial t}(\nabla \cdot \boldsymbol{D}) = 0 \tag{1.5}$$

Substituting Gauss's law for electric charges, Eq. (1.1), into Eq. (1.5), we derive the equation of the law of conservation of charge:

$$\frac{\partial \rho}{\partial t} + \nabla \cdot \boldsymbol{J} = 0 \tag{1.6}$$

Multiplying this particle conservation law by mass gives the law of conservation of mass, and multiplying it by the charge $q$ of a charged particle gives the law of conservation of charge from Eq. (1.6).

Suppose charged particles are stored with a charge density $\rho = qn$ inside a certain volume $V$. Integrating Eq. (1.6) with respect to the volume $V$, we get:

$$\int_V \frac{\partial \rho}{\partial t} \mathrm{d}V + \int_V \nabla \cdot \boldsymbol{J} \mathrm{d}V = 0 \tag{1.7}$$

If this volume $V$ does not change over time, the first term on the left side of Eq. (1.7) becomes:

$$\text{The first term on the left side} = \frac{\mathrm{d}Q}{\mathrm{d}t} \tag{1.8}$$

However, the second term on the left side of Eq. (1.7) is converted to an integral on the surface $S$ of the volume $V$ by Gauss's theorem (divergence theorem). Further, by using the relationship between the current density and the current in Eq. (1.7), we obtain:

$$\int_V \nabla \cdot \boldsymbol{J} \mathrm{d}V = \oint_S \boldsymbol{J} \cdot \mathrm{d}\boldsymbol{S} = I_{\mathrm{out}} \tag{1.9}$$

The last term indicates that the current flowing out from volume $V$ is calculated as positive because $\mathrm{d}\boldsymbol{S}$ is the vector pointing outward from volume $V$. If the current flowing into volume $V$ is $I$, then $I_{\mathrm{out}} = -I$. From this, we obtain the relationship between current and charge:

$$I = \frac{\mathrm{d}Q}{\mathrm{d}t} \tag{1.10}$$

The relationship between electric current and charge is obtained. Equation (1.10) is the law of current and charge.

## 1.3 Kirchhoff's Current Law

Derivation of Kirchhoff's laws from Maxwell's equations is explained based on Ref. [1]. If there is no stored charged particles and the density of charged particles does not change over time, i.e., $\partial\rho/\partial t = 0$ in Eq. (1.6), the law of conservation of charge becomes:

(Equation of current continuity)

$$\nabla \cdot \boldsymbol{J} = 0 \tag{1.11}$$

Let us consider the case where N conductors are connected at a certain point, and a current $I$ is flowing through the conductors. Considering the volume $V$ surrounding the connection point and integrating Eq. (1.11) over it, we get:

$$\int_V \nabla \cdot \boldsymbol{J} \mathrm{d}V = \oint_S \boldsymbol{J} \cdot \mathrm{d}\boldsymbol{S} = \sum_{\mathrm{i}=1}^{\mathrm{N}} \oint_{S_{\mathrm{i}}} \boldsymbol{J}_{\mathrm{i}} \cdot \mathrm{d}\boldsymbol{S} = 0 \tag{1.12}$$

where $\boldsymbol{J}_{\mathrm{i}}$ is the current density of the current flowing through the ith conductor and represents the cross-section of the ith conductor. Furthermore, by using the relationship between current density and current in the third equation of Eq. (1.12), we obtain:

$$\sum_{\mathrm{i}=1}^{\mathrm{N}} I_{\mathrm{i}} = 0 \quad \text{(Kirchhoff's current law)} \tag{1.13}$$

This leads to the conclusion that "the sum of the currents flowing into any node in an electric circuit is zero." However, the sum of currents flowing out of a node is

calculated by assuming that a negative current flows in. This relationship is called Kirchhoff's current law.

## 1.4 Ohm's Law and Linear Circuit Element

Ohm's law and linear circuit element are explained based on Ref. [1]. Let us consider in more detail the situation where a collection of charged particles moves at a uniform speed through a conductor at an average speed of $\overline{u}$. Consider the tube illustrated in Fig. 1.1 with a cross-sectional area of $S$ and length of $L$. Furthermore, assume that an electric field $E$ is applied in the longitudinal direction of the tube. If there are freely moving charged particles (e.g., free electrons) with a charge of $q$ and mass $m$ inside this tube, they will be subjected to the Coulomb force due to the electric field. When a charged particle moves due to the Coulomb force, it will collide with solid particles. In the following, we will assume that all of the momentum of the charged particle is lost due to the collision with the particles.

$$\text{Momentum lost in one collision} = -m\boldsymbol{u} \tag{1.14}$$

Collisions with the particles become a kind of friction force for the motion of the charged particle. If the average collision time from when the charged particle starts moving until it collides is $\tau$, the equation of motion for each charged particle is

$$m\frac{\mathrm{d}\boldsymbol{u}}{\mathrm{d}t} = q\boldsymbol{E} - \frac{m\boldsymbol{u}}{\tau} \tag{1.15}$$

Although each particle has accelerated motion with a different velocity, the average velocity of the particles is the velocity at which the frictional and Coulomb forces are balanced. By setting the left side of the above equation to $\mathbf{0}$, the averaged velocity $\overline{\boldsymbol{u}}$ is expressed as follows:

$$\overline{\boldsymbol{u}} = \frac{q\tau}{m}\boldsymbol{E} \tag{1.16}$$

Furthermore, by using the relationship between the current density $\boldsymbol{J}$ and $\overline{\boldsymbol{u}}$, $\boldsymbol{J} = nq\overline{\boldsymbol{u}}$, it can be rewritten as follows:

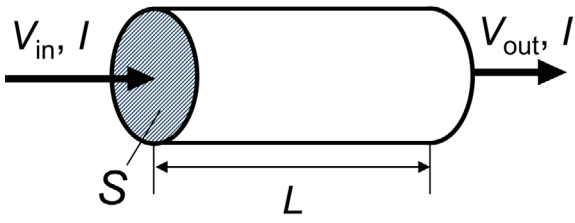


**Fig. 1.1** Model of moving charges in a tube [1]

$$\boldsymbol{J} = \frac{n\tau q^2}{m}\boldsymbol{E} \tag{1.17}$$

Equation (1.17) shows that the current density $\boldsymbol{J}$ is proportional to the electric field $\boldsymbol{E}$. The proportionality coefficient is called the electrical conductivity and is defined by the following equation:

$$\sigma = \frac{n\tau q^2}{m} \tag{1.18}$$

Using the electrical conductivity $\sigma$, Eq. (1.17) becomes:

$$\boldsymbol{J} = \sigma\boldsymbol{E} \tag{1.19}$$

Equation (1.19) is called Ohm's law in electromagnetism. The reciprocal of conductivity $\sigma$ is called resistivity $\rho$, and indicates how difficult it is for current to flow.

$$\rho = \frac{1}{\sigma} \tag{1.20}$$

These quantities represent the electrical properties of a material and are independent of the shape (length and cross-sectional area) of the material. Now, let us consider Fig. 1.1 again. Assume that the potential on the inlet side and the potential on the outlet side differ by a voltage of $V$. If the electric field is spatially uniform, the magnitude of the electric field is $E = V/L$. However, if we take the cross-sectional area of the rectangular solid as $S$, integrate $\boldsymbol{J}$ there, and then use Eq. (1.19), we get:

$$I = \int_S \boldsymbol{J} \cdot \mathrm{d}\boldsymbol{S} = JS = \sigma ES = \frac{\sigma S}{L}V \tag{1.21}$$

If we rearrange Eq. (1.21) with respect to $V$, we get:

$$V = \frac{L}{\sigma S}I \tag{1.22}$$

If the proportionality coefficient in the above formula is set to $R$,

$$V = RI \quad \text{(Ohm's law)} \tag{1.23}$$

$$R = \frac{L}{\sigma S} = \frac{\rho L}{S} \tag{1.24}$$

Equation (1.23) is usually called Ohm's law in electrical circuits. The resistance is called electrical resistance, or simply resistance, and its unit is Ω (ohm).

## 1.5 Kirchhoff's Voltage Law

Kirchhoff's voltage law from Maxwell's equations is derived based on Ref. [1]. Let us consider a closed circuit formed using resistors. By integrating the differential form of Ohm's law Eq. (1.19) around the closed curve, we get:

$$\oint_{\mathrm{C}} \boldsymbol{J} \cdot \mathrm{d}\boldsymbol{l} = \sigma \oint_{\mathrm{C}} \boldsymbol{E} \cdot \mathrm{d}\boldsymbol{l} = \int_{\mathrm{S}} \nabla \times \boldsymbol{E} \cdot \mathrm{d}\boldsymbol{S} \tag{1.25}$$

where C represents the integral path along the closed curve, and S represents the surface enclosed by Stokes' theorem is used to transform the second equation into the right-hand side. Considering an electromagnetic field that does not change over time and assuming that a direct current flows through the circuit, Faraday's law gives us the following:

$$\nabla \times \boldsymbol{E} = \boldsymbol{0} \tag{1.26}$$

$$\oint_{\mathrm{C}} \boldsymbol{J} \cdot \mathrm{d}\boldsymbol{l} = 0 \tag{1.27}$$

As shown, the contour integral of the current density along the circuit is zero. Since this is true for any C, it means that $\boldsymbol{J}$ is not equal to $\boldsymbol{0}$, which contradicts our experience of electric current flowing in a closed circuit. To resolve the difficulties, it is necessary to extend the differential form of Ohm's law shown in Eq. (1.19) as follows:

$$\boldsymbol{J} = \sigma\left(\boldsymbol{E} + \boldsymbol{E}'\right) \tag{1.28}$$

Equation (1.28) is called the generalized Ohm's law. $\boldsymbol{E}'$ is an electric field generated by effects outside the scope of electromagnetic considerations and should only be considered in the power supply portion of an electric circuit. Typically, it refers to the electric field generated by chemical reactions inside a battery and has the property of $\nabla \times \boldsymbol{E}' \neq 0$. Therefore, by integrating Eq. (1.28) along a closed circuit, we obtain:

$$\oint_{\mathrm{C}} \boldsymbol{J} \cdot \mathrm{d}\boldsymbol{l} = \oint_{\mathrm{C}} \sigma\left(\boldsymbol{E} + \boldsymbol{E}'\right) \cdot \mathrm{d}\boldsymbol{l} = \int_{\mathrm{S}} \sigma \nabla \times \boldsymbol{E}' \cdot \mathrm{d}\boldsymbol{S} \neq 0 \tag{1.29}$$

This explains how current flows in an electric circuit. When there are the number K electromotive forces in the integral of the power supply section,

$$\int_{\mathrm{C_P}} \boldsymbol{E}' \cdot \mathrm{d}\boldsymbol{l} = \sum_{\mathrm{k}=1}^{\mathrm{K}} V_{\mathrm{k}}' \tag{1.30}$$

and

$$\sum_{k=1}^{K} V'_k = \sum_{i=1}^{N} V_i \quad \text{(Kirchhoff's voltage law)} \tag{1.31}$$

holds. In other words, the sum of the electromotive forces present in a closed circuit and the sum of the voltages across the resistors are equal. Equation (1.31) is called Kirchhoff's voltage law.

## 1.6 Displacement Current

Displacement current is a current that arises when the surface integral of the normal component of the electric flux density on a closed surface changes over time.

$$I = \frac{d}{dt} \int_S \boldsymbol{D} \cdot d\boldsymbol{S} = 0 \tag{1.32}$$

Normally, electric current occurs due to the movement of electric charges; however, displacement current is not caused by the movement of electric charges, hence the name "displacement." Its unit is the ampere, similar to conventional current. Examples of displacement current include the current flowing through a dielectric inside a capacitor or between the internal electrodes of a plasma reactor. Although a dielectric is an insulator with no movement of electric charges inside, displacement current as described by Eq. (1.32) does flow.

(Poisson's equation)

$$\nabla^2 \phi = -\frac{\sigma}{\varepsilon} \tag{1.33}$$

where $\sigma$ is the space charge volume density (C/m$^3$) and is necessary to calculate the space potential $\phi$. It is generally difficult to calculate σ, so an approximate solution that expresses it as a function is used.

In this section, when deriving Kirchhoff's voltage law, we have considered a DC circuit with a battery as the power source and a resistor as the load. This law also applies to AC circuits as well as DC circuits. The power source can be something other than a battery, and the load can be a linear element such as a capacitor or coil, as will be shown in the following chapters, or even a nonlinear element such as a diode or transistor. However, it should be noted that Kirchhoff's voltage law no longer holds when the displacement current is significant.

## 1.7 DC Circuit and Calculations

Next, applications of electromagnetic theory for electrical circuits are explained based on Ref. [3]. Systems such as those shown in Fig. 1.1 are frequently found in magnetohydrodynamics (MHD) and plasma fluid system.

Discharge plasma forms in the MHD reactor in Fig. 1.2a and the plasma reactor in Fig. 1.2b. Its magnetohydrodynamic characteristics must be analyzed using equations; however, the electromagnetic circuit characteristics can be simplified to an equivalent circuit connected to a power supply + *LCR* in the steady state where the plasma is stabilized.

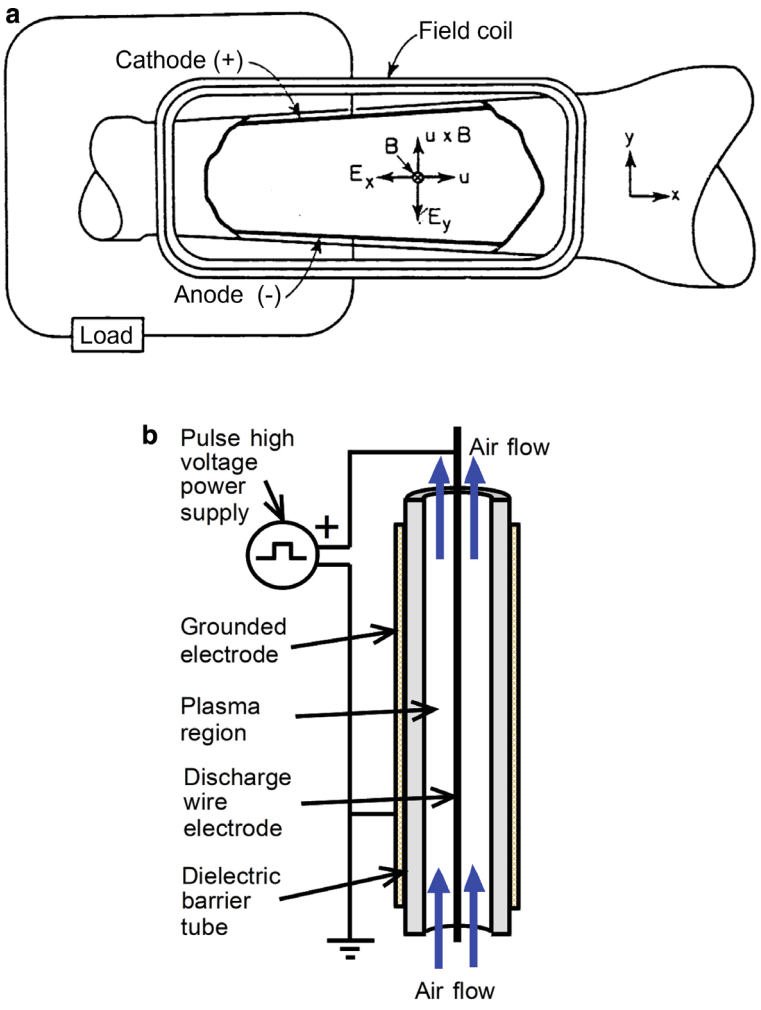


**Fig. 1.2** Target system: **a** MHD power generator [18] and **b** environmental plasma system [19]

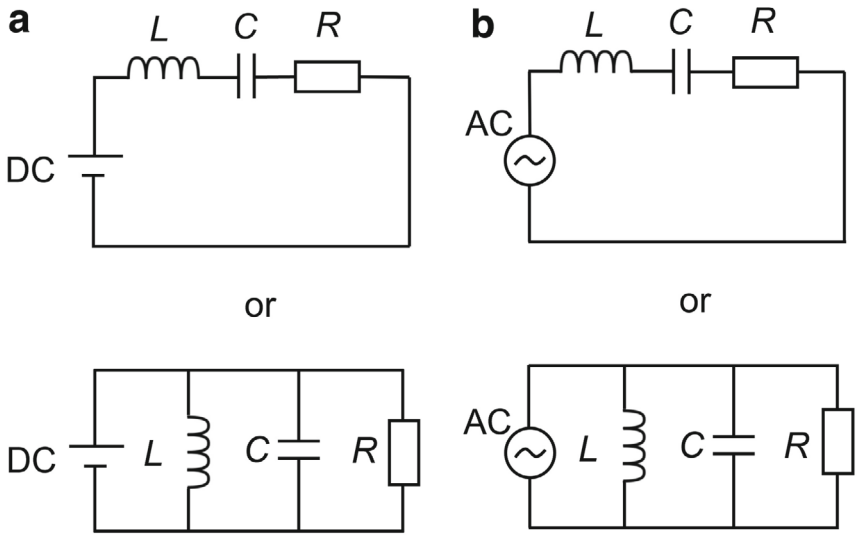


**Fig. 1.3** Equivalent circuit: **a** for the MHD power generator and **b** for the environmental plasma system

Whether the series circuit of the variable *LCR* power supply in the figure becomes a parallel circuit depends on the situation. Selection should be made appropriately to maximize power. In Chaps. 2–6, we explain the analysis method and matching of the circuit as illustrated in Fig. 1.3. This chapter covers the basics of power supplies and calculations.

An electric circuit is a combination of elements such as capacitance, electrical resistance, and inductance, connected by paths through which current flows. When analyzing an electric circuit, we do not consider the distribution of current density within a current path or the electric or magnetic fields surrounding it. The current path is treated as a thin conductor without resistance, inductance, or capacitance between other conductors.

Capacitance, resistance, and inductance have two terminals, and the physical conditions within them are not considered; only the voltage between the terminals and the current through the terminals are of concern. Since charge does not accumulate or dissipate along the current path, the value of the current remains constant throughout the path. Voltage and current whose magnitude and direction do not change over time are termed DC voltage and DC current, respectively, and form a DC circuit, which is essentially a combination of a DC power source and electrical resistance, as illustrated in Fig. 1.4.

DC power sources are usually represented as batteries. A power source moves charges using forces beyond electrostatic fields, creating an electromotive force between its terminals. Ohm's law is assumed to hold for resistance.

When resistors with resistance values $R_1$, $R_2$, … are connected in series, as illustrated in Fig. 1.5, the current $I$ through each resistor is common, and the voltage $V$

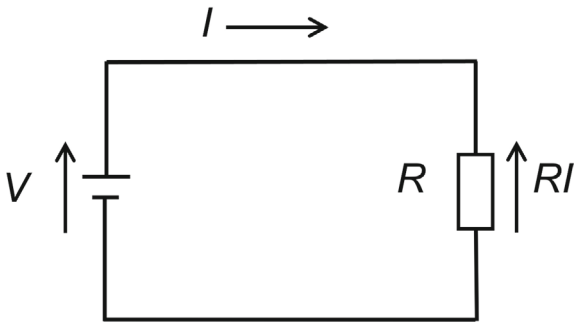


**Fig. 1.4** DC circuit

across the entire circuit is the sum of individual voltages: $V_1 = R_1 I$, $V_2 = R_2 I$, …, etc.

$$V = V_1 + V_2 + \cdots = (R_1 + R_2 + \cdots)I \tag{1.34}$$

The total resistance $R$ is given as follows:

$$R = \frac{V}{I} = R_1 + R_2 + \cdots \tag{1.35}$$

Thus, the total combined resistance equals the sum of the individual resistances. If resistors $R_1$ and $R_2$ are connected in series and a voltage $V$ is applied across them (Fig. 1.6), the current is as follows:

$$I = \frac{V}{R_1 + R_2} \tag{1.36}$$

The voltage $V_1$ across $R_1$ is as follows:

$$V_1 = R_1 I \tag{1.37}$$

Therefore,

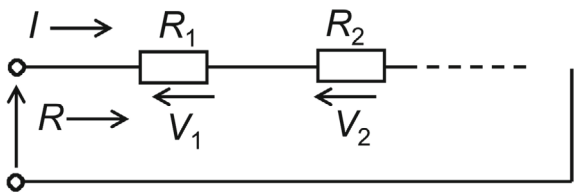


**Fig. 1.5** Series connection of resistors

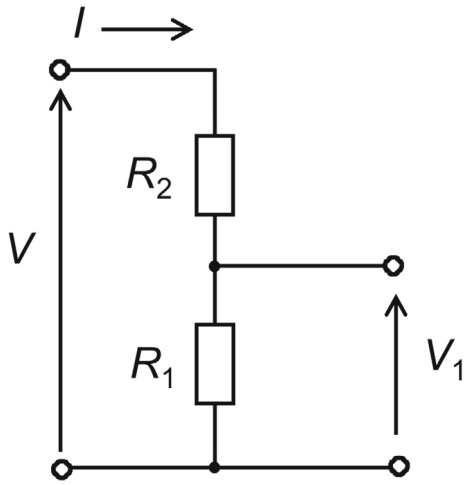


**Fig. 1.6** Voltage division by resistors

$$\frac{V_1}{V} = \frac{R_1}{R_1 + R_2} \tag{1.38}$$

The voltage $V$ is distributed in proportion to the resistance ratio. A series combination of resistors extracting an exact fraction of a given voltage is termed a voltage divider, frequently used in voltage measurement.

When resistors with resistances $R_1, R_2, \ldots$ are connected in parallel, as illustrated in Fig. 1.7, the voltage $V$ across each resistor is common, and the total current I is the sum of individual currents $I_1 = V/R_1, I_2 = V/R_2$, that flow through each resistor.

$$I = I_1 + I_2 + \cdots = \left(\frac{1}{R_1} + \frac{1}{R_2} + \cdots\right)V \tag{1.39}$$

The total combined resistance $R$ is

$$\frac{1}{R} = \frac{I}{V} = \frac{1}{R_1} + \frac{1}{R_2} + \cdots \tag{1.40}$$

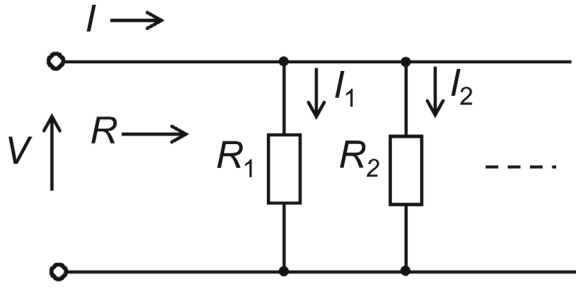


**Fig. 1.7** Parallel connection of resistors

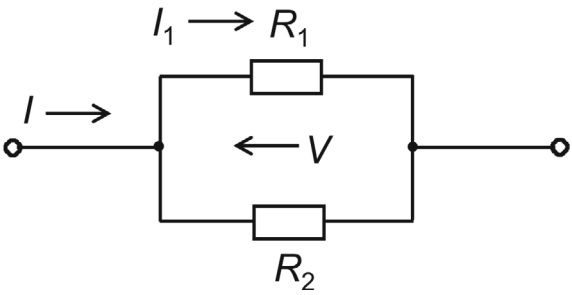


**Fig. 1.8** Shunt resistor

The reciprocal of the total resistance equals the sum of the reciprocals of individual resistances.

The conductance of each resistor is $G_1 = 1/R_1$, $G_2 = 1/R_2$, etc., so the total conductance $G = 1/R$ is

$$G = G_1 + G_2 + \cdots \tag{1.41}$$

For two resistors $R_1$ and $R_2$ connected in parallel, the combined resistance $R$ is

$$R = \frac{1}{\frac{1}{R_1} + \frac{1}{R_2}} = \frac{R_1 R_2}{R_1 + R_2} \tag{1.42}$$

If resistors $R_1$ and $R_2$ are connected in parallel and a current $I$ flows through them (Fig. 1.8), the voltage $V$ across both resistors is common:

$$V = \frac{R_1 R_2}{R_1 + R_2} I \tag{1.43}$$

The current $I_1$ through $R_1$ is

$$I_1 = \frac{V}{R_1} = \frac{R_2}{R_1 + R_2} I \tag{1.44}$$

Therefore,

$$\frac{I_1}{I} = \frac{R_2}{R_1 + R_2} \tag{1.45}$$

The current $I$ is distributed in the inverse ratio of the resistances. A resistor connected in parallel to extract a specific fraction of a current is termed a current shunt, often used in current measurement.

In circuits with complex resistor combinations, such as series and parallel configurations, they can often be broken into simpler series and parallel components. For example, in the combination illustrated in Fig. 1.9, the parallel combination of $R_2$

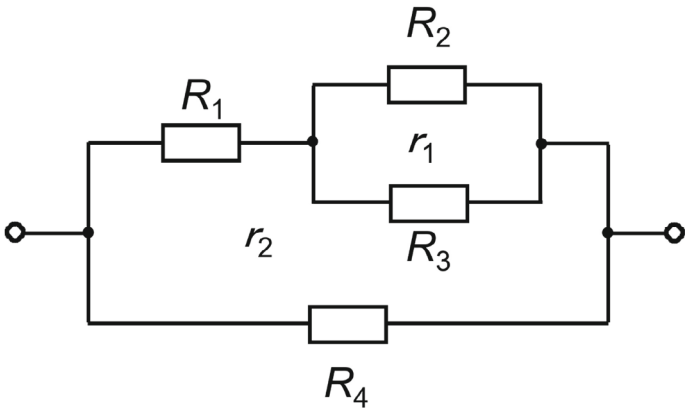


**Fig. 1.9** Series–parallel circuit of resistors

and $R_3$ yields a combined value $r_1$:

$$r_1 = \frac{R_2 R_3}{R_2 + R_3} \tag{1.46}$$

Next, combining this with $R_1$ in series gives the resistance $r_2$ of the upper path:

$$r_2 = R_1 + r_1 = R_1 + \frac{R_2 R_3}{R_2 + R_3} = \frac{R_1 R_2 + R_1 R_3 + R_2 R_3}{R_2 + R_3} \tag{1.47}$$

Finally, the total resistance is $r_2$ and $R_4$ in parallel, yielding:

$$R = \frac{R_4 r_2}{R_4 + r_2} = \frac{R_4 \frac{R_1 R_2 + R_1 R_3 + R_2 R_3}{R_2 + R_3}}{R_4 + \frac{R_1 R_2 + R_1 R_3 + R_2 R_3}{R_2 + R_3}} = \frac{R_1 R_2 + R_1 R_3 + R_2 R_3}{R_2 R_4 + R_3 R_4 + R_1 R_2 + R_1 R_3 + R_2 R_3} R_4 \tag{1.48}$$

## 1.8 AC Circuit and Calculation

For an AC circuit, resistance, inductance, and capacitance can be considered analogous to resistance in a DC circuit. Resistance in an AC circuit is termed impedance $Z$. The voltage drops across these elements in an AC circuit are expressed as follows:

**Inductance**: The inductance of the coil is expressed as a complex number $i\omega LI$:

$$V_L = L\frac{\mathrm{d}I}{\mathrm{d}t} = i\omega LI \tag{1.49}$$

**Resistance**: The voltage drop is the same as in a DC circuit:

$$V_R = IR \tag{1.50}$$

**Capacitance**: The voltage drop is determined by the relationship $\mathrm{d}Q/\mathrm{d}t = I$:

$$V_C = \frac{Q}{C} = \frac{1}{C}\int I\,\mathrm{d}t = \frac{I}{i\omega C}, \quad \left(\frac{\mathrm{d}Q}{\mathrm{d}t} = I\right) \tag{1.51}$$

where $i$ is the imaginary unit ($i = \sqrt{-1}$). The total voltage drop across the series circuit is the sum of these individual voltage drops:

$$V_L + V_R + V_C = L\frac{\mathrm{d}I}{\mathrm{d}t} + IR + \frac{1}{C}\int I\,\mathrm{d}t = \left(i\omega L + R + \frac{1}{i\omega C}\right)I = ZI \tag{1.52}$$

where $Z$ is the impedance of the series circuit. Using a similar method as explained in Sect. 1.7 for DC circuits, calculations should be performed. A detailed procedure will be treated in Chap. 2.

## 1.9 Transient Phenomena in DC and AC Circuits

### *1.9.1 Transient Phenomena in DC Circuit*

In this section, we explain the transient phenomena in an *LCR* series circuit connected to a DC power source based on the explanation of Ref. [4]. DC circuits and steady-state solutions, as well as non-steady-state solutions or transient phenomena in *LCR* series circuits, are described as an example for the treatment of electrical circuits.

Figure 1.10 illustrates an *RLC* series circuit connected to a DC power source $E$, resistance $R$, inductance $L$, and capacitance $C$. Here, $C$ is assumed to be uncharged before the switch is turned on. Applying Ohm's law to the circuit, the circuit equation is

$$L\frac{\mathrm{d}I}{\mathrm{d}t} + RI + \frac{1}{C}\int I\,\mathrm{d}t = E \tag{1.53}$$

When solving Eq. (1.53) to determine the current $I$, the solution to the equation is

$$I = I_\mathrm{t} + I_\mathrm{s} \tag{1.54}$$

Substituting Eq. (1.54) into Eq. (1.53) we obtain two equations for $I_\mathrm{t}$ and $I_\mathrm{s}$

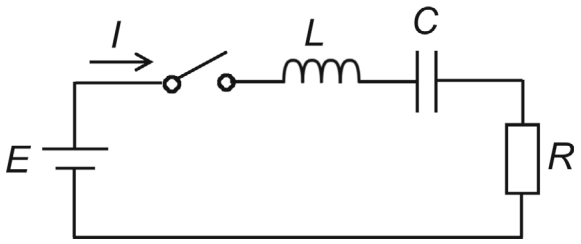


**Fig. 1.10** DC *LCR* series circuit

$$L\frac{\mathrm{d}I_\mathrm{t}}{\mathrm{d}t} + RI_\mathrm{t} + \frac{1}{C}\int I_\mathrm{t}\mathrm{d}t = 0 \tag{1.55}$$

$$L\frac{\mathrm{d}I_\mathrm{s}}{\mathrm{d}t} + RI_\mathrm{s} + \frac{1}{C}\int I_\mathrm{s}\mathrm{d}t = E \tag{1.56}$$

Equation (1.55) is an equation that should only be considered in the transient state (mathematically, it is a homogeneous equation), and both sides converge to 0 as $t \to \infty$. Equation (1.56) holds in the steady state. Equation (1.55) should be first solved to find the transient solution $I_\mathrm{t}$. Differentiating both sides of Eq. (1.55) with respect to $t$:

$$L\frac{\mathrm{d}^2 I_\mathrm{t}}{\mathrm{d}t^2} + R\frac{\mathrm{d}I_\mathrm{t}}{\mathrm{d}t} + \frac{I_\mathrm{t}}{C} = 0 \tag{1.57}$$

Let the solution of Eq. (1.57) be $I_\mathrm{t} = A\mathrm{e}^{Bt}$ ($A$ and $B$ are complex constants). $B$ is determined as follows:

$$B = -\frac{R}{2L} \pm \sqrt{\left(\frac{R}{2L}\right)^2 - \frac{1}{LC}} \tag{1.58}$$

Therefore, the transient solution $I_\mathrm{t}$ is given by:

$$I_\mathrm{t} = \mathrm{e}^{-\frac{R}{2L}t}\left[A_1\mathrm{e}^{\sqrt{\left(\frac{R}{2L}\right)^2 - \frac{1}{LC}}t} + A_2\mathrm{e}^{-\sqrt{\left(\frac{R}{2L}\right)^2 - \frac{1}{LC}}t}\right] \tag{1.59}$$

where $A_1$ and $A_2$ are complex constants.

The behavior of $I_\mathrm{t}$ depends on the magnitude of $\alpha^2$ and ${\omega_0}^2$, as the sign of $\left\{[R/(2L)]^2 - 1/(LC)\right\}$ in the square root in Eq. (1.58) determines the behavior. From now on, we set $\alpha = R/(2L)$, $\omega_0 = 1/\sqrt{LC}$, and $\left\{[R/(2L)]^2 - 1/(LC)\right\} = \alpha^2 - \omega_0^2$.

### 1.9.1.1 Case of $\alpha^2 > {\omega_0}^2$

When $\alpha^2 - {\omega_0}^2 > 0$, that is, $\alpha^2 > {\omega_0}^2$, Eq. (1.59) becomes:

$$I_{\mathrm{t}} = \mathrm{e}^{-\alpha t}\left(A_1 \mathrm{e}^{\sqrt{\alpha^2-\omega_0^2}t} + A_2 \mathrm{e}^{-\sqrt{\alpha^2-\omega_0^2}t}\right) \tag{1.60}$$

To determine $A_1$ and $A_2$, check the initial conditions at $t = 0$. At $t = 0$, immediately after the switch is turned on, no current flows through the circuit in Fig. 1.10 due to the action of inductance $L$:

$$I|_{t=0} = A_1 + A_2 = 0 \tag{1.61}$$

At this time, the voltage across $L$ is equal to the DC power supply voltage $E$, therefore,

$$A_1 = \frac{E}{2L\sqrt{\alpha^2 - \omega_0^2}} = -A_2 \tag{1.62}$$

Substituting Eq. (1.62) into Eq. (1.60), the transient solution $I_{\mathrm{t}}$ becomes:

$$\begin{aligned} I_{\mathrm{t}} &= \frac{E}{2L\sqrt{\alpha^2 - \omega_0^2}} \mathrm{e}^{-\alpha t}\left(\mathrm{e}^{\sqrt{\alpha^2-\omega_0^2}t} - \mathrm{e}^{-\sqrt{\alpha^2-\omega_0^2}t}\right) \\ &= \frac{E}{L\sqrt{\alpha^2 - \omega_0^2}} \mathrm{e}^{-\alpha t} \sinh\sqrt{\alpha^2 - \omega_0^2}t \end{aligned} \tag{1.63}$$

This represents a hyperbolic function decaying with time.

### 1.9.1.2 Case of $\alpha^2 = \omega_0^2$

When $\alpha^2 - {\omega_0}^2$=0, that is, $\alpha^2 = {\omega_0}^2$, the solution of Eq. (1.57) is set as $I_{\mathrm{t}} = A(t)\mathrm{e}^{-\alpha t}$. Substituting this into Eq. (1.57):

$$L\frac{\mathrm{d}^2A(t)}{\mathrm{d}t^2} + (-2\alpha L + R)\frac{\mathrm{d}A(t)}{\mathrm{d}t} + \left(\alpha^2 L - \alpha R + \frac{1}{C}\right)A(t) = 0 \tag{1.64}$$

The coefficients of the second and third terms of Eq. (1.64) are

$$-2\alpha L + R = -2\frac{R}{2L}L + R = 0 \tag{1.65}$$

$$\alpha^2 L - \alpha R + \frac{1}{C} = \omega_0^2 L - \alpha R + \frac{1}{C} = \frac{1}{C} - \frac{R^2}{2L} + \frac{1}{C} = 0 \tag{1.66}$$

Therefore, Eq. (1.64) becomes:

$$L\frac{\mathrm{d}^2A(t)}{\mathrm{d}t^2} = 0 \tag{1.67}$$

and

$$A(t) = A_1 + A_2 t \tag{1.68}$$

where $A_1$ and $A_2$ are constants. From Eq. (1.68), the transient solution $I_\mathrm{t}$ is

$$I_\mathrm{t} = (A_1 + A_2 t)e^{-\alpha t} \tag{1.69}$$

From the initial conditions at $t = 0$, $I_\mathrm{t}|_{t=0} = 0$ and $L(\mathrm{d}I_\mathrm{t}/\mathrm{d}t)|_{t=0} = E$, we obtain $A_2 = E/L$. Therefore, the transient solution $I_\mathrm{t}$ is

$$I_t = \frac{E}{L} t e^{-\alpha t} \tag{1.70}$$

#### 1.9.1.3 Case of $\alpha^2 < \omega_0{}^2$

When $\alpha^2 - \omega_0{}^2 < 0$, that is, $\alpha^2 < \omega_0{}^2$, Eq. (1.59) becomes:

$$I_\mathrm{t} = e^{-\alpha t}\left(A_1 \mathrm{e}^{i\sqrt{\omega_0^2-\alpha^2}t} + A_2 \mathrm{e}^{-i\sqrt{\omega_0^2-\alpha^2}t}\right) \tag{1.71}$$

where $i = \sqrt{-1}$. From the initial conditions at $t = 0$, $I_\mathrm{t}|_{t=0} = 0$, $L(\mathrm{d}I_\mathrm{t}/\mathrm{d}t)|_{t=0} = E$,

$$I|_{t=0} = A_1 + A_2 = 0 \tag{1.72}$$

$$\begin{aligned} L\left.\frac{\mathrm{d}I_\mathrm{t}}{\mathrm{d}t}\right|_{t=0} &= L\Big[-\alpha \mathrm{e}^{-\alpha t}\left(A_1 \mathrm{e}^{i\sqrt{\omega_0^2-\alpha^2}t} + A_2 \mathrm{e}^{-i\sqrt{\omega_0^2-\alpha^2}t}\right) \\ &\quad + \mathrm{e}^{-\alpha t}\left(i\sqrt{\omega_0^2-\alpha^2}A_1 \mathrm{e}^{i\sqrt{\omega_0^2-\alpha^2}t} - i\sqrt{\omega_0^2-\alpha^2}A_2 \mathrm{e}^{-i\sqrt{\omega_0^2-\alpha^2}t}\right)\Big]\Big|_{t=0} \\ &= L\left[-\alpha(A_1 + A_2) + i\sqrt{\omega_0^2-\alpha^2}A_1 - i\sqrt{\omega_0^2-\alpha^2}A_2\right] \\ &= i2L\sqrt{\omega_0^2-\alpha^2}A_1 = E \end{aligned} \tag{1.73}$$

Therefore

$$A_1 = \frac{E}{2iL\sqrt{\omega_0^2-\alpha^2}} = -A_2 \tag{1.74}$$

Substituting Eq. (1.74) into Eq. (1.71), the transient solution $I_\mathrm{t}$ becomes:

$$I_{\mathrm{t}} = \frac{E}{i2L\sqrt{\omega_0^2 - \alpha^2}} \mathrm{e}^{-\alpha t} \left( \mathrm{e}^{i\sqrt{\omega_0^2 - \alpha^2}t} - \mathrm{e}^{-i\sqrt{\omega_0^2 - \alpha^2}t} \right)$$
$$= \frac{E}{L\sqrt{\omega_0^2 - \alpha^2}} \mathrm{e}^{-\alpha t} \sin \sqrt{\omega_0^2 - \alpha^2}\, t \tag{1.75}$$

#### 1.9.1.4 Derivation of Steady-State Solution

Next, Eq. (1.56) is solved to obtain the steady-state solution. Differentiating both sides of Eq. (1.56) with respect to $t$,

$$L\frac{\mathrm{d}^2 I_{\mathrm{s}}}{\mathrm{d}t^2} + R\frac{\mathrm{d}I_{\mathrm{s}}}{\mathrm{d}t} + \frac{I_{\mathrm{s}}}{C} = 0 \tag{1.76}$$

Equation (1.76) is also valid in the steady state, that is, when $t \to \infty$. In this case, as there is no variation in the current value, we obtain:

$$\frac{\mathrm{d}^2 I_{\mathrm{s}}}{\mathrm{d}t^2} = 0, \quad \frac{\mathrm{d}I_{\mathrm{s}}}{\mathrm{d}t} = 0, \quad I_{\mathrm{s}} = 0 \tag{1.77}$$

Therefore, the steady-state solution is $I_{\mathrm{s}}$ vanishes. In other words, no current flows in the circuit in the steady state.

#### 1.9.1.5 General Solution for DC Circuit

To summarize the results in the previous sections, the general solution of the current flowing in the circuit in Fig. 1.10 is

$$I = \begin{cases} \frac{E}{L\sqrt{\alpha^2 - \omega_0^2}} e^{-\alpha t} \sinh \sqrt{\alpha^2 - \omega_0^2}\, t & \left(\alpha^2 > \omega_0^2\right) \\ \frac{E}{L} t e^{-\alpha t} & \left(\alpha^2 = \omega_0^2\right) \\ \frac{E}{L\sqrt{\omega_0^2 - \alpha^2}} e^{-\alpha t} \sin \sqrt{\omega_0^2 - \alpha^2}\, t & \left(\alpha^2 < \omega_0^2\right) \end{cases} \tag{1.78}$$

where $\alpha = R/(2L)$, $\omega_0 = 1/\sqrt{LC}$, $f_0 = 1/(2\pi\sqrt{LC})$.

Figure 1.11 illustrates the graph of the obtained current $I$. From the figure, when $\alpha^2 > {\omega_0}^2$ (orange waveform), the current slowly decays over time (overdamping). When the values of $R$, $L$, and $C$ are such that $\alpha^2 = {\omega_0}^2$ (gray waveform), the damping is most rapid (critical damping). Furthermore, when $\alpha^2 < {\omega_0}^2$ (blue waveform), the current oscillates while damping (damped oscillation or underdamping).

### 1.9.2 Transient Phenomena in AC Circuit

We explain the transient phenomena in an *LCR* series circuit connected to an AC power source. AC circuits and steady-state solutions, as well as non-steady-state solutions or transient phenomena in *LCR* series circuits, are described based on the explanation of Ref. [5] as an example for the treatment of electrical circuits.

Figure 1.12 illustrates an *LCR* series circuit connected to an AC power source $E = E_{\mathrm{m}} \sin \omega t$ with a peak value $E_{\mathrm{m}}$ and frequency $\omega$, resistance $R$, inductance $L$, and capacitance $C$. Note that $C$ is not charged before the switch is turned on. When Kirchhoff's second law is applied to an AC circuit with power source $E = E_{\mathrm{m}} \sin \omega t$ in Fig. 1.12, the circuit equation is

$$L\frac{\mathrm{d}I}{\mathrm{d}t} + RI + \frac{1}{C}\int I\,\mathrm{d}t = E_{\mathrm{m}} \sin \omega t \tag{1.79}$$

The solution of the circuit equation is obtained. When solving Eq. (1.79) for the current $I$, assuming the transient solution $I_{\mathrm{t}}$ and the steady-state solution $I_{\mathrm{s}}$, the solution of Eq. (1.79) is

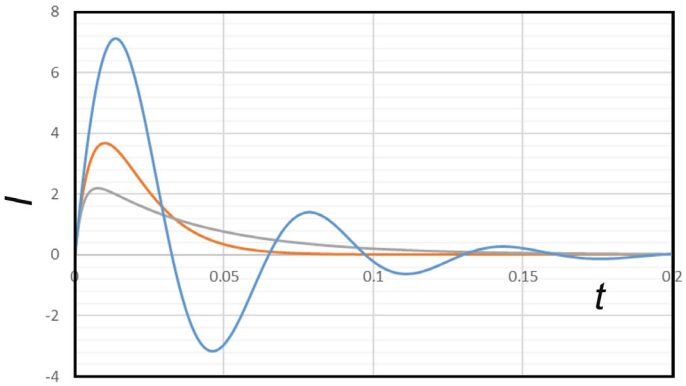


**Fig. 1.11** Graph of current in *LCR* series circuit ($L = 0.1$ μH, $C = 0.1$ μF, $R = 0.5$, 2, 4 Ω, and $E_{\mathrm{m}} = 10$ V)

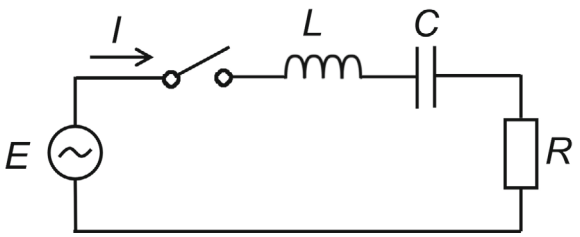


**Fig. 1.12** AC *LCR* series circuit

$$I = I_\mathrm{t} + I_\mathrm{s} \tag{1.80}$$

Substituting Eq. (1.80) into Eq. (1.79):

$$\left(L\frac{\mathrm{d}I_\mathrm{t}}{\mathrm{d}t} + RI_\mathrm{t} + \frac{1}{C}\int I_\mathrm{t}\mathrm{d}t\right) + \left(L\frac{\mathrm{d}I_\mathrm{s}}{\mathrm{d}t} + RI_\mathrm{s} + \frac{1}{C}\int I_\mathrm{s}\mathrm{d}t\right) = E_\mathrm{m}\sin\omega t \tag{1.81}$$

Equation (1.81) is separated into two equations for $I_\mathrm{t}$ and $I_\mathrm{s}$, respectively,

$$L\frac{\mathrm{d}I_\mathrm{t}}{\mathrm{d}t} + RI_\mathrm{t} + \frac{1}{C}\int I_\mathrm{t}\mathrm{d}t = 0 \tag{1.82}$$

$$L\frac{\mathrm{d}I_\mathrm{s}}{\mathrm{d}t} + RI_\mathrm{s} + \frac{1}{C}\int I_\mathrm{s}\mathrm{d}t = E_\mathrm{m}\sin\omega t \tag{1.83}$$

Equation (1.82) is an equation that should only be considered in the transient state, and both sides converge to 0 as $t \to \infty$. Equation (1.83) is an equation that holds in the steady state with a non-zero right-hand side. To solve the target Eq. (1.79), first, we should obtain the transient solution $I_\mathrm{t}$. From Eq. (1.82),

$$L\frac{\mathrm{d}^2 I_\mathrm{t}}{\mathrm{d}t^2} + R\frac{\mathrm{d}I_\mathrm{t}}{\mathrm{d}t} + \frac{I_\mathrm{t}}{C} = 0 \tag{1.84}$$

Equation (1.84) can be solved in the same way as for the DC circuit in previous section, and the solution is the same as Eq. (1.59) and

$$\begin{aligned} I_\mathrm{t} &= A_1\mathrm{e}^{\left[-\frac{R}{2L}+\sqrt{\left(\frac{R}{2L}\right)^2-\frac{1}{LC}}\right]t} + A_2\mathrm{e}^{\left[-\frac{R}{2L}-\sqrt{\left(\frac{R}{2L}\right)^2-\frac{1}{LC}}\right]t} \\ &= \mathrm{e}^{-\alpha t}\left(A_1\mathrm{e}^{\sqrt{\alpha^2-\omega_0^2}t} + A_2\mathrm{e}^{-\sqrt{\alpha^2-\omega_0^2}t}\right) \end{aligned} \tag{1.85}$$

where $A_1$ and $A_2$ are constants, and $\alpha = R/(2L)$, $\omega_0 = 1/\sqrt{LC}$.

Next, derivation of steady-state solution is explained.

$$L\frac{\mathrm{d}I_\mathrm{s}}{\mathrm{d}t} + RI_\mathrm{s} + \frac{1}{C}\int I_\mathrm{s}\mathrm{d}t = E_\mathrm{m}\sin\omega t \tag{1.86}$$

is solved to obtain the steady-state solution. Differentiating both sides of Eq. (1.86) with respect to $t$,

$$L\frac{\mathrm{d}^2 I_\mathrm{s}}{\mathrm{d}t^2} + R\frac{\mathrm{d}I_\mathrm{s}}{\mathrm{d}t} + \frac{1}{C}I_\mathrm{s} = \omega E_\mathrm{m}\cos\omega t \tag{1.87}$$

The detailed method of solving this equation for steady-state solution will be explained in next Chap. 2 using complex analysis. Only the result is presented here. The steady-state solution $i_\mathrm{s}$ is

$$I_s = \frac{E_\mathrm{m}}{\sqrt{R^2 + \left(\omega L - \frac{1}{\omega C}\right)^2}} \sin(\omega t - \varphi) \tag{1.88}$$

where, $\varphi = \tan^{-1}\{[\omega L - 1/(\omega C)]/R\}$. Equation (1.88) is the steady-state solution of Eq. (1.86). Substituting Eqs. (1.85) and (1.88) into Eq. (1.80), the current $I$ is determined as

$$I = \mathrm{e}^{-\alpha t}\left(A_1 \mathrm{e}^{-\alpha+\beta t} + A_2 \mathrm{e}^{-\alpha-\beta t}\right) + I_\mathrm{m} \sin(\omega t - \varphi) \tag{1.89}$$

where $\beta = \sqrt{\alpha^2 - \omega_0^2}$, $I_\mathrm{m} = E_\mathrm{m}/\sqrt{R^2 + [\omega L - 1/(\omega C)]^2}$.

For Eq. (1.89), the next three cases are considered.

#### 1.9.2.1 Transient Solution: Case of $\alpha^2 > \omega_0{}^2$

When $\alpha^2 - \omega_0{}^2 > 0$, that is, $\alpha^2 > \omega_0{}^2$, integrating both sides of Eq. (1.89) with respect to $t$ gives the circuit charge $q$:

$$q = \frac{A_1}{-\alpha + \beta} \mathrm{e}^{(-\alpha+\beta)t} + \frac{A_2}{-\alpha - \beta} \mathrm{e}^{(-\alpha-\beta)t} - \frac{I_\mathrm{m}}{\omega} \cos(\omega t - \varphi) \tag{1.90}$$

where the integral constant is calculated as 0. At $t = 0$, the circuit current $I$ and charge $q$ are 0, so from Eqs. (1.89) and (1.90):

$$I|_{t=0} = A_1 + A_2 - I_\mathrm{m} \sin\varphi = 0 \tag{1.91}$$

$$q|_{t=0} = \frac{A_1}{-\alpha + \beta} + \frac{A_2}{-\alpha - \beta} - I_\mathrm{m} \cos\varphi = 0 \tag{1.92}$$

From Eqs. (1.91) and (1.92), $A_1$ and $A_2$ are

$$A_1 = \frac{I_\mathrm{m}}{2\beta}\left[(-\alpha + \beta)\sin\varphi - \frac{\alpha^2 - \beta^2}{\omega}\cos\varphi\right] \tag{1.93}$$

$$A_2 = \frac{I_\mathrm{m}}{2\beta}\left[(\alpha + \beta)\sin\varphi + \frac{\alpha^2 - \beta^2}{\omega}\cos\varphi\right] \tag{1.94}$$

Therefore, from Eq. (1.89), the current $I$ is

$$I = \frac{I_\mathrm{m}}{2\beta}\mathrm{e}^{-\alpha t}\left\{\left[(-\alpha + \beta)\sin\varphi - \frac{\alpha^2 - \beta^2}{\omega}\cos\varphi\right]\mathrm{e}^{\beta t} + \left[(\alpha + \beta)\sin\varphi + \frac{\alpha^2 - \beta^2}{\omega}\cos\varphi\right]\mathrm{e}^{-\beta t}\right\} + I_\mathrm{m}\sin(\omega t - \varphi)$$

$$= I_{\mathrm{m}}\left\{\mathrm{e}^{-\alpha t}\left[\sin\varphi\cosh\beta t - \left(\frac{\alpha}{\beta}\sin\varphi + \frac{\alpha^2-\beta^2}{\omega\beta}\cos\varphi\right)\sinh\beta t\right]\right.$$
$$\left. + \sin(\omega t-\varphi)\right\} \tag{1.95}$$

### 1.9.2.2 Transient Solution: Case of $\alpha^2 = {\omega_0}^2$

When $\alpha^2 - {\omega_0}^2 = 0$, that is, $\alpha^2 = {\omega_0}^2$, the current $I$ can be obtained by setting $\beta \to 0$ in Eq. (1.95). Using the formula for the limit value of hyperbolic functions:

$$\lim_{\beta\to 0}\cosh\beta t = 1 \tag{1.96}$$

$$\lim_{\beta\to 0}\frac{\sinh\beta t}{\beta} = t \tag{1.97}$$

From Eq. (1.95):

$$I = \lim_{\beta\to 0} I_{\mathrm{m}}\mathrm{e}^{-\alpha t}\left[\sin\varphi\cosh\beta t - \left(\alpha\sin\varphi + \frac{\alpha^2-\beta^2}{\omega}\cos\varphi\right)\frac{\sinh\beta t}{\beta}\right]$$
$$+ I_{\mathrm{m}}\sin(\omega t-\varphi)$$
$$= I_{\mathrm{m}}\left\{\mathrm{e}^{-\alpha t}\left[\sin\varphi - \left(\alpha\sin\varphi + \frac{\alpha^2}{\omega}\cos\varphi\right)t\right] + \sin(\omega t-\varphi)\right\} \tag{1.98}$$

### 1.9.2.3 Transient Solution: Case of $\alpha^2 < {\omega_0}^2$

When $\alpha^2 - {\omega_0}^2 < 0$, that is, $\alpha^2 < {\omega_0}^2$, the current $I$ can be obtained by setting $\beta = i\sqrt{\omega_0^2 - \alpha^2} = i\gamma$ in Eq. (1.95), where $i = \sqrt{-1}$. In this case, the relationship between hyperbolic functions and trigonometric functions:

$$\cosh i\gamma t = \frac{\mathrm{e}^{i\gamma t} + \mathrm{e}^{-i\gamma t}}{2} = \cos\gamma t \tag{1.99}$$

$$\sinh i\gamma t = i\frac{\mathrm{e}^{i\gamma t} - \mathrm{e}^{-i\gamma t}}{2i} = i\sin\gamma t \tag{1.100}$$

holds. Therefore, Eq. (1.95) can be expressed as follows:

$$I = I_{\mathrm{m}}\mathrm{e}^{-\alpha t}\left\{\left[\sin\varphi\cos\gamma t - \left(\frac{\alpha}{\gamma}\sin\varphi + \frac{\alpha^2+\gamma^2}{\omega\gamma}\cos\varphi\right)\sin\gamma t\right] + \sin(\omega t-\varphi)\right\} \tag{1.101}$$

#### 1.9.2.4 General Solution for AC Circuit

To summarize the discussion up to the previous section, the general solution of the current flowing through the circuit in Fig. 1.11 is given by Eqs. (1.95), (1.98), and (1.101):

$$I = \begin{cases} I_{\mathrm{m}}\left\{\mathrm{e}^{-\alpha t}\left[\sin\varphi\cosh\beta t - \left(\dfrac{\alpha}{\beta}\sin\varphi + \dfrac{\alpha^2-\beta^2}{\omega\beta}\cos\varphi\right)\sinh\beta t\right] + \sin(\omega t-\varphi)\right\} \\ \left(\alpha^2 > \omega_0^2\right) \\ I_{\mathrm{m}}\left\{\mathrm{e}^{-\alpha t}\left[\sin\varphi - \left(\alpha\sin\varphi + \dfrac{\alpha^2}{\omega}\cos\varphi\right)t\right] + \sin(\omega t-\varphi)\right\} \\ \left(\alpha^2 = \omega_0^2\right) \\ I_{\mathrm{m}}\left\{\mathrm{e}^{-\alpha t}\left[\sin\varphi\cos\gamma t - \left(\dfrac{\alpha}{\gamma}\sin\varphi + \dfrac{\alpha^2+\gamma^2}{\omega\gamma}\cos\varphi\right)\sin\gamma t\right] + \sin(\omega t-\varphi)\right\} \\ \left(\alpha^2 < \omega_0^2\right) \end{cases} \tag{1.102}$$

where $I_{\mathrm{m}} = E_{\mathrm{m}}/\sqrt{R^2+[\omega L-1/(\omega C)]^2}$, $\varphi = \tan^{-1}[\omega L-1/(\omega C)]/R$, $\alpha = R/(2L)$, $\omega_0 = 1/\sqrt{LC}$, $\beta = \sqrt{\alpha^2-\omega_0^2}$, $\gamma = \sqrt{\omega_0^2-\alpha^2}$.

Figure 1.13 illustrates a graph of the calculated current $I$. From the figure, when $\alpha^2 > {\omega_0}^2$ (orange waveform), the peak value is suppressed near $t = 0$ when the switch is turned on due to the influence of the transient term. However, as time t progresses, the waveform approaches a sine wave, representing the steady-state term (overdamping). When the values of $R$, $L$, and $C$ are changed and $\alpha^2 = {\omega_0}^2$ is set (gray waveform), the influence of the transient term is the largest (critical damping). Furthermore, when $\alpha^2 < {\omega_0}^2$ (blue waveform) is set, the waveform oscillates and damps to reach a steady oscillation (damped oscillation or underdamping).

## 1.10 Conclusions

In this chapter, we treat the analysis of both direct current and alternating current circuits. DC circuits, characterized by constant currents and voltages, provide a straightforward context for applying Kirchhoff's laws and Ohm's law. Conversely, AC circuits introduce complexities due to their time-varying currents and voltages. To understand these circuits, one must grasp additional concepts such as impedance and phase angles, which are thoroughly discussed.

The chapter also addresses transient phenomena in DC and AC circuits, which occur during state changes such as when a switch is opened or closed. These phenomena are marked by temporary deviations from the steady-state behavior of the circuits, and comprehending them is crucial for the precise analysis and design of electrical systems.

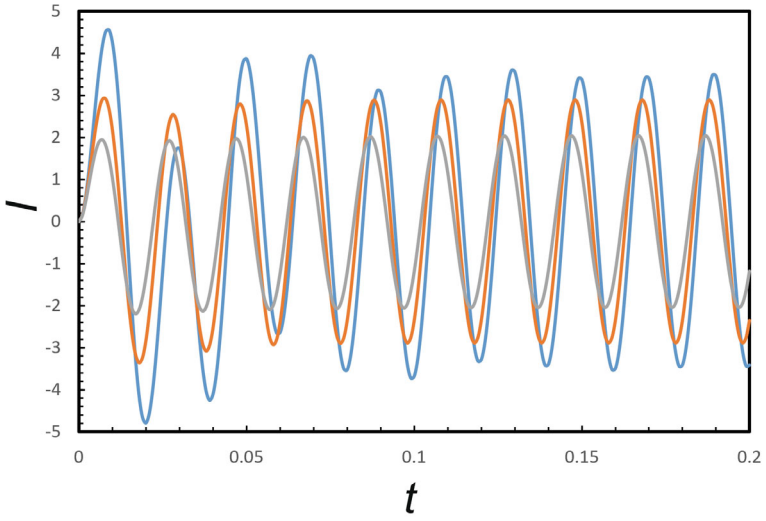


**Fig. 1.13** Graph of current in AC *LCR* series circuit ($L = 0.1$ μH, $C = 0.1$ μF, $R = 0.5, 2, 4$ Ω, $E_m = 10$ V, and $\omega = 314.16$ rad/s)

In conclusion, this chapter equips you with the fundamental laws and techniques necessary to analyze both simple and complex electrical circuits. By mastering these concepts, you are well-prepared to address a broad spectrum of challenges in electrical engineering and related fields.

## Chapter 1 Exercises

**Problem 1**: Nonlinear resistor

A voltage source of 12 V is connected in series with a linear resistor $R_1 = 50$ Ω and a nonlinear resistor that has a voltage-current relationship given by $V = I^2 \times 10$ Ω. Determine the current through the circuit.

**Problem 2**: Wheatstone bridge

A Wheatstone bridge circuit consists of four resistors. Resistors $R_1 = 100$ Ω and $R_2 = 150$ Ω are in one branch, and $R_3 = x$ Ω and $R_4 = 200$ Ω are in the other. If the bridge is balanced when $x = 120$ Ω, what is the supply voltage if the voltage drop across $R_2$ is 6 V?

**Problem 3**: Battery internal resistance

A 9 V battery with an internal resistance of 0.5 Ω is connected to a resistor $R = 8.5$ Ω. An ammeter, having a negligible resistance, is connected in series to measure the current, and a voltmeter, with a very high internal resistance, is connected across the resistor to measure the voltage. Calculate the reading of the ammeter and the voltmeter.

**Problem 4**: Voltage divider

A voltage divider circuit is formed with two resistors, $R_1 = 200\ \Omega$ and $R_2 = 300\ \Omega$, connected in series across a 15 V source. Calculate the voltage across $R_2$.

**AC Circuit Problems**

**Problem 5**: Impedance calculation

An AC circuit consists of a resistor $R = 50\ \Omega$, an inductor $L = 0.1$ H, and a capacitor $C = 50\ \mu$F connected in series. The frequency of the AC source is 60 Hz. Calculate the total impedance of the circuit.

**Problem 6**: Resonance frequency

Determine the resonance frequency of a series *LC* circuit where $L = 200$ mH and $C = 100\ \mu$F.

**Problem 7**: Voltage drop across components

A resistor ($R = 100\ \Omega$) and a capacitor ($C = 22\ \mu$F) are connected in series to a 120 $V_{RMS}$, 50 Hz AC source. Calculate the voltage drop across the capacitor.

**Transient Phenomena in Circuits**

**Problem 8**: Graph drawing for DC and AC circuits

Draw the graphs shown in Figs. 1.11 and 1.13, using Excel for $L$, $C$, $R$, $E_m$, and $\omega$parameters shown in the captions of the figures.

**Problem 9**: *CR* charging circuit

A capacitor $C = 100\ \mu$F is connected in series with a resistor $R = 1\ k\Omega$ and a DC source of 5 V. Determine the time constant of the circuit and calculate the voltage across the capacitor after one time constant.

**Problem 10**: *LCR* series circuit at resonance

A series *LCR* circuit is driven by a sinusoidal source at its resonant frequency. The values are $L = 10$ mH, $C = 10\ \mu$F, and $R = 50\ \Omega$. Assuming initial conditions of zero, calculate the voltage across the resistor at a time equal to three times the resonant period after the source is switched on.

## References

1. K. Sasaki, S. Tomioka, *Essence Denki Denshi Kairo* (English translated title: *Essentials of Electrical and Electronic Circuits*) (Kyoritsu Shuppan Co., Ltd., Tokyo, Japan, 2013), pp. 172. ISBN: 9784320086425 (in Japanese)
2. H. Fujita, *Denjikigaku Note (kaiteiban) and Zoku Denjikigaku Note* (English translated title: *Notes on electromagnetism* (revised edition) and *Note on electromagnetism 2*) (Corona Publishing Co., Ltd., Tokyo, Japan, 1971), pp. 228 and pp. 277 (in Japanese)

3. M. Nishimaki, *Denki Gaku* (English translated title: *Electricity*) (Morikita Publishing Co., Ltd., Tokyo, Japan, 1973), pp. 222 (in Japanese)
4. *Denki no Shinzui* (English translated title: *The Essence of Electricity*), in Transient phenomena in LCR series circuits (DC circuits). https://denki-no-shinzui.com/transient-rlc-s-dc/. Accessed 2024.12.01 (in Japanese)
5. *Denki no Shinzui* (English translated title: *The Essence of Electricity*), in Transient phenomena in LCR series circuits (AC circuits). https://denki-no-shinzui.com/transient-rlc-s-ac/. Accessed 2024.12.01 (in Japanese)
6. N. Ida, *Engineering Electromagnetics*, 4th edn. (Springer Nature Switzerland AG, 2021), pp. 1028. ISBN 978-3-030-15559-9, ISBN 978-3-030-15557-5 (eBook). https://doi.org/10.1007/978-3-030-15557-5
7. D.E. LaLond, J.A. Ross, *Experiments in Principle of Electronic Devices and Circuits* (Delmar Publishers Inc., New York, USA, 1994), pp. 310. ISBN 0-8273-4664-6
8. M. Rahmani-Andebili, *AC Electrical Circuit Analysis, Practice Problems, Methods, and Solutions* (Springer Nature Switzerland AG, 2021), pp. 229. ISBN 978-3-030-60985-6, ISBN 978-3-030-60986-3 (eBook). https://doi.org/10.1007/978-3-030-60986-3
9. A.R. Bergen, V. Vittal, *Power System Analysis*, 2nd edn. (Pearson India Education Services Pvt. Ltd., Uttar Pradesh, India, 2000), pp. 629. ISBN 978-81-7758-819-4
10. C. Bowick, J. Blyler, C. Ajluni, *RF Circuit Design* (Newnes, an imprint of Elsevier, Oxford, UK, 2008), pp. 232. ISBN-13: 978-0-7506-85184, ISBN-10: 0-7506-8518-2
11. D. Torrungrueng, *Meta-Smith Charts and Their Potential Applications*, in A Publication in the Springer Series, Synthesis Lectures on Antennas, Lecture #10 (Springer Nature Switzerland AG, 2022), pp. 98. ISBN: 978-3-031-00411-7 paperback, ISBN: 978-3-031-01539-7 ebook. https://doi.org/10.1007/978-3-031-01539-7
12. S. Ohshita, *Syokai Denki Kairo Ensyu Jyo*, *Ge* (English translated title: *Detailed Explanation of Electric Circuit Exercises, Volume 1 and Volume 2*) (Kyoritsu Shuppan Co., Ltd., Tokyo, Japan, 1979, 1980), pp. 338 and pp. 384. ISBN 978-4-320-08433-9 and ISBN 978-4-320-08434-6
13. H. Kusama, Y. Sato, N. Isshiki, Y. Abu, *Kikai Kogaku Gairon* (Dai 3 Pan) (English translated title: *Introduction to Mechanical Engineering*, 3rd edn.) (Ohmsha, Ltd., Tokyo, Japan, 1992), pp. 240. ISBN: 978-4-274-06977-2
14. L.D. Landau, E.M. Lifshitz, *The Classical Theory of Fields*, in Course of Theoretical Physics Volume 2 (Pergamon Press, 1975), pp. 402
15. E.M. Lifshitz, L.P. Pitaevskii, *Physical Kinetics*, in Course of Theoretical Physics Volume 10 (Pergamon Press, 1981), pp. 452
16. R.E. Rosensweig, *Ferrohydrodynamics* (Cambridge University Press, Appendix, 1985), pp. 344
17. C. Adachi, *Bekutoru to Tensoru* (English translated title: *Vectors and Tensors*) (Baifukan Co., Ltd., Tokyo, Japan, 1957), pp. 159 (in Japanese)
18. R.J. Rosa, *Magnetohydrodynamic Energy Conversion* (McGraw-Hill Inc., 1968), pp. 234
19. T. Shimada, H. Yamasaki, M. Okubo, Evolution of streamer groups and radical generation in high-voltage multiple-pulse-induced nonthermal plasma. Phys. Plasmas **30**, 103508 (2023)

# Chapter 2
# Fundamentals of AC Electrical Circuits (1): Complex Notation, AC Circuits, and Mechanical–Electrical System Analogy


**Abstract** This chapter discusses the fundamentals of AC electrical circuits and mechanical systems (1). Complex notation, AC circuits, and mechanical–electrical system analogy are mainly covered. Systems of linear ordinary differential equations, general solution, special solution, and complex notation and review are covered. Following these, vibration in electrical circuits, mechanical–electrical analogy, equivalent circuit networks, and principle of superposition are explained. The chapter is concluded by the conclusions and exercise problems.

## 2.1 Introduction

This chapter and Chaps. 3–6 of *Sustainable Electrical Energy for Mechanical Engineers* address the principles of electrical circuits, impedance matching, and energy conversion. Specifically, they provide a comprehensive explanation of alternating current (AC) electrical circuits. For additional reference materials, please consult the list of references at the end of this chapter [1–4]. This chapter focuses on Fundamentals of AC electrical circuits (1): Complex notation, AC circuits, and mechanical–electrical system analogy.

The primary goal of this book is to offer a thorough understanding of how mechanical engineering principles intersect with electrical systems in industrial applications. In particular, it aims to equip readers with the techniques and knowledge necessary for designing and manufacturing mechanical systems, given that a solid understanding of electrical circuits and electrical engineering is vital for designing and building efficient and functional mechanical systems. In this chapter and Chaps. 3–6, we focus on the flow of electrical energy from the power source to the load within an electrical circuit powering a mechanical system. We also explore methods to optimize this energy flow. Starting with the fundamentals of electrical circuit analysis, these chapters introduce key principles and concepts related to the transmission and conversion of electrical energy. A detailed explanation is provided on determining circuit parameters to maximize the energy delivered to the load through impedance



M. Okubo, *Electrical Sustainable Energy for Mechanical Engineering*,
https://doi.org/10.1007/978-981-96-5170-2_2

matching. Beyond theoretical exploration, this book emphasizes practical applications in circuit design, offering guidance that enables students and engineers to apply theory in real-world scenarios. This book seeks to help students and mechanical engineers grasp the fundamental principles of electrical engineering, acquire essential skills in electrical circuit design and analysis, and apply these concepts within the mechanical engineering domain. By doing so, it aims to contribute to the development of more effective and efficient mechanical systems. The combination of theoretical knowledge and practical skills presented here lays a strong foundation for future engineers to effectively navigate the challenges of sustainable energy systems.

## 2.2 Systems of Linear Ordinary Differential Equations with Constant Coefficients

We begin by reviewing the solutions of linear ordinary differential equations with constant coefficients. Equation (2.1) represents such an equation, which appears in various fields:

$$m\frac{\mathrm{d}^2x}{\mathrm{d}t^2} + \beta\frac{\mathrm{d}x}{\mathrm{d}t} + kx = F_0 \sin \omega t \tag{2.1}$$

### *2.2.1 General Solution*

The general solution of Eq. (2.1) has been studied in mechanical engineering majors in courses such as mechanical dynamics. The general solution is the sum of the damping vibration (general solution) and forced vibration (special solution), which is also known as the steady-state vibration.

The general solution of Eq. (2.1) is commonly studied in mechanical engineering courses, such as machine mechanics. It consists of the sum of the damped free vibration (general solution) and the forced (also referred to as steady-state) vibration (special solution). The general solution, also known as the damped free vibration, corresponds to the solution of the associated homogeneous equation obtained by setting the right-hand side of Eq. (2.1) to zero. Readers are encouraged to review or study the methods for solving such equation, as detailed in the recommended Ref. [4].

For example, the general solution when $\beta^2 < 4\ km$ is as follows:

$$\beta^2 < 4km$$

$$x = Ce^{-\frac{\beta}{2m}t}\cos\left(\sqrt{\frac{k}{m}-\frac{\beta^2}{4m^2}}t\right)t + De^{-\frac{\beta}{2m}t}\sin\left(\sqrt{\frac{k}{m}-\frac{\beta^2}{4m^2}}\right)t \tag{2.2}$$

This book does not provide an in-depth explanation of how to derive this solution, references for self-study are shown in Ref. [4]. The general solution of Eq. (2.1) indicates that, when $t$ becomes infinity, $x$ is attenuated. The special solution, which represents the forced or steady vibration, is addressed in next Sect. 2.2.2. In this chapter, we explain the methodology to calculate this type solution, particularly in the context of electrical circuits.

### 2.2.2 Special Solution

One approach to finding the special solution $x_1$ is to assume a solution form $x_1 = A\sin\omega t + B\cos\omega t$ and then substitute it into Eq. (2.1) to determine coefficients $A$ and $B$. This yields the steady vibration solution represented by Eqs. (2.3) and (2.4):

$$x = F_0\frac{\left(k-m\omega^2\right)\sin\omega t - \beta\omega\cos\omega t}{\left(k-m\omega^2\right)^2+\beta^2\omega^2} = \frac{F_0\sin(\omega t-\varphi)}{\sqrt{\left(k-m\omega^2\right)^2+\beta^2\omega^2}} \tag{2.3}$$

$$\tan\varphi = \frac{\beta\omega}{k-m\omega^2} \tag{2.4}$$

As shown in Eq. (2.3), the form $A\sin\omega t + B\cos\omega t$ can also be expressed as a single sine function using trigonometric identities and defining $\tan\varphi$ as in Eq. (2.4).

When the equation of interest is as simple as Eq. (2.1), its solution is relatively straightforward to analyze. However, when the complexity of the problem increases, such as when solving a system of multiple simultaneous differential equations, calculating the solution becomes more challenging. For such cases, there is an easier method to address the problem: using complex notation, which will be explained in the following section.

### 2.2.3 Complex Notation

In this section, we introduce the basics of analysis using complex numbers, particularly as applied to AC electrical circuits in the context of mechanical engineering. First, the fundamentals of complex numbers are reviewed. Consider a complex number $x = a + ib$, where $a$ is the real component and $b$ is the imaginary component. In polar coordinates, $x$ can be written as $|x|e^{i\varphi}$, where $|x|$ is the absolute value or magnitude of $x$, which is expressed in the form $r = \sqrt{a^2+b^2}$. When plotting $x$ on a complex plane, the horizontal and vertical axes represent, respectively, the real and

imaginary parts of the complex number. Therefore, $x$ can be described as a point in a complex plane, with argument $\varphi$ and magnitude $r$. This argument is tan $\varphi$ = b/a. If we express this using the inverse function, we get $\varphi = \tan^{-1} b/a$ or $\varphi = \arctan^{-1} b/a$. If we express $x$ itself in polar coordinates, it takes the form $r(\cos \varphi + i \sin \varphi)$.

Write down the ordinary differential equation. It will take the form shown here. When using complex notation to find the solution, only take the real or imaginary part at the end.

$$m\frac{\mathrm{d}^2x}{\mathrm{d}t^2} + \beta\frac{\mathrm{d}x}{\mathrm{d}t} + kx = F_0\mathrm{e}^{i\omega t} \tag{2.5}$$

Let us assume that $x$ is expressed in complex notation, which is equal to $C(\cos \omega t + i \sin \omega t)$ in real notation, as shown in Eq. (2.6):

$$x = Ce^{i\omega t} = C(\cos \omega t + i \sin \omega t) \tag{2.6}$$

where $C$ is a complex number. Next, by substituting $x$ as expressed in Eq. (2.6) into the differential Eq. (2.5), the left-hand side becomes:

$$\begin{aligned}\text{Left term} &= Cm(i\omega)^2\mathrm{e}^{i\omega t} + \beta i\omega C\mathrm{e}^{i\omega t} + kC\mathrm{e}^{i\omega t}\left(= F_0\mathrm{e}^{i\omega t}\right)\\ &= \left[m(i\omega)^2 + \beta i\omega + k\right]x = Z(i\omega)x\end{aligned} \tag{2.7}$$

Let $Z(i\omega)$ represent the term in brackets on the right-hand side of Eq. (2.7), where $Z(i\omega)$ is a complex number with argument $i\omega$. Setting Eq. (2.7) equal to $F_0\ \mathrm{e}^{i\omega t}$, we obtain:

$$x = \frac{F_0\,\mathrm{e}^{i\omega t}}{Z(i\omega)} \tag{2.8}$$

### 2.2.4 *Review for Complex Number Relations*

A critical point in working with complex numbers is that when dividing two complex numbers, the magnitude of the result is the quotient of their magnitudes, and the argument of the result is the difference of their arguments. In other words, when dividing complex numbers $Y_1$ and $Y_2$, the following relationship holds:

$$Y_1 = |Y_1|\mathrm{e}^{i\omega_1 t},\quad Y_2 = |Y_2|\mathrm{e}^{i\omega_2 t},\quad \frac{Y_1}{Y_2} = \frac{|Y_1|}{|Y_2|}\mathrm{e}^{i(\omega_1-\omega_2)t} \tag{2.9}$$

Applying this to $x$, the magnitude of $x$ is the quotient between the magnitude of $F_0\ \mathrm{e}^{i\omega t}$, i.e., $F_0$, and the magnitude of $Z$:

$$|x| = \frac{F_0}{|Z|} = \frac{F_0}{\sqrt{\left(k - m\omega^2\right)^2 + \beta^2\omega^2}} \tag{2.10}$$

$$x = \frac{F_0}{\sqrt{\left(k - m\omega^2\right)^2 + \beta^2\omega^2}} \mathrm{e}^{i(\omega t - \varphi)} \tag{2.11}$$

Consequently, $Z$ and the magnitude of $Z$ can be expressed as:

$$\begin{aligned} Z(i\omega) &= m(i\omega)^2 + \beta i\omega + k = -m\omega^2 + \beta i\omega + k \\ &= \left(k - m\omega^2\right) + \beta i\omega \end{aligned} \tag{2.12}$$

$$|Z| = \sqrt{\left(k - m\omega^2\right) + (\beta\omega)^2} \tag{2.13}$$

and the argument is given by:

$$\tan\varphi = \frac{\beta\omega}{k - m\omega^2} \tag{2.14}$$

$$\varphi = \tan^{-1}\frac{\beta\omega}{k - m\omega^2} \tag{2.15}$$

If we plot $Z$ on a complex plane, it is shown in Fig. 2.1. Using these relationships, we determine the steady-state or special solution to Eq. (2.5).

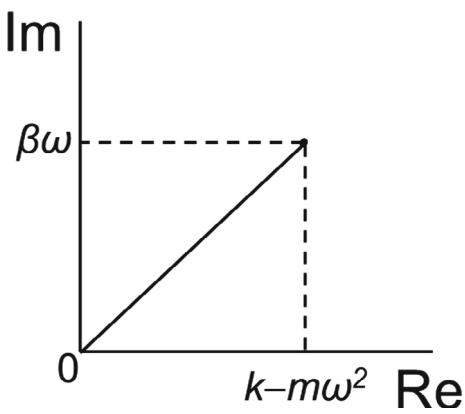


**Fig. 2.1** Real and imaginary parts of $Z$ in Eq. (2.12) in the complex plane

## 2.3 Vibration in Electrical Circuits

This section explains the oscillation behavior of electrical circuits. While $V = IR$ applies to direct current (DC) circuits, the AC case requires a more complex analysis, as explained in Fig. 2.2. Consider an AC circuit where an inductor $L$, capacitor $C$, and resistor $R$ are connected in series, as shown in Fig. 2.2. If an alternating voltage $V = V_0\, e^{i\omega t}$ is applied across the circuit, the voltage drop across each element depends on the current $I = I_0\, e^{i\omega t}$, where $I_0$ is a complex number. The current is represented as a complex number because its phase usually differs from the applied voltage $V$. Differentiation and integration of $I$ with respect to time are given by:

$$\frac{dI}{dt} = i\omega I_0 e^{i\omega t} = i\omega I \tag{2.16}$$

$$\int I dt = \frac{1}{i\omega} I_0 e^{i\omega t} + \text{const.} = \frac{1}{i\omega} I + \text{const.} \tag{2.17}$$

where "const." in Eq. (2.17) is the integration constant, which can typically be set to zero for simplicity. Therefore, the voltage drops across each element is expressed as follows:

**Inductance**: The voltage drop is determined by the next relationship:

$$V_L = L\frac{dI}{dt} = (i\omega L) I \tag{2.18}$$

**Resistance**: The voltage drop is the same as in a DC circuit:

$$V_R = IR \tag{2.19}$$

**Capacitance**: The voltage drop is determined by the relationship $dQ/dT = I$:

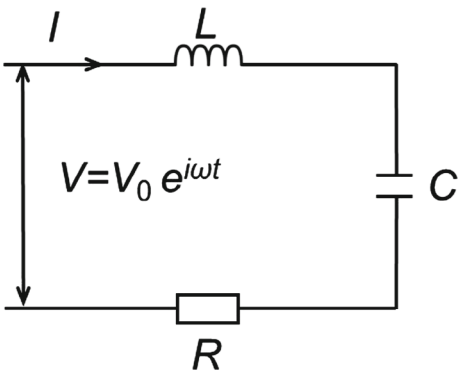


**Fig. 2.2** *LCR* AC circuit

$$V_{\mathrm{C}} = \frac{Q}{C} = \frac{1}{C}\int I\,\mathrm{d}t = \frac{I}{i\omega C}, \quad \left(\frac{\mathrm{d}Q}{\mathrm{d}t} = I\right) \tag{2.20}$$

The total voltage drop across the series circuit is the sum of these individual voltage drops:

$$V_{\mathrm{L}} + V_{\mathrm{R}} + V_{\mathrm{C}} = L\frac{\mathrm{d}I}{\mathrm{d}t} + IR + \frac{1}{C}\int I\,\mathrm{d}t = V \tag{2.21}$$

This introduces the concept of impedance, which is equivalent to resistance in a DC circuit. As shown above, the impedances of $L$, $R$, and $C$ are equal to $i\omega L$, $R$, and $1/(i\omega C)$, respectively.

Next, we analyzed the basic equation of this series circuit using complex numbers. Let us consider current $I_0\,\mathrm{e}^{i\omega t}$, where $I$ and $I_0$ are complex numbers. By substituting this expression for $I$ in the basic equation, we obtain:

$$\left(i\omega L + R + \frac{1}{i\omega C}\right) I_0 \mathrm{e}^{i\omega t} = V_0 \mathrm{e}^{i\omega t} \tag{2.22}$$

$$I_0 = \frac{V_0}{i\omega L + R + \frac{1}{i\omega C}} = \frac{V_0}{R + i\left(\omega L - \frac{1}{\omega C}\right)} = \frac{V_0}{Z} = \frac{V_0}{|Z|\mathrm{e}^{i\varphi}} = \frac{V_0}{|Z|}\mathrm{e}^{-i\varphi} \tag{2.23}$$

By multiplying the numerator and denominator of the first equation of Eq. (2.23) by $i$ and given that $1/i = -i$, we obtain the second equation. Subsequently, by substituting $Z$ in the denominator, we obtain the third equation, where $Z$ is the circuit impedance. Finally, by expressing $Z$ in polar coordinates as $|Z|\mathrm{e}^{i\varphi}$, where $\varphi$ represents the argument of $Z$, we obtain the fifth equation on the right-hand side. The definitions $\varphi$ and $|Z|$ are as follows (Fig. 2.3):

$$\varphi = \tan^{-1}\left(\frac{\omega L - \frac{1}{\omega C}}{R}\right) \tag{2.24}$$

$$|Z| = \sqrt{R^2 + \left(\omega L - \frac{1}{\omega C}\right)^2} \tag{2.25}$$

## 2.4 Mechanical–Electrical Analogy

Next, we explore the similarity between mechanical and electrical systems. The fundamental equations for this analogy are as follows:

Electrical circuit:

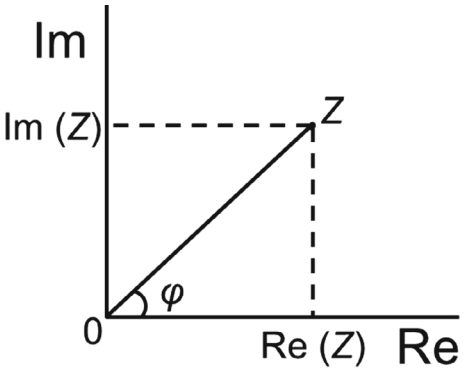


**Fig. 2.3** Real and imaginary parts of $Z$ in the complex plane

$$L\frac{\mathrm{d}^2 I}{\mathrm{d}t^2} + R\frac{\mathrm{d}I}{\mathrm{d}t} + \frac{I}{C} = i\omega V_0 \mathrm{e}^{i\omega t} \tag{2.26}$$

Mechanical vibration:

$$m\frac{\mathrm{d}^2 x}{\mathrm{d}t^2} + \beta\frac{\mathrm{d}x}{\mathrm{d}t} + kx = F \tag{2.27}$$

Rotational system:

$$I\frac{\mathrm{d}^2 \theta}{\mathrm{d}t^2} + \beta\frac{\mathrm{d}\theta}{\mathrm{d}t} + k\theta = T \tag{2.28}$$

These systems are shown in Figs. 2.4, 2.5 and 2.6. The correspondence between elements in these systems is summarized in Table 2.1: the inductance $L$, resistance $R$, capacitance $C$, and applied voltage $V$ in electrical circuits correspond to the mass $m$, damper $\beta$, spring $k$, and forced excitation $F$ in mechanical systems, and to the moment of inertia $I$, damping (fluid resistance) $\beta$, torsional spring $k$, and torque $T$ in rotational systems.

Equations (2.26), (2.27), and (2.28) are all second-order linear ordinary differential equations with constant coefficients, making them mathematically analogous. Thus, by thoroughly studying Eq. (2.26), one can apply similar methods to analyze problems represented by Eqs. (2.27) and (2.28). This similarity forms the basis of the mechanical–electrical analogy.

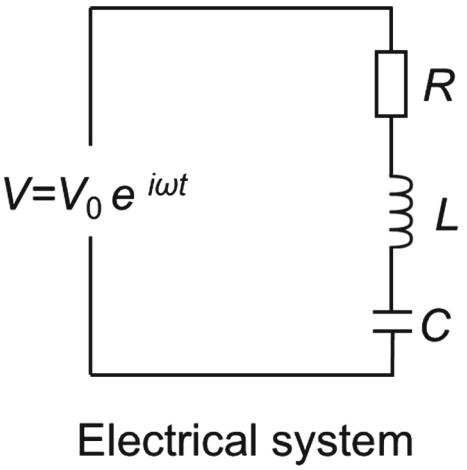


**Fig. 2.4** *LCR* electrical circuit

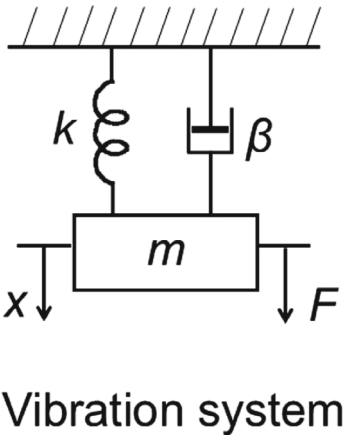


**Fig. 2.5** Spring-mass-damper system

## 2.5 Equivalent Circuit Networks

In electrical engineering, in addition to considering electrical circuits in their original sense, electrical machines or devices such as generators, motors, and transformers can be replaced with equivalent circuit networks. One example is the equivalent circuit of an electric motor.

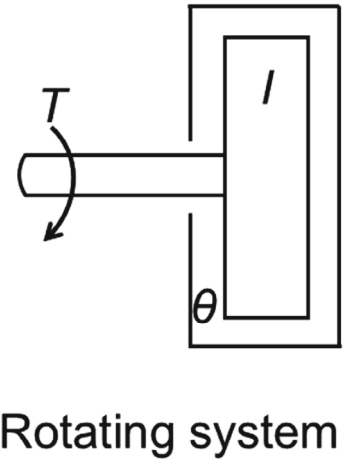


**Fig. 2.6** Torsional spring-moment of inertia-damper system

**Table 2.1** Correspondence between mechanical and electrical systems

| Equation (2.26) | Equation (2.27) | Equation (2.28) |
|---|---|---|
| Inductance | Mass | Moment of inertia |
| Resistance | Damper | Damper (fluid resistance) |
| Capacitance | Spring | Torsional spring (moment required to produce unit relative angle) |
| Voltage | Excitation force | Torque |

## 2.6 Principle of Superposition

The principle of superposition is a key concept in analyzing linear systems—physical systems governed by linear differential equations or integral equations with constant coefficients. For instance, Eqs. (2.26), (2.27), and (2.28) represent linear ordinary differential equations that describe the system's response to external forces. An external force can be expressed as a Fourier series:

$$F(t) = \sum_{\mathrm{n}=1}^{\mathrm{m}} F_{\mathrm{n}} \mathrm{e}^{in\omega t} \tag{2.29}$$

In the case of electrical circuits, this external force corresponds to voltage. If the system impedance is $Z(in\omega)$, the solution for the circuit's response can be expressed as:

$$x(t) = \sum_{\mathrm{n}=1}^{\mathrm{m}} F_n \frac{\mathrm{e}^{in\omega t}}{Z(in\omega)} = \sum_{\mathrm{n}=1}^{\mathrm{m}} c_{\mathrm{n}} \mathrm{e}^{in\omega t} \tag{2.30}$$

where

$$c_{\mathrm{n}} = \frac{1}{T}\int_0^T x(t)\mathrm{e}^{-i\mathrm{n}\omega t}\mathrm{d}t \quad \text{(Complex Fourier series)} \tag{2.31}$$

## 2.7 Conclusions

In conclusion, this chapter integrates fundamental principles of mechanical and electrical engineering, offering theoretical and practical tools for analyzing and designing AC circuits. By leveraging the analogy between mechanical and electrical systems, the chapter highlights methods for achieving efficient energy use in engineering applications. The main points are summarized as follows:

(1) Fundamentals of AC circuits

This chapter introduces the foundational principles of AC circuits, using complex notation to analyze the analogy between mechanical vibration systems and electrical circuits. It emphasizes understanding energy flow in electrical circuits and determining circuit constants to optimize energy transmission.

(2) Theory of vibrations and forced oscillations

Solution methods for linear ordinary differential equations, particularly those describing damped free vibrations and forced oscillations, are described. These solutions are frequently applied to AC circuits to understand the oscillatory behavior of electrical circuits.

(3) Complex notation as a method of analysis

Complex notation simplifies the solution of differential equations, making it particularly effective for AC circuit analysis. It aids in handling the real and imaginary components of oscillating systems, providing insights into physical phenomena.

(4) Mechanical–electrical analogy

The chapter demonstrates the analogy between mechanical and electrical systems, showing that the analysis of vibrational and rotational systems can be performed similarly to that of electrical circuits. This analogy enables mechanical engineers to apply electrical circuit principles to optimize mechanical system designs.

(5) Equivalent circuits and the principle of superposition

Representing electrical machines such as generators and motors with equivalent circuits simplifies the analysis of complex systems. Additionally, the principle of superposition enables the determination of system responses to multiple external forces, which is applicable to both electrical and mechanical domains.

## Chapter 2 Exercises

**Problem 1**: *LR* series circuit

If a voltage with an amplitude of 12 V and an angular frequency of 4000 rad/s is applied to a series circuit with resistance $R = 1.2$ kΩ and inductance $L = 0.5$ H, as shown in Fig. 2.7, calculate the current $I$ flowing between terminals a and b, and the voltages $V_R$ and $V_L$ across $R$ and $L$.

**Problem 2**: *CR* parallel circuit

If a voltage with an amplitude of 12 V and an angular frequency of 4000 rad/s is applied to a parallel circuit with resistance $R = 5$ kΩ and capacitance $C = 0.1$ μF, as shown in Fig. 2.8, calculate the currents $I_R$ and $I_C$ flowing through the resistor $R$ and capacitor $C$, as well as the total current $I$.

**Problem 3**: *LCR* series circuit I

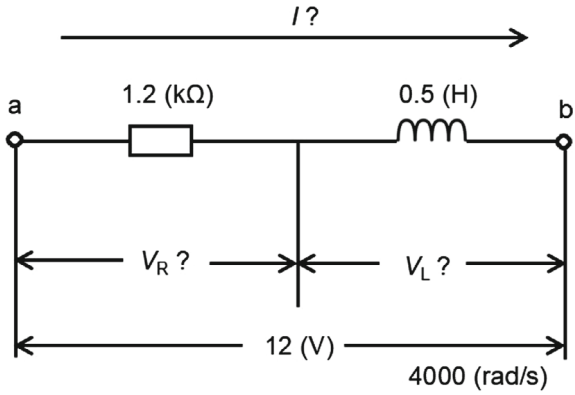


**Fig. 2.7** *LR* series circuit

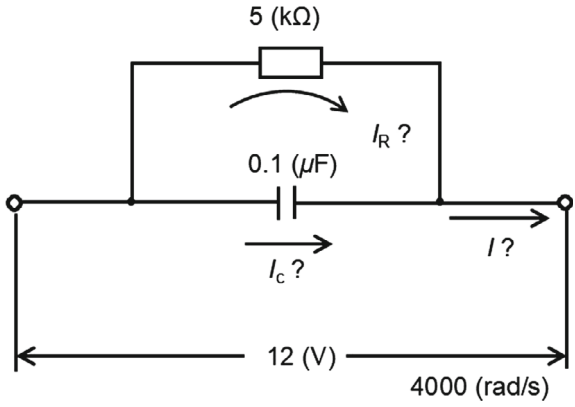


**Fig. 2.8** *CR* parallel circuit

Consider an *LCR* series circuit with an inductor $L = 0.1$ H, a capacitor $C = 100$ μF, and a resistor $R = 10\ \Omega$, connected to an AC source with a voltage $V(t) = 50 \sin(1000t)$. The units of $V(t)$ and $t$ are volts and seconds, respectively. Calculate the total impedance $Z$ of the circuit, and the amplitude of the current $I_0$.

**Problem 4**: Mechanical system analogious to *LCR* series circuit

Consider a mechanical system analogous to an *LCR* series circuit, where the mass, damping coefficient, and spring coefficient are $m = 0.5$ kg, $\beta = 1$ Ns/m, and $k = 100$ N/m, respectively. The system is subjected to a sinusoidal driving force given by $F(t) = 10 \sin(10t)$. The units of $F(t)$ and $t$ are Newton and seconds, respectively. Write the equation of motion for the system and find the steady-state solution.

**Problem 5**: *LCR* series circuit II

Consider an AC circuit with two voltage sources applied to a series *LCR* circuit with $L = 0.05$ H, $C = 200$ μF, and $R = 5\ \Omega$. The first voltage source is $V_1(t) = 40 \sin(100t)$, and the second is $V_2(t) = 30 \sin(200t)$. Find the total current through the circuit using the principle of superposition.

## References

1. K. Sasaki, S. Tomioka, *Essence Denki Denshi Kairo* (English translated title: *Essentials of Electrical and Electronic Circuits*) (Kyoritsu Shuppan Co., Ltd., Tokyo, Japan, 2013), pp. 172. ISBN: 9784320086425 (in Japanese)
2. M. Nishimaki, *Denki Gaku* (English translated title: *Electricity*) (Morikita Publishing Co., Ltd., Tokyo, Japan, 1973), pp. 222 (in Japanese)
3. T. von Kármán, M.A. Biot, *Mathematical Methods in Engineering* (McGraw-Hill, 1940), pp. 505
4. H. Kusama, Y. Sato, N. Isshiki, Y. Abu, *Kikai Kogaku Gairon* (Dai 3 Pan) (English translated title: *Introduction to Mechanical Engineering*, 3rd edn.) (Ohmsha, Ltd., Tokyo, Japan, 1992), pp. 240. ISBN: 978-4-274-06977-2

# Chapter 3
# Fundamentals of AC Electrical Circuits: (2) Resonant Circuits and Various AC Circuits


**Abstract** This chapter discusses the fundamentals of AC electrical circuits (2). Resonant circuits and various AC circuits are mainly covered. Series resonant circuits, role of series resonant circuits, and example of a series resonant circuit are explained. Following these, properties of complex numbers, basic characteristics of *LCR* circuits, and various AC circuits of example problems are reviewed and explained. The chapter is concluded by the conclusions and exercise problems.

## 3.1 Introduction

In this chapter, we explain the fundamentals of AC electrical circuits and devices, with a particular focus on the theory and practical applications of series resonant circuits. Resonance is a crucial concept in electrical engineering, essential for understanding the behavior of current and voltage in AC systems. For series resonant circuits, we explore in detail how inductance, capacitance, and resistance interact under specific conditions to minimize the circuit's impedance and maximize the current. This chapter aims to equip readers with a clear understanding of how these components work together to transmit and control energy, providing practical knowledge for circuit design and analysis. As noted in the previous chapter, this explanations below cover only the "steady-state solutions" after sufficient time has elapsed. The descriptions are still referred by Refs. [1–4].

## 3.2 Series Resonant Circuits

Consider the circuit illustrated in Fig. 3.1, representing a series resonant circuit. The relationship between voltage $V$, current $I$, and impedance $Z$ is $V = IZ$. In the figure, $\omega$ is angular frequency and equal to $2\pi f$, and $f$ is frequency of the power source. The total impedance of the circuit, its magnitude, and phase are:



M. Okubo, *Electrical Sustainable Energy for Mechanical Engineering*,
https://doi.org/10.1007/978-981-96-5170-2_3

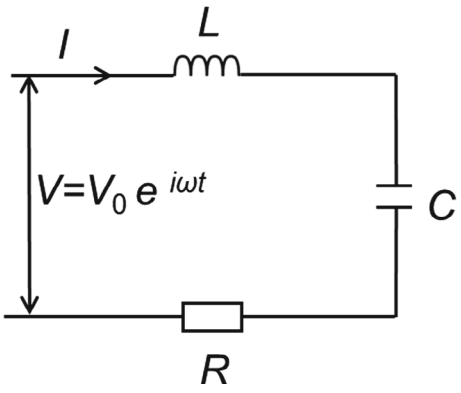


**Fig. 3.1** *LCR* AC circuit

$$Z = i\omega L + R + \frac{1}{i\omega C} = R + i\left(\omega L - \frac{1}{\omega L}\right) = |Z|\mathrm{e}^{i\varphi} \tag{3.1}$$

$$|Z| = \sqrt{R^2 + \left(\omega L - \frac{1}{\omega C}\right)^2}, \quad \varphi = \tan^{-1}\frac{\omega L - \frac{1}{\omega C}}{R} \tag{3.2}$$

Let $I = I_0\,\mathrm{e}^{i\omega t}$ and $V = V_0\,\mathrm{e}^{i\omega t}$, where $I_0$ is a complex number given by:

$$I_0 = \frac{V_0}{Z} = \frac{V_0}{|Z|\mathrm{e}^{i\varphi}} = \frac{V_0}{|Z|}\mathrm{e}^{-i\varphi} \tag{3.3}$$

Equations (3.2) and (3.3) indicate that $I_0$ is maximized when:

$$\omega L - \frac{1}{\omega C} = 0 \quad \text{or} \quad f = \frac{1}{2\pi}\sqrt{\frac{1}{LC}} \tag{3.4}$$

This condition, known as series resonance, is illustrated in Fig. 3.2, where horizontal axis represents the frequency $f$, and the vertical axis represents the current amplitude $I_0$.

## 3.3 Role of Series Resonant Circuits

### *3.3.1 Example of a Series Resonant Circuit*

A series resonant circuit is used to allow a large current to flow at a specific high frequency through a circuit containing $R$ and $L$, by inserting an appropriate $C$. The impedance of the $R$ and $L$ circuit is expressed as follows:

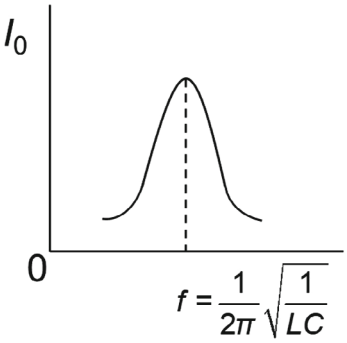


**Fig. 3.2** Series resonance

$$|Z| = \sqrt{R^2 + \omega^2 L^2} \tag{3.5}$$

When the frequency ( $f$ or $\omega = 2\pi f$) is very high, $Z$ increases, making it difficult for current to flow under constant $V$, thereby reducing the current flowing through the circuit. To address this, a capacitor is added in series, with its capacitance $C$ chosen to satisfy the resonance condition $\omega = \sqrt{1/(LC)}$. If this is done, the impedance becomes:

$$|Z| = \sqrt{R^2 + \left(\omega L - \frac{1}{\omega C}\right)^2} = R \tag{3.6}$$

Thus, at resonance, |Z| is minimized and $I$ is maximized. A schematic of this process is shown in Fig. 3.3.

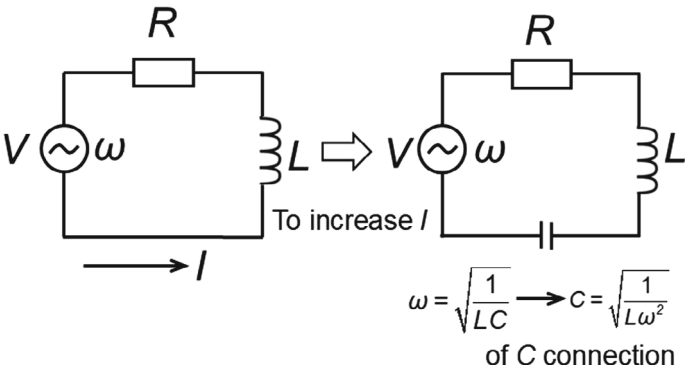


**Fig. 3.3** Schematic of a series resonant circuit

### 3.3.2 *Properties of Complex Numbers*

For a circuit with impedance $Z$, the amplitude of the current $I_0$, the magnitude of the impedance $|Z|$, and the phase $\varphi$ are given by the following equations:

$$I_0 = \frac{V_0}{a+ib} = \frac{V_0}{|Z|e^{i\varphi}} = \frac{V_0}{|Z|}e^{-i\varphi}, \quad |Z| = \sqrt{a^2+b^2}, \quad \tan\varphi = \frac{b}{a} \tag{3.7}$$

In these equation, $I$ and $Z$ can be expressed as:

$$I = \frac{V}{Z}, \quad Z = R + iX \tag{3.8}$$

where $R$ is the resistance and $X$ is the reactance. Adjusting the circuit constants such that $X = 0$ corresponds to series resonance.

Defining the admittance of the circuit, $Y$, as the reciprocal of $Z$, then the current can be rewritten as $I = YV$. The admittance can also be expressed as a complex number $Y = G + iB$, where $G$ is the conductance and $B$ is the susceptance. Adjusting the circuit constants such that $B = 0$ corresponds to parallel resonance.

## 3.4 Basic Characteristics of *LCR* Circuits (Review)

Let the voltage be $V = V_0\, e^{i\omega t}$, where $V_0$ is a real number. The unknown quantities are $Q = Q_0\, e^{i\omega t}$ and $I = I_0\, e^{i\omega t}$, with $Q_0$ and $I_0$ being complex numbers to account for phase differences. The voltage drops across each circuit element are expressed as:

Inductance:

$$V_L = L\frac{dI}{dt} = i\omega LI \tag{3.9}$$

Resistance:

$$V_R = IR \tag{3.10}$$

Capacitance:

$$V_C = \frac{Q}{C} = \frac{1}{C}\int I\,dt = \frac{I}{i\omega C}, \quad \left(\frac{dQ}{dt} = I\right) \tag{3.11}$$

When $R$, $L$, and $C$ are connected in series (see Fig. 3.4). The resulting basic equation for a series circuit is:

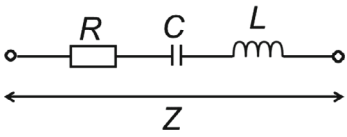


**Fig. 3.4** *LCR* series circuit

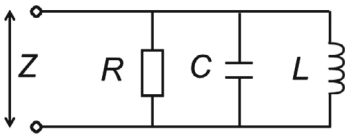


**Fig. 3.5** *LCR* parallel circuit

$$L\frac{\mathrm{d}I}{\mathrm{d}t} + IR + \frac{1}{C}\int I\,\mathrm{d}t = V \tag{3.12}$$

where the unknown quantity is $I$. It is often convenient to analyze a series circuit in terms of the impedance $Z$. The impedance can be expressed as:

$$Z = i\omega L + R + \frac{1}{i\omega C} = R + i\left(\omega L - \frac{1}{\omega C}\right) \tag{3.13}$$

If $\omega = \sqrt{1/(LC)}$, the magnitude of $Z$ is minimized and $I$ is maximized, corresponding to the series circuit resonance.

In the case of parallel circuits, it is more convenient to analyze them in terms of admittance $Y$ instead of impedance; therefore, let us consider the parallel circuit shown in Fig. 3.5. $Y$ is expressed as:

$$Y = \frac{1}{Z} = \frac{1}{R} + \frac{1}{i\omega L} + \frac{1}{\frac{1}{i\omega C}} = \frac{1}{R} + i\left(\omega C - \frac{1}{\omega L}\right) \tag{3.14}$$

Because the magnitudes of $Y$ and $I$ are minimized for $\omega = \sqrt{1/(LC)}$, this defines the parallel resonance condition.

## 3.5 Various AC Circuits (Example Problems)

Next, we examine various AC circuits that are useful for solving practical problems. Examples of such circuits are illustrated in Fig. 3.6a–f.

Considering the circuit in Fig. 3.6f, the impedance $Z_1$ of the section containing $R$ and $C$ is:

$$\frac{1}{Z_1} = \frac{1}{R} + \frac{1}{\frac{1}{i\omega C}} = \frac{1}{R} + i\omega C \tag{3.15}$$

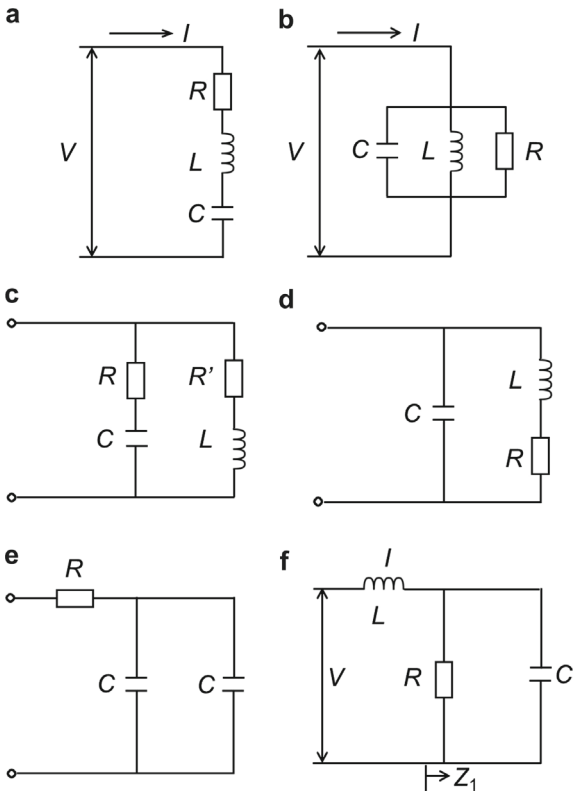


**Fig. 3.6** Various types of AC circuits

The total impedance $Z$ of the circuit is:

$$Z = Z_1 + i\omega L = \frac{1}{i\omega C + \frac{1}{R}} + i\omega L \tag{3.16}$$

Similar calculations can be performed to determine the impedance or admittance of the other circuits. To solve these problems efficiently, you need to become familiar with a scientific calculator capable of handling complex numbers. Such calculators are readily available commercially, and students are encouraged to practice using them. Problems 1 and 2 in Chap. 3 exercises are recommended for homework.

## 3.6 Conclusions

In conclusion, this chapter has provided an in-depth exploration of the fundamentals of AC electrical circuits and devices, focusing especially on the theory and practical applications of series resonant circuits. Understanding resonance is vital in electrical engineering for grasping how current and voltage behave in AC systems. The chapter detailed the interaction of inductance, capacitance, and resistance in series resonant circuits, demonstrating how these elements work together under specific conditions to minimize impedance and maximize current flow. This knowledge is crucial for anyone involved in circuit design and analysis, ensuring that readers are well-prepared to handle and optimize energy transmission and control within these systems.

### Chapter 3 Exercises

**Problem 1**: Calculation of the impedance

Calculate the impedance $Z$ of an electrical circuit formed by the series and parallel connections of $R$ and $C$.

**Problem 2**: Parallel circuit

For the circuit shown in Fig. 3.7, demonstrate that, if the relationship $R = \sqrt{L/C}$ holds, then the connection between terminals A and B is equivalent to a resistor $R$.

**Problem 3**: *LCR* AC circuit

Consider the *LCR* AC circuit shown in Fig. 3.8. An AC voltage $V = V_0 \cos \omega t$ is applied between terminals A and B.

(1) If the impedance of the circuit is $Z$, then the magnitude $|1/Z|$ and argument $\varphi$ of the admittance can be expressed as follows:

$$|1/Z| = \sqrt{\frac{1}{a^2} + \frac{1}{b^2}}, \quad \tan\varphi = -\frac{a}{b}$$

Write these expressions in terms of real numbers $a$ and $b$ using parameters $\omega$, $L$, $C$, and $R$.

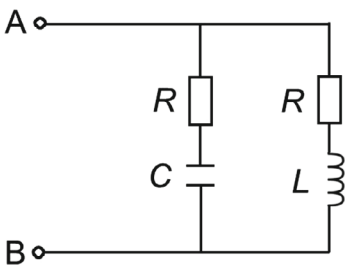


**Fig. 3.7** AC parallel circuit

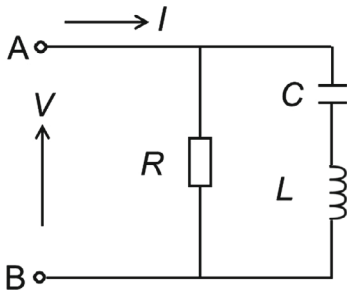


**Fig. 3.8** *LCR* series-parallel AC circuit

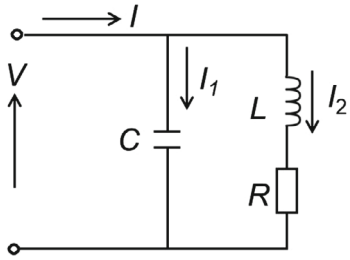


**Fig. 3.9** *LCR* parallel resonant circuit

(2) Express the current $I$ flowing through the circuit as a real number using the admittance magnitude |1/Z|, phase difference $\varphi$, and other relevant parameters.
(3) Suppose the circuit between A and B is connected to a household outlet with $V_0 = 141$ (V, volts) and $\omega = 2\pi \times 60 = 377$ rad/s. Given $R = 500$ (Ω), $L = 2$ (H), and $C = 3$ (μF) (H), calculate the amplitude (A, amperes) of the AC current $I$ and the tangent of the phase difference (tan $\varphi$). (Note: The SI units for $L$ and $C$ are Henry (H) and Farad (F), respectively, with μ representing $10^{-6}$.)

**Problem 4**: *LCR* parallel resonant circuit

An AC voltage is applied to the *LRC* parallel circuit shown in Fig. 3.9. Let the current flowing through $C$ be $I_1 = I_{01}e^{i\omega t}$, the current flowing through $L$ and $R$ be $I_2 = I_{02}e^{i\omega t}$, and the total current be $I = I_0 e^{i\omega t}$.

(1) Derive an equation for the circuit and three equations that relate $I_{01}$, $I_{02}$, and $I_0$.
(2) Express $I_0$ with $V_0$, using the form $a + bi$ ($a$, $b$: real numbers), where the real and imaginary parts of the complex number are separated.
(3) Determine the resonant angular frequency, i.e., the angular frequency at which the current reaches its maximum under a constant voltage:

$$\omega_0 = \frac{1}{\sqrt{LC}}\sqrt{1 - R^2\frac{C}{L}}$$

## References

1. K. Sasaki, S. Tomioka, *Essence Denki Denshi Kairo* (English translated title: *Essentials of Electrical and Electronic Circuits*) (Kyoritsu Shuppan Co., Ltd., Tokyo, Japan, 2013), pp. 172. ISBN: 9784320086425 (in Japanese)
2. M. Nishimaki, *Denki Gaku* (English translated title: *Electricity*) (Morikita Publishing Co., Ltd., Tokyo, Japan, 1973), pp. 222 (in Japanese)
3. H. Kusama, Y. Sato, N. Isshiki, Y. Abu, *Kikai Kogaku Gairon* (Dai 3 Pan) (English translated title: *Introduction to Mechanical Engineering*, 3rd edn.) (Ohmsha, Ltd., Tokyo, Japan, 1992), pp. 240. ISBN: 978-4-274-06977-2
4. S. Ohshita, *Syokai Denki Kairo Ensyu Jyo, Ge* (English translated title: *Detailed Explanation of Electric Circuit Exercises, Volume 1 and Volume 2*) (Kyoritsu Shuppan Co., Ltd., Tokyo, Japan, 1979, 1980), pp. 338 and pp. 384. ISBN: 978-4-320-08433-9 and ISBN: 978-4-320-08434-6

# Chapter 4
# Impedance Matching and Energy Conversion (1): Power Calculation and Impedance Matching Apparatus


**Abstract** This chapter covers the impedance matching and energy conversion (1); power calculation and impedance matching apparatus are mainly explained. On calculating the average value of the product of two periodic complex numbers, explanations are presented. On power consumption of *LR* circuit, explanation is presented. Power consumption in capacitor and coil, circuit impedance matching both for cases with DC and AC circuits are covered. The chapter is concluded by the conclusions and exercise problems.

## 4.1 Introduction

This chapter provides a detailed explanation of how to calculate the average value of the product of periodic complex numbers. In particular, it focuses on calculating the time-averaged value of the product of their real parts when two periodic complex numbers, $A$ and $B$ are given. Specifically, as a nonlinear calculation is required to obtain the products of $A$ and $B$, a method is proposed to calculate only the real part. In addition, a formula for the time-averaged value that is convenient for calculations is derived, and examples of its proof and concrete application are shown. This allows readers to deepen their understanding of how to handle complex numbers and calculate the average value of periodic signals. The descriptions are referred by Refs. [1–7].

## 4.2 On Calculating the Average Value of the Product of Two Periodic Complex Numbers

Regarding the calculation of the average value of the product of two periodic complex numbers, the explanation is related to Problem 1 at the end of the chapter. Let the periodic complex numbers be $A = A_0\, e^{i\omega t}$ and $B = B_0\, e^{i\omega t}$, and let $A_0$ and $B_0$ be complex numbers. Because calculating the product of $A$ and $B$ is a nonlinear



M. Okubo, *Electrical Sustainable Energy for Mechanical Engineering*,
https://doi.org/10.1007/978-981-96-5170-2_4

calculation, the real part is considered, and the calculation is performed in the form of $\mathrm{Re}(A) \times \mathrm{Re}(B)$, where Re denotes the real part. However, if only the time-averaged value needs to be calculated, this formula holds [1].

$$\overline{\mathrm{Re}(A) \cdot \mathrm{Re}(B)} = \frac{1}{2}\mathrm{Re}\left(AB^*\right) \tag{4.1}$$

The time average value of $\mathrm{Re}(A)$ and $\mathrm{Re}(B)$, i.e., the real part of $A$ multiplied by the real part of $B$, is $\mathrm{Re}(AB^*)/2$. On the right side, $B^*$ represents the number of conjugated complexes. For example, if there is a complex number $a + ib$, its conjugate is $a - ib$; in other words, if the imaginary part is positive, it becomes negative, and if it is negative, it becomes positive. This is known as the conjugate complex number. The left-hand side represents the time-averaged value of the product of the real parts of $A$ and $B$, which can be expressed by the integral.

$$\overline{\mathrm{Re}(A) \cdot \mathrm{Re}(B)} = \frac{1}{T}\int_0^T \mathrm{Re}(A) \cdot \mathrm{Re}(B)\mathrm{d}t \tag{4.2}$$

Equation (4.1) holds true when it is necessary to calculate the time-averaged value. The proof of this formula is as follows.

***Proof*** It is well known that the following formula holds in relation to conjugate complex numbers.

$$\left(A^*\right)^* = A, \tag{4.3}$$

$$(AB)^* = A^*B^*, \tag{4.4}$$

$$\mathrm{Re}(A) = \left(A + A^*\right)/2, \tag{4.5}$$

$$\mathrm{Re}(AB) = \left(AB + A^*B^*\right)/2 \tag{4.6}$$

From this, we obtain the following equation:

$$\mathrm{Re}\left(AB^*\right) = \frac{1}{2}\left(AB^* + A^*B\right) \tag{4.7}$$

$$\begin{aligned}\mathrm{Re}(A) \cdot \mathrm{Re}(B) &= \frac{1}{4}\left(A_0\mathrm{e}^{i\omega t} + A_0^*\mathrm{e}^{-i\omega t}\right)\left(B_0\mathrm{e}^{i\omega t} + B_0^*\mathrm{e}^{-i\omega t}\right) \\ &= \frac{1}{4}\left(A_0B_0e^{2i\omega t} + A_0B_0^* + A_0^*B_0 + A_0^*B_0^*e^{-2i\omega t}\right)\end{aligned} \tag{4.8}$$

The terms in () including $\mathrm{e}^{2i\omega t}$ and $\mathrm{e}^{-2i\omega t}$ and become zero when the time average is taken, and we obtain the following formula or the formula for the average value of the product of complex numbers:

$$\overline{\mathrm{Re}(A)\cdot\mathrm{Re}(B)} = \frac{1}{4}\left(A_0B_0^* + A_0^*B_0\right) = \frac{1}{4}\left(AB^* + A^*B\right) = \frac{1}{2}\mathrm{Re}\left(AB^*\right) \tag{4.9}$$

(Proof is completed.)

The application of this formula will be explored in future studies. Note that complex analytical representations are generally unavailable for nonlinear systems. However, using this formula, the time-averaged value, which is a nonlinear calculation, can be calculated easily. This is the explanation related to Problem 1 at the end of the chapter.

## 4.3 Power Consumption of *LR* Circuit

As mentioned earlier, in Problem 1, calculate the instantaneous power $P = VI$ and average power $\overline{P} = \int_0^T VI\mathrm{d}t/T = \overline{VI}$ of the *LR* circuit shown below, where $T$ is the period, $\omega = 2\pi/T$. This indicated the power consumption of the circuit.

Answer and another solution using formula (4.1) are shown below.

### *4.3.1 Solution by Calculating the Real Part*

First, we will answer by calculate the real part. As the actual applied voltage is $V_0$ cos ωt, we ultimately consider the real part. This is the basic principle of the process.

By performing calculations for this circuit, we obtain the following:

$$I = I_0e^{i\omega t}, \quad (R + i\omega L)I_0 = V_0, \quad I_0 = \frac{V_0}{R + i\omega L} = \frac{V_0}{Z} \tag{4.10}$$

$$|Z| = \sqrt{R^2 + \omega^2L^2}, \quad \tan\varphi = \frac{\omega L}{R}, \quad I = \frac{V_0}{\sqrt{R^2 + \omega^2L^2}}\mathrm{e}^{i(\omega t - \varphi)} \tag{4.11}$$

Now, we consider the real part. Equation (4.12) is obtained.

$$I = \frac{V_0}{\sqrt{R^2 + \omega^2L^2}}\cos(\omega t - \varphi) \tag{4.12}$$

Since the instantaneous power consumption $P$ is $VI$, equation (4.13) is obtained.

$$\begin{aligned} P = VI &= \frac{V_0^2}{\sqrt{R^2 + \omega^2L^2}}\cos(\omega t)\cos(\omega t - \varphi) \\ &= \frac{V_0^2}{2\sqrt{R^2 + \omega^2L^2}}[\cos(2\omega t - \varphi) + \cos\varphi] \end{aligned} \tag{4.13}$$

This form is obtained from the formula for converting the product of cosine functions into a sum. For mathematical formulas, please refer to mathematical formulas book such as Ref. [8]. Various formulae have been described. Nowadays, we can use mathematical processing software such as Mathematica, instead of the formula book. Take the average of this Eq. (4.13) or the average of $P$. Represent the average with a superscript bar. Note that $\overline{\cos(2\omega t - \varphi)} = 0$ this is because it is periodic over time and the average of trigonometric functions is 0. Therefore

$$\overline{P} = \frac{V_0^2}{2\sqrt{R^2 + \omega^2 L^2}} \cos\varphi = \frac{V_e^2}{\sqrt{R^2 + \omega^2 L^2}} \cos\varphi \tag{4.14}$$

This is the answer. If we express the effective voltage as $V_e$, we can obtain the second equation, which also provides an answer. In this equation, $\cos\varphi$ is the power factor, and $V_e = V_0/\sqrt{2}$ is called the effective voltage.

### 4.3.2 *Alternative Solution Using the Formula for the Average Value of the Product*

An alternative solution is explained. In other words, if there are time-varying quantities $A$ and $B$, taking their real values and multiplying them yields an average $\mathrm{Re}(A \times B^*)/2$. This is explained by Eq. (4.1). This is used to calculate the power. To find that the averages of $VI$, $A$ and $B$ are now $V$ and $I$, we apply them to Eq. (4.1). The average value of $VI$ is expressed as follows, using the above formula:

$$\begin{aligned}\overline{VI} &= \frac{1}{2}\mathrm{Re}\left[\frac{V_0^2}{\sqrt{R^2 + \omega^2 L^2}} e^{i\omega t} e^{-i(\omega t - \varphi)}\right] = \frac{1}{2}\mathrm{Re}\left[\frac{V_0^2}{\sqrt{R^2 + \omega^2 L^2}} e^{i\varphi}\right] \\ &= \frac{V_0^2}{2\sqrt{R^2 + \omega^2 L^2}} \cos\varphi \end{aligned} \tag{4.15}$$

Please note that the exponent of $e^{-i(\omega t - \varphi)}$ in the second term on the right-hand side has negative signed phase. As we proceed with the calculation, we obtain if we consider the real part of this equation, we obtain the same result as if we are extracting the real part of the calculation. This is an important expression.

Next, we explain misunderstandings and mistakes. By multiplying $V$ and $I$ directly, the instantaneous power $P = VI$ becomes

$$P = VI = \frac{V_0^2}{\sqrt{R^2 + \omega^2 L^2}} e^{i(2\omega t - \varphi)} \tag{4.16}$$

This is a mistake. Multiplication must be performed by separating the real parts, but it is a mistake to simply multiply them. Moreover, the average value of $P$ is zero in this equation, which is a complete mistake. Please be careful for this mistake.

## 4.4 Power Consumption in Capacitor and Coil

In this section, the power consumption of the capacitor and coil are explained. Although it is written here, this item is a reference advanced topic. Please read the manuscript if you are interested. First, the results are explained. It has been proven that, generally, when the voltage is only a sine wave, the power consumption of the capacitor alone and the coil alone in a series circuit with a resistor is zero, and the power is consumed only by the resistor. If you are interested, please study the examples in Sect. 4.4.1 below.

### *4.4.1 Power Consumption in Resistance and Coil*

***Example 1*** In a series circuit of $R$ and $L$ as shown in Fig. 4.1, the power is consumed by $R$ and $L$.

**Answer**

$$I = \frac{V_0}{\sqrt{R^2 + \omega^2 L^2}} \mathrm{e}^{i(\omega t - \varphi)} \tag{4.17}$$

$$\tan \varphi = \frac{\omega L}{R} \tag{4.18}$$

Therefore (see Fig. 4.2), the total power of the entire circuit is

$$\overline{P} = \frac{1}{2} \mathrm{Re}\left(VI^*\right) = \frac{V_0^2}{2\sqrt{R^2 + \omega^2 L^2}} \cos \varphi \tag{4.19}$$

On the other hand, the voltage $V_R$ applied to $R$ is given by the following equation.

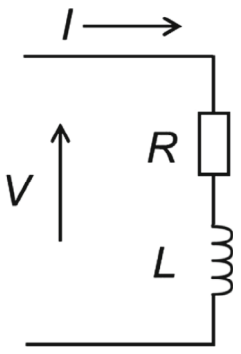


**Fig. 4.1** *LR* AC circuit with power source $V = V_0 \cos \omega t$

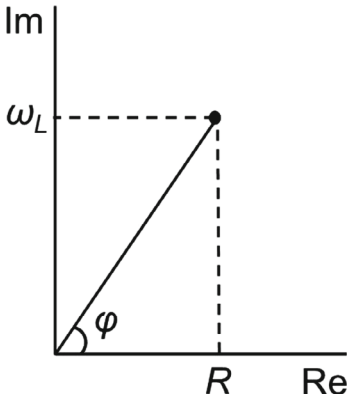


**Fig. 4.2** Complex plane of the circuit in Fig. 4.1

$$V_R = \frac{V_0 R\,\mathrm{e}^{i\omega t}}{R + i\omega L} = V_0 \frac{R\,\mathrm{e}^{i\omega t}}{\sqrt{R^2 + \omega^2 L^2}\mathrm{e}^{i\varphi}} = V_0 \cos\varphi \cdot \mathrm{e}^{i(\omega t - \varphi)} \tag{4.20}$$

The power is calculated using Eqs. (4.17) and (4.20) as follows:

$$\begin{aligned} \overline{P}_R &= \frac{1}{2}\mathrm{Re}\left(V_R I^*\right) \\ &= \frac{1}{2}\mathrm{Re}\left[V_0 \cos\varphi \cdot \mathrm{e}^{i(\omega t-\varphi)} \frac{V_0}{\sqrt{R^2 + \omega^2 L^2}} \mathrm{e}^{-i(\omega t-\varphi)}\right] \\ &= \frac{V_0^2}{2\sqrt{R^2 + \omega^2 L^2}} \cos\varphi \end{aligned} \tag{4.21}$$

This is the same as Eq. (4.19). On the other hand, the voltage $V_L$ applied to $L$ is

$$V_L = \frac{i\omega L V_0 \mathrm{e}^{i\omega t}}{R + i\omega L} = V_0 \frac{\omega L i \mathrm{e}^{i\omega t}}{\sqrt{R^2 + \omega^2 L^2}\mathrm{e}^{i\varphi}} = V_0 \sin\varphi \cdot i\mathrm{e}^{i(\omega t - \varphi)} \tag{4.22}$$

The power is calculated from Eqs. (4.17) and (4.22) as follows:

$$\overline{P} = \frac{1}{2}\mathrm{Re}\left(V_L I^*\right) = \frac{1}{2}\mathrm{Re}\left(V_0 \sin\varphi \cdot i\frac{V_0}{R^2 + \omega^2 L^2}\right) = 0 \tag{4.23}$$

Therefore, it can be seen that the power consumed by reactance $L$ is 0, and all power is consumed by resistance $R$.

***Example 2*** In a circuit with resistor $R$ and capacitors $C$ and $C'$ connected as shown in Fig. 4.3, calculate the power consumption $P$ of $C'$.

**Answer**

The total impedance is given by the following formula:

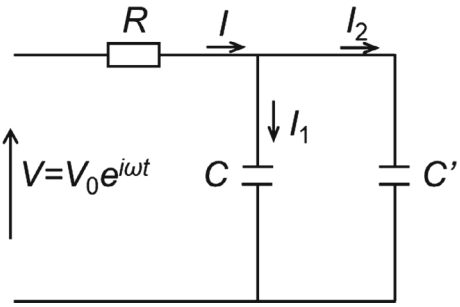


**Fig. 4.3** Circuit in which resistor $R$ and capacitors $C$ and $C'$ are connected

$$Z = R + \frac{1}{i\omega(C + C')} = R - i\frac{1}{\omega(C + C')} \tag{4.24}$$

The total current $I = I_0\, \mathrm{e}^{i\omega t}$ is obtained as follows.

$$I_0 = \frac{V_0}{Z} = \frac{V_0}{|Z|}\mathrm{e}^{-i\varphi} \quad (\varphi < 0) \tag{4.25}$$

(see Fig. 4.4).

$$|Z| = \sqrt{R^2 + \frac{1}{\omega^2(C + C')^2}}, \quad \tan\varphi = \frac{-1}{R\omega(C + C')} \tag{4.26}$$

On the other hand, if the currents to $C$ and $C'$ are $I_1$ and $I_2$, $I_1 = I_{01}\, \mathrm{e}^{i\omega t}$ and $I_2 = I_{02}\, \mathrm{e}^{i\omega t}$, and the following equation is obtained:

$$I_0 = I_{01} + I_{02} \tag{4.27}$$

If the voltage applied to $C$ and $C'$ is $V' = V'_0\, \mathrm{e}^{i\omega t}$, the following equation is obtained:

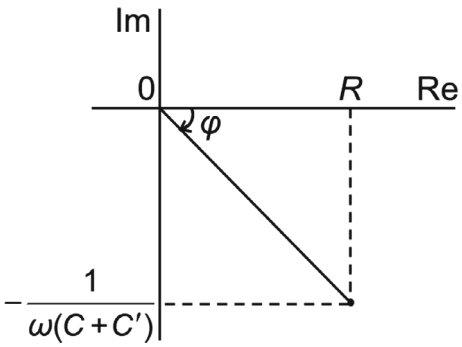


**Fig. 4.4** Complex plane of the circuit in Fig. 4.3

$$V_0' = \frac{I_{01}}{i\omega C} = \frac{I_{02}}{i\omega C'}, \quad \text{Therefore,} \quad I_{01} = I_{02}\frac{C}{C'} \tag{4.28}$$

From Eq. (4.27),

$$I_0 = I_{02}\left(1 + \frac{C}{C'}\right) \tag{4.29}$$

From Eqs. (4.25) and (4.29), we obtain

$$I_{02} = \frac{1}{\left(1 + \frac{C}{C'}\right)}\frac{V_0}{|Z|}\mathrm{e}^{-i\varphi} \tag{4.30}$$

$$I_2 = \frac{1}{\left(1 + \frac{C}{C'}\right)}\frac{V_0}{|Z|}\mathrm{e}^{i(\omega t-\varphi)} \tag{4.31}$$

Furthermore, the voltage applied to $C'$ is given by the following equation from the relationship in Eq. (4.30) and $1/i = -i = \mathrm{e}^{-i\pi/2}$

$$V_2 = V_0'\mathrm{e}^{i\omega t} = \frac{I_{02}}{i\omega C'}\mathrm{e}^{i\omega t} = \frac{V_0}{\omega(C + C')}\frac{1}{|Z|}\mathrm{e}^{i\left(\omega t-\varphi-\frac{\pi}{2}\right)} \tag{4.32}$$

From Eqs. (4.31) and (4.32), and $\overline{P} = \overline{\mathrm{Re}(V_2)\mathrm{Re}(I_2)} = \mathrm{Re}\left(V_2 I_2^*\right)/2$

$$\begin{aligned} V_2 I_2^* &= \frac{V_0}{|Z|\omega(C + C')}\mathrm{e}^{i\left(\omega t-\varphi-\frac{\pi}{2}\right)}\frac{C'}{C + C'}\frac{V_0}{|Z|}\mathrm{e}^{-i(\omega t-\varphi)} \\ &= \frac{V_0^2 C'}{|Z|^2\omega(C + C')^2}\mathrm{e}^{-\frac{i\pi}{2}} = \frac{V_0^2 C'}{\frac{1}{\omega} + R^2\omega(C + C')^2}(-i) \end{aligned} \tag{4.33}$$

Therefore,

$$P = \frac{1}{2}\mathrm{Re}\left(V_2 I_2^*\right) = 0 \tag{4.34}$$

From the above, it can be observed that the power consumption of the capacitor alone is zero, and power is consumed only by the resistor.

## 4.5 Circuit Impedance Matching

Impedance matching involves adjusting the circuit constants such that the power supply can deliver maximum power (energy) to the load. This concept is important in this context.

### 4.5.1 Case with DC Circuit

We now explain the importance of circuit impedance matching. Impedance matching involves adjusting the circuit constants so that the power supply can send the maximum amount of energy to the load. First, we consider the case of a DC circuit. We consider the circuit diagram shown in Fig. 4.5. There is a power supply that has internal resistance $r$ and voltage $V$. Consider a DC circuit to which load resistance $R$ is connected. In the diagram, the DC power supply always has internal resistance $r$. When this power supply sends power $P = V_R I$ to load resistance $R$, the question is at what load resistance $R$ will power $P$ be maximized, and matching is achieved.

The results are presented in this section. The power is maximized when $R = r$. The proof or explanation is provided below.

***Proof***

$$I = \frac{V}{r + R} \tag{4.35}$$

Therefore, we obtain the following equation for the power $P$:

$$P = IR^2 = \frac{V^2 R}{(r + R)^2} = \frac{V^2 R}{r^2 + 2Rr + R^2} = \frac{V^2}{\frac{r^2}{R} + 2r + R} \tag{4.36}$$

Differentiate denominator $= r^2/(R + 2r + R)$ with respect to $R$ and set this value to 0. In other words, if we set d(denominator)$/$d$R = 1 - r^2/R^2 = 0$, then because $R > 0$, when $R = r$ it will be a minimum. The denominator is the minimum, and we write this increase/decrease in Table 4.1. This is also the minimum value. In other words, $P$ is the maximum value. This implies that in this circuit, power is maximized when $R = r$.


**Fig. 4.5** Circuit in which the load resistance $R$ and internal resistance $r$ at the power supply are connected

**Table 4.1** Increase/decrease table for the denominator of Eq. 4.36 when changing $R$

| $R$ | | $r$ | |
|---|---|---|---|
| d(denominator)/dR | − | 0 | + |
| denominator | ↘ | Local minimum | ↗ |

### 4.5.2 Case with AC Circuit

Next, we examine the case of AC circuit. In Fig. 4.6, the AC power source $V$ always has an internal impedance $Z_S$ ($= R_S + iX_S$: constant). When this power source sends power $P = V_R I$ to a load impedance $Z_R$ ($= R_R + iX_R$: variable), the problem is what load impedance resistance $Z_R$ is required to maximize power $P$ and achieve circuit matching. In conclusion, the power is maximized when the following conditions are satisfied: $Z_S = Z_R{}^*$ or $R_S = R_R$, $X_S = -X_R$, that is, when $Z_S$ and $Z_R$ are complex conjugates, the power is maximized.

A representation of the complex plane is shown in Fig. 4.7. The proof is more complicated than the DC circuit case as shown below.

***Proof*** Assuming this $V = V_0\, e^{i\omega t}$, we obtain the following equation:

$$I = \frac{V}{Z_S + Z_R} = \frac{V_0}{|Z_S + Z_R|} e^{i(\omega t - \varphi)}, \quad \tan\varphi = \frac{\mathrm{Im}(Z_S + Z_R)}{\mathrm{Re}(Z_S + Z_R)} = \frac{X_S + X_R}{R_S + R_R} \tag{4.37}$$

If we calculate power using the average value formula, we get the following formula.

$$P = \frac{1}{2}\mathrm{Re}\left(V_R I^*\right) = \frac{1}{2}\mathrm{Re}\left(Z_R I \cdot I^*\right) = \frac{1}{2}\mathrm{Re}\left(Z_R |I|^2\right)$$

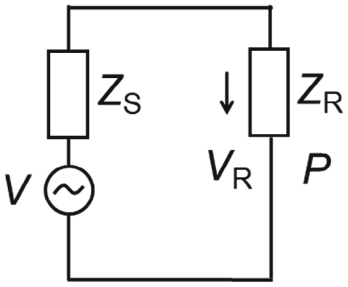


**Fig. 4.6** Circuit in which load impedance $Z_R$ and internal impedance $Z_S$ at the power supply are connected

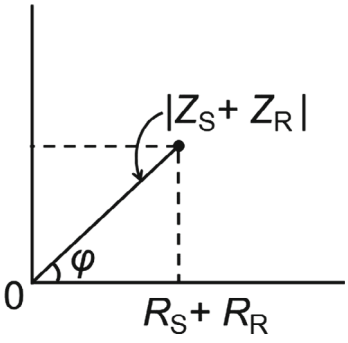


**Fig. 4.7** Complex plane of the circuit in Fig. 4.6

**Table 4.2** Increase/decrease table for the denominator of Eq. 4.39 when changing $R$

| $R$ | | $r$ | |
|---|---|---|---|
| $\partial$(denominator)/$\partial R_R$ | − | 0 | + |
| denominator | ↘ | Local minimum | ↗ |

$$= \frac{1}{2}\mathrm{Re}\left[(R_R + iX_R)\frac{V_0^2}{|Z_S + Z_R|^2}\right]$$
$$= \frac{V_0^2 R_R}{2|Z_S + Z_R|} = \frac{V_0^2}{2}\frac{R_R}{\left[(R_S + R_R)^2 + (X_S + X_R)^2\right]} \tag{4.38}$$

Note that $R_S$ and $R_R$ are always positive, whereas $X_S$ and $X_R$ are negative. Differentiating the denominator of $P$ with respect to $X_R$.

If we put $\partial(\text{denominator})/\partial X_R = 2(X_S + X_R) = 0$, $X_S = -X_R$ and $P$ becomes maximum. In other words, $P$ reaches a maximum when $|X_S| = |X_R|$ and $X_S$ have signs opposite to $X_R$. Therefore,

$$P = \frac{V_0^2}{2}\frac{R_R}{(R_S + R_R)^2} = \frac{V_0^2}{2}\frac{1}{\left(\frac{R_S^2}{R_R} + 2R_S + R_R\right)} \tag{4.39}$$

If we set $\partial(\text{denominator})/\partial R_R = 1 - R_S^2/R_R^2 = 0$, then the denominator is the minimum and $P$ is the maximum for $R_S = R_R$ and $R_S > 0$ and $R_R > 0$, respectively (see Table 4.2).

In summary, to achieve impedance matching that satisfies the conditions $R_S = R_R$ and $X_S = -X_R$, a matching circuit consisting of $C$ and $L$ is inserted between $Z_S$ and $Z_R$ to maximize the change in electrical energy from the power supply to the load. As previously explained, if it is a complex conjugate, the power is maximized.

## 4.6 Matching for the Plasma Apparatus

In an inductively coupled plasma (ICP) [9] cleaning system and a capacitively coupled plasma (CCP) system, a matching circuit is installed between the power supply and the coil to apply the maximum energy to the coil with a high frequency to form a plasma. For example, it consists of two variable capacitors, $C_1$ and $C_2$, as shown in Fig. 4.8. $C_1$ is semi-fixed, and $C_2$ can be adjusted for matching. The output impedance of the power supply is typically designed to be 50 Ω. The induction coil has a high impedance of several hundred ohms or more when no plasma is generated; however, the impedance drops sharply when plasma is formed. Considering the problem of matching the load of $Z = 16 + 30i$ to the power supply of $Z_c = 50\ \Omega$ at $f = 13.56$ MHz, $C_1 = 1.68$ nF and $C_2 = 510$ pF are determined as the matched values using a Smith chart. A normal variable capacitor is used for $C_1$, a vacuum variable

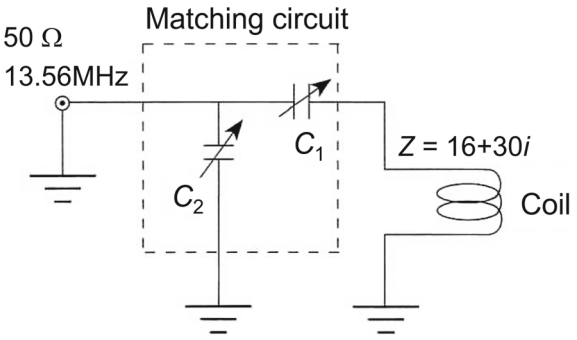


**Fig. 4.8** Matching circuit with the ICP apparatus [9]

capacitor is usually used for $C_2$, and is electrically changed by servo mechanisms for automatic matching. In other words, plasma irradiation is possible by simply turning on the switch. Remarks, to achieve impedance matching so that $R_S = R_R$ and $X_S = -X_R$ are satisfied, a matching circuit consisting of $C$ and $L$ is inserted between $Z_S$ and $Z_R$. This maximizes electrical energy conversion from the power supply to the load.

## 4.7 Conclusions

In conclusion, this section has effectively provided a comprehensive guide on how to calculate the average value of the product of periodic complex numbers, particularly emphasizing the calculation of the time-averaged value of the real parts of two given periodic complex numbers, $A$ and $B$. The process requires a nonlinear approach to obtaining the products of $A$ and $B$, and a specialized method has been proposed to focus solely on calculating the real part. Moreover, a formula has been derived that simplifies the calculation of the time-averaged value, supported by examples of its proof and practical application. This detailed exposition enables readers to enhance their understanding of complex numbers and effectively compute the average value of periodic signals. Following this, impedance matching and energy conversion using Smith chart and matching circuit design methods are further discussed in next Chap. 5.

### Chapter 4 Exercises

**Problem 1**: Products of two complex variables

When there are any two periodic complex unknown variables, $A = A_0\, e^{i\omega t}$ and $B = B_0\, e^{i\omega t}$ ($A_0$ and $B_0$ are also complex variables), the method described in this section cannot be used for equations that contain their products, i.e., nonlinear equations (systems). To calculate the products, the real (or imaginary) parts must first be separated. However, as is often the case, the product in an equation that governs the

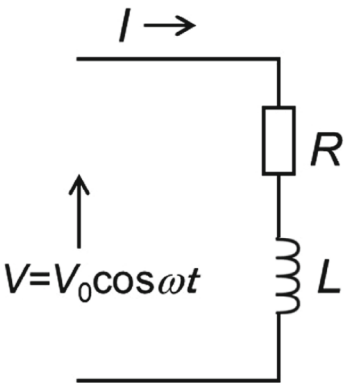


**Fig. 4.9** A series circuit ($V = V_0 \cos \omega t$)

time average value can be calculated as Re($AB^*$)/2 as the time average value. Prove this. Note that Re( ) represents the real part and * represents the complex conjugate number.

**Problem 2**: Instantaneous and average powers

Calculate the instantaneous and average powers of the series circuits $R$ and $L$ shown in Fig. 4.9.

**Problem 3**: Equivalent circuit network of the transformer

Figure 4.10 shows the equivalent circuit network of the transformer. The impedance is measured at 60 Hz

(1) Calculate the current when an AC voltage of 130 V is applied between terminals A and B, and three Ω resistors are connected between terminals C and D.
(2) Calculate the current at 500 Hz when terminals C and D are short circuited.

**Problem 4**: *LCR* parallel AC circuit

Figure 4.11 shows an $L$, $C$, $R$ parallel AC circuit

(1) The reciprocal $Y = 1/Z$ of the circuit impedance $Z$ is called the admittance. Find the complex expression for $Y$ and its magnitude.

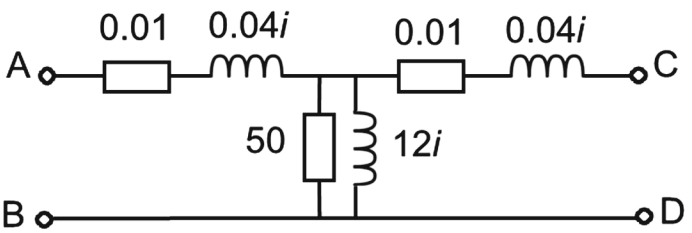


**Fig. 4.10** Equivalent circuit network of the transformer

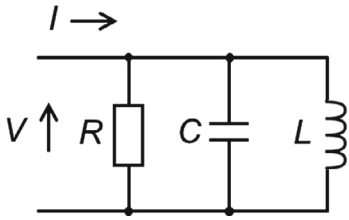


**Fig. 4.11** *LCR* parallel AC circuit

(2) If an AC voltage $V = V_0 \cos \omega t$ is applied to the circuit, derive an expression for the current $I$ flowing through the circuit from the relationship $I = Y\,V$. Note that $\tan^{-1}$ may be included in the result.

## References

1. L.D. Landau, E.M. Lifshitz, *The Classical Theory of Fields, Course of Theoretical Physics Volume 2* (Pergamon Press, 1975), pp. 402
2. N. Ida, *Engineering Electromagnetics*, 4th edn. (Springer Nature Switzerland AG, 2021), pp. 1028. ISBN: 978-3-030-15559-9, ISBN: 978-3-030-15557-5 (eBook). https://doi.org/10.1007/978-3-030-15557-5
3. D.E. LaLond, J.A. Ross, *Experiments in Principle of Electronic Devices and Circuits* (Delmar Publishers Inc., New York, USA, 1994), pp. 310. ISBN: 0-8273-4664-6
4. C. Bowick, J. Blyler, C. Ajluni, *RF Circuit Design* (Newnes, an Imprint of Elsevier, Oxford, UK, 2008), pp. 232. ISBN-13: 978-0-7506-85184, ISBN-10: 0-7506-8518-2
5. M. Rahmani-Andebili, *AC Electrical Circuit Analysis, Practice Problems, Methods, and Solutions* (Springer Nature Switzerland AG, 2021), pp. 229. ISBN: 978-3-030-60985-6, ISBN: 978-3-030-60986-3 (eBook). https://doi.org/10.1007/978-3-030-60986-3
6. A.R. Bergen, V. Vittal, *Power System Analysis*, 2nd edn. (Pearson India Education Services Pvt. Ltd., Uttar Pradesh, India, 2000), pp. 629. ISBN: 978-81-7758-819-4
7. S. Ohshita, *Syokai Denki Kairo Ensyu Jyo, Ge* (English translated title: *Detailed Explanation of Electric Circuit Exercises, Volume 1 and Volume 2*) (Kyoritsu Shuppan Co., Ltd., Tokyo, Japan, 1979 and 1980), pp. 384 and pp. 338. ISBN: 978-4-320-08433-9 and ISBN: 978-4-320-08434-6
8. S. Moriguchi, K. Udagaw, S. Hitotsumatsu, *Sugaku Koshiki I, II, and III* (English translated title: *Mathematical Formula I, II, and III*) (Iwanami Shoten, Publishers, Tokyo, Japan, 1956, 1957, and 1960), pp. 318, pp. 340, and pp. 310 (in Japanese)
9. K. Chayama, *ICP nitsuite* (English translated title: *On the ICP (Inductively Coupled Plasma)*). http://kccn.konan-u.ac.jp/chemistry/ia/contents_05/05.html. Accessed 2024.12.01 (in Japanese)

# Chapter 5
# Impedance Matching and Energy Conversion (2): Smith Chart and Matching Circuit Design Method


**Abstract** This chapter covers the impedance matching and energy conversion (1). Smith chart and matching circuit design method are explained. First, the circuit impedance matching method is summarized. Design of matching circuit using Smith chart and impedance chart and admittance chart are explained. Trajectories on Smith chart are explained for cases of connecting $C$ in series to a load, connecting $L$ in series to a load, connecting $R$ in series to an impedance load, connecting $C$ in parallel to a load, connecting $L$ in parallel to a load, connecting $R$ in parallel to an impedance load, and connecting a transmission line to an impedance load. The chapter is concluded by the conclusions and exercise problems.

## 5.1 Introduction

Impedance matching is an essential concept for optimizing the power transfer between each component in a circuit and plays a fundamental role in electrical engineering. By adjusting the circuit constants, impedance matching ensures that maximum power is transferred from the source to the load. This principle is particularly important in applications requiring efficient power transfer such as antenna designs, radio frequency (RF) circuits, and various electronic devices. Maximum power transfer is achieved when the source impedance ($Z_S$) is the complex conjugate of the load impedance ($Z_R$*). Engineers have used a powerful graphical tool called the Smith chart to assist in this matching process. The Smith chart simplifies complex calculations and allows the visualization of impedance transformations. Despite advances in computer tools, the Smith chart holds value, especially for helping understand and visualize impedance transformations. This section describes the design and application of impedance-matching circuits using a Smith chart. Important topics are covered, including impedance and admittance charts, trajectory plots, and practical examples of the series and parallel connections of $R$, $L$, and $C$ components. Mastering these techniques enables engineers to achieve the desired



M. Okubo, *Electrical Sustainable Energy for Mechanical Engineering*,
https://doi.org/10.1007/978-981-96-5170-2_5

impedance matching to ensure efficient and reliable operation of a variety of electronic systems. References in this chapter are [1–3]. A Smith chart sheet is obtained in Ref. [3].

## 5.2 Circuit Impedance Matching (Summary)

First, we review the contents of the previous chapter regarding circuit impedance control procedure in the following bullet points.

- Adjusting the circuit constants such that the power supply can send maximum power (energy) to the load is called impedance matching.
- If the power supply impedance is $Zs$ and the load impedance is $Z_R$, then $Z_S = Z_R{}^*$ or $R_S = R_R$ and $X_S = -X_R$; in other words, the power input to the load is maximized when $Z_S$ and $Z_R$ are complex conjugates. It is important to design the matching circuit appropriately.
- For example, $Z_S$ can be a power supply, and $Z_R$ can be an antenna, electronic, or electrical equipment.

## 5.3 Design of Matching Circuit Using Smith Chart

The design of the matching circuit is explained using the Smith chart. By assuming the shape of the matching circuit using the complex number calculations we have practiced so far, we can determine the constants of the matching circuit such that $R_S = R_R$ and $X_S = -X_R$ are satisfied. Smith charts are widely used to design matching circuits. With the development of computers, its necessity has somewhat diminished, but as explained below, it does not require complex algebraic calculations and is useful for understanding matching conditions. The trajectory drawn on the Smith chart when connecting *L, C, R* or a transmission line between the power supply and load is explained below.

### *5.3.1 Impedance Chart and Admittance Chart*

We explain the paths or trajectories that appears on the Smith chart when a *LCR* or transmission line is connected between a power supply and a load. First, we describe the impedance and admittance charts. In Fig. 5.1, the circular diagram is the impedance chart, and the diagram on the right is the admittance chart.

An impedance chart is used to connect $L$ or $C$ in series to the electrical circuit, and an admittance chart is used to connect $L$ or $C$ in parallel to the circuit.

Figure 5.2 shows a complex plane. An impedance chart is created by bending the endpoints along the axis. This is the impedance chart. The horizontal axis indicates

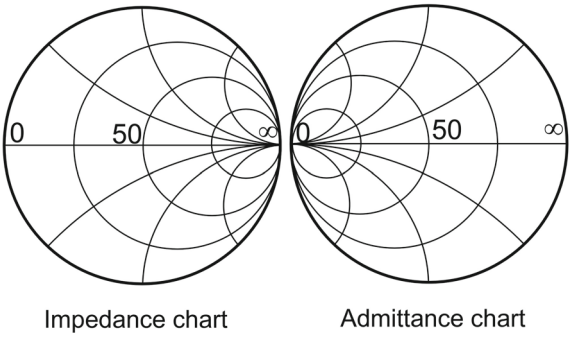


**Fig. 5.1** Impedance and admittance charts

resistance. A complex coordinate axis exists on the upper side, ranging from zero to infinity, where $i$ is an imaginary unit. It moves in the directions of plus and minus infinity. By bending the endpoints, the chart is transformed into a circle, as shown in Fig. 5.3, and by following these steps, the endpoints can be bent along the axis to create an impedance chart. The admittance chart represents the inverse of the impedance chart.

The chart in Fig. 5.4 is an impedance chart and admittance chart superimposed on each other. To read this chart, the horizontal line that divides a circle in half vertically represents pure resistance, with the left end being 0 Ω (short circuit), the right end being $\infty$ Ω (open circuit), and the center being 50 Ω. However, the Smith chart paper described later lists the normalized impedance of 1 Ω, which is obtained by dividing all impedances by 50. This is an important point.

We review the terminology. Impedance is defined as $Z = R + iX$, where $R$ is the resistance and $X$ is the reactance. The admittance is $Y = 1/Z = G + iB$, where $G$ is the conductance and $B$ is the susceptance.

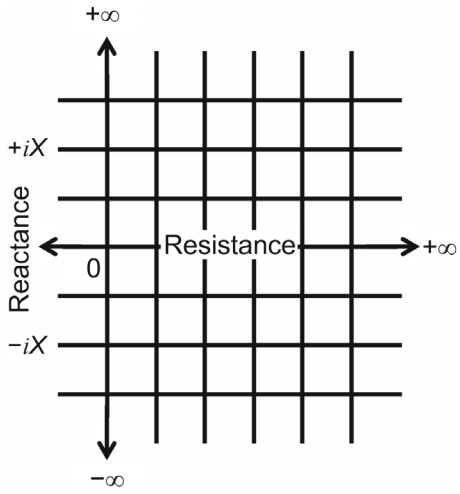


**Fig. 5.2** Resistance and reactance space

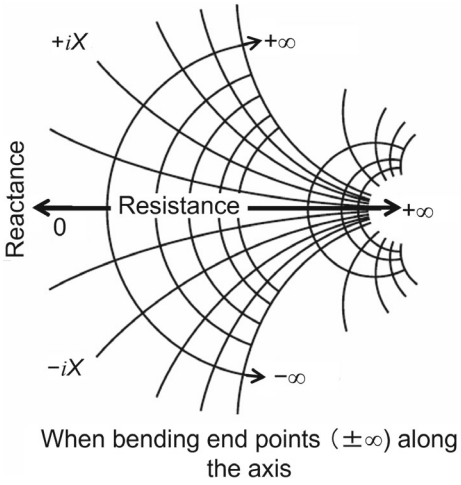


**Fig. 5.3** Resistance and reactance space when bending end points ($\pm\infty$) along the axis

It is important to note that the impedance chart on the left side of Fig. 5.5 is shown as a red line in the Smith chart sheet, where the value $Z = R + iX$ is indicated. Below the horizontal line, the value of reactance $X$ is negative. However, the absolute values are shown without negative signs in the sheet.

The admittance chart on the right side of Fig. 5.5 is a blue line in the Smith chart sheet, where the value $Y = G + iB$ is indicated. Above the horizontal line, the value of susceptance $B$ is negative. However, the absolute values are shown without negative signs in the sheet.

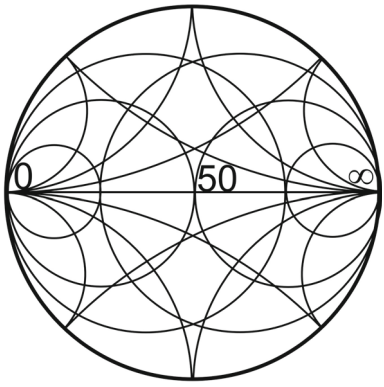


**Fig. 5.4** Impedance and admittance charts inside a circle

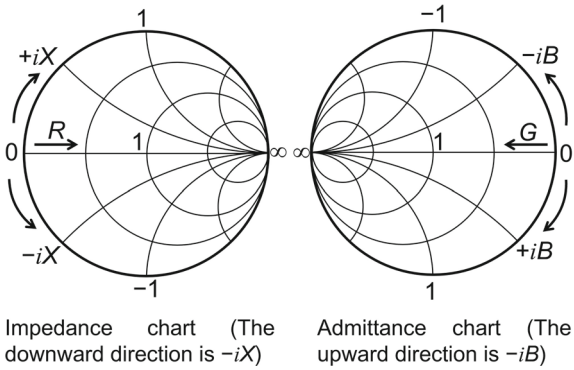


**Fig. 5.5** Impedance chart (the downward direction is $-iX$) and admittance chart (the upward direction is $-iB$)

## *5.3.2 Trajectories on Smith Chart*

### 5.3.2.1 Connecting *C* in Series to a 50 Ω Load

Next, we will explain the trajectory in the Smith chart [3]. In the case of a series connection, we should use the red diagram. When a capacitor $C$ is connected in series to a 50 Ω load, the impedance follows a trajectory like the chart in Fig. 5.6, and as the capacitance of $C$ becomes smaller and approaches 0 pF, the trajectory eventually reaches infinity. This is the behavior when $C$ is connected in series to a 50 Ω resistor.

### 5.3.2.2 Connecting *L* in Series to a 50 Ω Load

Next, if an inductance $L$ is connected in series to a 50 Ω load, the impedance will follow a path like the chart in Fig. 5.7, and as $L$ gets larger, the trajectory will eventually reach infinity.

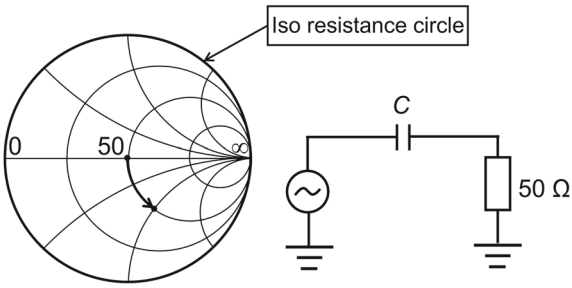


**Fig. 5.6** Connecting $C$ in series to a 50 Ω load

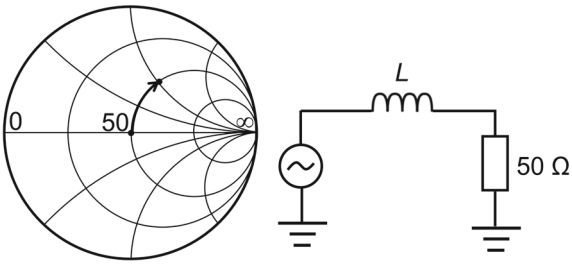


**Fig. 5.7** Connecting $L$ in series to a 50 Ω load

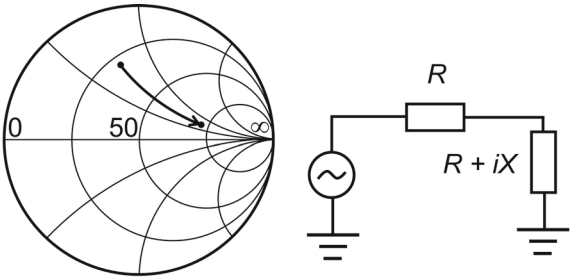


**Fig. 5.8** Connecting $R$ in series to an impedance load

#### 5.3.2.3 Connecting *R* in Series to an Impedance Load

Next, if you connect $R$ in series to a load of $R + iX$, the impedance will follow a trajectory like the chart in Fig. 5.8, and as $R$ gets larger, the trajectory eventually reaches infinity.

#### 5.3.2.4 Connecting *C* in Parallel to a 50 Ω Load

When a capacitor is connected in parallel to a 50 Ω load, the admittance follows a path as shown in the chart in Fig. 5.9, and as the capacitance of $C$ increases, the trajectory eventually reaches 0 on the iso conductance circle.

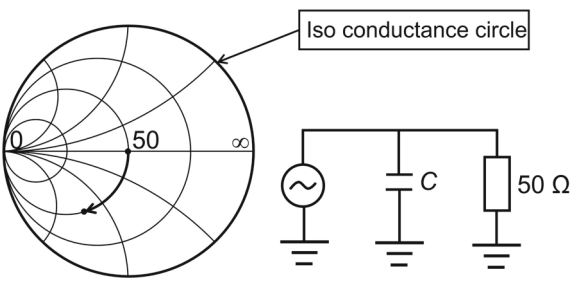


**Fig. 5.9** Connecting $C$ in parallel to a 50 Ω

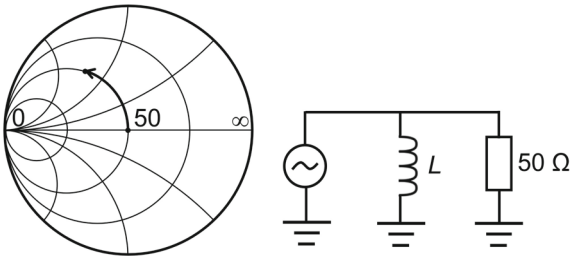


**Fig. 5.10** Connecting $L$ in parallel to a 50 Ω load

#### 5.3.2.5 Connecting *L* in Parallel to a 50 Ω Load

When an inductance is connected in parallel to a 50 Ω load, the admittance follows a path like the chart in Fig. 5.10, and as $L$ becomes smaller, the trajectory eventually reaches 0.

#### 5.3.2.6 Connecting *R* in Parallel to an Impedance Load

When $R$ is connected in parallel to a load of $R + iX$ Ω, the admittance follows a path as shown in the chart in Fig. 5.11, and as $R$ becomes smaller, the trajectory eventually reaches 0.

#### 5.3.2.7 Connecting a Transmission Line to an Impedance Load

When an element with a time delay, such as a coaxial cable or stripline, is inserted, it moved clockwise along the bold line on the left side as shown in Fig. 5.12. The bold line is called an "equal SWR circle." The amount of rotation $2\theta$ corresponds to the time it takes to travel round trip through the delay line. $\theta = 360$ (length)/(effective wavelength), where unit is degree. Effective wavelength is the wavelength shortened by $1/\sqrt{\varepsilon_r}$ when the transmission line is wrapped in a dielectric material. If the dielectric is Teflon, it is approximately 70% of the time in vacuum. If the

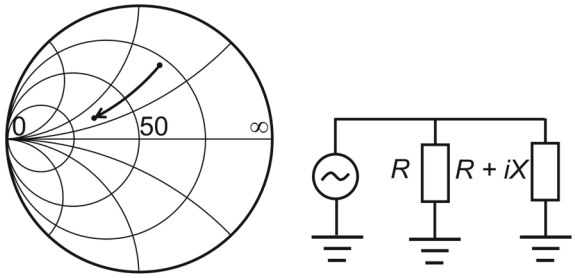


**Fig. 5.11** Connecting $R$ in parallel to an impedance load

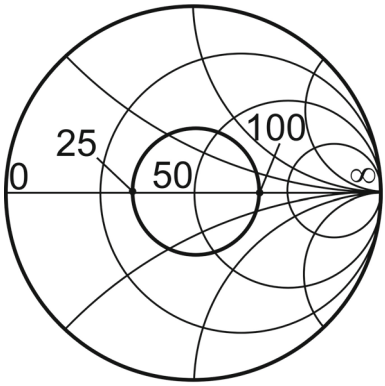


**Fig. 5.12** Connecting a transmission line to an impedance load

characteristic impedance of the delay line is different from the normalized impedance ($Z_0$), the center of rotation is on the other position.

The circuit shown in Fig. 5.13 is the trajectory when a transmission line of $Z = 50\ \Omega$ is connected between a 100 Ω load and an input, and moves in an arc on a circle centered at $Z = 50\ \Omega$ and tangent to the load $Z_r = 100\ \Omega$. In the example below, for a transmission line of $\lambda/4$ length, the impedance seen from the input is a pure resistance of $Z_i = Z^2/Z_r = 50^2/100 = 25\ \Omega$.

About transmission lines, in an actual circuit, when connecting $L$, $C$, etc. to the circuit, there will always be physical distance between the components; therefore, it is necessary to consider the components as having transmission lines between them. The theory of transmission lines (electrical transmission lines) will not be explained in detail in this book. Please refer to Refs. [1, 2].

Related remarks on the Smith Chart are noted. Smith chart-related software Smith Ver. 4 [4]. Please refer to these addresses for details on the free software that can be used to design circuits using Smith charts and how to use them. The web page [5] provides a detailed explanation of how to use Smith V3.10. Furthermore, several smartphone apps have also been released. For example, the Android version of Smith Chart Matching Calc. In this software, the load is placed on the left and the power supply is placed on the right. The website of Online Smith Chart Tool is also useful for matching calculation.

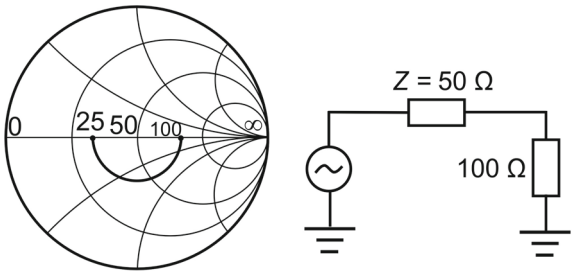


**Fig. 5.13** Connecting a transmission line of $Z = 50\ \Omega$ to an impedance load

## 5.4 Conclusions

In conclusion, this section underscores the critical importance of impedance matching in optimizing power transfer across circuit components, a key principle in electrical engineering. By tuning circuit constants, impedance matching maximizes power delivery from the source to the load, crucial in efficient power applications like antenna design, RF circuits, and various electronic devices. Optimal power transfer is achieved when the source impedance matches the complex conjugate of the load impedance. Engineers leverage the Smith chart, a robust graphical tool, to facilitate this matching process. The Smith chart not only simplifies complex calculations but also aids in visualizing impedance transformations. Despite technological advancements, the Smith chart remains invaluable, particularly in helping to comprehend and visualize impedance transformations. This section has detailed the design and application of impedance-matching circuits using the Smith chart, covering essential topics such as impedance and admittance charts, locus plots, and practical examples involving series and parallel connections of resistors, inductors, and capacitors. Mastery of these techniques ensures engineers can effectively achieve desired impedance matching, leading to efficient and reliable electronic system operations. Following this, impedance matching and energy conversion of example problems, transformers analysis, and induction motor analysis are explained in next Chap. 6.

**Chapter 5 Exercises**

**Problem 1**: Calculation of complex values

Familiarity with the Smith chart calculations and the calculation of $(1 + i)/(1 - 9i)$ using a scientific calculator.

**Problem 2**: Calculation for AC *LCR* circuit I

In the *LCR* circuit in Fig. 5.14,

(1) Find the admittance (reciprocal of impedance) between terminals A and B. Express it as $a + bi$ ($a$ and $b$ are real numbers, $i$ is an imaginary unit).
(2) Find the expression (amplitude and phase) of current $I$ that flows through the circuit when an AC voltage is applied between terminals A and B. $\omega$ is the angular frequency.
(3) Explaining whether resonance occurs in the circuit. If so, we find the expression for the resonant angular frequency.

**Problem 3**: Calculation for AC *LCR* circuit II

In the circuit in Fig. 5.15, the impedance is shown in ohms for 60 Hz. In this case, we calculated the magnitude and phase of the current when a 60 Hz frequency, 100 V AC voltage is applied between terminals A and B, and a 1.0 mF capacitor is connected between terminals C and D.

**Problem 4**: **(Advanced problem)** Disks with periodical torque

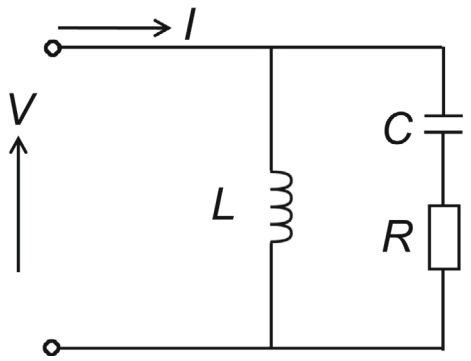


**Fig. 5.14** AC circuit I

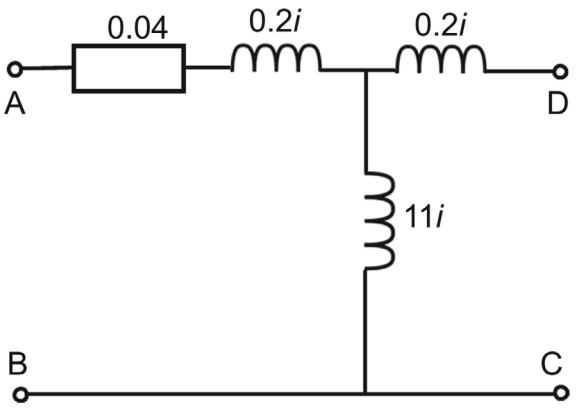


**Fig. 5.15** AC circuit II

Three equal disks are attached at equal intervals to an elastic shaft. The spring constant between the disks (torque required to displace the disks by a unit angle) is $C$.

(1) Find the natural frequency of this two-degree-of-freedom system.
(2) Find an expression for the angular displacement of the three disks when a periodic torque is applied to the leftmost disk.
(3) Show that when the angular frequency $\omega$ or $3\omega$ of the periodic torque is equal to the natural frequency, the angular displacement of the disks becomes infinite (resonance phenomenon due to excitation at the natural frequency).

## References

1. P. Wilson, *The Circuit Designer's Companion*, 4th edn. (Newnes, an imprint of Elsevier, 2018), pp. 479 ISBN: 978-0-08-101764-7
2. D. Torrungrueng, *Meta-Smith Charts and Their Potential Applications*, in A Publication in the Springer Series. Synthesis Lectures on Antennas, Lecture #10 (Springer Nature Switzerland AG,

2022), pp. 98. ISBN: 978-3-031-00411-7 paperback, ISBN: 978-3-031-01539-7 ebook. https://doi.org/10.1007/978-3-031-01539-7
3. T. Fujiwara, The art of analog circuits. https://wista.jp/SmithChart.htm, https://wista.jp/misc/smith-immit.pdf. Accessed 2024.12.01
4. Fritz Dellsperger, Smith-Chart Software and Related Documents. http://www.fritz.dellsperger.net/smith.html. Accessed 2024.12.01
5. TKA, http://take103.blog.fc2.com/blog-entry-194.html. Accessed 2024.12.01 (in Japanese)

# Chapter 6
# Impedance Matching and Energy Conversion (3): Example Problems, Transformers, and Induction Motors


**Abstract** This chapter covers the impedance matching and energy conversion part (3): example problems on Smith chart, transformers, and induction motors are mainly covered. First, an example problem of matching circuits and formula for calculating $C$ and $L$ are explained. Other solutions for example problem are presented. Next, inductive coupling circuits for transformers and induction motor are discussed. Equivalent circuits of a transformer and an induction motor are covered. Three-phase induction motor characterization are discussed with a circle diagram. The chapter is concluded by the conclusions and exercise problems.

## 6.1 Introduction

This chapter describes impedance matching, a critical aspect of energy-conversion engineering. In particular, we focus on the theoretical and practical applications of impedance matching in electronics and communication engineering. Impedance matching is essential for minimizing power loss and preventing signal reflection, ensuring efficient transmission of signals from transmitters to receivers.

The chapter begins by introducing basic concepts of impedance and admittance, explaining their impact on the design and performance of electronic circuits. This includes the calculation of impedance and an analysis of how different components—resistors, capacitors, and inductors—contribute to the overall circuit impedance.

The continues by addressing impedance matching methods based on Smith charts, a powerful tool for visually representing complex impedance values and easily deriving solutions to matching problems. Readers will learn how to interpret Smith charts and apply them to real-world circuits.

The chapter also describes matching methods using series and parallel connections, providing detailed explanations of their applications in circuit design. Practical exercises with actual circuit examples are included, bridging the gap between theoretical knowledge and practical implementation. In the second half of the chapter, examples of impedance-matching techniques are presented, offering readers opportunities to analyze problems and derive their own solutions. This approach helps



M. Okubo, *Electrical Sustainable Energy for Mechanical Engineering*,
https://doi.org/10.1007/978-981-96-5170-2_6

readers solidify the understanding of impedance matching principles and strengthen the ability to apply them to real-world problems of induction motors.

Finally, the chapter provides a comprehensive understanding of impedance matching as it relates to energy conversion engineering, illustrating its role in enhancing technological efficiency [1–4]. The combination of detailed explanations, practical examples, and numerous diagrams ensures an effective balance between theory and practice, making the content accessible and valuable for both engineering students and professionals.

## 6.2 Example Problem 1 of Impedance Matching

In this section, the normalized impedance $z$ (lower case letter), which is obtained by dividing the impedance $Z$ by 50 Ω, and the corresponding admittance $y = 1/z$, are represented within curly brackets {}. The problems and solving method are considered based on Ref. [1].

**Example Problem 1**

Consider the matching a load with $Z_A = 16 + 30i\ \Omega\ \{z_1 = 0.32 + 0.6i\}$ at a frequency of 1 GHz (= $10^9$ Hz) to a power source with $Z_C = 50\ \Omega\ \{z_C = 1\}$.

**Solution 1**

Three matching methods can be applied in this case. solution 1 is explained in this section, whereas solutions 2 and 3 are detailed in Sect. 6.4.

In Fig. 6.1, point A corresponds to $Z_A = 16 + 30i\ \{z_A = 0.32 + 0.6i\}$. An equal-resistance circle is drawn on the impedance chart through this point. In addition, an equal-conductance circle is drawn on the admittance through the final point C, $50 + 0i\ \{1 + 0i\}$. From the Smith chart, point B, where $Z_B = 16 - 23.33i\ \Omega\ \{z_B = 0.320 - 0.4666i,\ y_B = 1/z_B = 0.9996390 + 1.4575986i\}$, is defined as the intersection of both circles. Note that $y_B$ can be calculated using a scientific calculator from $z_B$.

In summary, if a capacitor with capacitance $C$ is connected in series at point A, the impedance moves to point B. Next, if an inductor with inductance $L$ is connected in parallel at point B, the impedance moves to point C to achieve matching. In this case, the values of $C$ and $L$ are calculated as follows: (Note: capacitors should be connected closest to the load.)

- The capacitance connected in series, based on the reactance difference between A and B, is:

$$\left|\frac{1}{i\omega C}\right| = [0.6 - (-0.4666)] \times 50 = 53.33$$
$$C = \frac{1}{2 \times \pi \times 10^9 \times 53.33} = 2.98434 \times 10^{-12}\,\mathrm{F} = 2.9846\,\mathrm{pF} \tag{6.1}$$

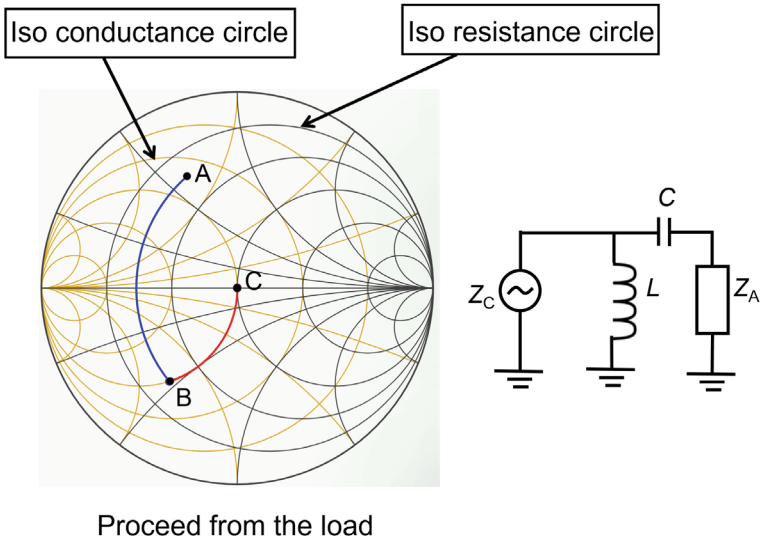


**Fig. 6.1** Matching process using Smith chart for a circuit with $C$ and $L$ for $z_A = 16 + i30$

- The inductance connected in parallel, based on the susceptance difference between B and C, is:

$$\left|\frac{1}{i\omega L}\right| = [0 - (-1.4575986)]/50 = 0.029151972$$
$$L = \frac{1}{2 \times \pi \times 10^9 \times 0.029151972} = 5.459 \times 10^{-9}\,\mathrm{H} = 5.459\,\mathrm{nH} \tag{6.2}$$

## 6.3 Formula for Calculating $C$ and $L$

To calculate $C$ and $L$, use the following equations:

- **In the case of series-connection**, if the difference in normalized reactance (the imaginary part of $z$) is $|\Delta X|$, the capacitance is given by:

$$50|\Delta X| = \frac{1}{2\pi f C} \text{ and } C = \frac{1}{2\pi f \times 50|\Delta X|} \tag{6.3}$$

where $2\pi f = \omega$. The inductance of the series-connected coils is:

$$50|\Delta X| = 2\pi f L \text{ and } L = \frac{50|\Delta X|}{2\pi f} \tag{6.4}$$

- **In the case of parallel-connection**, if the difference in normalized susceptance (the imaginary part of $y$) is $|\Delta B|$, the capacitance is given by:

$$\frac{|\Delta B|}{50} = 2\pi f C \text{ and } C = \frac{|\Delta B|}{2\pi f \times 50} \tag{6.5}$$

The inductance of the parallel-connected coils is:

$$\frac{|\Delta B|}{50} = \frac{1}{2\pi f L} \text{ and } L = \frac{50}{2\pi f \times |\Delta B|} \tag{6.6}$$

## 6.4 Other Solutions 2 and 3, and Example Problem 2

Let us now explain the other two solutions to the example problem considered in Sect. 6.2.

**Solution 2**

Starting at point A, where $Z_A = 16 + 30i\ \Omega$ $\{z_A = 0.32 + 0.6i\}$, connect capacitance $C_1$ in parallel. This causes the impedance to rotate clockwise along the equal-conductance circle on the admittance chart, reaching point D, where $Z_D = 50 + 37.5i$ $\{z_D = 1.0 + 0.75i,\ y_D = 1/z_D = 0.640 - 0.480i\}$. Next, at point D, connect capacitance $C_2$ in series. This moves the impedance counterclockwise along the equal-resistance circle on the impedance chart, ultimately reaching point C, $50 + 0i$.

**Solution 3**

From point A, connect capacitance $C_3$ in series. This causes a slight counterclockwise rotation along the equal resistance circle on the impedance chart, reaching point E, where $Z_E = 16 + 23i$ $\{z_E = 0.320 + 0.460i,\ y_E = 1/z_E = 1.01911 - 1.46497i\}$. Next, at point E, connect capacitance $C_4$ in parallel. This rotates impedance clockwise along the equal-conductance circle on the admittance chart, to reach point C, $50 + 0i$.

Both solutions 2 and 3 require two capacitors, making them more cost-efficient than solution 1.

**Example Problem 2**

Draw solutions 2 and 3 on a Smith chart, as well as diagram of each circuit, and calculate the circuit constants and capacitances $C_1$, $C_2$, $C_3$, and $C_4$.

**Answer**

See Figs. 6.2 and 6.3 for the answers: $C_1 = 2.66$ pF, $C_2 = 4.77$ pF, $C_3 = 23.84$ pF, $C_4 = 4.64$ pF.

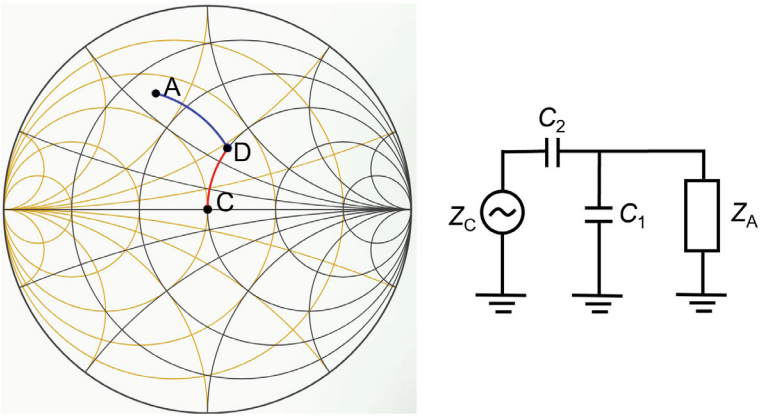


**Fig. 6.2** Matching process using Smith chart for another circuit with $C_1$ and $C_2$ for $Z_A = 16 + 30i\ \Omega$

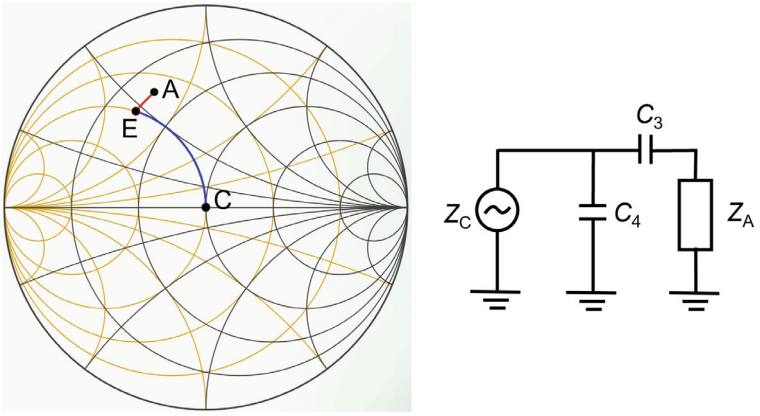


**Fig. 6.3** Matching process using Smith chart for another circuit with $C_3$ and $C_4$ for $Z_A = 16 + 30i$

Solving problems 1, 2, and 3 in this chapter exercises are related with the Smith chart usage.

## 6.5 Inductive Coupling Circuits

### *6.5.1 Transformers*

This section examines inductive coupling circuits, including transformers and induction motors, using the previously introduced impedance calculation methods [2]. Inductive coupling circuits transmit AC power and signals through magnetic flux

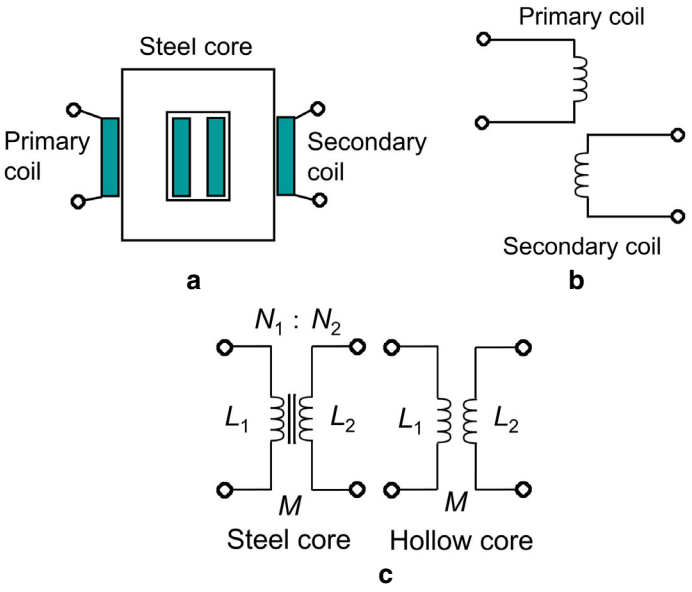


**Fig. 6.4** Transformers [2]: **a** iron-core transformer; **b** high-frequency transformer; and **c** circuit diagram

between coils without direct electrical connections. These circuits are used to adjust AC voltage, match impedance, and block DC in AC circuits.

An example circuit diagram is shown in Fig. 6.4, the circuit configuration depends on whether an iron core is present and whether the frequency is low or high. At low frequencies, an iron core is used (Fig. 6.4a). At high frequencies, two air-core coils are placed close together to allow magnetic flux coupling (Fig. 6.4b). Circuit diagrams of both configurations are shown in Fig. 6.4c, where $N_1$ is the number of primary turns, $N_2$ is the number of secondary turns, $L_1$ and $L_2$ are the reactances of the primary and secondary windings, respectively, and $M$ is the mutual inductance.

### 6.5.2 *Relationships for Transformers*

In Fig. 6.5, the load impedance is inductively coupled to the power supply with voltage $V_1$ through a coupling coil with self-inductances $L_1$ and $L_2$ and mutual inductance $M$. The following equations describe the currents in the primary and secondary coils ($I_1$ and $I_2$):

$$V_1 = i\omega L_1 I_1 \pm i\omega M I_2 \tag{6.7}$$

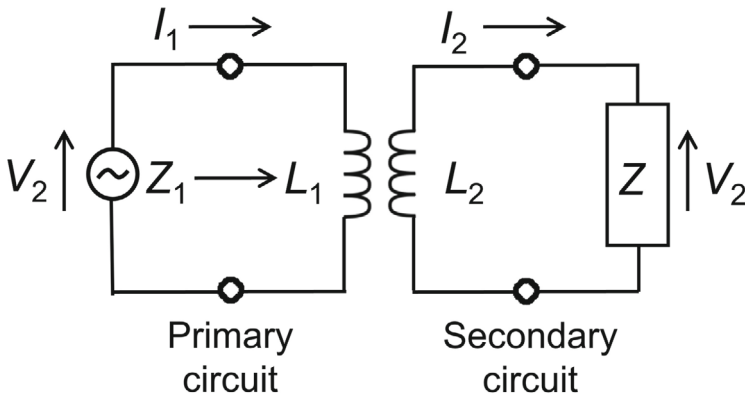


**Fig. 6.5** Typical inductively coupled circuit [2]

$$\pm i\omega M I_1 = i\omega L_2 I_2 + Z I_2 \tag{6.8}$$

When the directions of $I_1$ and $I_2$ are such that their magnetic fluxes assist each other, the compound sign $\pm$ is $+$, and when the fluxes oppose each other, the compound sign $\pm$ is $-$. From Eqs. (6.7) and (6.8),

$$V_1 = \left(i\omega L_1 + \frac{\omega^2 M^2}{i\omega L_2 + Z}\right) I_1 = Z_1 I_1 \tag{6.9}$$

where $Z_1$ is the impedance on the primary side. By rearranging, we obtain the following solution:

$$Z_1 = \frac{\omega^2 M^2 r}{r^2 + (\omega L_2 + x)^2} + i\left[\omega L_1 - \frac{\omega^2 M^2 (\omega L_2 + x)}{r^2 + (\omega L_2 + x)^2}\right] \tag{6.10}$$

In the case of a short-circuited secondary coil ($Z = 0$), $r = x = 0$. Consequently, Eq. (6.10) reduces to:

$$Z_1 = i\omega\left(L_1 - \frac{M^2}{L_2}\right) \tag{6.11}$$

where $|Z| < L_1$. If there is no leakage flux, the impedance transforms directly from $M^2 = L_1 L_2$ to $Z_1 = 0$, similar to a primary short circuit.

### 6.5.3 Transformer Coupled Circuit

In the case of transformer coupling, leakage flux is designed to be minimum. Referring to Fig. 6.5, if the number of primary windings is $N_1$ and the number of secondary windings is $N_2$, then the impedance $Z_1$ observed from the primary side of the circuit is given by:

$$Z_1 = i\omega L_1 + \frac{\omega^2 L_1 L_2}{i\omega L_2 + Z} = \frac{1}{\frac{1}{(L_1/L_2)Z} + \frac{1}{i\omega L_1}} \tag{6.12}$$

If no leakage flux exists:

$$L_1 = KN_1^2, \quad L_2 = KN_2^2 \quad (K : \text{constant}) \tag{6.13}$$

$$\text{Therefore,} \quad \frac{L_1}{L_2} = \left(\frac{N_1}{N_2}\right)^2 \tag{6.14}$$

Substituting Eq. (6.14) into Eq. (6.12) yields:

$$Z_1 = \frac{1}{\frac{1}{(N_1/N_2)^2 Z} + \frac{1}{i\omega L_1}} \tag{6.15}$$

where $Z_1$ is the impedance of $(N_1/N_2)^2 Z$ and $L_1$ is connected in parallel. The current flowing through $L_1$, known as the excitation current, is usually designed to be negligible by increasing $L_1$. In this case, the following relationship holds:

$$Z_1 \cong \left(\frac{N_1}{N_2}\right)^2 Z \tag{6.16}$$

In other words, when passing through a transformer, the impedance changes by a factor of $(N_1/N_2)^2$. In this case, the relationship between the secondary voltage $V_2$ and current $I_2$, and the primary voltage $V_1$ and current $I_1$ is:

$$\frac{V_2}{V_1} = \pm\frac{N_2}{N_1}, \quad \frac{|V_2|}{|V_1|} = \frac{N_2}{N_1} \tag{6.17}$$

$$\frac{I_2}{I_1} \cong \pm\sqrt{\frac{L_1}{L_2}} = \pm\frac{N_1}{N_2} \tag{6.18}$$

In Eq. (6.18), $I_1/I_2$ is the reciprocal of the ratio between $N_1$ and $N_2$.

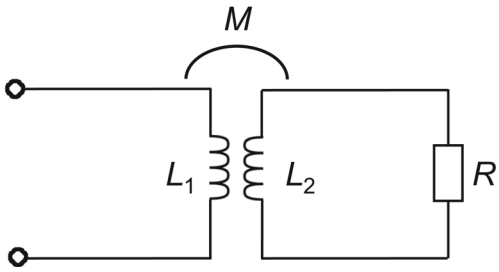


**Fig. 6.6** Inductively coupled circuit ($L_1 = 7$ mH, $L_2 = 2$ mH, $M = 3$ mH, $R = 50\ \Omega$)

### Example Problem

Using complex notation, calculate the impedance $Z_1$ seen from terminals a and b in the inductively coupled circuit shown in Fig. 6.6, whose frequency is $f = 1$ kHz.

### Answer

Using Eq. (6.9), we obtain:

$$\begin{aligned} Z_1 &= i\omega L_1 + \frac{\omega^2 M^2}{i\omega L_2 + Z} = i \cdot 2\pi \times 10^3 \times 7 \times 10^{-3} + \frac{\left(2\pi \times 10^3\right)^2 \times \left(3 \times 10^{-3}\right)^2}{i2\pi \times 10^3 \times 2 \times 10^{-3} + 50} \\ &= i \cdot 43.98 + \frac{355.31}{i12.566 + 50} \\ &= 6.68 + 42.3i\ \Omega \quad \text{(Answer)} \end{aligned} \tag{6.19}$$

$Z_1$ can also be calculated using the equivalent circuit in Fig. 6.7.

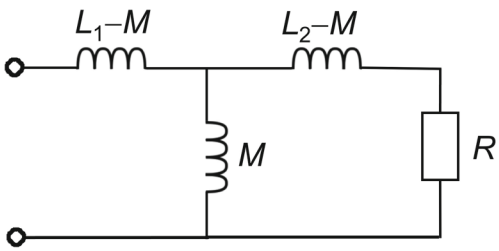


**Fig. 6.7** Equivalent circuit

## 6.6 Induction Motor

### 6.6.1 *Equivalent Circuit of a Transformer related with an Induction Motor*

The equivalent circuit of an induction motor that rotates due to induction between the primary and secondary windings can be derived by considering the equivalent circuit of a transformer [3, 4]. As shown in Fig. 6.8a, when secondary current $I_2$ flows through the secondary side of the transformer, a corresponding primary current $I_1$ is induced. If the induced electromotive forces in both the primary and secondary windings are $V_1$ and $V_2$, the power transmitted between the windings, ignoring the losses, is given by:

$$V_1 I_1 = V_2 I_2 \tag{6.20}$$

From Eq. (6.20):

$$\frac{|V_1|}{|V_2|} = \frac{I_2}{I_1} = \frac{N_1}{N_2} = \alpha \tag{6.21}$$

where $\alpha$ is referred to as the turns ratio. Equation (6.21) indicates that connecting $r_2$, $x_2$, and $R$ to the secondary through a transformer is equivalent to connecting $\alpha_2 r_2$, $\alpha_2 x_2$, and $\alpha_2 R$ directly to the primary. Therefore, the circuit shown in Fig. 6.8a can be transformed into the circuit shown in Fig. 6.8b. To account for the magnetizing current (reactive component) that generates magnetic flux in the iron core and the small active current that supplies iron loss, excitation impedances $r_{\mathrm{M}}$ and $x_{\mathrm{M}}$ are added to the circuit in Fig. 6.8b, resulting in the more accurate equivalent circuit shown in Fig. 6.8c.

### 6.6.2 *Equivalent Circuit of an Induction Motor*

In an induction motor, when the rotor of the secondary motor rotates with a slip $s$, the effective work equivalent to the load is expressed as $sf$ where $f$ is the frequency of the primary voltage. Consequently, the magnitude of the secondary voltage is $sV_2$, the reactance is $sx_2$, and the secondary current is:

$$I_2 = \frac{sV_2}{\sqrt{r_2^2 + (sx_2)^2}} = \frac{V_2}{\sqrt{(r_2/s)^2 + x_2^2}} = \frac{V_2}{\sqrt{[r_2 + (r_2/s - r_2)]^2 + x_2^2}} \tag{6.22}$$

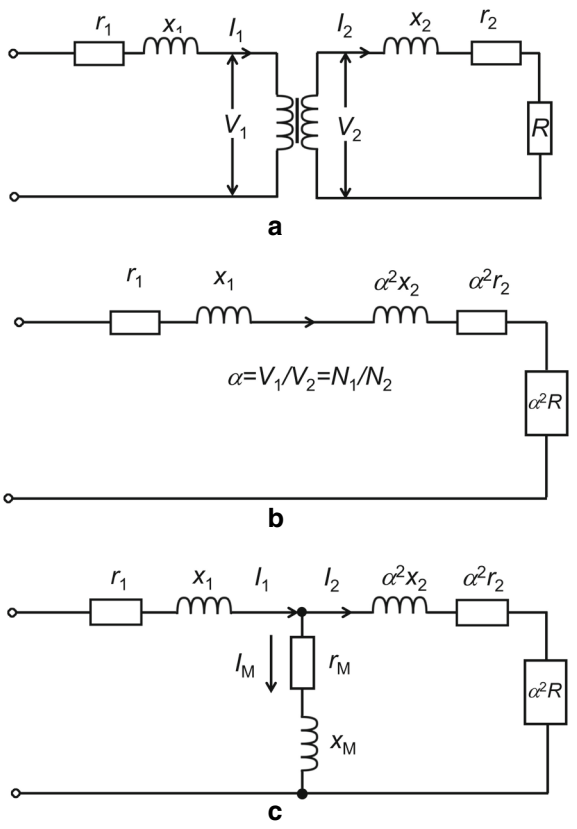


**Fig. 6.8** Transformer equivalent circuit: **a** transformer circuit, **b** equivalent circuit I, and **c** equivalent circuit II

From this equation, it is evident that as the induction motor rotates, the resistance $r_2$ changes to $r_2/s$. The winding resistance of the rotating motor $r_2$ satisfies the following relationship:

$$\frac{r_2}{s} - r_2 = \frac{1-s}{s} r_2 \tag{6.23}$$

This can be considered that the load resistance in Eq. (6.23) are inserted in the circuit. Therefore, the equivalent circuit of the induction motor can be drawn as shown in Fig. 6.9.

Since the excitation current $\pm M$ is often small enough to be ignored, the excitation circuit $r_0\, x_0$ can be approximately transferred to the terminal side, as shown in Fig. 6.10. This simplified circuit can also be considered a no-load circuit. Furthermore, the mechanical and copper losses are included in $x_0$ and $r_0$. The circuit depicted in Fig. 6.9 is called a T-type equivalent circuit, whereas that in Fig. 6.10 is known as an L-type equivalent circuit.

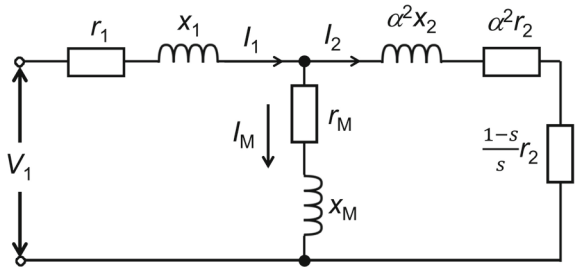


**Fig. 6.9** T-type equivalent circuit of an induction motor

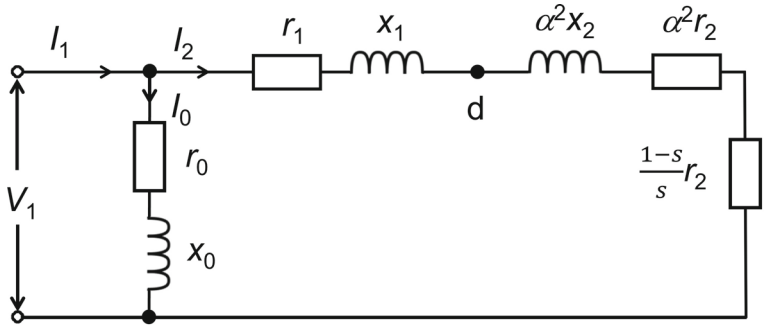


**Fig. 6.10** L-type equivalent circuit of an induction motor

These diagrams are drawn for one phase. For a three-phase induction motor, if the line voltage is $V_{1l}$ and the line current is $I$, then in the equivalent circuit, $V_1 = V_{1l}/\sqrt{3}$ and quantities such as $r_1$ and $x_1$ are converted to per-phase values of a Y-connection, and the result must be multiplied by three when calculating power or torque. An equivalent circuit can also be drawn for a $\Delta$ single-phase connection. In this case, quantities such as $r_1$ and $x_1$ are converted to per-phase values of the $\Delta$ connection. When the slip changes, the tip of the $I_1$ vector describes a circular path. This technique, known as the circle-diagram method, is used to effectively calculate the motor's characteristics.

### *6.6.3 Three-Phase Induction Motor Characterization*

To determine various characteristics of a three-phase induction motor we can draw a circular diagram from the results obtained from primary winding resistance measurements, no-load tests, and locked-in tests [5].

#### 6.6.3.1 Principles and Equivalent Circuits of Three-Phase Induction Motors

A three-phase induction motor comprises three symmetrical windings (*u*-, *v*-, and *w*-phase) on the stator (primary) side. When a symmetrical three-phase AC voltage is applied, a rotating magnetic field is generated in the iron core. The rotor (secondary) side can be considered to have three equivalent short-circuited symmetrical windings, generating torque due to the interaction between the rotating magnetic field and the current induced by the electromotive force in the rotor winding derived from said field. The speed at which the magnetic field rotates, called the synchronous speed, is expressed as

$$\text{Synchronous speed} \quad N_s = \frac{120f}{P} \quad \left(\text{min}^{-1}\right) \tag{6.24}$$

where $f$ is the power supply frequency, and $P$ is the number of poles. During steady-state operation, the rotor speed $N_r$ is slightly lower than the synchronous speed $N_s$. The ratio between the speed difference and the synchronous speed is called slip, $s$:

$$s = \frac{N_s - N_r}{N_s} \times 100 \quad (\%) \tag{6.25}$$

When $s = 0$, the rotor speed equals the synchronous speed, resulting in no relative motion between the rotor and the magnetic field. Consequently, no electromotive force, current, or torque is generated in the rotor circuit, which corresponds to a no-load state (idle rotation). As the load increases starting from a no-load state, the rotor speed decreases, causing the $s$ to increase. However, even under full load, the slip typically remains below 10%, meaning the speed does not significantly change. In other words, three-phase induction motors tend to maintain a nearly constant speed regardless of load fluctuations.

The L-type equivalent circuits for each of the three phases of the induction motor are shown in Fig. 6.10, where $r_1 + \alpha^2 r_2$ is winding resistance of the stator and rotor converted to the primary side, $x_1 + \alpha^2 x_2$ $(= x)$ is winding leakage reactance, $r_0$ is resistance representing iron and mechanical losses (equivalent to the total power consumed by these losses), $x_0$ is excitation reactance, $s$ is slip, and $(1 - s)\, r_2/s$ is resistance representing the mechanical output (infinite at no load, and zero when the rotor is stationary).

#### 6.6.3.2 No-Load and Locked-In Tests

In the no-load test, the motor operates without a load while voltage, current, and power are measured. In this state, $s \cong 0$; therefore, the resistance $(1 - s)r_2/s$ of the equivalent circuit in Fig. 6.10 can be considered infinite, effectively making it open-circuited. The measured current in this state equals the excitation current $I_0$ and the measured power corresponds to the losses in $r_0$, which include the iron and mechanical losses.

In the locked-in test, the rotor is prevented from rotating, and a small voltage is applied while current and power are measured. Under these conditions, $N_r = 0$ and $s = 1$; therefore, $(1 - s)r_2/s = 0$, effectively short-circuiting this resistor. Since the rotor is stationary, there are no mechanical losses, and the applied voltage is sufficiently small to make the iron loss negligible. Thus, the measured power in this test represents the power consumption at resistance $r_1 + \alpha^2 r_2$, that is, the primary and secondary copper losses.

#### 6.6.3.3 Circle Diagram

The circle diagram represents the vector trajectry (path described by a vector's head) of the primary current when the applied voltage is constant, and the load (or slip, $s$) varies. This diagram can be constructed using the results of the primary winding resistance, no-load test, and locked-in test. From the circle diagram, it is possible to estimate key characteristics of a three-phase induction motor, such as efficiency, power factor, and speed, for various load conditions, ranging from no load to full load, without physically applying a load to the motor. From the equivalent circuit, the primary current is:

$$I_1 = I_0 + I_2 = \frac{V_1}{r_0 + ix_0} + \frac{V_1}{r_1 + r_2/s + ix} \tag{6.26}$$

When the slip $s$ varies from $-\infty$ to $+\infty$, with the primary voltage as the reference, the head of the primary current vector describes a circle with a radius of $V_1/2x$, where $x = x_1 + \alpha^2 x_2$, as shown in Fig. 6.11. In the no-load state, $s = 0$; therefore, the second term of Eq. (6.26) is zero, and $I_1 = I_0$, with the vector $I_1$ corresponding to O′O. The active component of $I_1$, that is, the component parallel to $V_1$, represents the current required to supply the sum of the iron and mechanical losses. In the locked-in state, $s = 1$; thus, the vector $I_1$ corresponds to O′Q in the circle diagram. The active component of $I_2$ represents the sum of the primary and secondary copper losses. During normal operation, $0 \leq s \leq 1$, which is described by the movement of vector $I_1$ along the arc between O and Q on the circle diagram.

This type of circle diagram, based on the L-shaped equivalent circuit, is commonly referred to as an L-shaped circle diagram.

## 6.7 Conclusions

In conclusion, this chapter thoroughly explores the subject of impedance matching, emphasizing the utilization of Smith charts and series and parallel connections to optimize power transfer in electrical circuits. The chapter begins by detailing the use of Smith charts, a vital visual tool for representing complex impedance values and simplifying the solution of matching problems. Readers are guided on how to interpret and apply Smith charts to real-world circuit scenarios. Furthermore, the chapter delves into practical applications of series and parallel connections in circuit

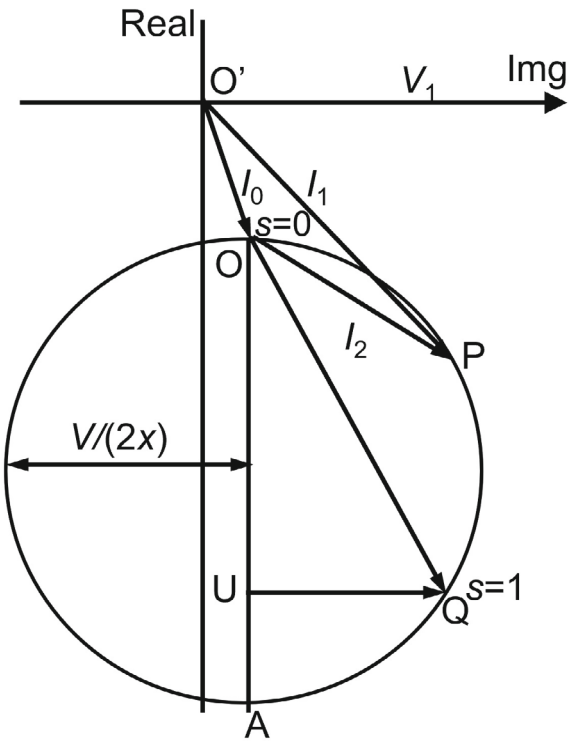


**Fig. 6.11** Circle diagram of an induction motor

design, supplemented by hands-on exercises with actual circuit examples that bridge theoretical knowledge with practical implementation.

Particularly highlighted in this chapter are example problems focused on electrical circuit matching, transformers, and induction motors analysis. These examples furnish readers with opportunities to analyze impedance-matching challenges, fostering a deeper comprehension of the principles involved and enhancing their ability to address real-world engineering issues related to induction motors and other complex systems.

Ultimately, the chapter culminates in a comprehensive understanding of impedance matching within the context of energy conversion engineering. By presenting detailed explanations, practical examples, and numerous diagrams, the chapter strikes an effective balance between theory and practice, rendering the content highly accessible and beneficial for both engineering students and professionals. This ensures a robust grasp of how impedance matching can significantly enhance technological efficiency across various applications.

## Chapter 6 Exercises

**Problem 1**: Smith chart drawing

Draw solutions 1, 2, and 3 in Sects. 6.2–6.4 on a Smith chart sheet, read the chart, and determine the circuit constants of $C$, $L$, $C_1$, $C_2$, $C_3$, and $C_4$.

**Problem 2**: Matching circuit I

In the circuit with inductance $L$ and capacitance $C$ shown in Fig. 6.12, determine the values of $L$ and $C$ required to match a source impedance $Z_0 = 50\ \Omega$ at $f = 7$ MHz to a load impedance $Z_a = 25 - 5i\ \Omega$. Express the results in nH and pF (n: $10^{-9}$ and p: $10^{-12}$). This is called L-type matching configuration.

**Problem 3**: Matching circuit II

For the circuit shown in Fig. 6.13, which includes an inductance $L$ and two capacitances $C_1$ and $C_2$ in a $\pi$-type matching configuration, calculate the values of $L$, $C_1$, and $C_2$ required to match a source impedance $Z_0 = 50\ \Omega$ at $f = 21.4$ MHz to a load impedance $Z_a = 20.33 - 123.3i\ \Omega$. Express the results in nH and pF.

**Problem 4**: Alternative circuits

Propose alternative circuits, other than the one in Fig. 6.13, that can achieve impedance matching. For example, T-type matching configuration can be considered.

**Problem 5**: Induction motor's equivalent circuit [4]

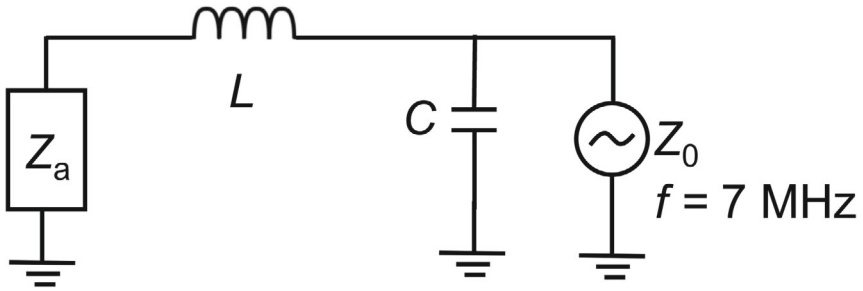


**Fig. 6.12** Matching circuit I

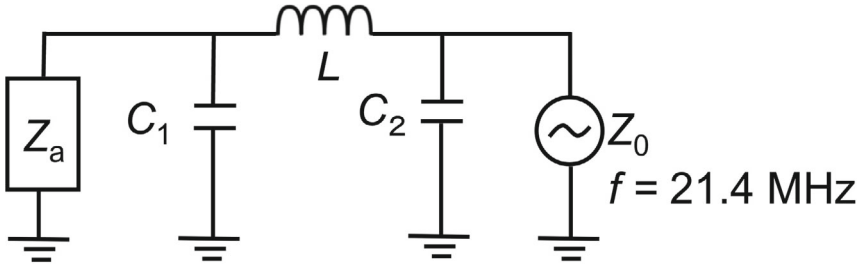


**Fig. 6.13** Matching circuit II

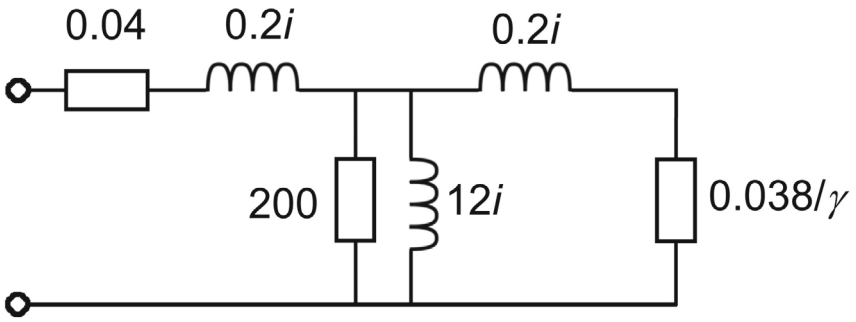


**Fig. 6.14** Equivalent circuit of an induction motor

In the induction motor's equivalent circuit shown in Fig. 6.14, the numbers represent the impedances corresponding to a 60 Hz current, with the real part representing the resistance in ohms, and the imaginary part representing the value of $2\pi 60Li$ when $L$ is expressed in Henry. One of these resistances is given as a function of slip $s$. Note that $s$ is proportional to the speed difference between the rotating magnetic field and the rotor: $s \approx 0$ at no load, and $s = 1$ when the rotor is braked under full load. A vector diagram is drawn at an applied voltage of 577 V. Using an applied voltage of 577 V, represent the voltage vector as fixed on the imaginary axis and illustrate how the current vector changes with $s$. Furthermore, show that the tip of the current vector traces a circle, which is a general property of induction motors regardless of circuit values. Calculate and draw the circles for $s = 0$, $s = 0.1$, and $s = \infty$.

## References

1. T. Fujiwara, The art of analog circuit, making a matching policy using the Smith chart. https://wista.jp/Smithchart.htm. Accessed 2024.12.01 (in Japanese)
2. M. Nishimaki, *Denki Gaku* (English translated title: *Electricity*) (Morikita Publishing Co., Ltd., Tokyo, Japan, 1973), pp. 222 (in Japanese)
3. S. Tsuboshima, *Zukai Yudo Dendoki—Kiso kara Seigyo made* (English translated title: *Illustrated Induction Motor—Fundamental to Control*) (Tokyo Denki University Press, Tokyo, Japan, 1979), pp. 199 (in Japanese)
4. T. von Kármán, M.A. Biot, *Mathematical Methods in Engineering* (McGraw-Hill, 1940), pp. 505
5. Nagasaki Institute of Applied Science, 2. Sanso Yudou Dendouki no Tokusei Shiken (English translated title: 2. Characteristics test of three-phase induction motor). https://edison.elc.nias.ac.jp/eerc/experiment/eeee1. Accessed 2025.04.01 (in Japanese)

# Chapter 7
# Energy Principle and Approximated Solution of Energy Systems


**Abstract** This chapter discusses the energy principle and approximated solution of energy systems. The principles of least action, variational theory, energy principles, and approximate solutions using variational methods in electrical and mechanical engineering are mainly discussed. Variational theory and energy principle are explained based on various example problems. Following these, approximate solution methods using variational methods are explained based on various example problems. The chapter is concluded by the conclusions and exercise problems.

## 7.1 Introduction

In this chapter, we elucidate the energy principle, a fundamental concept in energy conversion engineering that plays a crucial role in various engineering disciplines. The energy principle is integral to the understanding of how energy transformations underpin the functionality of mechanical systems, fluid dynamics, and electrical circuits. We explore both the theoretical underpinnings and practical applications of this principle, illustrating its broad utility in design and analysis.

In particular, our discussion encompasses the application of the energy principle in mechanics, where it provides a framework for analyzing forces and motion in systems ranging from simple machines to complex mechanical structures. In the realm of fluid engineering, we examine how this principle helps in understanding the fluid behavior under different flow and pressure conditions, contributing to the design of more efficient hydraulic systems and pipelines. Furthermore, in electrical engineering, the energy principle is pivotal for the analysis and design of electrical circuits to ensure energy efficiency and system stability.

Additionally, we cover the principle of least action, a sophisticated approach that seeks to minimize the action, or integral of the Lagrangian, of a system. This principle is crucial for optimizing processes and systems across various engineering fields. It not only underscores the concept of minimal energy usage but also facilitates a detailed analysis and solution of complex problems. By employing the principle of



M. Okubo, *Electrical Sustainable Energy for Mechanical Engineering*,
https://doi.org/10.1007/978-981-96-5170-2_7

least action, engineers can derive equations of motion for systems in a manner that guarantees that the most energy-efficient path or trajectory is taken [1].

## 7.2 Principle of Least Action

### *7.2.1 Case of Single Variable*

First, the principle of the least action is considered. First, we treat a motion of a mass point. Consider the movement of a mass point from one location to another in a gravitational field. Assume an alternative trajectory (2) for the real trajectory (1) of a mass point (Fig. 7.1).

*KE*: kinetic energy becomes

$$\frac{m}{2}|\boldsymbol{u}|^2 = \frac{m}{2}\left|\frac{\mathrm{d}\boldsymbol{x}}{\mathrm{d}t}\right|^2 \tag{7.1}$$

and *PE*: Potential energy. The action equation is written as follows:

$$\int_{t_1}^{t_2}\left[\frac{m}{2}\left|\frac{\mathrm{d}\boldsymbol{x}}{\mathrm{d}t}\right|^2 - V(\boldsymbol{x})\right]\mathrm{d}t \tag{7.2}$$

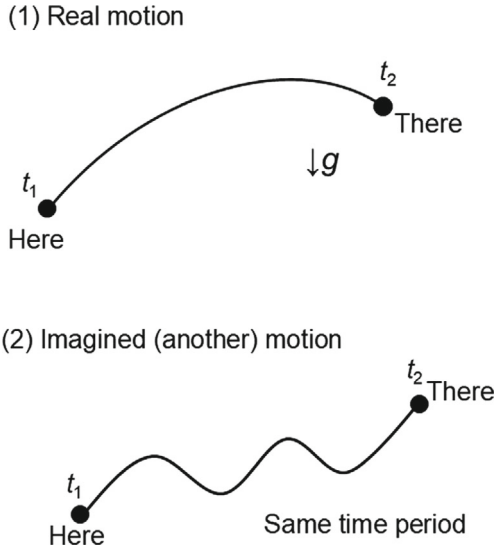


**Fig. 7.1** Real and imaginary motion

For the same time interval, the value of the action integral for the assumed alternative trajectory is greater than that of the action integral for the real trajectory. The integral value is smallest in trajectry (1) and smaller than that in trajectory (2). A function of functions is called functional. The derivative of functional is known as variation. Generally, $\boldsymbol{x}$ is determined such that the action integral (function of functions, $KE$ and $PE$)

$$S = \int_{t_1}^{t_2} (KE(\boldsymbol{x}) - PE(\boldsymbol{x}))\mathrm{d}t \tag{7.3}$$

is minimal. This principle is equivalent to Newton's 2nd Law, expressed as $\boldsymbol{F} = m\,\boldsymbol{a}$, where $\boldsymbol{F}$: force, $m$: mass, and $\boldsymbol{a}$: acceleration.

The minimal point is determined such that $\mathrm{d}f/\mathrm{dx} = 0$ when differentiated with respect to the general function $f(x)$. The derivative of functional such as Eq. (7.3) is known as a variation. Determining a function that minimizes the value of functional is known as variation principle. This is also known as the principle of least action, $\delta S = 0$. This is expressed as the variation principle of mechanics. Landau–Lifschitz's *Mechanics* [2] begins here. Finding a trajectory $\boldsymbol{x}$, where functional $S$ is minimal, is known as a variation problem. The purpose of this chapter is to solve equations in mechanics, fluids, electricity, and electromagnetism using the principle of least action. It is also possible to analyze various other differential equations.

Generally speaking, a characteristic of a minimum is that when the function deviates from the minimum to the first order, the deviation of it from the minimum is only of the second order. In cases of normal function $f(x)$ differentiation,

$$f(x + \Delta x) = f(x) + f'(x)\Delta x + \frac{1}{2}f''(x)(\Delta x)^2 + O\left((\Delta x)^3\right) \tag{7.4}$$

$f'(x) = 0$ corresponds to a minimum,

$$f(x + \Delta x) - f(x) = O\left((\Delta x)^2\right) \tag{7.5}$$

and the right-hand side is two or more orders of $\Delta x$, making it a minimum.

We seek the variation $\delta S$ of the functional $S$ for the one-dimensional motion $x = x(t)$ in the following Eq. (7.6).

$$S(x) = \int_{t_1}^{t_2} (KE - PE)\mathrm{d}t = \int_{t_1}^{t_2} \left[\frac{m}{2}\left(\frac{\mathrm{d}x}{\mathrm{d}t}\right)^2 - V(x)\right]\mathrm{d}t \tag{7.6}$$

The answer is shown below. Let the true trajectory be $\bar{x}$ and assume $x = \bar{x} + \eta$ as shown in Fig. 7.2.

$$S(\bar{x} + \eta) = \int_{t_1}^{t_2} \left[\frac{m}{2}\left(\frac{\mathrm{d}\bar{x}}{\mathrm{d}t} + \frac{\mathrm{d}\eta}{\mathrm{d}t}\right)^2 - V(\bar{x} + \eta)\right]\mathrm{d}t \tag{7.7}$$

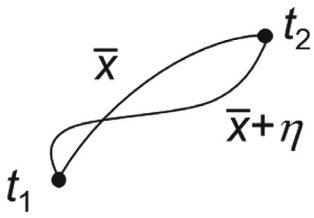


**Fig. 7.2** Optimum and tested paths

$$\text{Right 1st term} = \frac{m}{2}\left[\left(\frac{\mathrm{d}\bar{x}}{\mathrm{d}t}\right)^2 + 2\frac{\mathrm{d}\bar{x}}{\mathrm{d}t}\frac{\mathrm{d}\eta}{\mathrm{d}t} + \left(\frac{\mathrm{d}\eta}{\mathrm{d}t}\right)^2\right] \tag{7.8}$$

$$\text{Right 2nd term} = V(\bar{x}) + \eta V'(\bar{x}) + O\left(\eta^2\right) \tag{7.9}$$

Order of $\eta^2$ terms or $O(\eta^2)$ is omitted and $S$ becomes $S_1(\bar{x}+\eta)$ which includes first order terms.

$$S_1(\bar{x}+\eta) = \int_{t_1}^{t_2}\left[\frac{m}{2}\left(\frac{\mathrm{d}\bar{x}}{\mathrm{d}t}\right)^2 - V(\bar{x}) + m\frac{\mathrm{d}\bar{x}}{\mathrm{d}t}\frac{\mathrm{d}\eta}{\mathrm{d}t} - \eta V'(\bar{x})\right]\mathrm{d}t \tag{7.10}$$

$$\delta S \equiv S_1(\bar{x}+\eta) - S(\bar{x}) = \int_{t_1}^{t_2}\left[m\frac{\mathrm{d}\bar{x}}{\mathrm{d}t}\frac{\mathrm{d}\eta}{\mathrm{d}t} - \eta V'(\bar{x})\right]\mathrm{d}t \tag{7.11}$$

This is the same procedure as determining the differential $f'(x)$ of the ordinary function $f(x)$. Using the partial integration formula, the term $\mathrm{d}\eta/\mathrm{d}t$ is eliminated from Eq. (7.11).

$$\frac{\mathrm{d}}{\mathrm{d}t}(\eta f) = \eta\frac{\mathrm{d}f}{\mathrm{d}t} + f\frac{\mathrm{d}\eta}{\mathrm{d}t} \tag{7.12}$$

The well-known Eq. (7.12) is integrated to obtain the following equation:

$$\int f\frac{\mathrm{d}\eta}{\mathrm{d}t} = \eta f - \int \eta\frac{\mathrm{d}f}{\mathrm{d}t}\mathrm{d}t \tag{7.13}$$

When applied to the previous Eq. (7.11),

$$\begin{aligned}\delta S &= \int_{t_1}^{t_2}\left[m\frac{\mathrm{d}\bar{x}}{\mathrm{d}t}\frac{\mathrm{d}\eta}{\mathrm{d}t} - \eta V'\right]\mathrm{d}t \\ &= \left[\eta m\frac{\mathrm{d}\bar{x}}{\mathrm{d}t}\right]_{t_1}^{t_2} - \int_{t_1}^{t_2}\left[\eta m\frac{\mathrm{d}^2\bar{x}}{\mathrm{d}t^2} + \eta V'\right]\mathrm{d}t \\ &= \left[m\frac{\mathrm{d}\bar{x}}{\mathrm{d}t}\eta\right]_{t_1}^{t_2} - \int_{t_1}^{t_2}\left[m\frac{\mathrm{d}^2\bar{x}}{\mathrm{d}t^2} + V'\right]\eta\mathrm{d}t\end{aligned} \tag{7.14}$$

The first term on the integrated right-hand side disappears, because the trajectry of $\eta(t_1) = \eta(t_1) = 0$ is known as the natural boundary condition (BC), which we will test. If the integral is 0 for any $\eta$, the coefficient of $\eta$ is 0, and the following equation holds for $\delta S = 0$.

$$\delta S = \int_{t_1}^{t_2} \left[ m\frac{\mathrm{d}^2\overline{x}}{\mathrm{d}t^2} + V' \right] \eta \mathrm{d}t = 0 \quad \text{or} \quad m\frac{\mathrm{d}^2\overline{x}}{\mathrm{d}t^2} + V' = 0 \tag{7.15}$$

Therefore, the principle of $\delta S = 0 \leftrightarrow \boldsymbol{F} = m\boldsymbol{a}$ holds. This principle is known as the principle of least action by the calculus of variations. The procedure of solving the calculus of variations is summarized below.

(1) For the functional $S(x)$, let $x \to \overline{x} + \eta$ and consider $S(\overline{x} + \eta)$.
(2) Expand $S(\overline{x} + \eta)$ and take only the first-order term (define this $S_1$).
(3) Find the variation from $\delta S = S_1(\overline{x} + \eta) - S(\overline{x})$.
(4) Apply partial integration to $\delta S$ to remove $\mathrm{d}\eta/\mathrm{d}t$.
(5) Use the natural BCs to

$$\delta S = \int_{t_1}^{t_2} [\,]\eta \mathrm{d}t = 0$$

make it into the form.
(6) $[\,] = 0$ holds.

To summarize the above, in the case of functions,

$$f(x + \Delta x) - f(\mathrm{x}) = f'(x)\Delta x + O\left((\Delta x)^2\right) \tag{7.16}$$

because

$$\mathrm{d}f = f_1(x + \Delta x) - f(x) = f'(x)\Delta x \tag{7.17}$$

where $f_1$ represents only the first-order term. When $df = 0, f'(x) = 0$, which is an extreme value. A similar procedure is possible for functions with multiple variables.

Next, we consider the case of functional $S$. Because direct differentiation cannot be considered as in the case of normal functions, calculate $S(\overline{x} + \eta) - S(\overline{x})$ and leave the first-order term with respect to $\eta$.

$$\delta S = S_1(\overline{x} + \eta) - \mathrm{S}(\overline{x}) \tag{7.18}$$

The extreme value occurs when $\delta S = 0$. A similar handling is possible for functions with multiple variables.

### 7.2.2 Case of Multiple Variables

Next, the problem of finding $y$ that minimizes the integral

$$J(y) = \int_{x_0}^{x_1} F\left(x, y, y'\right) \mathrm{d}x \tag{7.19}$$

for the function $F(x, y, y')$ under the conditions $y(x_0) = y_0$ and $y(x_1) = y_1$ is as follows:

$$\delta J = 0 \quad \text{or} \quad \frac{\partial F}{\partial y} - \frac{\mathrm{d}}{\mathrm{d}x}\left(\frac{\mathrm{d}F}{\mathrm{d}y'}\right) = 0 \tag{7.20}$$

Solving Eq. (7.20) yields $y$. Equation (7.20) is known as the Euler equation for this problem.

Here, we describe Hamilton's principle (principle of least action). The motion of the dynamic system realized between times $t_0$ and $t_1$ occurs such that

$$J = \int_{t_0}^{t_1} L(q_1, \ldots, q_{\mathrm{N}}, \dot{q}_1, \ldots \dot{q}_N) \mathrm{d}t \tag{7.21}$$

takes an extreme value, that is, $\delta J = 0$. $J$ denotes the action, $L$ denotes the Lagrangian $= KE - PE$, and $q_1$, …, $q_{\mathrm{N}}$ denote the generalized coordinates. The Euler equation for this problem

$$\frac{\mathrm{d}}{\mathrm{d}t}\left(\frac{\partial L}{\partial \dot{q}_{\mathrm{i}}}\right) - \frac{\partial L}{\partial q_{\mathrm{i}}} = 0, \quad (\mathrm{i} = 1, \ldots, \mathrm{N}) \tag{7.22}$$

is known as the Lagrange equation. This can be derived using the aforementioned solution method.

## 7.3 Variational Theory and Energy Principle

Next, we discuss the theory of variation and the energy principle. As mentioned above, this is the same principle as least action and Hamilton's principle. The differential equations corresponding to these principles are the Euler or Lagrange equations. For details, please refer to Reference books [3] and [4]. Below, we derive the Euler–Lagrange equation and provide additional explanations. For simplicity, if we assume one dimension, the functional is:

$$J(q_1, \dot{q}_1) = \int_{t_0}^{t_1} L(q_1, \dot{q}_1) \mathrm{d}t \tag{7.23}$$

where $\cdot$ denotes $\mathrm{d}/\mathrm{d}t$. The variation of functional $J$, $\delta J$ is

$$\delta J = J_1\left[q_1 + \eta, \frac{\mathrm{d}}{\mathrm{d}t}(q_1 + \eta)\right] - J(q_1, \dot{q}_1) \tag{7.24}$$

where the first term on the right-hand side, $J_1$, represents the first-order term of $\eta$. The following equation is obtained using partial integration.

$$\begin{aligned}\delta J &= \int_{t_0}^{t_1} \left\{L_1\left[q_1 + \eta, \frac{\mathrm{d}}{\mathrm{d}t}(q_1 + \eta)\right] - L(q_1, \dot{q}_1)\right\}\mathrm{d}t \\ &= \int_{t_0}^{t_1} \left[\frac{\partial}{\partial q_1}L(q_1, \dot{q}_1)\eta + \frac{\partial}{\partial \dot{q}_1}L(q_1, \dot{q}_1)\frac{\mathrm{d}\eta}{\mathrm{d}t}\right]\mathrm{d}t \\ &= \left[\frac{\partial}{\partial q_1}L(q_1, \dot{q}_1)\eta\right]_{t_0}^{t_1} - \int_{t_0}^{t_1}\left[-\frac{\partial}{\partial q_1}L + \frac{\mathrm{d}}{\mathrm{d}t}\left(\frac{\partial}{\partial \dot{q}_1}L\right)\right]\eta\mathrm{d}t\end{aligned} \tag{7.25}$$

The first term on the right-hand side in the third equation is zero owing to the natural BC. As $\delta J = 0$, the second term is $\int [\,]\eta = 0$, equivalent to the form $[\,] = 0$. Therefore,

$$\frac{\mathrm{d}}{\mathrm{d}t}\left(\frac{\partial}{\partial \dot{q}_1}L\right) - \frac{\partial}{\partial q_1}L = 0 \tag{7.26}$$

We obtain the Euler or Lagrange equation (7.26).

Next, as a supplementary matter, we explain the Hamilton equation that appears in the analysis of mechanical systems.

$$\mathrm{d}L = \frac{\partial L}{\partial q}\mathrm{d}q + \frac{\partial L}{\partial \dot{q}}\mathrm{d}\dot{q} \tag{7.27}$$

where

$$\frac{\partial L}{\partial \dot{q}} = p \quad \text{(generalized momentum)} \tag{7.28}$$

$$\frac{\partial L}{\partial q} = \dot{p} \quad \text{(Lagrange formula)} \tag{7.29}$$

From these equations

$$\mathrm{d}L = \dot{p}\mathrm{d}q + p\mathrm{d}\dot{q} \tag{7.30}$$

To write this equation in terms of $\mathrm{d}q$ and $\mathrm{d}p$, $\mathrm{d}(p\dot{q}) = \dot{q}\mathrm{d}p + p\mathrm{d}\dot{q}$,

$$\mathrm{d}L = \dot{p}\mathrm{d}q + \mathrm{d}(p\dot{q}) - \dot{q}\mathrm{d}p \quad \text{or} \quad \mathrm{d}(L - p\dot{q}) = \dot{p}\mathrm{d}q - \dot{q}\mathrm{d}p \tag{7.31}$$

is obtained as the Hamilton relationship

$$\dot{q} = \frac{\partial H}{\partial p}, \quad \dot{p} = -\frac{\partial H}{\partial q} \tag{7.32}$$

where $H = p\dot{q}$ - $L$ is Hamiltonian. Next, the Hamilton–Jacobi equation is explained as a supplementary item. For system of N degrees of freedom,

$$H(q_1, q_2 \cdots q_{\mathrm{N}}, p_1, p_2 \cdots p_{\mathrm{N}}) = \sum_{\mathrm{i}}^{\mathrm{N}} p_{\mathrm{i}} q_{\mathrm{i}} - L \tag{7.33}$$

For action $S = \int_{t_0}^{t_1} L\mathrm{d}t$

$$\frac{\mathrm{d}S}{\mathrm{d}t} = L \quad (\text{Perfect derivative, function of } t) \tag{7.34}$$

$$\frac{\mathrm{d}S}{\mathrm{d}t} = \frac{\partial S}{\partial t} + \sum \frac{\partial S}{\partial q_{\mathrm{i}}} \dot{q}_{\mathrm{i}} = \frac{\partial S}{\partial t} + \sum p_{\mathrm{i}} \dot{q}_{\mathrm{i}} \quad (\text{when viewed as a function of } t \text{ and } q) \tag{7.35}$$

Equation (7.35) is obtained by the following equations.

$$\delta S = \frac{\partial L}{\partial \dot{q}} \mathrm{d}q \Big|_{t_0}^{t_1} + \int_{t_0}^{t_1} \left( \frac{\partial L}{\partial q} - \frac{\mathrm{d}}{\mathrm{d}t} \frac{\partial L}{\partial \dot{q}} \right) \mathrm{d}q\mathrm{d}t \tag{7.36}$$

$$\begin{aligned} &\frac{\partial L}{\partial \dot{q}} = p, \quad \frac{\partial L}{\partial q} - \frac{\mathrm{d}}{\mathrm{d}t} \frac{\partial L}{\partial q} = 0 \quad \text{for real path} \\ &\delta S = \sum p_{\mathrm{i}} \mathrm{d}q, \ \text{therefore}, \ \frac{\partial S}{\partial q_{\mathrm{i}}} = p_{\mathrm{i}} \end{aligned} \tag{7.37}$$

$$L = \frac{\partial S}{\partial t} + \sum p_{\mathrm{i}} \dot{q}_{\mathrm{i}} \tag{7.38}$$

or

$$\frac{\partial S}{\partial t} + H = 0 \quad (\text{Hamilton} - \text{Jacobi equation}) \tag{7.39}$$

### *7.3.1 Example Problem 1, Euler's Equation*

The followings are some example problems.

Find the equation (Euler's equation) to minimize functionals (1) and (2).

$$(1)\ J(y) = \int_1^2 \left[ x\left(\frac{\mathrm{d}y}{\mathrm{d}x}\right)^2 - y\frac{\mathrm{d}y}{\mathrm{d}x} + y \right] \mathrm{d}x \tag{7.40}$$

$$(2)\ J(y) = \int_0^1 \left[ \left(\frac{\mathrm{d}y}{\mathrm{d}x}\right)^2 + k^2 \cos y \right] \mathrm{d}x \tag{7.41}$$

**Solution**

(1) Calculate the following equation:

$$J(\overline{y}+\eta) = \int_1^2 \left\{ x\left[\frac{\mathrm{d}(\overline{y}+\eta)}{\mathrm{d}x}\right]^2 - (\overline{y}+\eta)\frac{\mathrm{d}(\overline{y}+\eta)}{\mathrm{d}x} + (y+\eta) \right\} \mathrm{d}x \tag{7.42}$$

Leave only the first-order term of $\eta$. Denote it as $J_1$.

$$J_1(\overline{y}+\eta) = \int_1^2 \left[ x\left(\frac{\mathrm{d}\overline{y}}{\mathrm{d}x}\right)^2 + x\cdot 2\frac{\mathrm{d}\overline{y}}{\mathrm{d}x}\frac{\mathrm{d}\eta}{\mathrm{d}x} - \overline{y}\frac{\mathrm{d}\overline{y}}{\mathrm{d}x} - \overline{y}\frac{\mathrm{d}\eta}{\mathrm{d}x} - \eta\frac{\mathrm{d}\overline{y}}{\mathrm{d}x} + (y+\eta) \right] \mathrm{d}x \tag{7.43}$$

$$\delta J = J_1(\overline{y}+\eta) - J(\overline{y}) = \int_1^2 \left[ \left(2x\frac{\mathrm{d}\overline{y}}{\mathrm{d}x} - \overline{y}\right)\frac{\mathrm{d}\eta}{\mathrm{d}x} - \eta\frac{\mathrm{d}\overline{y}}{\mathrm{d}x} + \eta \right] \mathrm{d}x \tag{7.44}$$

Integrate by parts to remove $\mathrm{d}\eta/\mathrm{d}x$

$$\delta J = \left[ \left(2x\frac{\mathrm{d}\overline{y}}{\mathrm{d}x} - \overline{y}\right)\eta \right]_1^2 - \int_1^2 \left[ \frac{\mathrm{d}}{\mathrm{d}x}\left(2x\frac{\mathrm{d}\overline{y}}{\mathrm{d}x} - \overline{y}\right)\eta + \eta\frac{\mathrm{d}\overline{y}}{\mathrm{d}x} - \eta \right] \mathrm{d}x \tag{7.45}$$

The first term disappears because of the natural BC. Therefore, we obtain

$$\delta J = -\int_1^2 \left[ \frac{\mathrm{d}}{\mathrm{d}x}\left(2x\frac{\mathrm{d}\overline{y}}{\mathrm{d}x}\right) - 1 \right] \eta \mathrm{d}x \tag{7.46}$$

Euler's equation becomes

$$\frac{\mathrm{d}}{\mathrm{d}x}\left(2x\frac{\mathrm{d}y}{\mathrm{d}x}\right) = 1 \tag{7.47}$$

By solving this problem, we obtain:

$$y = \frac{x}{2} + C_1 \log x + C_2 \tag{7.48}$$

as the answer.

$$(2)\ J(\bar{y}+\eta)=\int_0^1\left\{\left[\frac{\mathrm{d}(\bar{y}+\eta)}{\mathrm{d}x}\right]^2+k^2\cos(\bar{y}+\eta)\right\}\mathrm{d}x \tag{7.49}$$

If only the first order of $\eta$ remains, we obtain the following $J_1$

$$J_1(\bar{y}+\eta)=\int_0^1\left[\left(\frac{\mathrm{d}\bar{y}}{\mathrm{d}x}\right)^2+2\frac{\mathrm{d}\bar{y}}{\mathrm{d}x}\frac{\mathrm{d}\eta}{\mathrm{d}x}+k^2\cos\bar{y}-k^2\sin\bar{y}\cdot\eta\right]\mathrm{d}x \tag{7.50}$$

where we use the expansion of $\cos(\bar{y}+\eta)$ in the following equation:

$$\cos(\bar{y}+\eta)=\cos\bar{y}-\sin\bar{y}\cdot\eta+O\left(\eta^2\right) \tag{7.51}$$

$$\delta J=J_1(\bar{y}+\eta)-J(\bar{y})=\int_0^1\left(2\frac{\mathrm{d}\bar{y}}{\mathrm{d}x}\frac{\mathrm{d}\eta}{\mathrm{d}x}-k^2\sin\bar{y}\cdot\eta\right)\mathrm{d}x \tag{7.52}$$

Integrate by parts to obtain the following equation:

$$\delta J=\left[2\frac{\mathrm{d}\bar{y}}{\mathrm{d}x}\eta\right]_0^1-\int_0^1\left(2\frac{\mathrm{d}^2\bar{y}}{\mathrm{d}x^2}+k^2\sin\bar{y}\right)\eta\mathrm{d}x \tag{7.53}$$

The first term disappears owing to natural BC

$$\delta J=-\int_0^1\left(2\frac{\mathrm{d}^2\bar{y}}{\mathrm{d}x^2}+k^2\sin\bar{y}\right)\eta\mathrm{d}x \tag{7.54}$$

We obtain Euler's equation.

$$2\frac{\mathrm{d}^2y}{\mathrm{d}x^2}+k^2\sin y=0 \tag{7.55}$$

We obtain the following equation as the solution:

$$x=\pm\int\frac{\mathrm{d}y}{k\sqrt{C_1+\cos y}}+C_2 \tag{7.56}$$

### *7.3.2 Example Problem 2, Hamilton's Principle*

A mass $m$ is supported by a spring moving vertically ($x$-axis: downward is positive). Gravity and resistance force $-kx$ ($x$ denotes the displacement from the equilibrium position) act on this mass. Hamilton's principle yields

$$\delta \int_{t_0}^{t_1} \left( \frac{1}{2} m\dot{x}^2 + mgx - \frac{1}{2} kx^2 \right) \mathrm{d}t = 0 \tag{7.57}$$

and derive Euler's equation of motion by calculating the variation on the left-hand side (Fig. 7.3).

**Answer**

Hamilton's principle determines function $x$ that minimizes the functional $U(x)$. If we simply write as $x$, we can obtain Euler's equation using partial integration from $\delta U = 0$ when $\delta U = U_1(x + \eta) - U(x)$ (taking only the first-order terms). In the following,

$$U(x, \dot{x}) = \int_{t_0}^{t_1} \left( \frac{1}{2} m\dot{x}^2 + mgx - \frac{1}{2} kx^2 \right) \mathrm{d}t \tag{7.58}$$

$$\begin{aligned} U(x+\eta) &= \int_{t_0}^{t_1} \left[ \frac{m}{2} \left( \frac{\mathrm{d}x}{\mathrm{d}t} + \frac{\mathrm{d}\eta}{\mathrm{d}t} \right)^2 + mg(x+\eta) - \frac{k}{2}(x+\eta)^2 \right] \mathrm{d}t \\ &= U(x) + \int_{t_0}^{t_1} \left( m \frac{\mathrm{d}x}{\mathrm{d}t} \frac{\mathrm{d}\eta}{\mathrm{d}t} + mg\eta - kx\eta \right) \mathrm{d}t + O\left(\eta^2\right) \end{aligned} \tag{7.59}$$

Therefore, the variation is as follows:

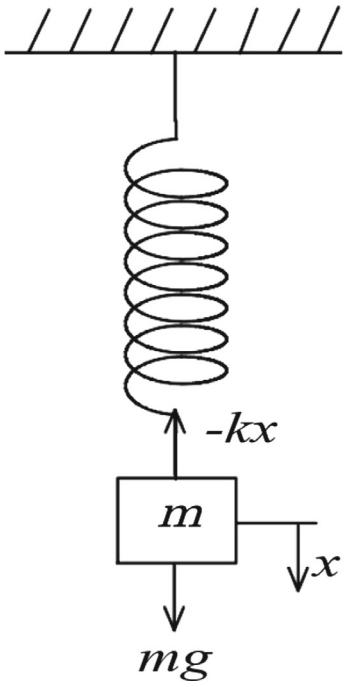


**Fig. 7.3** System with mass, gravitational force, and spring

$$\begin{aligned}\delta U &= \int_{t_0}^{t_1} \left( m\frac{\mathrm{d}x}{\mathrm{d}t}\frac{\mathrm{d}\eta}{\mathrm{d}t} + mg\eta - kx\eta \right) \mathrm{d}t \\ &= \left[ m\frac{\mathrm{d}x}{\mathrm{d}t}\eta \right]_{t_0}^{t_1} - \int_{t_0}^{t_1} \left( m\frac{\mathrm{d}^2x}{\mathrm{d}t^2} - mg + kx \right) \eta \mathrm{d}t \end{aligned} \tag{7.60}$$

The first term on the right-hand side is 0. Because $\delta U = 0$, the integrand becomes

$$m\frac{\mathrm{d}^2x}{\mathrm{d}t^2} - mg + kx = 0 \tag{7.61}$$

### 7.3.3 *Example Problem 3, System of Multiple Degrees of Freedom*

Next, consider a problem with multiple degrees of freedom. The Lagrange function (Lagrangian) of the spring-mass system ($m$ denotes mass, $k$ denotes stiffness or spring constant) shown in Fig. 7.4 is

$$L = \frac{1}{2}\left[ m_1\dot{x}_1^2 + m_2\dot{x}_2^2 + m_3\dot{x}_3^2 - k_1x_1^2 - k_2(x_2 - x_1)^2 - k_3(x_3 - x_2)^2 \right] \tag{7.62}$$

No damping force is considered. Next, we derive the Lagrange equation from the principle of least action.

**Answer**

Because $L = KE - PE$, we can determine $L$ by determining the kinetic energy $KE$ and potential energy $PE$ of each mass and adding them. $KE$ is

$$KE = \frac{1}{2}\left( m_1\dot{x}_1^2 + m_2\dot{x}_2^2 + m_3\dot{x}_3^2 \right) \tag{7.63}$$

Considering the relative displacement of each mass point and $PE$ becomes

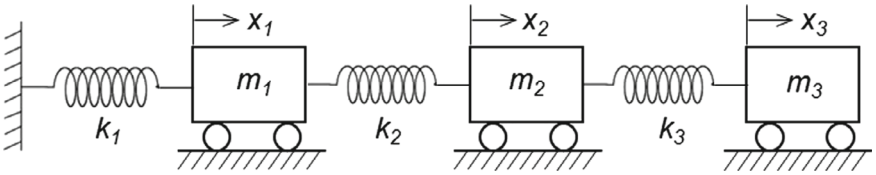


**Fig. 7.4** System with three masses and springs

$$PE = \frac{1}{2}\left[k_1 x_1^2 + k_2(x_2 - x_1)^2 + k_3(x_3 - x_2)^2\right] \tag{7.64}$$

Because we only need to consider the energies of each mass point, the analysis is easier. From the above, we obtain Eq. (7.62) as a Lagrangian expression. The principle of least action (Hamilton principle) is as follows:

$$\delta S = \delta_1 \int_{t_1}^{t_2} L\mathrm{d}t = 0 \tag{7.65}$$

The Euler equation for this problem is the Lagrange equation. Variations can be performed as follows in the case of multiple variables similar to the case of one variable.

$$x_1 = \bar{x}_1 + \eta_1, \quad x_2 = \bar{x}_2 + \eta_2, \quad x_3 = \bar{x}_3 + \eta_3 \tag{7.66}$$

We obtain the following equation:

$$\begin{aligned} &S(\bar{x}_1 + \eta_1, \bar{x}_2 + \eta_2, \bar{x}_3 + \eta_3) \\ &= \int_{t_1}^{t_2} \left\{ \frac{m_1}{2}\left[\frac{\mathrm{d}}{\mathrm{d}t}(\bar{x}_1 + \eta_1)\right]^2 + \frac{m_2}{2}\left[\frac{\mathrm{d}}{\mathrm{d}t}(\bar{x}_2 + \eta_2)\right]^2 + \frac{m_3}{2}\left[\frac{\mathrm{d}}{\mathrm{d}t}(\bar{x}_3 + \eta_3)\right]^2 \right. \\ &\left. -\frac{k_1}{2}(\bar{x}_1 + \eta_1)^2 - \frac{k_2}{2}(\bar{x}_2 - \bar{x}_1 + \eta_2 - \eta_1)^2 - \frac{k_3}{2}(\bar{x}_3 - \bar{x}_2 + \eta_3 - \eta_2)^2 \right\}\mathrm{d}t \end{aligned} \tag{7.67}$$

The variation is as follows:

$$\begin{aligned} \delta S &= S_1(\bar{x}_1 + \eta_1, \bar{x}_2 + \eta_2, \bar{x}_3 + \eta_3) - S(\bar{x}_1, \bar{x}_2, \bar{x}_3) \\ &= \int_{t_1}^{t_2} \left[ m_1 \frac{\mathrm{d}\bar{x}_1}{\mathrm{d}t}\frac{\mathrm{d}\eta_1}{\mathrm{d}t} + m_2 \frac{\mathrm{d}\bar{x}_2}{\mathrm{d}t}\frac{\mathrm{d}\eta_2}{\mathrm{d}t} + m_3 \frac{\mathrm{d}\bar{x}_3}{\mathrm{d}t}\frac{\mathrm{d}\eta_3}{\mathrm{d}t} - k_1\bar{x}_1\eta_1 \right. \\ &\left. - k_2(\bar{x}_2 - \bar{x}_1)(\eta_2 - \eta_1) - k_3(\bar{x}_3 - \bar{x}_2)(\eta_3 - \eta_2)\right]\mathrm{d}t \end{aligned} \tag{7.68}$$

where $S_1$ is in first order of $\eta$. By partial integration, we obtain the following equation:

$$\begin{aligned} \delta S = &\left[ m_1 \frac{\mathrm{d}\bar{x}_1}{\mathrm{d}t}\eta_1 \right]_{t_1}^{t_2} + \left[ m_2 \frac{\mathrm{d}\bar{x}_2}{\mathrm{d}t}\eta_2 \right]_{t_1}^{t_2} + \left[ m_3 \frac{\mathrm{d}\bar{x}_3}{\mathrm{d}t}\eta_3 \right]_{t_1}^{t_2} \\ &- \int_{t_1}^{t_2} \left[ m_1 \frac{\mathrm{d}^2\bar{x}_1}{\mathrm{d}t^2}\eta_1 + m_2 \frac{\mathrm{d}^2\bar{x}_2}{\mathrm{d}t^2}\eta_2 + m_3 \frac{\mathrm{d}^2\bar{x}_3}{\mathrm{d}t^2}\eta_3 \right. \\ &+ k_1\bar{x}_1\eta_1 + k_2(\bar{x}_2 - \bar{x}_1)\eta_2 - k_2(\bar{x}_2 - \bar{x}_1)\eta_1 \\ &\left. + k_3(\bar{x}_3 - \bar{x}_2)\eta_3 - k_3(\bar{x}_3 - \bar{x}_2)\eta_2 \right]\mathrm{d}t \end{aligned} \tag{7.69}$$

Natural boundary condition is

$$\eta_1|_{t_1}^{t_2} = \eta_2|_{t_1}^{t_2} = \eta_3|_{t_1}^{t_2} = 0 \tag{7.70}$$

Therefore, the first term on the right-hand side of Eq. (7.69) becomes 0.

$$\begin{aligned}\delta S = &-\int_{t_1}^{t_2}\left[m_1\frac{\mathrm{d}^2\bar{x}_1}{\mathrm{d}t^2} + k_1\bar{x}_1 - k_2(\bar{x}_2 - \bar{x}_1)\right]\eta_1\mathrm{d}t \\ &-\int_{t_1}^{t_2}\left[m_2\frac{\mathrm{d}^2\bar{x}_2}{\mathrm{d}t^2} + k_2(\bar{x}_2 - \bar{x}_1) - k_3(\bar{x}_3 - \bar{x}_2)\right]\eta_2\mathrm{d}t \\ &-\int_{t_1}^{t_2}\left[m_3\frac{\mathrm{d}^2\bar{x}_3}{\mathrm{d}t^2} + k_3(\bar{x}_3 - \bar{x}_2)\right]\eta_3\mathrm{d}t\end{aligned} \tag{7.71}$$

The Euler (Lagrange) equation is obtained by setting the integrands of the three integrals to 0.

$$\begin{aligned}&m_1\frac{\mathrm{d}^2\bar{x}_1}{\mathrm{d}t^2} + k_1\bar{x}_1 - k_2(\bar{x}_2 - \bar{x}_1) = 0 \\ &m_2\frac{\mathrm{d}^2\bar{x}_2}{\mathrm{d}t^2} + k_2(\bar{x}_2 - \bar{x}_1) - k_3(\bar{x}_3 - \bar{x}_2) = 0 \\ &m_3\frac{\mathrm{d}^2\bar{x}_3}{\mathrm{d}t^2} + k_3(\bar{x}_3 - \bar{x}_2) = 0\end{aligned} \tag{7.72}$$

### *7.3.4 Example Problem 4, System with Damping*

The variation principle for a particle falling under gravity with an air resistance force proportional to velocity is given by Eq. (7.73), where $m$ is the mass of the particle, $g$ is the gravitational acceleration, $k$ is the damping coefficient for air resistance, and $x(t)$ is the position of the particle as a function of time. Taking its variation of the first term of Eq. (7.73), we obtain Eq. (7.74).

$$\delta\int_{t_0}^{t_1}\left(\frac{1}{2}m\dot{x}^2 + mgx\right)\mathrm{d}t - \int_{t_0}^{t_1} c\dot{x}\eta\,\mathrm{d}t = 0 \tag{7.73}$$

$$\delta S = \delta\int_{t_0}^{t_1}\left(\frac{1}{2}m\dot{x}^2 + mgx\right)\mathrm{d}t = \int_{t_0}^{t_1}(m\dot{x}\dot{\eta} + mg\eta)\mathrm{d}t \tag{7.74}$$

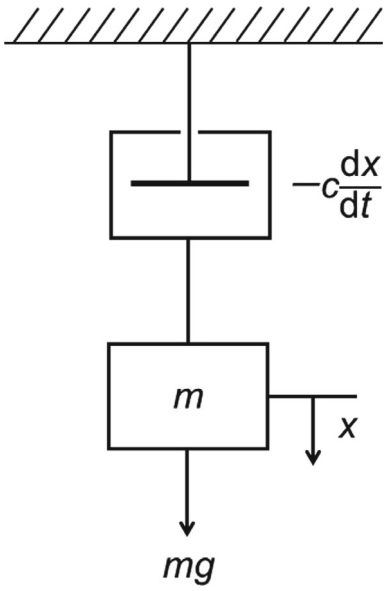


**Fig. 7.5** System with mass, damper, and spring

The system is schematically shown in Fig. 7.5.

Using integration by parts, we rewrite the first term. Assuming the boundary conditions $\eta = 0$ at the initial and final times. Thus, the variation simplifies to:

$$\delta S = \int_{t_0}^{t_1} (-m\ddot{x} + mg)\eta \, \mathrm{d}t \tag{7.75}$$

From Eqs. (7.73) and (7.75), we obtain

$$\int_{t_0}^{t_1} (-m\ddot{x} + mg - c\dot{x})\eta \, \mathrm{d}t = 0 \tag{7.76}$$

Since this must hold for all variations $\eta$, the integrand must be zero:

$$m\ddot{x} = mg - c\dot{x} \quad \text{or} \quad m\frac{\mathrm{d}^2x}{\mathrm{d}t^2} = mg - c\frac{\mathrm{d}x}{\mathrm{d}t} \tag{7.77}$$

## 7.4 Approximate Solution Method Using Variational Method

For boundary value problems, the problem of the calculus of variations is reduced to a Euler equation. Therefore, Hamilton's principle is reduced to the Lagrange equation. It is difficult to solve the Euler or Lagrange equations directly, which have several degrees of freedom. These problems can be solved using numerical calculations. Direct methods have been developed to deal with variational problems directly. One such approach is the Ritz method. An approximation method can be considered in which a given differential equation is reduced to a variational problem that coincides with the Euler equation, which is solved by a direct method. This is known as the Ritz method. This concept is important in the finite element method (FEM). Unlike numerical calculations, the solution can be expressed using a versatile formula. However, only problems that can be converted into variational problems are valid.

### *7.4.1 Example Problem 5, Ritz Method*

$$x\frac{\mathrm{d}^2u}{\mathrm{d}x^2}+\frac{\mathrm{d}u}{\mathrm{d}x}+\frac{x^2-1}{x}u+x^2=0,\quad 1\le x\le 2 \tag{7.78}$$

Solve this equation using the Ritz method with BC $u(1)=u(2)=0$.

**Solution**

The functional (function of functions) for the corresponding variation problem is as follows:

$$J(u)=\int_1^2\left[x\left(\frac{\mathrm{d}u}{\mathrm{d}x}\right)^2-\frac{x^2-1}{x}u^2-2x^2u\right]\mathrm{d}x \tag{7.79}$$

Note that it is necessary to find the functional. The approximate equation that satisfies the BC is tested

$$u_1=C_1(x-1)(2-x)=C_1w_1,\quad w_1=(x-1)(2-x) \tag{7.80}$$

is tested as a test function. We assume ${w_1}'=\mathrm{d}w_1/\mathrm{d}x$.

$$J(u_1)=C_1^2\int_1^2\left(x{w_1'}^2-\frac{x^2-1}{x}w_1^2\right)\mathrm{d}x-C_1\int_1^2 2x^2w_1\mathrm{d}x \tag{7.81}$$

Now calculate the integral whose value is known.

$$I_1 = \int_1^2 \left( x w_1'^2 - \frac{x^2 - 1}{x} w_1^2 \right) \mathrm{d}x = 0.47260 \tag{7.82}$$

$$I_2 = \int_1^2 x^2 w_1 dx = 0.38333 \tag{7.83}$$

The integrals can be obtained using Mathematica, a book on mathematical formulas [5], and numerical integration.

$$J(u_1) = C_1^2 I_2 - 2C_1 I_2 \tag{7.84}$$

To make $J$ an extreme value

$$\frac{\partial J}{\partial C_1} = 2I_2 C_1 - 2I_2 = 2(I_1 C_1 - I_2) = 0 \quad \text{or} \quad C_1 = \frac{I_2}{I_1} = \frac{0.38333}{0.47260} = 0.811 \tag{7.85}$$

The approximate solution is

$$u_1 = 0.811(x - 1)(2 - x) \tag{7.86}$$

Therefore, $u_1(1.5) = 0.20275$. The exact solution is

$$u(x) = 3.6072 J_{B1}(x) + 0.75195 Y_1(x) - x \tag{7.87}$$

where $J_{B1}(x)$ and $Y_1(x)$ are Bessel functions. For Eq. (7.87), $u(1.5) = 0.2024$; thus, Eq. (7.86) is a good approximation.

### *7.4.2 Example Problem 6, Ordinary Differential Equation*

For the ordinary differential equation,

$$u'' + \left(1 + x^2\right)u + 1 = 0, \quad -1 \le x \le 1 \tag{7.88}$$

obtain the approximate solution using the Ritz method, where $u' = \mathrm{d}u/\mathrm{d}x$, and the BC is $u(-1) = u(1) = 0$. Use

$$u = C_1\left(1 - x^2\right) + C_2\left(1 - x^4\right) + C_3\left(1 - x^6\right) \tag{7.89}$$

as the linear test function.

**Solution**

The functionals for the corresponding variation problem is as follows:

$$J(u) = \int_{-1}^{1} \left[u'^2 - \left(1 + x^2\right)u^2 + u\right]\mathrm{d}x \tag{7.90}$$

$$J(\overline{u} + \eta) = \int_{-1}^{1} \left[(\overline{u} + \eta)'^2 - \left(1 + x^2\right)(\overline{u} + \eta)^2 + (\overline{u} + \eta)\right]\mathrm{d}x \tag{7.91}$$

$$J_1(\overline{u} + \eta) - J(\overline{u}) = \int_{-1}^{1} \left[2\overline{u}'\eta' - 2\left(1 + x^2\right)\overline{u}\eta + \eta\right]\mathrm{d}t \tag{7.92}$$

where $J_1$ includes first order terms only. The first term on the right-hand side of Eq. (7.92) is transformed as follows:

$$2\int_{-1}^{1} \overline{u}'y'\mathrm{d}t = 2\left[\overline{u}'\eta\right]_{-1}^{1} - 2\int_{-1}^{1} \overline{u}''\eta\mathrm{d}t \tag{7.93}$$

The first term varnishes. From the above, we obtain the following:

$$\begin{aligned}\delta J = J_1(\overline{u} + \eta) - J(\overline{u}) &= \int_{-1}^{1} \left[-2\overline{u}''\eta - 2\left(1 + x^2\right)\overline{u}\eta + \eta\right]\mathrm{d}t \\ &= -2\int_{-1}^{1} \left[\overline{u}'' + \left(1 + x^2\right)\overline{u} + 1\right]\eta\mathrm{d}t\end{aligned} \tag{7.94}$$

From $\delta J = 0$ in Eq. (7.94), Eq. (7.88) is obtained. Substituting Eq. (7.89) into Eq. (7.90), $J$ can be expressed in terms of $C_1$, $C_2$, and $C_3$. They can be calculated from the conditions:

$$\frac{\partial J}{\partial C_1} = 0, \quad \frac{\partial J}{\partial C_2} = 0, \quad \frac{\partial J}{\partial C_3} = 0 \tag{7.95}$$

$C_1$, $C_2$, and $C_3$ are determined from Eq. (7.95). The approximated solution is as follows:

$$u = 0.9664776\left(1 - x^2\right) - 0.00047361\left(1 - x^4\right) - 0.029671\left(1 - x^6\right) \tag{7.96}$$

### 7.4.3 *Example Problem 7, Poiseuille Flow*

The energy principle for steady axial laminar flow (Poiseuille flow) in a circular pipe with radius $a$, whose cross section is shown in Fig. 7.6, is

$$U(w) = \int_0^a \left[r\left(\frac{\mathrm{d}w}{\mathrm{d}r}\right)^2 + 2r\beta w\right]\mathrm{d}r, \quad \beta = \frac{1}{\mu}\frac{\mathrm{d}p}{\mathrm{d}x} = \text{constant} \tag{7.97}$$

The variation in the functional $U$ is $\delta U = 0$, where $w$: axial velocity, $p$: pressure, $\mu$: viscosity coefficient, $r$: radial coordinate, and $x$: axial coordinate.

(1) Calculate $\delta U$ and derive the differential equation that $w$ satisfies by setting it to zero under the natural BCs.
(2) Obtain the flow velocity distribution using the Ritz method. Assume that the test function for the velocity distribution is

$$w = Ar(r - a) \tag{7.98}$$

and find parameter $A$.

**Answer**

$$(1)\ U(w+\eta) = \int_0^a \left\{ r\left[\frac{\mathrm{d}(w+\eta)}{\mathrm{d}r}\right]^2 + 2r\beta(w+\eta)\right\}\mathrm{d}r \tag{7.99}$$

If we express this $U_1(w+\eta)$ with only the first-order term of $\eta$ as

$$\begin{aligned}\delta U &= U_1(w+\eta) - U(w) = \int_0^a \left(2r\frac{\mathrm{d}w}{\mathrm{d}r}\frac{\mathrm{d}\eta}{\mathrm{d}r} + 2r\beta\eta\right)\mathrm{d}r \\ &= \left[2r\frac{\mathrm{d}w}{\mathrm{d}r}\eta\right]_0^a - \int_0^a 2\frac{\mathrm{d}}{\mathrm{d}r}\left(r\frac{\mathrm{d}w}{\mathrm{d}r}\right)\eta\mathrm{d}r + \int_0^a 2r\beta\eta\mathrm{d}r \\ &= -2\int_0^a \left[\frac{\mathrm{d}}{\mathrm{d}r}\left(r\frac{\mathrm{d}w}{\mathrm{d}r}\right) - \beta r\right]\eta\mathrm{d}r = 0\end{aligned} \tag{7.100}$$

Then, we obtain the following equation:

$$\frac{\mathrm{d}}{\mathrm{d}r}\left(r\frac{\mathrm{d}w}{\mathrm{d}r}\right) - \beta r = 0 \quad \text{or} \quad r\frac{\mathrm{d}^2w}{\mathrm{d}r^2} + \frac{\mathrm{d}w}{\mathrm{d}r} - \beta r = 0 \tag{7.101}$$

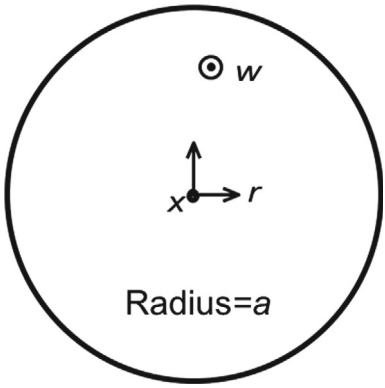


**Fig. 7.6** Poiseuille flow system

(2) The calculation is performed as follows for the test function $w$:

$$w = Ar(r-a) = Ar^2 - Ara \tag{7.102}$$

$$\frac{\mathrm{d}w}{\mathrm{d}r} = 2Ar - Aa \tag{7.103}$$

$$\left(\frac{\mathrm{d}w}{\mathrm{d}r}\right)^2 = 4A^2r^2 - 4A^2ar + A^2a^2 \tag{7.104}$$

Substituting this into the expression for $U$, we obtain the following equation:

$$\begin{aligned} U &= \int_0^a \left(4A^2r^3 - 4A^2ar^2 + A^2a^2r + 2\beta Ar^3 - 2\beta Aar^2\right)\mathrm{d}r \\ &= 4A^2\frac{a^4}{4} - 4A^2\frac{a^4}{3} + A^2\frac{a^4}{2} + 2\beta A\frac{a^4}{4} - 2\beta A\frac{a^4}{3} \\ &= A^2a^4\left(1 - \frac{4}{3} + \frac{1}{2}\right) + 2\beta Aa^4\left(\frac{1}{4} - \frac{1}{3}\right) = \frac{A^2a^4}{6} - \frac{\beta Aa^4}{6} \end{aligned} \tag{7.105}$$

Differentiate $U$ with respect to $A$ as follows:

$$\frac{\partial U}{\partial A} = \frac{Aa^4}{3} - \frac{\beta a^4}{6} = 0 \tag{7.106}$$

The value of $A$ that yields the minimum value is obtained as follows:

$$A = \frac{\beta}{2} \tag{7.107}$$

The velocity distribution is therefore as follows:

$$w = \frac{\beta}{2}r(r-a) \tag{7.108}$$

The procedure for obtaining the above approximate solution is summarized below.

(1) Transform the differential equation into a variation problem that matches the Euler formula.
(2) Substitute a linear test function that satisfies the BCs.
(3) Set $\partial J/(\partial C_\mathrm{i}) = 0$ and find $C_1 \ldots C_\mathrm{N}$.

The Rayleigh–Ritz method for finding an approximate eigenvalue problem using the calculus of variations is well known; however, it is not covered in this book.

### 7.4.4 Example Problem 8, Capacitor

Next, we solve the electrical problem [1]. A cylindrical capacitor exists with an inner conductor of radius $a$ and a potential (potential function) of $V$, along with an outer conductor of radius $b$ and a potential of 0 as shown in Fig. 7.7. When no charge is observed between the conductors and if the potential function between the conductors is $\phi$, then the volume integral

$$\frac{\varepsilon_0}{2}\int (\nabla\phi)^2 \mathrm{d}V \tag{7.109}$$

is equal to the energy of capacitor $CV^2/2$. Consider the problem of determining an approximate value of $C$.

**Solution**

In cylindrical coordinates, if we consider one-dimensional $a < r < b$ in the $r$-direction, we obtain

$$\nabla\phi = \frac{\partial\phi}{\partial r} + \frac{1}{r}\frac{\partial\phi}{\partial\theta} + \frac{\partial\phi}{\partial z} = \frac{\mathrm{d}\phi}{\mathrm{d}r} \tag{7.110}$$

Moreover,

$$\mathrm{d}V = 2\pi r \cdot L\mathrm{d}r \tag{7.111}$$

$L$: axial length; thus, if we set the unit axial length $L = 1$, we obtain:

$$C = \frac{\varepsilon_0}{V^2}\int (\nabla\phi)^2 \mathrm{d}V = \frac{\varepsilon_0}{V^2}\int_a^b \left(\frac{\mathrm{d}\phi}{\mathrm{d}r}\right)^2 2\pi r\mathrm{d}r \tag{7.112}$$

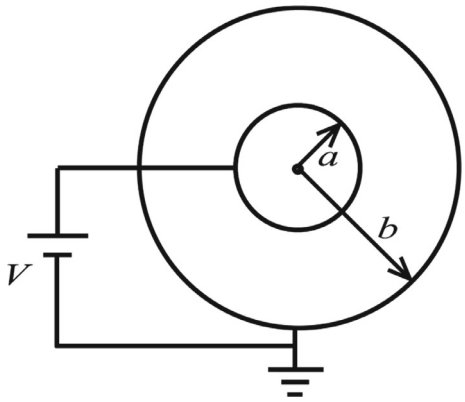


**Fig. 7.7** Coaxial condenser system

**Table 7.1** $C/(2\pi\varepsilon_0)$

| $B = b/a$ | Exact solution | First order approximation solution | Second order approximation solution | Third order approximation solution |
|---|---|---|---|---|
| 1.1 | 10.492070 | 10.500000 | 10.492065 | 10.492058 |
| 1.5 | 2.4662 | 2.50 | 2.4667 | 2.4663 |
| 2 | 1.4423 | 1.500 | 1.444 | 1.4427 |
| 4 | 0.721 | 0.833 | 0.733 | 0.722 |
| 10 | 0.434 | 0.612 | 0.475 | 0.445 |
| 100 | 0.267 | 0.51 | 0.346 | 0.290 |

First, we consider a linear expression of the radial coordinate $r$ as a test function.

$$\phi = V\left(1 - \frac{r-a}{b-a}\right) \tag{7.113}$$

Substituting into Eq. (7.40), we obtain the expression for $C/(2\pi\varepsilon_0)$.

$$\frac{C}{2\pi\varepsilon_0} = \frac{b+a}{2(b-a)} \tag{7.114}$$

Naturally, it differs from the exact solution:

$$\frac{C}{2\pi\varepsilon_0} = \frac{1}{\ln\left(\frac{b}{a}\right)} \tag{7.115}$$

However, the comparison in Table 7.1 shows that this first order approximation solution is acceptable. Next, we consider the quadratic expression of $r$ as the test function. The most general quadratic expression, where $\phi = 0$ at $r = b$ and $\phi = V$ at $r = a$ is

$$\phi = V\left[1 + \alpha\left(\frac{r-a}{b-a}\right) - (1+\alpha)\left(\frac{r-a}{b-a}\right)^2\right] \tag{7.116}$$

and the result of the substitution calculation is

$$\frac{C}{2\pi\varepsilon_0} = \frac{a}{(b-a)}\left[\frac{b}{a}\left(\frac{\alpha^2}{6} + \frac{2\alpha}{3} + 1\right) + \frac{\alpha^2}{6} + \frac{1}{3}\right] \tag{7.117}$$

We are aware that the true value is smaller than any of the values we will calculate; therefore, regardless of the value of $\alpha$, the answer we obtain will be excessively large. However, if we vary $\alpha$ and reduce it to the maximum extent, the lowest value will be closer to the true value than any other value. Therefore, the next step is to select

$\alpha$ that yields the minimum $C$. Using ordinary differential calculus, we observe that the minimum $C$ occurs at $\alpha = -2b/(b+a)$. Substituting this into the equation, we obtain the minimum capacitance as follows:

$$\frac{C}{2\pi\varepsilon_0} = \frac{b^2 + 4ab + a^2}{3\left(b^2 - a^2\right)} \tag{7.118}$$

This is a second order approximation solution. Calculated results are shown in Table 7.1. Next, we use the cubic expression of $r$ with unknowns $\beta_1$, $\beta_2$, and $\beta_3$ as the test function:

$$\phi = V\left[1 + \beta_1\left(\frac{r-a}{b-a}\right) + \beta_2\left(\frac{r-a}{b-a}\right)^2 + \beta_3\left(\frac{r-a}{b-a}\right)^3\right] \tag{7.119}$$

From the boundary conditions of $\phi(a) = V$ and $\phi(b) = 0$, we derive an equation that satisfies $\beta_1, \beta_2$, and $\beta_3$:

$$\beta_1 = -1 - \beta_2 - \beta_3 \tag{7.120}$$

We obtain an approximation of the capacitance $C$ of the capacitor using the following procedure. Then, we eliminate $\beta_1$.

$$\begin{aligned}
I &= \int (\nabla\phi)^2 \mathrm{d}V = 2\pi \int_a^b \left(\frac{\partial\phi}{\partial r}\right)^2 r\mathrm{d}r \\
&= 2\pi V^2 \int_a^b \left[\frac{\beta_1}{b-a} + 2\beta_2\frac{r-a}{(b-a)^2} + 3\beta_3\frac{(r-a)^2}{(b-a)^3}\right]^2 r\mathrm{d}r \\
&= \frac{1}{(b-a)^2}\int_a^b \left[(-1-\beta_2-\beta_3) + 2\beta_2\frac{r-a}{b-a} + 3\beta_3\frac{(r-a)^2}{(b-a)^2}\right]^2 r\mathrm{d}r \\
&= \frac{1}{(b-a)^2}\int_a^b \left[-1 + \beta_2\frac{a-b+2(r-a)}{b-a} + \beta_3\frac{-(b-a)^2 + 3(r-a)^2}{(b-a)^2}\right]^2 r\mathrm{d}r
\end{aligned} \tag{7.121}$$

Then, assuming $A = 1/(b-a)$,

$$\begin{aligned}
I &= A^2 \times \int_a^b \left\{-1 + \beta_2 A(2r-a-b) + \beta_3 A^2\left[3(r-a)^2 - (b-a)^2\right]\right\}^2 r\mathrm{d}r \\
&= A^2\int_a^b r\mathrm{d}r + \beta_2^2 A^4 \int_a^b (2r-a-b)^2 r\mathrm{d}r \\
&\quad + \beta_3^2 A^6 \int_a^b \left[3(r-a)^2 - (b-a)^2\right]^2 r\mathrm{d}r - 2\beta_2 A^3 \int_a^b (2r-a-b) r\mathrm{d}r
\end{aligned}$$

$$+ 2\beta_2\beta_3 A^5 \int_a^b (2r - a - b)\left[3(r-a)^2 - (b-a)^2\right] r\mathrm{d}r$$
$$- 2\beta_3 A^4 \int_a^b \left[3(r-a)^2 - (b-a)^2\right] r\mathrm{d}r$$
$$= I_0 + I_1\beta_2^2 + I_2\beta_3^2 - 2I_3\beta_2 + 2I_4\beta_2\beta_3 - 2I_5\beta_3 \tag{7.122}$$

is obtained, where $I_0$, $I_1$, $I_2$, $I_3$, $I_4$, and $I_5$ are integrals including $A$ that appear on the right-hand side of Eq. (7.122). We partially differentiate with respect to $\beta_2$ and $\beta_3$ and set them to zero to determine the coefficients.

$$\frac{\partial I}{\partial \beta_2} = 2I_1\beta_2 - 2I_3 + 2I_4\beta_3 = 0 \tag{7.123}$$

$$\frac{\partial I}{\partial \beta_3} = 2I_2\beta_3 + 2I_4\beta_2 - 2I_5 = 0 \tag{7.124}$$

**Result**

$$\frac{C}{2\pi\varepsilon_0} = \frac{B+1}{2B-2} + \frac{10B^2 - 20B + 10}{38B + 11B^2 + 11} + \frac{20B^2 - 15B - 5}{38B + 11B^2 + 11}$$
$$+ \frac{160B + 240B^2 - 480B^3 + 200B^4 - 120}{836B + 1686B^2 + 836B^3 + 121B^4 + 121}$$
$$+ \frac{60B^2 - 480B + 800B^3 - 510B^4 + 130}{836B + 1686B^2 + 836B^3 + 121B^4 + 121}$$
$$+ \frac{450B - 600B^2 - 450B^3 + 675B^4 - 75}{1672B + 3372B^2 + 1672B^3 + 242B^4 + 242} \tag{7.125}$$

where $B = b/a$. As summarized in Table 7.1, the values of $C/2\pi\varepsilon_0$ for first, second, and third orders are calculated for $B = b/a = 1.1$, 1.5, 2, 4, 10, and 100, and a comparison table with the true values of exact solution is created. The third order approximation solution is more accurate.

## 7.5 Conclusions

In conclusion, this chapter comprehensively elucidates the energy principle, a cornerstone of energy conversion engineering that is essential across various engineering disciplines. It details how energy transformations are fundamental to the functionality of mechanical systems, fluid dynamics, and electrical circuits, illustrating the principle's broad applicability in both theoretical and practical realms.

Specifically, the chapter highlights the application of the energy principle in mechanics, providing a robust framework for analyzing forces and motion within

a range of systems from simple machines to complex mechanical structures. In fluid engineering, it examines the principle's role in understanding fluid behavior under varying flow and pressure conditions, aiding in the design of more efficient hydraulic systems and pipelines. In electrical engineering, the energy principle is pivotal for the design and analysis of electrical circuits, ensuring energy efficiency and system stability.

Additionally, the chapter discusses the principle of least action, a sophisticated approach aimed at minimizing the action, or integral of the Lagrangian, across various systems. This principle not only emphasizes the concept of minimal energy usage but also supports the detailed analysis and resolution of complex engineering problems. By applying the principle of least action, engineers can optimize processes and derive equations of motion in a way that ensures the most energy-efficient pathways are followed. This comprehensive exploration empowers engineers to effectively implement these principles to enhance efficiency and stability in their respective fields.

### Chapter 7 Exercises

**Problem 1**: Hamilton's principle

A mass point of mass $m$ falls vertically ($x$-axis: downward is positive) through the air in a gravitational field (gravitational acceleration $g$). Show the variation principle (Hamilton's principle) that governs the motion of the mass point, and derive Euler's equation by calculating the variation.

**Problem 2**: Forced oscillation

As shown in Fig. 7.8, a mass point of mass m moves vertically ($x$-axis: downward is positive). Gravity and spring resistance force $-kx$ (x denotes the displacement from the equilibrium position) act on this mass point. In addition, the support position of the spring is periodically displaced by $X = A\cos\omega t$. In this case, Hamilton's principle yields

$$\delta S(x) = \delta \int_{t_0}^{t_1} \left[ \frac{1}{2} m\dot{x}^2 + mgx - \frac{1}{2} k(x - A\cos\omega t)^2 \right] \mathrm{d}t = 0$$

By calculating the variation in this equation, derive Euler's equation of motion (a second-order ordinary differential equation).

**Problem 3**: Pendulum with spring

Consider a pendulum comprising a spring (resistance coefficient $k$) and mass m, as shown in Fig. 7.9. In the figure, $\ell_0$ denotes the length (constant) of the spring in its natural state, whereas $x$ denotes the extension of the spring. $\theta$ denotes the angle of swing from the vertical downwards. If we apply the principle of least action (Hamilton's principle) to this two-degree-of-freedom system, we obtain

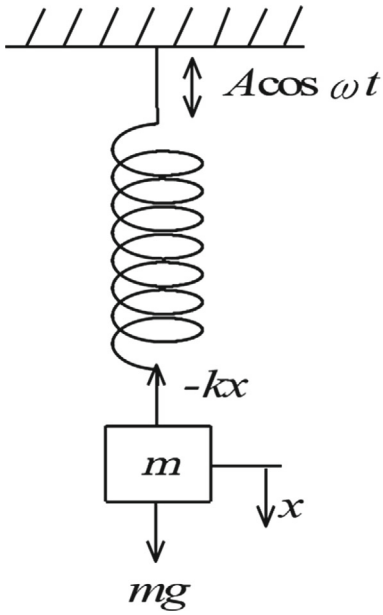


**Fig. 7.8** Systems with mass, gravitational force, springs, and support vibration

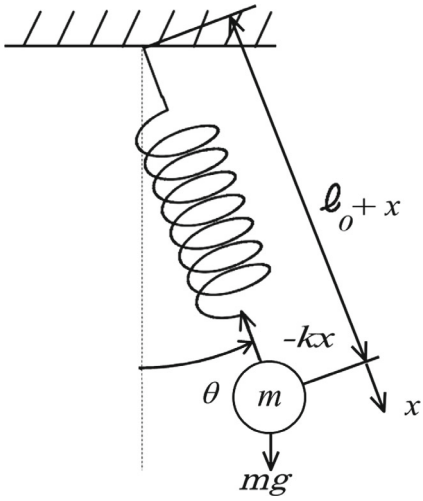


**Fig. 7.9** Pendulum system with mass, gravitational force, spring, and support vibrations

$$\delta S(x,\theta) = \delta \int_{t_0}^{t_1} \left\{ \frac{m}{2}\left[ \left(\frac{\mathrm{d}x}{\mathrm{d}t}\right)^2 + (\ell_0 + x)^2 \left(\frac{\mathrm{d}\theta}{\mathrm{d}t}\right)^2 \right] - \frac{k}{2}x^2 + mg(\ell_0 + x)\cos\theta \right\} \mathrm{d}t$$
$$= 0$$

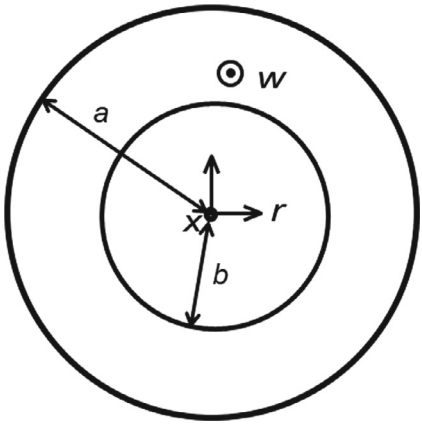


**Fig. 7.10** Laminar flow between two coaxial cylinders

By calculating the variation in this two-variable functional, derive Euler's equation of motion (two-order simultaneous ordinary differential equations). (Hint: Displace the two functions $x$ and $\theta$ independently and calculate the variations.)

**Problem 4**: Ritz method

Using the Ritz method, find an approximate solution for the steady laminar flow in a concentric double pipe with the inner radius of the outer pipe as $a$ and the outer radius of the inner pipe as $b$ (Fig. 7.10). Assume that the flow velocity distribution is $w = A(a - r)(r - b)$ with parameter $A$.

**Problem 5**: Cylindrical capacitor

As shown in Fig. 7.7 in the main text, a cylindrical capacitor with an inner conductor of radius $a$ and potential $V$ exists, along with an outer conductor of radius $b$ and potential 0. If the potential function between the conductors is $\phi$, it is determined such that the variation in energy per unit length

$$U = \frac{\varepsilon_0}{2} \int_a^b \left( \frac{\mathrm{d}\phi}{\mathrm{d}r} \right)^2 2\pi r \mathrm{d}r$$

is $\delta U = 0$.

(1) Calculate $\delta U$ and set it to 0 under the natural boundary conditions to derive the differential equation that $\phi$ satisfies, and solve the differential equation to determine the exact $\phi$.
(2) If $C$ denotes the capacitance of the capacitor,

$$U = \frac{1}{2} C V^2$$

holds true for the determined $\phi$. Express the capacitance $C$ in terms of $a$, $b$ $\pi$, and $\varepsilon_0$.

## References

1. R.P. Feynman, R.B. Leighton, M. Sands, *The Feynman Lectures on Physics, Volume II: Mainly Electromagnetism and Matter* (1963), pp. 592
2. L.D. Landau, E.M. Lifshitz, *Mechanics*, in Course of Theoretical Physics (Pergamon Press, 1960), pp. 165
3. Y. Tomita, A. Koizumi, H. Matsumoto, *Kougaku no tameno Suuri Kaiseki III* (English translated title: *Mathematical Analysis III for Engineering*) (Jikkyo Shuppan Co., Ltd., Tokyo, Japan, 1976), pp. 284 (in Japanese)
4. C. Lanczos, *The variational Principles of Mechanics* (Dover Publications, 1986), pp. 464
5. S. Moriguchi, K. Udagaw, S. Hitotsumatsu, *Sugaku Koshiki I, II, and III* (English translated title: *Mathematical Formula I, II, and III*) (Iwanami Shoten, Publishers, Tokyo, Japan, 1956, 1957, and 1960), pp. 310, pp. 318, and pp. 340 (In Japanese)

# Chapter 8
# Fundamentals of Continuum Thermal Energy Fluid Science


**Abstract** This chapter provides a comprehensive discussion on the integration of fluid dynamics, heat transfer engineering, and plasma engineering, disciplines that span the fields of mechanical engineering, chemical engineering, and electrical engineering. The chapter introduces a fundamental equation system for plasma heat transfer fluids and explores its key characteristics. In typical books, there is often a significant gap between fundamental theory and practical application. To bridge this divide, this chapter emphasizes an application-oriented perspective, ensuring that the concepts are presented in a manner relevant to real-world implementations. The derivation of fundamental equations and mathematical formulations is accompanied by practical examples related to plasma applications, facilitating a clearer understanding of their significance. Additionally, the mechanisms of heat transfer in both equilibrium and nonequilibrium plasmas are examined in detail. This discussion is structured around the fundamental equation system and includes concrete examples of computational analyses. The chapter concludes with a summary of key findings and a set of exercise problems to reinforce the concepts covered.

## 8.1 Introduction

Nonthermal plasma flows have found widespread applications across various industries. However, a significant gap remains between fundamental research and practical implementation. To effectively design and predict the performance of industrial plasma systems, it is crucial to develop numerical simulations and predictive models for nonthermal plasma fluid flows. This book seeks to integrate fluid dynamics, heat transfer engineering, and plasma engineering, disciplines that are commonly addressed within the fields of mechanical engineering, chemical engineering, and electrical engineering. A fundamental equation system for plasma heat transfer fluids is introduced, and its key characteristics are explained in detail.

The discussion then extends to several critical aspects of plasma heat transfer, including convective heat transfer, thermal conduction, streamer formation, electron temperature rise in nonequilibrium plasma flows, Joule heating induced by voltage



M. Okubo, *Electrical Sustainable Energy for Mechanical Engineering*,
https://doi.org/10.1007/978-981-96-5170-2_8

application, thermal conduction from electrodes to fluids, and nonequilibrium states in supersonic plasma flows. The analytical approach is structured around the heat transfer phenomena occurring within plasma systems, providing a comprehensive perspective on the subject.

The fundamental equation systems governing plasma heat transfer are reviewed based on prior studies and established literature [1–7]. Additionally, a separate study has examined these phenomena from an engineering application perspective [8]. In this chapter, we aim to review and present these concepts with a strong focus on practical applications. To facilitate understanding, the derivation of mathematical formulas and fundamental equations is provided alongside real-world application examples of nonthermal plasmas.

## 8.2 Fundamental System of Equations for Heat Transfer in Plasma Fluids

### *8.2.1 Plasma Fluid Concept*

As an example, when analyzing atmospheric pressure plasma, macroscopic "convection" plays a significant role. Therefore, when evaluating plasma heat transfer, it is essential to treat plasma as a "fluid" system. In this context, the plasma fluid is considered within the framework of continuum mechanics, meaning that the individual plasma components—neutral particles, ions, and radicals (collectively referred to as heavy particles)—are treated as a continuous medium rather than as discrete particles. Notably, these heavy particles are distinct from electrons, which exhibit different transport properties. To establish a meaningful continuum approximation, consider a small control volume ($\Delta V$) that is significantly smaller than the characteristic length $L$ of the system but still large enough compared to both the Langmuir length and the mean free path ($\lambda$) of the plasma particles. This ensures that the control volume contains a sufficient number of heavy particles and electrons, allowing for a statistically valid description of plasma behavior. Consequently, plasmas operating in high-vacuum conditions, where the mean free path is exceptionally long, fall outside the scope of this discussion.

A key parameter in determining whether the continuum assumption is valid is the Knudsen number ($K = \lambda/L$), which represents the ratio of the mean free path to the system's characteristic length. It is important to note that the continuum approximation remains applicable only when the Knudsen number is sufficiently small, indicating that particle interactions occur frequently enough for the plasma to be treated as a continuous medium.

The volume of this infinitesimal element, $\Delta V$, is considered to approach zero, $\Delta V \rightarrow 0$, and can be represented by the position vector $\boldsymbol{x}$ in a spatially fixed inertial reference frame. In other words, a fundamental aspect of continuum dynamics is the treatment of an infinitesimal volume as a point, the definition of a position vector, and

the consideration of the system in coordinates fixed to an inertial reference frame. In this framework, physical quantities such as the density and velocity of the plasma fluid at a given position vector $\boldsymbol{x}$ must be defined as the mean values of the particles contained within the infinitesimal volume element. For instance, density $\rho$ as a field quantity, momentum per unit volume, or mass flux density $\rho\boldsymbol{u}$ can be expressed as:

Density:

$$\rho(\boldsymbol{x}) = \lim_{\Delta V \to 0} \frac{\sum_{\mathrm{i}=1}^{\mathrm{N}} m_{\mathrm{i}}}{\Delta V} \tag{8.1}$$

Mass flux density:

$$\rho(\boldsymbol{x})\boldsymbol{u}(\boldsymbol{x}) = \lim_{\Delta V \to 0} \frac{\sum_{\mathrm{i}=1}^{\mathrm{N}} m_{\mathrm{i}} u_{\mathrm{i}}}{\Delta V} \tag{8.2}$$

where $m_{\mathrm{i}}$ and $u_{\mathrm{i}}$ are the mass and velocity of individual particles, respectively. Physical quantities appearing in the basic equations described in Sect. 8.2.7, namely specific enthalpy, temperature, component concentrations, or quantities of electromagnetic fields such as magnetic field $\boldsymbol{H}$, magnetic flux density $\boldsymbol{B}$, electric field $\boldsymbol{E}$, etc., are scalar or vector quantities similar to density or momentum. Therefore, field quantities can be defined as the average values of particles, similar to the approach used in Eqs. (8.1) and (8.2). Additionally, while it is challenging to apply the averaging operation to second-order tensor quantities such as stress, this difficulty can be addressed by specifying the normal vector of the acting surface at position $\boldsymbol{x}$. By doing so, stress can be transformed into a force vector through a linear transformation, allowing the average to be defined inversely based on this operation. On the other hand, if the fluid is assumed to behave as an ideal gas, the temperature of the fluid particles can be explicitly defined. This concept is further explored in the next section.

### *8.2.2 Plasma Fluid Temperature*

Temperature can be clearly defined only when the kinetic energy of individual particles follows the Maxwellian velocity distribution. The definition of temperature in non-Maxwellian states is not discussed in this context. For weakly ionized atmospheric nonthermal plasmas, the Maxwellian electron distribution provides a reasonably accurate approximation [9]. It has been confirmed that assuming a Maxwellian electron distribution is sufficient for the fundamental equations governing plasma heat transfer fluids. However, a more comprehensive treatment of non-Maxwellian effects should be considered in future research. In this framework, the electron temperature $T_{\mathrm{e}}$ is defined for electrons, the ion temperature for ions, and the gas

temperature $T_g$ for neutral gas molecules. Since the mass of electrons is significantly smaller than that of heavier particles such as neutral species, ions, and radicals, electron velocities are typically much higher. This results in a nonequilibrium plasma state, where the electron temperature is much greater than the gas temperature ($T_e >> T_g$).

The plasma electron temperature $T_e$ is explained as follows. It is assumed that within the plasma, electrons undergo frequent collisions with heavy particles. Furthermore, if these collisions are considered to be nearly completely elastic, the behavior of the electrons can be approximated using the ideal gas model. Under these conditions, while the electrons exhibit random motion, their overall behavior can be described by the following fundamental law:

$$\begin{aligned} \boldsymbol{u} &= (u_1, u_2, u_3) = \left(u_x, u_y, u_z\right) \\ f(u_i) &= \left(\frac{m_e}{2\pi k T_e}\right)^{\frac{1}{2}} \exp\left(-\frac{m_e u_i^2}{2kT_e}\right) \quad i = 1, 2, 3 \end{aligned} \tag{8.3}$$

$$F(u) = 4\pi \left(\frac{m_e}{2\pi k T_e}\right)^{\frac{3}{2}} u^2 \exp\left(-\frac{m_e u^2}{2kT_e}\right) \tag{8.4}$$

Each component ($u_1$, $u_2$, $u_3$) = ($u_x$, $u_y$, $u_z$) of the particle velocity $\boldsymbol{u}$ follows the probability density function of Eq. (8.3), and the magnitude $u$ follows the cumulative distribution function of Eq. (8.4). Here, electrons are used as an example, but heavy particles can be considered in the same way. Gas molecular kinetic theory is applied to gas molecules. In order to facilitate the demonstration of Eqs. (8.3) and (8.4), variable transformation is performed to introduce $x_i$ and $x_u$.

$$f(x_i) = \frac{1}{\sqrt{\pi}} \exp\left(-x_i^2\right), \quad x_i = \left(\frac{m_e}{2kT_e}\right)^{\frac{1}{2}} u_i \tag{8.5}$$

$$F(x_u) = \frac{4}{\sqrt{\pi}} x_u^2 \exp\left(-x_u^2\right), \quad x_u = \left(\frac{m_e}{2kT_e}\right)^{\frac{1}{2}} u \tag{8.6}$$

Equations (8.5) and (8.6) are illustrated in Fig. 8.1. The distribution of $f(x_i)$ is symmetric, reaching its maximum value at $x_i = 0$. In contrast, the distribution of $F(x_u)$ is asymmetrical, with its peak occurring at $x_u = 1$ and decreasing to zero at $x_u = 0$. Since $u$ represents the magnitude of velocity, it is always positive ($u > 0$), and consequently, $x_u$ is also positive. If the speed of the most probable electron, corresponding to $x_u = 1$, is denoted as $u_p$, then:

$$u_p = \left(\frac{2kT_e}{m_e}\right)^{\frac{1}{2}} \quad \text{or} \quad T_e = \frac{1}{2} m_e u_p^2 \tag{8.7}$$

Equation (8.7) defines the electron temperature.

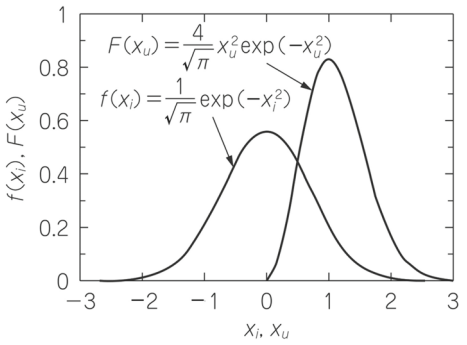


**Fig. 8.1** Shapes of functions $f(x_\mathrm{i})$ and $F(x_u)$

### 8.2.3 Kinetic Energy and Internal Energy

Let $x_\mathrm{C}$ represent the position vector of the center of gravity of the fluid particle under consideration, as illustrated in Fig. 8.2. The position vector of an individual particle i (which may be a heavy particle or an electron) within the fluid particle is denoted as $x_\mathrm{i}$, and the displacement relative to the center of gravity is given by $\Delta x_\mathrm{i}$, defined as the difference between $x_\mathrm{i}$ and $x_\mathrm{C}$. The total kinetic energy $K$ can be decomposed by expressing $x_\mathrm{i}$ as $x_\mathrm{C} + \Delta x_\mathrm{i}$, as follows:

$$K = \sum_{\mathrm{i}=1}^{\mathrm{N}} \frac{m_\mathrm{i}}{2} \left| \frac{\mathrm{d}\boldsymbol{x}_\mathrm{i}}{\mathrm{d}t} \right|^2 = \frac{M}{2} \left| \frac{\mathrm{d}\boldsymbol{x}_\mathrm{C}}{\mathrm{d}t} \right|^2 + \sum_{\mathrm{i}=1}^{N} \frac{m_\mathrm{i}}{2} \left| \frac{\mathrm{d}\Delta\boldsymbol{x}_\mathrm{i}}{\mathrm{d}t} \right|^2 = K_\mathrm{C} + K_\mathrm{M} \tag{8.8}$$

$K_\mathrm{C}$ is the kinetic energy of the center of gravity assumed to bear the total mass, and $K_\mathrm{M}$ is the sum of the kinetic energies around the center of gravity. In other words, $K_\mathrm{C}$ is the energy of the macroscopic motion of fluid particles, $K_\mathrm{M}$ is the energy of the thermal motion of individual particles in it, and the internal energy $U$ in the case

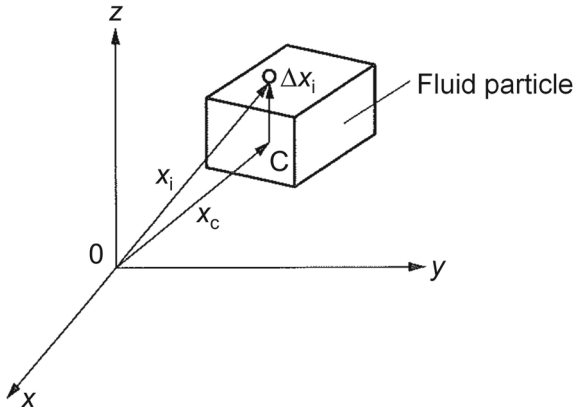


**Fig. 8.2** Position vector $\boldsymbol{x}_\mathrm{C}$ of the center of gravity of fluid particles, position vector $\boldsymbol{x}_\mathrm{i}$ of individual particle i, and the difference between $\boldsymbol{x}_\mathrm{i}$ and $\boldsymbol{x}_\mathrm{C}$, $\Delta\boldsymbol{x}_\mathrm{i}$

of an ideal gas. The relationship between the distribution functions, i.e., Eqs. (8.3) and (8.8), is as follows:

$$U = K_{\mathrm{M}} = \frac{1}{\mathrm{N}} \sum_{\mathrm{i}=1}^{\mathrm{N}} \frac{m_{\mathrm{i}}}{2} \left| \frac{\mathrm{d}\Delta \boldsymbol{x}_{\mathrm{i}}}{\mathrm{d}t} \right|^2 = \int_{\Delta V} \frac{1}{2} mu^2 f(u) \mathrm{d}V \tag{8.9}$$

In the description above, which considers a system of mass points, the kinetic energy relative to the center of gravity and the potential energy of the forces acting on each point are regarded as internal energy. If rotational and vibrational motions are present, all kinetic and potential energies associated with these degrees of freedom must also be included as part of the internal energy. Furthermore, in the case of fluids, incorporating specific enthalpy, defined as $h = U + pV$, in the fundamental equations is useful for accounting for work done by pressure. Even within the framework of continuum mechanics, macro-fluid particles can be defined in a manner analogous to kinetic modeling.

### *8.2.4 Thermal Conduction, Convection, and Radiation*

The fundamental principles of heat transfer, which are incorporated into the basic equations, are discussed. Heat or energy naturally flows from a region of higher temperature to one of lower temperature. This irreversible process is referred to as heat transfer and occurs in three primary forms: thermal conduction, convective heat transfer, and thermal radiation.

#### 8.2.4.1 Thermal Conduction

In solids and fluids (liquids and gases), heat transfer that occurs through direct contact between substances is known as thermal conduction. The amount of heat transferred per unit area per unit time, referred to as heat flux $q$, is directly proportional to the temperature gradient in the direction of heat flow. This relationship is described by Fourier's law.

$$q = -\lambda \nabla T \tag{8.10}$$

The negative sign on the right side indicates that heat is transmitted in the direction of decreasing temperature. The constant of proportionality, $\lambda$, varies with materials and is called thermal conductivity.

#### 8.2.4.2 Heat Transfer

Heat transfer that occurs between a solid surface and a fluid flowing in contact with it is referred to as convective heat transfer. In flowing fluids, conductive heat transfer is closely linked to fluid motion. When fluid flow is driven solely by buoyancy forces resulting from temperature differences, it is known as free convection or natural convection heat transfer. In contrast, when fluid movement is induced by an external force, such as a pump or fan, the process is referred to as forced convection heat transfer.

When examining the temperature distribution of a fluid undergoing convective heat transfer along a wall surface, it is often observed that temperature changes occur rapidly within a relatively thin region near the wall. This effect is particularly pronounced when the fluid velocity is high. This thin region is known as the thermal boundary layer. Beyond this layer, the fluid is considered part of the mainstream flow. For clarity, the subscript w is used to denote the wall surface, while the subscript $\infty$ represents the mainstream flow. The heat flux at the wall surface is generally expressed as a function of the temperature difference between the wall surface and the mainstream flow, and is given by the following equation:

$$q = -h(T_{\mathrm{w}} - T_{\infty}) \tag{8.11}$$

where $h$ is the heat transfer coefficient, which depends on the shape and size of the object, the type of fluid, the cause of flow, and its state.

#### 8.2.4.3 Thermal Radiation

In plasmas, high-temperature gases (such as those generated in pulverized coal combustion) and fluids exchange energy by emitting and absorbing electromagnetic waves. This process is known as thermal radiation. In general, the radiant energy emitted from the surface of an object is proportional to the fourth power of its absolute temperature. In high-temperature plasmas, radiation heat transfer often becomes the dominant mode of energy transfer.

### *8.2.5 Method to Express Inertia Term for Field Quantities*

To formulate an equation for analyzing the volume-averaged behavior of particles as described above, it is necessary to express the state of the flow at a given moment using the position vector $\boldsymbol{x}$ and time $t$ as independent variables. This approach is known as Euler's method. In this representation, the time derivative $\partial A/\partial t$ of a physical quantity $A$ at a specific position $\boldsymbol{x}$ does not correspond to the time variation of $A$ for a single plasma fluid particle. Instead, it represents the time-dependent change observed as different plasma fluid particles successively pass through the position

$\boldsymbol{x}$. In other words, the Eulerian description provides an overview of the entire flow field at each instant rather than tracking the motion of individual fluid particles. Conversely, when $x_0$ represents the position coordinate of a specific volume element at time t, the Lagrangian formulation is used to describe the behavior of the plasma thermal fluid, treating $x_0$ and $t$ as independent variables. The relationship between the Lagrangian time derivative (left-hand side of Eq. (8.12)) and the Eulerian time derivative (right-hand side of Eq. (8.12)) for a given physical quantity $A$ is expressed as follows:

$$\frac{\mathrm{D}A}{\mathrm{D}t} = \frac{\partial \boldsymbol{A}}{\partial t} + (\boldsymbol{u} \cdot \nabla)\boldsymbol{A} \tag{8.12}$$

The Lagrangian time derivative is represented by D/D$t$. In ordinary continuum mechanics texts, the Euler equation, which is suitable for describing field quantities, is used to describe basic equations. We will also adopt this below.

### 8.2.6 Constitutive Equation

The strain tensor, which is the spatial gradient of the displacement vector $\boldsymbol{w}$ and the field quantity, is as follows:

$$\boldsymbol{\varepsilon} = \frac{1}{2}\left[\nabla \boldsymbol{w} + (\nabla \boldsymbol{w})^{\mathrm{T}}\right] \tag{8.13}$$

Among solids, the "elastic body" is defined by a continuum where the internal stress $\boldsymbol{\tau}$ is proportional to $\boldsymbol{\varepsilon}$. This is called Hooke's law of elasticity, and is written in the form.

Elastic body:

$$\boldsymbol{\tau} = \boldsymbol{E} : \boldsymbol{\varepsilon} \tag{8.14}$$

where $\boldsymbol{E}$ is a fourth-order symmetric tensor, written using subscripts, e.g., $E_{\mathrm{ijkl}}$. This is also one of the quantities of fields.

On the other hand, the strain rate tensor, which is the spatial gradient of the velocity field vector $\boldsymbol{u}$, can be given as

$$\boldsymbol{e} = \frac{1}{2}\left[\nabla \boldsymbol{u} + (\nabla \boldsymbol{u})^{\mathrm{T}}\right] \tag{8.15}$$

A "fluid" is defined by a continuum where the internal stress $\boldsymbol{\tau}$ is proportional to $\boldsymbol{e}$. This can be assumed for ordinary fluids such as water, air, and plasma. This is called Newton's law of viscosity and is written in the form:

Fluid (Newton fluid):

$$\boldsymbol{\tau} = \boldsymbol{C}' + \boldsymbol{C} : \boldsymbol{e} \tag{8.16}$$

where $\boldsymbol{C}'$ and $\boldsymbol{C}$ are tensors of the second- and fourth-orders, respectively. It is noted from Eqs. (8.13) and (8.15) that the dimensions of $\boldsymbol{\varepsilon}$ and $\boldsymbol{e}$ differ only by time. In Eq. (8.14) for the elastic body, the stress is $\boldsymbol{\tau} = \boldsymbol{0}$ for $\boldsymbol{\varepsilon} = \boldsymbol{0}$. In other words, no internal stress exists when the strain $\boldsymbol{\varepsilon}$ is $\boldsymbol{0}$. However, in fluids, it becomes a constant value of $\boldsymbol{\tau} = \boldsymbol{C}'$ at $\boldsymbol{e} = 0$. $\boldsymbol{C}'$ is called pressure. From the viewpoint of classical mechanics of the field, fluid mechanics deals with fluids, solid mechanics the theory of elasticity, and the strength of materials deals with solids (elastic bodies). It is noted that the subject of this paper is limited to plasma as a "fluid."

If $\boldsymbol{C}'$ represents the isotropic pressure and the symmetry of $\boldsymbol{e}$, $\boldsymbol{e} = \boldsymbol{e}^{\mathrm{T}}$ is taken into account, and the fluid stress tensor equation of Eq. (8.16) finally becomes

$$\boldsymbol{\tau} = (-p + \chi_{\mathrm{V}}\boldsymbol{e} : \boldsymbol{I})\boldsymbol{I} + 2\mu\left[\boldsymbol{e} - \frac{1}{3}(\boldsymbol{e} : \boldsymbol{I})\boldsymbol{I}\right] \tag{8.17}$$

where $p$ represents the pressure, $x_{\mathrm{V}}$ denotes the volume viscosity (which is approximately zero), $I$ is the unit tensor (equal to δij), and $\mu$ is the viscosity coefficient. This relationship is known as the stress constitutive equation. By substituting this equation into Cauchy's equation of motion of Eq. (8.18), which describes the general motion of a continuum, the equation of motion of Eq. (8.20) can be derived.

$$\frac{\partial(\rho\boldsymbol{u})}{\partial t} + \nabla \cdot (\rho\boldsymbol{u}\boldsymbol{u}) = \boldsymbol{F} + \nabla \cdot \boldsymbol{\tau} \tag{8.18}$$

### 8.2.7 *Fundamental Equations for Plasma Heat Transfer Fluids*

To analyze heat transfer in plasma fluids and their associated dynamics, it is essential to examine the fundamental equations alongside Maxwell's equations, which govern the electromagnetic field. Heat transfer and fluid dynamics are inherently interconnected. However, unlike conventional fluid dynamics, plasma fluid dynamics lacks a fully established set of fundamental equations, and analytical methods in this field are still undergoing development. Building upon previous studies and literature from various researchers [1–29], this section presents a generalized formulation of the fundamental equations for two-temperature nonequilibrium plasmas. These equations have been widely applied in plasma analysis and have been validated through practical evaluations.

Continuity equation (law of conservation of mass):

$$\frac{\partial\rho}{\partial t} + \nabla \cdot (\rho\boldsymbol{u}) = 0 \tag{8.19}$$

Equation of motion (law of conservation of momentum):

$$\frac{\partial(\rho \boldsymbol{u})}{\partial t} + \nabla \cdot (\rho \boldsymbol{u}\boldsymbol{u}) = -\nabla p + \nabla \cdot (\mu \nabla \boldsymbol{u}) + \frac{1}{3}\mu \nabla(\nabla \cdot \boldsymbol{u}) + \boldsymbol{F} \tag{8.20}$$

$$\boldsymbol{F} = \rho_{\mathrm{e}} \boldsymbol{E} + \boldsymbol{J} \times \boldsymbol{B}$$

when electrostatic and Lorentz forces are considered.

Heavy particle energy equation (equation of state and law of conservation of energy):

$$p = \rho R T \tag{8.21}$$

$$\frac{\partial(\rho h)}{\partial t} + \nabla \cdot (\rho \boldsymbol{u} h) = \nabla \cdot (\lambda \nabla T) + \psi_{\mathrm{D}} + S_{\mathrm{c}} + n_{\mathrm{e}} \sum_{\mathrm{k}} \varepsilon_{\mathrm{k}} n_{\mathrm{k}} K_{\mathrm{k}} \tag{8.22}$$

$$\psi_{\mathrm{D}} = 2\mu \left[ \left( \boldsymbol{e} - \frac{1}{3}\boldsymbol{e} : \boldsymbol{I} \right) \boldsymbol{I} \right] : \left[ \left( \boldsymbol{e} - \frac{1}{3}\boldsymbol{e} : \boldsymbol{I} \right) \boldsymbol{I} \right] \tag{8.23}$$

Assuming an ideal gas, $\mathrm{d}h = C_p \, \mathrm{d}T$ strictly holds between specific enthalpy $h$ and heavy particle temperature $T$. Therefore, Eq. (8.22) is expressed using $T$ as follows:

$$C_{\mathrm{p}} \left[ \frac{\partial(\rho T)}{\partial t} + \nabla \cdot (\rho \boldsymbol{u} T) \right] = \nabla \cdot (\lambda \nabla T) + \psi_{\mathrm{D}} + S_{\mathrm{c}} + n_{\mathrm{e}} \sum_{\mathrm{k}} \varepsilon_{\mathrm{k}} n_{\mathrm{k}} K_{\mathrm{k}} \tag{8.24}$$

Chemical species transport equation (species conservation law):

$$\frac{\partial(\rho Y_{\mathrm{i}})}{\partial t} + \nabla \cdot (\rho \boldsymbol{u} Y_{\mathrm{i}}) = \nabla \cdot J_{\mathrm{i}} + M_{\mathrm{i}} \omega_{\mathrm{i}} \tag{8.25}$$

$$J_{\mathrm{i}} = -\rho D_{\mathrm{i}} \nabla Y_{\mathrm{i}} + \rho Y_{\mathrm{i}} u_{\mathrm{di}} + J_{\mathrm{ci}} \tag{8.26}$$

$$\omega_{\mathrm{i}} = \sum_{\mathrm{j}=1}^{\mathrm{N_R}} \left( \nu''_{\mathrm{ij}} - \nu'_{\mathrm{ij}} \right) q_{\mathrm{j}} \tag{8.27}$$

$$q_{\mathrm{j}} = k_{\mathrm{j}} \left( \prod_{\mathrm{m}=1}^{\mathrm{N_s}} c_{\mathrm{m}}^{\nu'_{\mathrm{mj}}} - K_{\mathrm{cj}} \prod_{\mathrm{m}=1}^{\mathrm{N_s}} c_{\mathrm{m}}^{\nu''_{\mathrm{mj}}} \right) \tag{8.28}$$

$$k_{\mathrm{j}} = A_{\mathrm{j}} T_{\mathrm{j}}^{n} \exp\left( -E_{\mathrm{j}} / R T_{\mathrm{j}} \right) \tag{8.29}$$

or

$$k_{\mathrm{j}} = \int \sqrt{T_{\mathrm{e}}} \sigma_{\mathrm{col}}(T_{\mathrm{e}}) f(T_{\mathrm{e}}) \mathrm{d}T_{\mathrm{e}} \tag{8.30}$$

Electron transport equation (conservation law of electron number density):

$$\frac{\partial n_{\mathrm{e}}}{\partial t} + \nabla \cdot \boldsymbol{G}_{\mathrm{e}} = S_{\mathrm{e}} \tag{8.31}$$

$$\boldsymbol{G}_{\mathrm{e}} = \mu_{\mathrm{e}} n_{\mathrm{e}} \nabla \phi - D_{\mathrm{e}} \nabla n_{\mathrm{e}} \tag{8.32}$$

Electron energy equation (electron energy conservation law):

$$\frac{3}{2}\frac{\partial (n_{\mathrm{e}} T_{\mathrm{e}})}{\partial t} + \nabla \cdot \left( \frac{5}{2} T_{\mathrm{e}} \boldsymbol{G}_{\mathrm{e}} - \chi \nabla T_{\mathrm{e}} \right) = \boldsymbol{J} \cdot \boldsymbol{E} - n_{\mathrm{e}} \sum_{\mathrm{k}} n_{\mathrm{k}} K_{\mathrm{k}} - R_a \tag{8.33}$$

Maxwell's equations (electromagnetic field equations):

$$\nabla \times \boldsymbol{H} = \boldsymbol{J} + \frac{\partial \boldsymbol{D}}{\partial t} \tag{8.34}$$

$$\nabla \times \boldsymbol{E} = -\frac{\partial \boldsymbol{B}}{\partial t} \tag{8.35}$$

$$\nabla \cdot \boldsymbol{D} = \rho_{\mathrm{e}}, \quad \boldsymbol{D} = \varepsilon_{\mathrm{r}} \varepsilon_0 \boldsymbol{E} \tag{8.36}$$

$$\nabla \cdot \boldsymbol{B} = 0, \quad \boldsymbol{B} = \mu \boldsymbol{H} \tag{8.37}$$

$$\boldsymbol{J} = \rho_{\mathrm{e}} \boldsymbol{u} + \sigma (\boldsymbol{E} + \boldsymbol{u} \times \boldsymbol{B}) \tag{8.38}$$

Potential $\phi$ is introduced by $\boldsymbol{E} = -\nabla\phi$, and Poisson's equation is obtained from Eq. (8.36).

$$\nabla \cdot (\varepsilon_{\mathrm{r}} \varepsilon_0 \nabla \phi) = -\rho_{\mathrm{e}} \tag{8.39}$$

Furthermore, taking the divergence of both sides of Eq. (8.34) and considering Eq. (8.36), we obtain Eq. (8.40) for the continuity of the current density.

$$\frac{\partial \rho_{\mathrm{e}}}{\partial t} + \nabla \cdot \boldsymbol{J} = 0 \tag{8.40}$$

The symbols that appear in the basic equations are as follows: $t$: time, $\rho$: density, $\boldsymbol{u}$: velocity, $p$: pressure, $\mu$: viscosity coefficient, $R$: gas constant, $T$: absolute temperature, $h$: specific enthalpy, $\lambda$: thermal conductivity $\psi_{\mathrm{D}}$: dissipation energy loss, $S_{\mathrm{c}}$: Chemical reaction heat generation term, $n_{\mathrm{e}}$: electron number density, $\varepsilon_{\mathrm{k}}$: energy loss, $K_{\mathrm{k}}$: equilibrium constant, $n_{\mathrm{k}}$: number density of neutral particles, $C_{\mathrm{p}}$: specific heat at constant pressure, $Y_{\mathrm{i}}$: mass fraction, $J_{\mathrm{i}}$: mass flux, $M_{\mathrm{i}}$: molecular weight, $\omega_{\mathrm{i}}$: molecular formation rate, $D_{\mathrm{i}} = \mu/(\rho Sc)$: diffusion coefficient, $u_{\mathrm{di}}$: drift velocity, $J_{\mathrm{ci}}$: mass flux, $v'_{\mathrm{ij}}$

and $\nu''_{ij}$: forward and reverse equivalence coefficients, respectively, $N_R$: number of chemical reactions, $N_s$: number of chemical species, $c_m$: molar concentration, $K_{cj}$: equilibrium constant, $k_j$: reaction rate coefficient, $T_j$ ($= T_e$ or $T$): absolute temperature of species j, $A_j$, $n$, $E_j$: Coefficients related to chemical reaction for species j, $\sigma_{col}$: collision cross section of species j (function of $T_e$), $f$: electron energy distribution function (Maxwellian distribution), $\boldsymbol{G}_e$: electron density flux vector, $S_e$: chemical reaction, $\mu_e$: electron mobility ($= e/(m_e \nu_e)$, $e$: electron charge, $m_e$: electron mass, $\nu_e$: collision frequency), $D_e$: electron diffusion coefficient ($= \mu_e T_e$), $\phi$: potential, $\chi = 5 n_e D_e/2$: thermal diffusion coefficient, $\boldsymbol{J}$: current density, $\boldsymbol{E}$: electric field, $R_a$: radiation energy loss, $\boldsymbol{H}$: magnetic field, $\boldsymbol{D}$: electric flux density, $\boldsymbol{B}$: magnetic flux density, $\varepsilon_r$: relative permittivity, $\varepsilon_0$: vacuum permittivity, and $\rho_e$: volume charge density.

### 8.2.8 Boundary Conditions

To solve the fundamental equations mentioned above, it is necessary to consider three types of boundary conditions: (1) thermo-hydrodynamic boundary conditions, (2) electromagnetic field boundary conditions, and (3) plasma boundary conditions, which include electron and ion behavior. For thermo-hydrodynamic boundary conditions (1), several conditions may apply, such as zero velocity at the wall surface, a constant velocity gradient, constant temperature, constant heat flux, or free inflow and outflow conditions. For electromagnetic field boundary conditions (2), when a physical quantity such as the electric potential $\phi$ is specified at the boundary or when a boundary exists between two media with different electrical conductivities $\sigma$, certain continuity conditions must be satisfied. Specifically, the normal component of the current density $\boldsymbol{J}$ must be continuous, and the tangential component of the electric field $\boldsymbol{E}$ must also be continuous. Similarly, if an interface exists between two media with different magnetic permeabilities $\mu$, the normal component of the magnetic flux density $\boldsymbol{B}$ must be continuous, and the tangential component of the magnetic field $\boldsymbol{H}$ must also be continuous. For plasma boundary conditions (3), constraints include the conservation of electron number density at the boundary and the conservation of particle number density in surface chemical reactions.

Since boundary conditions must be specified according to the actual system under consideration, it is difficult to establish a single unified framework for describing them. Instead, they will be explained individually in the context of specific analysis examples presented later.

### 8.2.9 Analysis Procedure for the System of Fundamental Equations

The equations governing plasma heat transfer, as described above, are solved in a coupled manner to determine the velocity field, temperature field, concentration distribution, chemical reactions, and electromagnetic field within the plasma. Once these fields are obtained, the amount of heat transfer can be calculated. In this process, a system of partial differential equations must be solved. Both analytical and numerical methods exist for solving these equations. However, when dealing with highly complex scenarios, analytical solutions become impractical. Exact solutions can be derived for specific cases, such as parallel flows in pipes, which correspond to Poiseuille flow, and flows along flat plates, but these solutions are limited to highly simplified conditions. Consequently, for more complex systems, numerical methods are employed, and equations are formulated in a manner that facilitates computational solutions, as discussed in later sections.

## 8.3 Characteristics of Plasma Fluid Heat Transfer

Unlike conventional gas flows, heat transfer in plasma is significantly influenced by charged particles such as ions and electrons. Each term in the governing equations represents a specific contribution to this process. In particular, in atmospheric-pressure plasmas, convective heat transfer plays a much more dominant role compared to low-pressure plasmas. Additionally, heat transfer characteristics can vary depending on whether the plasma exhibits laminar or turbulent flow, as well as whether it behaves as a continuum or a free molecular flow. The specific terms used in the fundamental equations will be explained in detail.

### 8.3.1 Effect on Transport Coefficient

Physical properties, particularly transport coefficients, are strongly influenced by ionization, as they depend on collision processes between particles. For instance, the electrical conductivity $\sigma$ and the Hall coefficient $\beta$ of plasma can be expressed using the following equations based on the charged particle model.

$$\sigma = \frac{e^2 n_e}{m_e \nu_e} \tag{8.41}$$

$$\beta = \frac{eB}{m_e \nu_e} \tag{8.42}$$

where $e$ is the elementary charge of the electron. This collision process is determined by the potential between particles. The potential between charged particles is the Coulomb potential, which is an electrostatic field. Coulomb collisions are very likely to occur, resulting in a small transport coefficient, and the presence of charged particles has a negative effect on transport phenomena. Therefore, the physical property values of plasma do not change monotonously with temperature and have a maximum and minimum.

### *8.3.2 Effect on Thermal Conductivity*

Electrons have a mass of $9.109 \times 10^{-31}$ kg, making them significantly lighter than molecules and atomic ions. Since the speed of thermal motion is inversely proportional to the square root of mass, electrons, having such a small mass, exhibit extremely high velocities. Because transport coefficients are proportional to this thermal velocity, electrons play a crucial role in enhancing transport phenomena, in contrast to the effects of Coulomb collisions described earlier. However, due to their small mass, electrons contribute minimally to momentum transfer, resulting in a negligible effect on the viscosity coefficient. On the other hand, electrons play a significant role in thermal conductivity. Since they carry an equivalent amount of energy as heavier particles while moving at much higher speeds, they facilitate the transfer of a large amount of heat within the plasma.

### *8.3.3 Effects of Ionization and Chemical Reactions*

In plasma, ionization reactions, where neutral particles dissociate into ions and electrons, and recombination reactions, where ions and electrons combine to form neutral particles, continuously take place. Ions and electrons from high-temperature regions diffuse into lower-temperature regions, where they recombine and release ionization energy. In other words, ionization energy is transported through the mutual diffusion of ion–electron pairs and neutral particles. This mechanism plays a significant role in the overall heat transfer process within plasma. A similar phenomenon, where reaction energy is transported via diffusion, can also be observed in heat transfer processes involving reactive fluids, where chemical reactions contribute to energy exchange.

### 8.3.4 Effects of Electromagnetic Fields

The existence of charged particles in plasma indicates that it behaves as a conductive gas, with electrical conductivity comparable to that of metals. As a result, electromagnetic forces exert influence on the plasma, performing work that alters heat transfer characteristics. Additionally, when an electric current flows through the plasma, Joule heating occurs, further contributing to thermal energy generation. In cases where current enters or exits a material, energy transfer takes place, and anisotropic effects emerge. The properties of heat transfer differ significantly between the direction perpendicular to the magnetic field and the direction parallel to it. Consequently, the presence of an electromagnetic field has a substantial impact on the overall heat transfer process in plasma.

### 8.3.5 Effect of Joule Heating

When an electric field is present in plasma, current flows, leading to the generation of Joule heat, which increases the temperature within the plasma field. Furthermore, if there is a potential difference between the plasma and a solid object, such as a container wall or an electrode, current flows between the plasma and the object. In both cases, the electric field influences the amount of current that flows, which in turn affects the amount of heat transfer.

In conventional solid conductors, Joule heat is calculated as the product of resistance and the square of the current. Similarly, plasma, which acts as a gaseous conductor, follows the same principle. At a microscopic level, the mechanism of Joule heating in plasma can be explained as follows: first, charged particles, such as ions and electrons, gain energy from the electric field, leading to an increase in their kinetic energy. This energy is then transferred to neutral gas molecules through collisions. As these collisions occur, the energy is further distributed among surrounding particles. When collisional energy transfer is sufficiently efficient, all particles eventually reach the same energy state, resulting in an equilibrium plasma. In contrast, in a nonequilibrium plasma, the heat transfer process is insufficient, leading to significant acceleration of electrons due to their much lower mass compared to ions and neutral particles. This causes the electron temperature to be much higher than that of the heavier species, maintaining a nonequilibrium state.

The amount of Joule heat generated per unit volume per unit time, denoted as $q_{\mathrm{j}}$, is given by the equation of $q_{\mathrm{j}} = J^2/\sigma = \sigma\, E^2$, where $J$ represents the current density, $\sigma$ is the electrical conductivity, and $E$ is the electric field strength. From this equation, it is evident that Joule heat is transferred to fluid particles via charged particles, primarily electrons.

Additionally, in low-pressure plasmas, where collisions between particles are infrequent, the mean free path is long, and collisional energy transfer is often insufficient for complete thermalization. As a result, the increase in kinetic energy of

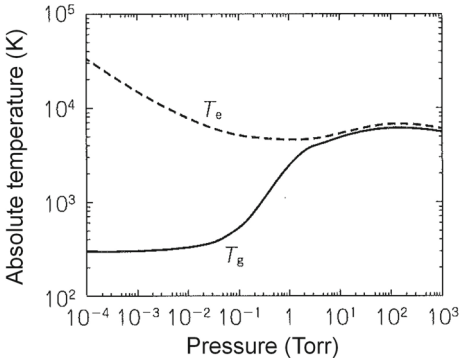


**Fig. 8.3** Relationship between plasma pressure, electron temperature $T_e$, and gas temperature $T_g$ (nonequilibrium plasma, 1 Torr is 133.3 Pa) in DC discharge of mercury and rare gas mixture at different gas pressures and the same current [30]

charged particles does not always lead to a corresponding rise in overall plasma temperature. Figure 8.3 illustrates the relationship between plasma pressure, electron temperature $T_e$, and gas temperature $T_g$. Because electrons transfer only a small amount of energy to heavier particles per collision, the energy gained from the electric field primarily serves to accelerate electrons. This often leads to a nonequilibrium plasma state, where the electron temperature remains significantly higher than the temperature of the gas molecules and ions.

In contrast, in atmospheric pressure plasmas, where collisions between particles occur frequently, an equilibrium plasma state is more likely to be established. However, nonequilibrium plasma with a high electron temperature can still be generated by rapidly accelerating electrons using techniques such as the application of high-voltage pulses at high frequencies between electrodes. This method enables electrons to gain energy efficiently from the electric field while minimizing thermalization with heavier particles. The time-averaged power consumption required for generating such nonequilibrium plasmas is relatively low, making them particularly suitable for applications that leverage their high chemical activity, such as exhaust gas treatment.

### *8.3.6 Meaning of Terms in the Fundamental Equations*

Next, we describe the characteristic terms that appear in the fundamental equations and introduce additional equations. Unlike conventional conservation equations in fluid dynamics, plasma behavior is influenced by electromagnetic effects, including ionization reactions, current flow, and magnetic field generation. As a result, additional terms are incorporated into the basic equations to account for these phenomena.

Equation of motion (8.20):

- $\boldsymbol{J} \times \boldsymbol{B}$: This body force acts perpendicular to both the current and magnetic field, which is the Lorentz force.

- $\rho_e \boldsymbol{E}$: Electrostatic force. If there is a charge density, this body force is exerted by the electric field.

Energy equation of heavy particle (8.21)–(8.24):

- $S_c$: Generation term of chemical reaction heat including ionization reaction.
- $n_e \sum_k \varepsilon_k n_k K_k$ represents the interphase energy transfer from electrons to heavy particles.

Transport equations of chemical species (8.25)–(8.30):

- In Eq. (8.25) for chemical species, not only chemical reactions but also ionization reactions are considered.
- $M_i \omega_i$ generation term. In reactive fluids, the components change due to reactions; thus, the conservation equation for the changing components requires terms for the generation and extinction rates associated with reactions.
- Equations (8.29) and (8.30) regarding ionization reactions are newly introduced.

Transport equations of electrons (8.31) and (8.32):

- These equations are newly introduced to represent the law of conservation of electron generation and vanishing.
- $\nabla \cdot \boldsymbol{G}_e$: Transfer term due to the electric field. This term is necessary in the electron transport equation because the electrons are forced to move by the electric field.
- $S_e$: An electron generation term. This term is required in the electron transport equation.

Energy equation of electrons (8.33):

- Newly introduced as the law of conservation of energy for electrons.
- $P_{elec} = \boldsymbol{J} \cdot \boldsymbol{E}$: Joule heating. When current flows in plasma, Joule heat is generated per unit volume and is given by the product of current density and electric field strength.
- $\nabla \cdot (5/2) T_e \boldsymbol{G}_e$: Electron enthalpy transfer due to current by drift flux model.
- $R_a$: Radiant energy. Plasma is hot and emits electromagnetic waves by several mechanisms. Higher densities and higher temperatures result in greater heat transfer.

### *8.3.7 Boundary Conditions for Current Flow and Heat Transfer*

The heat transfer associated with the inflow and outflow of electric current to and from an object can be evaluated as a boundary condition based on the following mechanism. When ions reach the surface of an object, they capture electrons from the surface and undergo recombination (current inflow), releasing ionization energy. In this process, the energy imparted to the object is determined by subtracting the

energy required to extract electrons (work function) from the total ionization energy. Consequently, the heat transfer rate $q_\mathrm{i}$ per unit time and unit area is given by:

$$q_\mathrm{i} = \frac{J_\mathrm{i}}{e}(E_\mathrm{i} - \phi_\mathrm{w}) \tag{8.43}$$

where $J_\mathrm{i}$ is the ion current density, $e$ is the unit charge, $E_\mathrm{i}$ is the ionization energy, and $\phi_\mathrm{w}$ is the work function. In contrast, when electrons are absorbed by the object (current outflows), an energy corresponding to the work function is transferred to the solid, and the heat flux $q_\mathrm{e}$ is

$$q_\mathrm{e} = \frac{J_\mathrm{e}}{e}\phi \tag{8.44}$$

where $J_\mathrm{e}$ is the electron current density. By analyzing the basic equation system, Eqs. (8.43) and (8.44) can be used to calculate, for example, the transfer of heat due to the inflow and outflow of current from the plasma to the object through the electrode, an example of which will be described later.

## 8.4 Analysis Example of Fundamental Equations Systems

Next, the author describes an analysis of a real system that the author's group performed using the above basic system of equations. We are interested in heat transfer and fluid flow emitted from a glass melting furnace [24], thermal fluid dynamics of streamers in atmospheric pressure plasma flow [25–27], and exhaust gas from semiconductor manufacturing equipment using inductively coupled plasma (ICP). Four example analyses included the heat transfer and pyrolysis of $CF_4$ [28] and the supersonic flow in nonequilibrium magnetohydrodynamic (MHD) generators [29]. From a computational cost perspective, each analysis does not incorporate all terms in the fundamental equations. Instead, approximations are made by neglecting terms that have minimal impact on the overall results. Additionally, the computational approach varies significantly depending on the specific flow and plasma conditions. The numerical methods used for nonequilibrium plasma, thermal equilibrium plasma, supersonic flow, and subsonic flow differ fundamentally, requiring tailored analytical techniques for each case. To provide clarity, each section begins with a self-contained summary, highlighting the key aspects of the analysis and relevant information. Readers seeking further details are encouraged to refer to the corresponding research papers for a more comprehensive explanation.

### 8.4.1 Heat Transfer and Fluid Flow of Emission from Glass Melting Furnace

As a basic example of flow, heat conduction, and convective heat transfer, we consider a heat transfer and fluid flow of emission from glass melting furnace [24].

Figure 8.4 shows a schematic of the glass bottle manufacturing factory system and the dry exhaust gas treatment process. The raw materials of glass such as silica sand, limestone, soda ash, sodium sulfate ($Na_2SO_4$), etc. are melted in a glass melting furnace at approximately 1500 °C using a fossil fuel such as city gas or C-heavy oil. Because of technical issues of glass melting, the furnace cannot be used for city gas firing alone. C-heavy oil is used at a ratio of approximately 1/4–1/3, which results in $SO_x$ generation. In a bottle manufacturing system, the melted glass is transformed into a bottle shape using a mold and then it is slowly cooled for distortion removal. Subsequently, it is used to develop a glass bottle product. However, the exhaust gas emitted by combustion contains air pollutants such as $SO_x$ derived from raw materials and fuels, $NO_x$ generated by high-temperature air combustion, and dust (mainly scattered materials). Therefore, exhaust gas treatment facilities are installed to reduce environmentally hazardous substances. The exhaust gas from the glass melting furnace passes through a thermal storage apparatus and is introduced into a downstream reaction tower called a stabilizer or a reactor. In this reaction tower, an aqueous solution of sodium hydroxide (NaOH) is sprayed, and $SO_x$ in the exhaust gas is removed. The removed $SO_x$ is converted to sodium sulfite ($Na_2SO_3$), which is oxidized and recovered as $Na_2SO_4$ and reused as a glass raw material. The generated fine particles of $Na_2SO_4$ and dust are removed by a dry electrostatic precipitator (EP) and a bag filter (BF), which are located downstream and are used as dust collectors. The dust is transported to the glass melting furnace by a chain conveyor. The cleaned

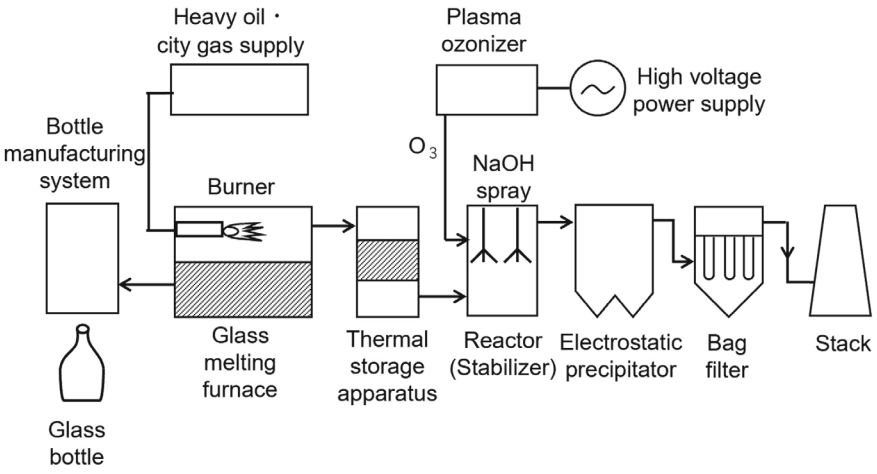


**Fig. 8.4** Schematic of glass bottle manufacturing system and dry exhaust gas treatment system

exhaust gas is discharged from the stack. However, because the exhaust gas contains a large amount of sticky dust produced by raw materials and high-concentration $SO_x$, De-$NO_x$ equipment has not been able to improve. $NO_x$ regulations ($NO_x < 350$ ppm at $O_2 = 15\%$) have been complied with by the reduction of $NO_x$ due to low air ratio combustion at the source side. However, because $NO_x$ reduction in low air ratio combustion is accompanied by a deterioration in fuel efficiency, the demand for energy-saving $NO_x$ reduction technology has increased.

A numerical design was used for the prediction of the system. Numerical simulation was carried out inside the two-phase chemical reaction flow of the stabilizer. Water-cooled $O_3$ is injected before the gas passes through the stabilizer. Figure 8.5 shows the analysis model. The simulated exhaust gas flows from the pipe ($z = 0$ mm) connected to the reactor (stabilizer). Water is then sprayed from a three-fluid nozzle installed at a position of $z = 2050$ mm and a two-fluid nozzle installed at a position of $z = 4050$ mm to form a local cooling area in the reactor. Further, ozone is ejected from the three-fluid nozzle to oxidize NO in the simulated exhaust gas. The treated simulated exhaust gas flows out through the pipe ($z = 14{,}900$ mm) connected to the upper part of the reactor. The gas does not flow out from the bottom of the reactor ($z = -4900$ mm). Heat dissipation and non-slip conditions at wall boundaries are used as boundary conditions. A steady three-dimensional simulation is performed using the finite volume method. CFD-ACE+ was used as the simulation software.

For the calculation of the thermal motion of spraying water droplets, the discrete particle method is simulated in the computational domain by solving the Lagrange equation. For the evaporation model, a water droplet is considered spherical and the temperature distribution inside the droplet is considered uniform without considering the circulation inside the droplet. The equation of motion of the droplet is expressed as follows:

$$m_\mathrm{i}\frac{\mathrm{d}\boldsymbol{v}_\mathrm{i}}{\mathrm{d}t} = C_\mathrm{D}\rho_\mathrm{d}(\boldsymbol{u}-\boldsymbol{v}_\mathrm{i})|\boldsymbol{u}-\boldsymbol{v}_\mathrm{i}|\frac{A_\mathrm{i}}{2} + m_\mathrm{i}\boldsymbol{g} \tag{8.45}$$

where i, $m$, $C_\mathrm{D}$, $\rho_\mathrm{d}$, $\boldsymbol{v}_\mathrm{i}$, and $A_\mathrm{i}$ are the droplet number, droplet mass, drag coefficient, droplet density, droplet velocity, and droplet projection surface area, respectively. The first term on the right side is the drag force that a single water droplet receives from the gas. The reaction force of the drag force, integrated over the number of droplets in one cell in Cartesian coordinates, is the drag force, that the gas receives. When a water droplet moves through gas at a high temperature, the droplet evaporates, and energy is exchanged. The energy equation for a droplet is expressed as follows:

$$m_\mathrm{i}C_\mathrm{p}\frac{\mathrm{d}T_\mathrm{i}}{\mathrm{d}t} = \pi d^2 s - \dot{m}_\mathrm{eva}L \tag{8.46}$$

where $C_\mathrm{p}$, $s$, $d$, $\dot{m}_\mathrm{eva}$, and $L$ are the specific heat of the droplet, sensible heat transferred to the droplet, diameter of the droplet, evaporation rate of the droplet, and latent heat, respectively.

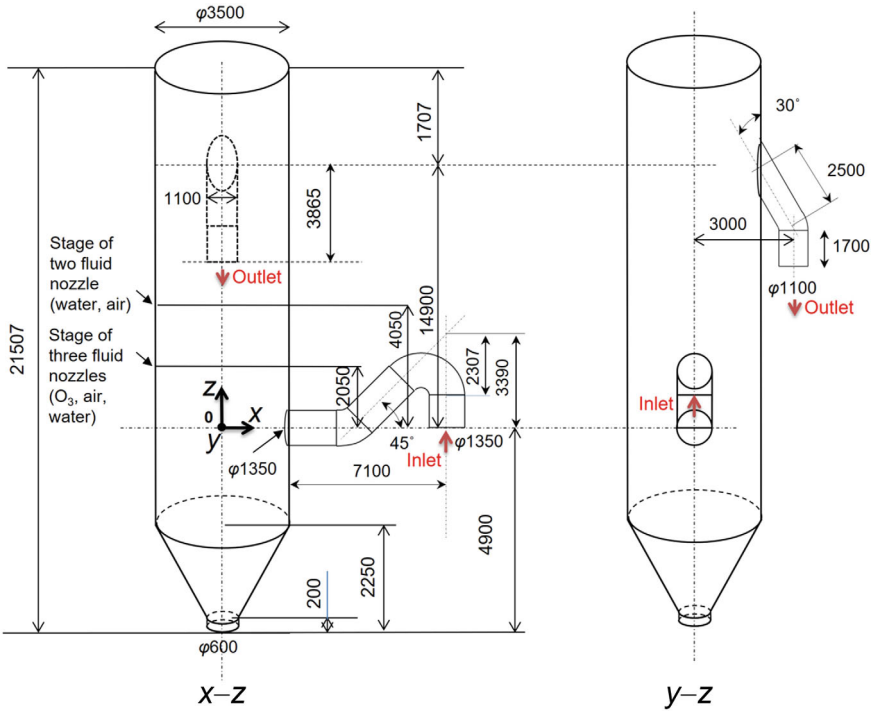


**Fig. 8.5** Three-dimensional analysis model for the stabilizer

The water droplet diameter, $d$, which decreases with evaporation, is expressed as follows:

$$\frac{\mathrm{d}\left(d_0^3 - d^3\right)}{\mathrm{d}t} = \frac{6}{\pi \rho_\mathrm{d}} \dot{m}_\mathrm{eva} \tag{8.47}$$

where subscript 0 denotes the start of the simulation iteration. The gas, density, velocity, temperature, pressure, and concentration of the species are obtained; the droplet trajectory, diameter, velocity, and temperature are obtained using Eqs. (8.45)–(8.47).

Numerical results are shown. Figure 8.6a, b shows the temperature distribution. It is found that the simulated exhaust gas flows in at 488 °C, is cooled by water spray from the three-fluid nozzle and the two-fluid nozzle, and flows out of the outlet at 260 °C. The exhaust gas flows out in a dry state due to the high temperature of 260 °C. At a position of $z = 2050$ mm (where the three fluid nozzles are mounted), a local cooling area is formed, and the simulated exhaust gas is cooled to a minimum temperature of 60 °C. Even at the spray position of $z = 4050$ mm (where the two-fluid nozzles are mounted), a local cooling area is still formed, and the gas is cooled to a minimum temperature of 100 °C. It is also found that the simulated exhaust

gas density increases with the decrease in the temperature so that a cooling region extends to the upstream ($z = 1000$ mm) from the spray position of the first stage.

Figure 8.6c, d shows $v_z$ or $w$ distribution. A strong upward flow near the wall ($x < -1750$ mm) is obtained. This is caused by the flow from the inlet colliding with the wall. The upward flow near the walls are also confirmed. This is due to the large vortex created by the convection of the simulated exhaust gas cooled by the

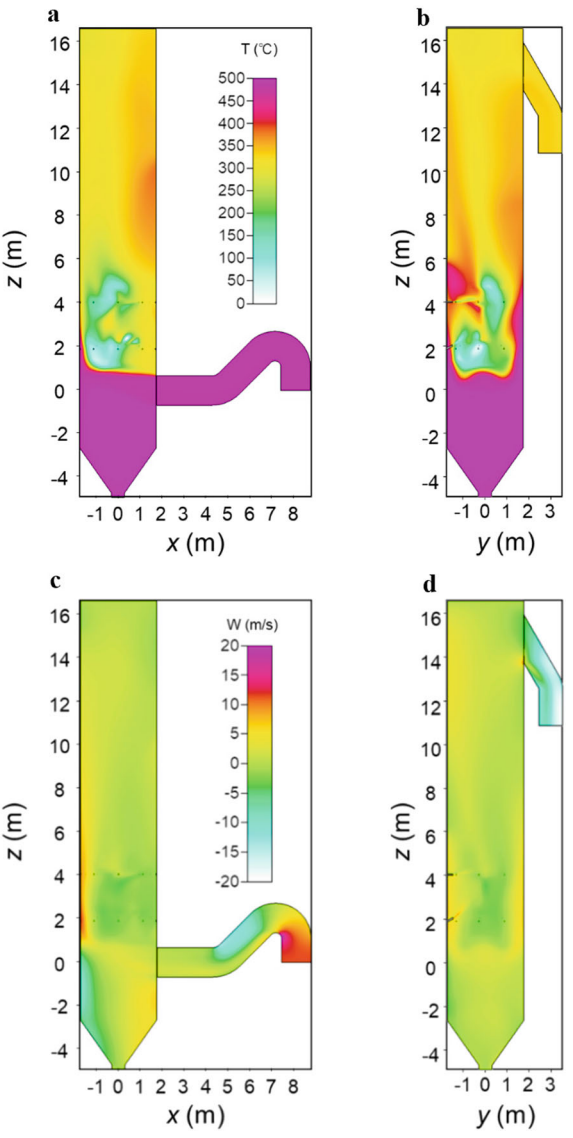


**Fig. 8.6** Temperature distributions of gaseous phase, **a** $x$–$z$ cross section **b** $y$–$z$ cross section, and counter of velocity in the $z$-direction, **c** $x$–$z$ cross section **d** $y$–$z$ cross section

three-fluid and two-fluid nozzles. It is found that $NO_2$ is diffused by the convection field generated by the cooling and advects by the upward flow.

## *8.4.2 Thermo-Fluid Dynamics of Streamers in Atmospheric Pressure Plasma*

Next, as an example of atmospheric nonequilibrium plasma streamer and nonequilibrium heat transfer, we consider environmental cleaning nonthermal plasma (NTP) obtained with nanosecond pulse corona discharge. Such a discharge and plasma reactor are widely used in basic experiments for environmental cleaning, such as those flowing exhaust gas through the reactor to clean it, as shown in Fig. 8.7.

### 8.4.2.1 Numerical Model and Analysis Method

For the analysis, we utilized the CFD-ACE+ software, a widely used computational fluid dynamics (CFD) simulation system specifically designed for analyzing plasma

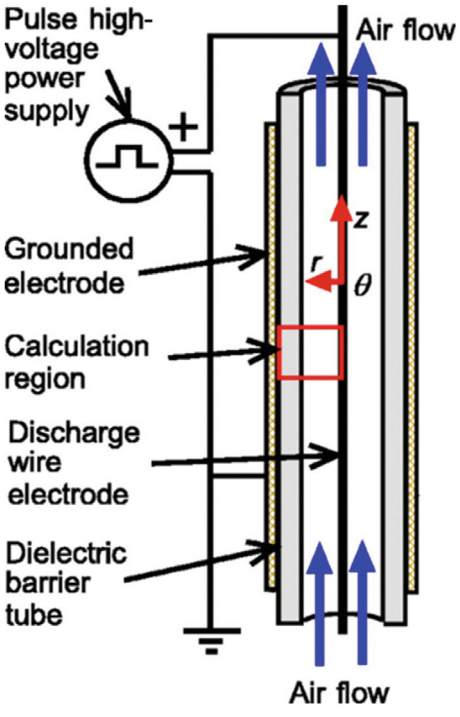


**Fig. 8.7** Model for numerical analysis of the plasma reactor [27]

reaction flows [25–27]. The plasma module within this system has undergone extensive enhancements by numerous researchers, primarily for applications in plasma chemical vapor deposition (CVD). However, its use in environmental protection technologies is a relatively recent development. In this section, we outline the analytical methodology using a two-dimensional modeling approach.

The model used in the numerical analysis conducted in this study is similar to that of a coaxial dielectric barrier-type atmospheric NTP reactor employed in our experimental study; it is shown in Fig. 8.7. It is also used in our experiments on pollution control. This is a coaxial-type plasma reactor that comprises a centered wire electrode (1.5 mm diameter, positive polarity) supported by a perforated polytetrafluoroethylene plate and a quartz glass tube (30 mm inner diameter and 34 mm outer diameter), which is surrounded by a copper mesh grounded electrode. The reactor is energized by a nanosecond-pulse high-voltage power supply.

Figure 8.8 shows the nonuniform computational grids and cells used in the simulation. The reactor is set up so that the $r$-axis is the radial direction of the reactor and the $z$-axis is the axial direction of the high-voltage wire electrode. The total number of cells is 1950 (65 in the $r$-direction and 30 in the $z$-direction). A three-dimensional ($r$, $\theta$, $z$) numerical model is employed, and only the radial $r$-direction is spatially considered to be axisymmetric ($\partial/\partial\theta = 0$). In other words, it is a model in which physical quantities are averaged in the $\theta$-direction, and it is possible to understand the detailed structure of nonuniform streamers in the $z$-direction. In the radial direction, the calculation region encompassed $r = 0.75$–17 mm and is divided into 65 nonuniform cells. The surface of the high-voltage wire electrode is positioned at $r = 0.75$ mm, while the surface of the grounded electrode is placed at $r = 17$ mm. The region corresponding to $r = 15$–17 mm is a dielectric barrier quartz glass. The mesh size is smaller near the high-voltage wire electrode because of larger gradients of physical quantities. In the axial direction, the calculation region encompasses $z = 0$–15 mm and is divided into 30 uniform cells. The plasma is induced in the region corresponding to $r = 0.75$–15 mm.

### 8.4.2.2 Analysis Procedure

A total of 197 gas phase reactions for 25 chemical species (N, $N^+$, $N_2$, $N_2^+$, $N_2(a^1\Sigma_u^+)$, $N_2(A^3\Sigma_u^+)$, $N_2(B^3\Pi_g)$, $N_2(X^3\Pi_u)$, $N_3^+$, $N_4^+$, O, $O(^1D)$, $O(^1S)$, $O^+$, $O^-$, $O_2$, $O_2$**, $O_2(a^1\Delta)$, $O_2(b^1\Sigma)$, $O_2^+$, $O_2^-$, $O_2(v)$, $O_3$, $O_3^-$, and $O_4^+$) and 21 surface reactions on the inner glass wall surface are analyzed in an air plasma under atmospheric pressure on the basis of the results presented in previous studies [9, 25, 31, 32]. The values of the electron collision cross-section for the momentum transfer of ozone, used for the ozone formation reaction are improved. The chemical model and many reaction rates used are provided as supplementary material provided by Ref. [27]. All calculation conditions and boundary conditions are determined based on experimental conditions.

Figure 8.9 shows the pulse voltage waveform applied to the reactor. The waveform is approximated as a sinusoidal function with a peak-to-peak voltage of 34 kV and a

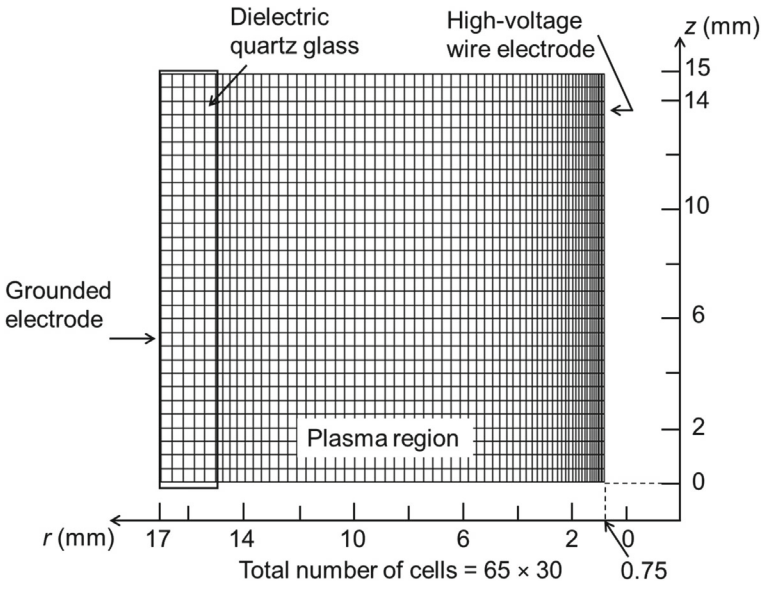


**Fig. 8.8** Computational grids and cells [27]

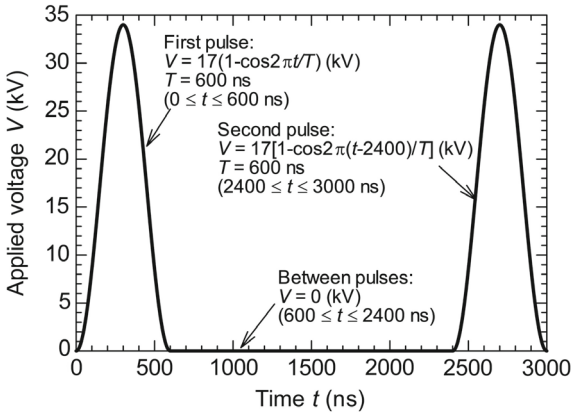


**Fig. 8.9** Waveform of the nanosecond-pulse applied voltage [27]

period of 600 ns; these values were determined by experiments. The use of a pulsed voltage with a very short rise time (~ 100 ns) and short duration (~ 1 ms) is known to be useful for efficient gas cleaning. The calculations in this study consider the effects of the high-speed rise of the applied voltage and multiple streamer propagation. At the interface between the plasma and dielectric barrier (i.e., the quartz glass region), the following conditions are used to solve Poisson equation (8.39):

$$[\varepsilon_r \varepsilon_0 (\nabla \phi)_n] = \sigma_S \tag{8.48}$$

$$[(\nabla\phi)_t] = 0 \tag{8.49}$$

where the square parentheses indicate the difference at the interface, $(\nabla\phi)_n$ and $(\nabla\phi)_t$ are normal and tangential components of the electric field, respectively, and σs is used for the surface charge density.

The system of governing equations is simultaneously solved by the CFD-ACE+ solver. The fluid, heat, and species transport equations of Eqs. (8.19–8.30) are solved using the time-implicit SIMPLEC method [33]. A Sharfetter–Gummel (exponential) scheme is used for the plasma analysis of Eqs. (8.31–8.33) [30]. An implicit Poisson equation solver is used for electrical potential analysis of Eq. (8.39).

The initial conditions are set as follows: temperature $T = 300$ K, electron temperature $T_e = 0.2$ eV under quasi-neutrality condition, uniform electron number density $n_e = 8 \times 10^8$ m$^{-3}$, electric potential $\phi = 0$, and $N_2$: $O_2 = 79$: 21. The viscosity is calculated from Sutherland's law. The Schmidt and Prandtl numbers are set as 0.7 and 0.707, respectively. The thermal conductivity, specific heat, and relative dielectric constant εr of the quartz dielectric barrier are set as 2.0 W/(m K), 1000 J/(kg K), and 3.5, respectively. The electric field in the tangential direction $E_t$ and electric flux in the normal direction $D_n$ are continuous at the interface. The external load $C$ is set as $1 \times 10^{-8}$ F/m.

The biggest problem in unsteady calculations of plasma flow is the huge difference between the time constants of plasma and fluid changes. In the unsteady calculation of the plasma flow, the first-order Euler implicit scheme is adopted. In general, plasma flows require a small time step because the discharge process proceeds rapidly. In our calculations, we set $\Delta t = 3 \times 10^{-12}$ s = 3 ps. When $\Delta t$ exceeds this value, the calculation diverges. The total number of time steps and final time are 1,000,000 and 3000 ns, respectively. In this case, the plasma was simulated until the end of the second pulse of the applied voltage using a personal computer (CPU: Intel(R) Core(TM) i9-9980HK@2.40 GHz, 8 core/12 thread, RAM: 64.0 GB, Precision 5540 Workstation, Dell Technologies Japan Inc.). It takes approximately 28 days (672 h) to obtain the simulation results up to the end of the second pulse. The characteristics of the streamer group in the second pulse and the chemical reactions that occur between pulses are clarified. Although domain decomposition and adaptive mesh are possible in the plasma simulation [34], they are not carried out in the present study. The inflow condition is that a laminar flow with a parabolic velocity distribution at a temperature of 300 K is introduced at 5 L/min. The viscosity coefficient is calculated using Sutherland's law, with Schmidt and Prandtl numbers of 0.7 and 0.707, respectively. The thermal conductivity, specific heat, and dielectric constant of the quartz dielectric barrier are set to 2.0 W/(m K), 1000 J/(kg K), and 3.5, respectively.

#### 8.4.2.3 Calculation Results and Discussion

Figure 8.10 shows an example of the time-dependent distribution of the electron number density ne in the streamer propagation simulation. Figure 8.10a shows the

results from $t = 72$ to 600 ns for the first pulse. Both primary and secondary streamer generations can be observed. After the voltage increases on the discharge electrode, primary streamers are formed, and the length of the streamer develops to approximately 6 mm at $t = 264$ ns. However, the lengths of all streamers decrease near the peak voltage, from 264 to 408 ns. After 408 ns, secondary streamers begin to appear, with six secondary streamers observed at 456 ns, subsequently shortened at the end of the first pulse. Inside the primary streamer, the maximum of ne reaches $9.6 \times 10^{18}$ m$^{-3}$ at $t = 300$ ns. Given that a dielectric barrier wall exists in the reactor, the calculated value of ne is lower than those without barriers. The presence of the barrier wall makes the diameter of streamers larger and, as a result, nonuniform plasma may emerge. All secondary streamers are induced in the same channel in which the primary streamers are generated, similar to the experiments described in an experimental study [35], where the secondary streamers are always induced in the same paths as those of the primary streamers. The secondary streamers appear and disappear repeatedly, traveling only part of the distance (1–6 mm) to the wall, in the radial $r$-direction. Moreover, the secondary streamers seem to stay always attached to the positive discharge electrode, which is consistent with experimental observations [35].

Figure 8.10b shows the status of ne between the first and second pulses. Streamers remain from $t = 750$ to 2400 ns, although no voltage is applied. In addition, the value of $n_e$ increases until $t = 1800$ ns; subsequently, it decreases. The length of streamers changes because of the changing $n_e$. During this period from $t = 750$ to 1800 ns, electron generation is considered to be dominated by the following chemical reactions:

$$O^- + O \rightarrow O_2 + e \tag{8.50}$$

$$O^- + O_2 \rightarrow O_3 + e \tag{8.51}$$

$$O_2^- + O \rightarrow O_3 + e \tag{8.52}$$

$$O_3^- + O \rightarrow 2O_2 + e \tag{8.53}$$

The following is an explanation of the increase in $n_e$. Between 750 and 1800 ns, the rate constants for chemical reactions (8.50)–(8.53) are higher than $10^{-7}$ kmol/m$^3$/s, while the rate constants for the other 193 chemical reactions considered are less than $10^{-10}$ kmol/m$^3$/s; therefore, these reactions significantly contribute to electron generation, and $n_e$ increases over this period.

Figure 8.10b also shows that ne decreases between 1800 and 2400 ns because electrons are consumed according to the following chemical reactions:

$$e + N_4^+ \rightarrow 2N_2 \tag{8.54}$$

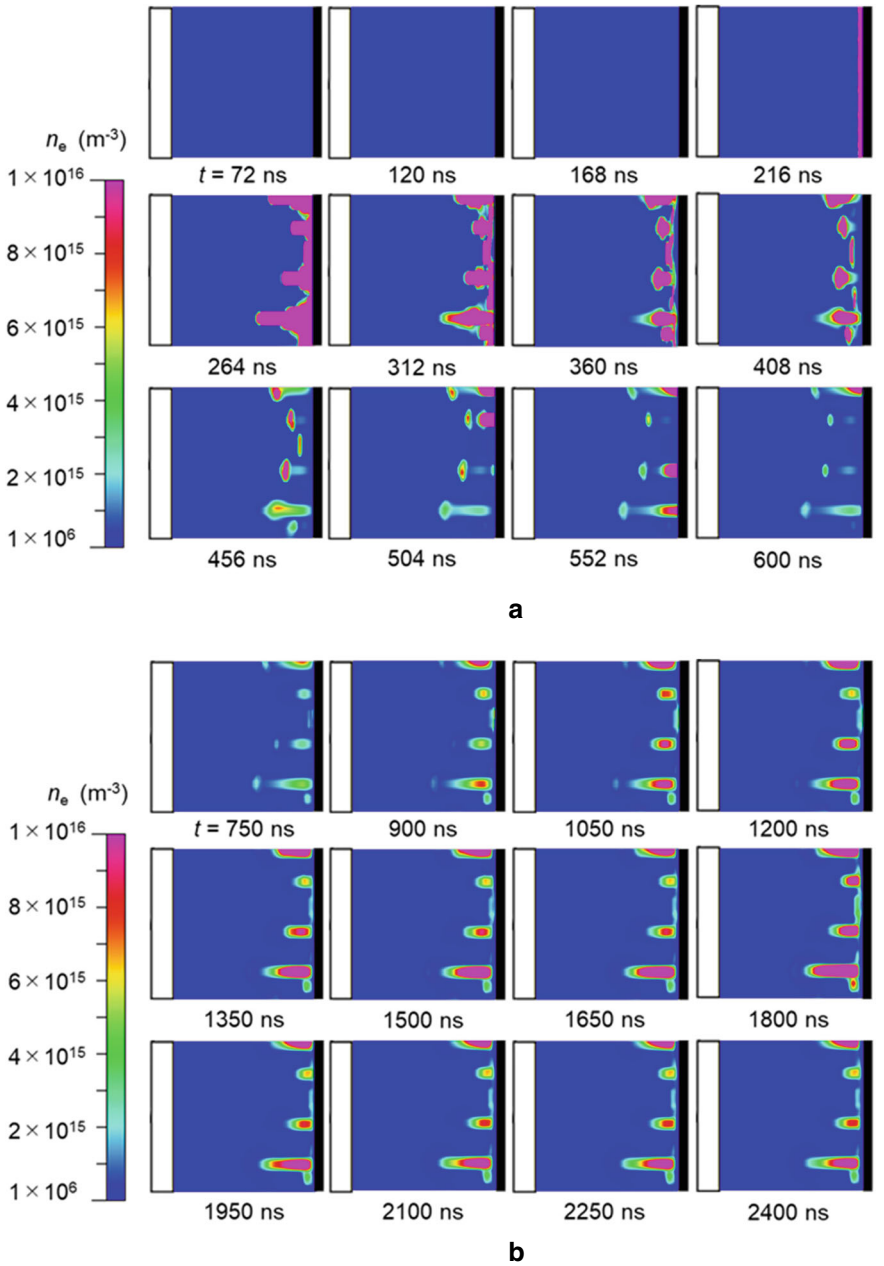


**Fig. 8.10** Time-dependent $n_e$ distributions in the simulation: **a** $t = 72$–$600$ ns during the first pulse, **b** $t = 750$–$2400$ ns between the pulses, and **c** $t = 2472$–$3000$ ns during the second pulse [27]

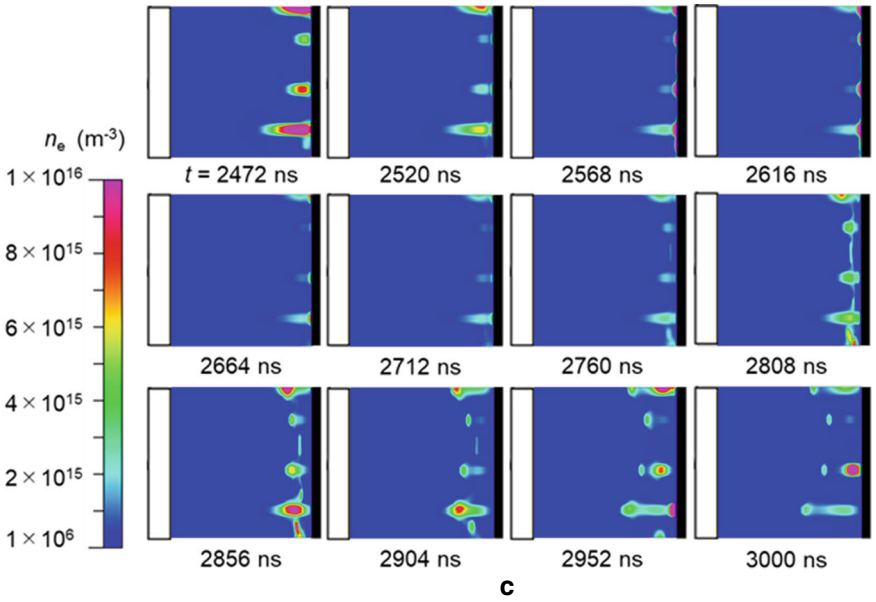


**Fig. 8.10** (continued)

$$e + O_4^+ \rightarrow 2O_2 \tag{8.55}$$

The following is an explanation of the decrease in $n_e$. The rate constants for chemical reactions (8.50)–(8.53) decrease from $10^{-5}$ to $10^{-7}$ kmol/m$^3$/s between 750 and 2400 ns; therefore, the rate of electron production by chemical reactions (8.50)–(8.53) decreases. The decrease in the concentrations of $O^-$, $O_2^-$, and $O_3^-$ between 750 and 2400 ns also contributes to the decrease in the rate of electron production. Moreover, the rate constants for chemical reactions (8.54) and (8.55) are higher than $10^{-6}$ kmol/m$^3$/s between 1800 and 2400 ns. These results show that electron consumption exceeds production and consequently $n_e$ decreases between 1800 and 2400 ns. It seems that the plasma channels formed by streamers during voltage pulses are preserved or frozen in the time intervals between pulses. However, the lengths of streamers change; therefore, they are unsteady and not completely frozen.

Figure 8.10c shows the status of $n_e$ for the second pulse from $t = 2472$ to 3000 ns. The value of ne decreases from the start of the second pulse until $t = 2700$ ns at the peak voltage. Given that the electrostatic charge is built up inside the plasma reactor after the first pulse, there is scarce formation of apparent primary streamer and few streamers. After $t = 2712$ ns, streamers are apparent again; six short streamers exist at 2856 ns. Almost all streamers are induced in the same channel as that in which the primary streamers are generated in the first pulse. The streamers appear and disappear repeatedly, traveling only part of the distance (1–3 mm) to the wall in the

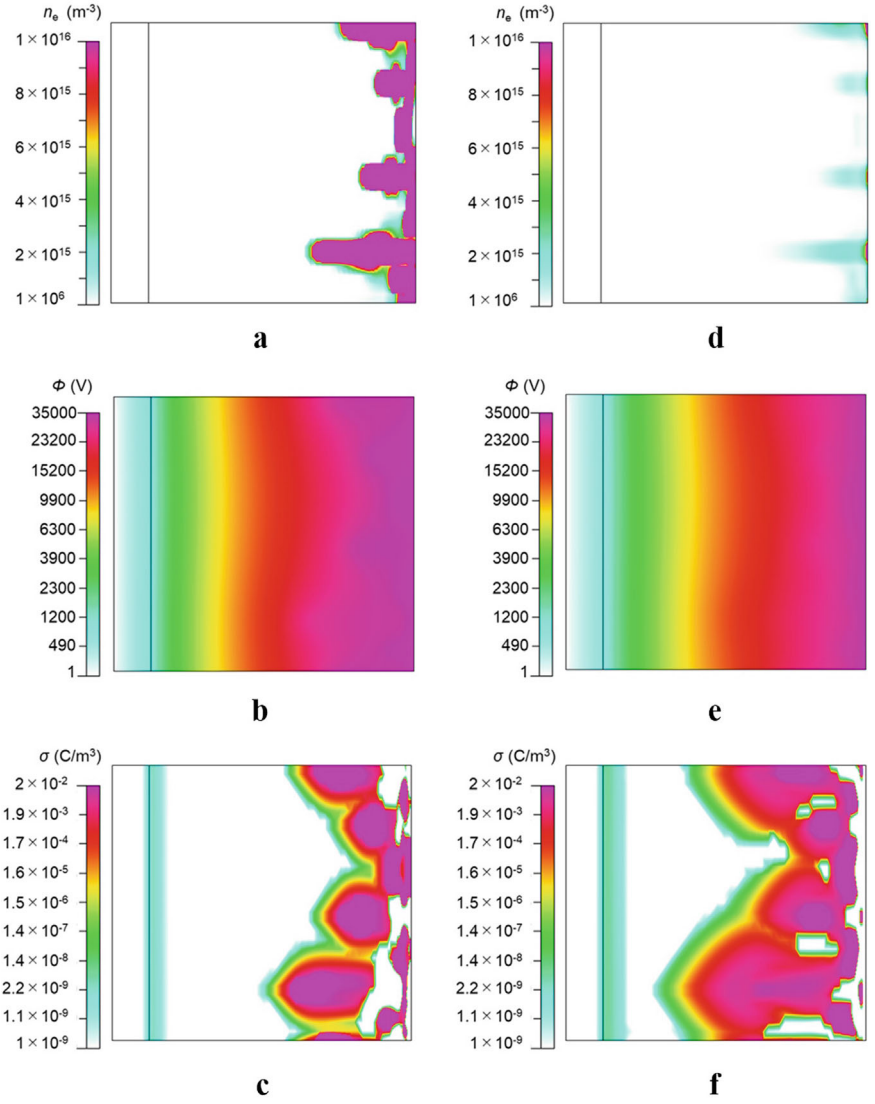


**Fig. 8.11** Time-dependent $n_e$, electronic potential $\phi$, and space-charge $r$ distributions in the simulation: **a–c** $n_e$, $\phi$, and $\sigma$ at $t = 300$ ns, **d–f** $n_e$, $\phi$, and $\sigma$ at $t = 2700$ ns [27]

radial $r$-direction. Moreover, the streamers always remain attached to the positive discharge electrode. However, the maximum value of ne for the second pulse reaches $7.0 \times 10^{17}$ m$^{-3}$ in the whole region, decreasing the value of ne from the first pulse. In addition, the length of streamers is also shorter. Note that photoionization is not considered in the present CFD-ACE+ system; it should be addressed in future work. The weak propagation of the streamer could be due to the lack of photoionization.

Figure 8.11 shows the detailed instantaneous distributions of $n_e$, electronic potential $\phi$, and space charge $\sigma$ during the first and second pulses. Details of the electrostatic charge build-up are provided in the figure. Figure 8.11a–c show the values of $n_e$, $\phi$, and $\sigma$ at 300 ns, which correspond to the moment of the peak voltage in the first pulse. Figure 8.11d–f show the values of $n_e$, $\phi$, and $\sigma$ at 2700 ns, corresponding to the peak voltage in the second pulse. Figure 8.11a, d show that the streamers seem to become suppressed during the second pulse, as opposed to the first pulse. In Fig. 8.11b, which depicts the instantaneous electrical potential $\phi$ at 300 ns, the gradient of electrical potential, i.e., the electric field strength, is 24.2 kV/cm at $r =$ 10 mm. However, in Fig. 8.11e, which shows the instantaneous electrical potential $\phi$ at 2700 ns, the gradient or the electric field strength is 20.1 kV/cm at $r = 10$ mm. Therefore, the electric field strength in the second pulse is 4 kV/cm lower than that in the first pulse owing to the space charge build-up, causing streamers in the second pulse to be suppressed and $n_e$ to be reduced. The suppressed growth of streamers can be also observed in Fig. 8.11c, f. It is known from these figures that more space charge $\sigma$ accumulates at 2700 ns than at 300 ns. In particular, $\sigma$ on the dielectric surface ($r = 15$ mm) is $3.3 \times 10^{-9}$ C/m$^3$ at 2700 ns in Fig. 8.11f, which is 1.8 times higher than $\sigma = 1.8 \times 10^{-9}$ C/m$^3$ at 300 ns in Fig. 8.11c. The difference, $\Delta\sigma = 1.5 \times 10^{-9}$ C/m$^3$, corresponds to a gradient equal to 0.12 kV/cm. Therefore, we conclude that the decrease in the electrical field gradient due to the space and surface charge build-up causes the suppression of the streamer evolution in the second pulse. This could be the first result obtained from a simulation of the charge build-up for a pulse-corona-induced NTP. Even if the streamer originating from the wire does not reach the barrier electrode, the surface charge is accumulated on the barrier because space charge exists near the dielectric. Neutral particles and space charges are also present in the plasma, causing field reduction. Quasi-neutrality in the plasma is not completely realized in a DC pulse corona discharge.

### 8.4.3 *Heat Transfer and Decomposition of $CF_4$ from Semiconductor Manufacturing*

One notable example of heat transfer mechanisms involving both conduction and convection through plasma is observed in the thermal decomposition process of exhaust gases from semiconductor manufacturing equipment. Specifically, this section examines the heat transfer characteristics and the decomposition of carbon tetrafluoride ($CF_4$) using inductively coupled plasma (ICP) technology [28].

$CF_4$ is a perfluorocarbon (PFC) widely used in semiconductor etching and cleaning processes due to its chemical stability and inert properties. However, $CF_4$ is a potent greenhouse gas with an extremely high global warming potential (GWP), approximately 7390 times that of $CO_2$ over a 100-year time horizon. Because of its long atmospheric lifetime—estimated to be around 50,000 years—its accumulation in the atmosphere poses a significant environmental challenge. Consequently,

effective decomposition methods are necessary to mitigate its environmental impact before it is released into the atmosphere.

In this study, ICP is employed as a highly efficient plasma-based method to facilitate the decomposition of $CF_4$ into less harmful byproducts. The fundamental principle behind this approach lies in the interaction between high-energy electrons in the plasma and $CF_4$ molecules, which leads to molecular dissociation through various reaction pathways. The thermal energy generated from ICP is transferred via conduction and convection from the plasma to the surrounding gas, ensuring sufficient activation energy for the dissociation of $CF_4$.

The decomposition process primarily involves breaking the C–F bonds in $CF_4$ molecules, which requires a high energy input due to their strong bond dissociation energy (~ 515 kJ/mol). The dissociation reactions in the plasma environment proceed as follows:

$$CF_4 \rightarrow CF_3 + F \tag{8.56}$$

$$CF_3 \rightarrow CF_2 + F \tag{8.57}$$

$$CF_2 \rightarrow CF + F \tag{8.58}$$

$$CF + O_2 \rightarrow CO_2 + F \tag{8.59}$$

$$F + H_2O \rightarrow HF + OH \tag{8.60}$$

Through controlled plasma conditions, $CF_4$ is ultimately converted into carbon dioxide ($CO_2$) and hydrogen fluoride (HF), both of which are far less environmentally persistent than $CF_4$ itself. The process is optimized by adjusting the plasma power, gas residence time, and the presence of oxidizing agents such as $O_2$ or $H_2O$, which enhance the reaction efficiency.

Given the severe environmental impact of $CF_4$ emissions, its decomposition before release into the atmosphere is a crucial step toward achieving sustainable semiconductor manufacturing practices. The use of ICP-based plasma treatment offers a promising pathway to effectively reduce $CF_4$ emissions and minimize its contribution to climate change.

#### 8.4.3.1 Analytical Model and Boundary Conditions

Figure 8.12 illustrates the computational domain used for the analysis. The reactor dimensions were chosen to match those used in our experimental setup to ensure consistency between simulations and practical observations.

In this system, a gas mixture containing carbon tetrafluoride ($CF_4$) and oxygen ($O_2$) flows through the reactor, where a high-frequency current of 2 MHz is applied

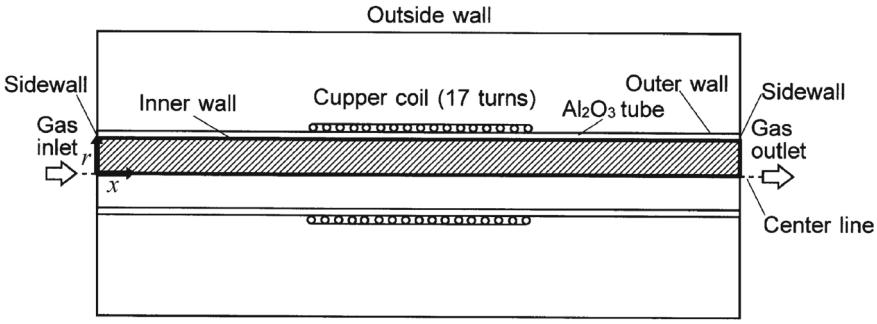


**Fig. 8.12** Computational domain for analysis of $CF_4$ decomposition [28]

to the coil. This induces plasma generation within the tube, providing the necessary energy to break down $CF_4$ molecules. Through this process, $CF_4$ undergoes decomposition, facilitated by the high-energy electrons and reactive species present in the plasma environment. For the basic equations, we derive and use stationary equations obtained by time-averaging physical quantities with nonstationary terms set to 0.

In addition, assuming an axisymmetric two-dimensional flow in a cylindrical coordinate system $(r, \theta, x)$, setting the velocity vector $\boldsymbol{u} = (u_r, 0, u_x)$ and the gas component mass fraction $Y_i$, the vector potential $\boldsymbol{A}$ of the magnetic flux density $\boldsymbol{B}$ is introduced by $\boldsymbol{B} = \nabla \times \boldsymbol{A}$, and the boundary conditions are given as follows:

- Inlet boundary condition (gas inlet):

$$u_r = \text{given},\ u_x = 0,\ p = p_0,\ T = T_0,\ Y_i = \text{given},\ \partial \boldsymbol{A}/\partial x = \boldsymbol{0} \tag{8.61}$$

  where $u_r$ is calculated from the mass flow rate given by computational conditions.
- Outlet boundary condition (gas outlet)

$$\partial u_r/\partial x = \partial u_x/\partial x = 0,\ p = p_0,\ \partial Y_i/\partial x = 0,\ \partial \boldsymbol{A}/\partial x = \boldsymbol{0} \tag{8.62}$$

- Conditions for the centerline of the reactor:

$$\partial u_r/\partial r = 0,\ u_x = 0,\ \partial T/\partial r = 0,\ \partial Y_i/\partial r = 0,\ \boldsymbol{A} = \boldsymbol{0} \tag{8.63}$$

- Inner wall boundary condition:

$$u_r = u_x = 0,\ \partial T/\partial r = 0 \tag{8.64}$$

- Outer wall boundary condition:

$$u_r = u_x = 0,\ \partial Y_i/\partial r = 0 \tag{8.65}$$

- Sidewall boundary condition:

**Table 8.1** Computational conditions used for numerical simulation ($CF_4$ decomposition) [28]

| | | |
|---|---|---|
| AC voltage frequency (MHz) | 2 | |
| Atmospheric temperature (K) | 293 | |
| Absolute pressure (Pa) | 80 | |
| Power (kW) | 2.0 | |
| Mass flow rate of gas (g/s) | 0.02107 | |
| Initial mass fraction of species | $CF_4$ | 0.5789 |
| | $O_2$ | 0.42105 |

$$u_r = u_x = 0,\ \partial T/\partial x = 0,\ Y_\mathrm{i} = 0,\ \partial \boldsymbol{A}/\partial x = \boldsymbol{0} \tag{8.66}$$

- Horizontal wall boundary condition:

$$u_r = u_x = 0,\ T = T_0,\ Y_\mathrm{i} = 0,\ \partial \boldsymbol{A}/\partial r = \boldsymbol{0},\ T_\mathrm{e} = 0 \tag{8.67}$$

- Vertical wall boundary condition:

$$u_r = u_x = 0,\ T = T_0,\ Y_\mathrm{i} = 0,\ \partial \boldsymbol{A}/\partial x = \boldsymbol{0},\ T_\mathrm{e} = 0 \tag{8.68}$$

#### 8.4.3.2 Computational Conditions

Table 8.1 shows the computational conditions for the numerical simulation. The AC current frequency, pressure, and power are the same as the experimental conditions. The mass flow rate and initial chemical species compositions are calculated from the $CF_4$ and $O_2$ flow rates. It is assumed that both inlet and outlet temperatures are equal to ambient temperature. The viscosity is obtained from Sutherland's Law. Thermal conductivity is selected with 3 W/(m K) for obtaining and stabilizing the calculation. Schmidt number is selected at 0.7. The gas temperature, electron temperature, electron number density, gas velocity, and chemical species number density are simulated by using CFD-ACE+ which employs the SIMPLEC method.

#### 8.4.3.3 Results and Discussion

Figure 8.13 shows the gas temperature distribution of the ICP reactor. As shown in this figure, the gas temperature is shifted slightly downstream of the plasma reactor and reaches 575 K. Because the thermal conductivity used in this simulation of 3 W/(m K) is two orders of magnitude higher than the actual situation, maximum gas temperature becomes lower as expected, and the gas temperature distribution is diffused in the computational domain.

Figure 8.14 shows the electron temperature distribution in the ICP reactor. The electron temperature increases as it moves out toward the inner wall from the centerline of the reactor. This is attributed to the skin effect, which is the tendency of

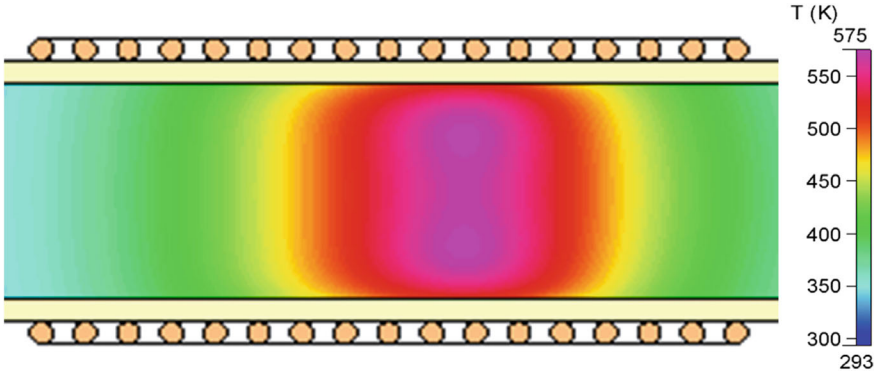


**Fig. 8.13** Gas temperature distribution inside the reactor [28]

an alternating electric current to distribute itself within a conductor so that the current density near the surface of the conductor becomes greater than that at its core, due to RF plasma operation. The electron temperature became 1.33 eV near the wall. Although C–F bond dissociation energy is approximately 5 eV, the $CF_4$ decomposition occurred, because the electron temperature of approximately 6% electron exceeded C–F dissociation energy based on the assumption of Boltzmann distribution.

Figure 8.15 shows the electron number density distribution in the ICP reactor, which is strongly correlated to the electron temperature. The maximum electron number density is located between the inner wall and the centerline, where a ring-shape distribution is formed.

According to these figures, the distributions of electron number density and electron temperature differ significantly from that of the gas temperature, indicating a

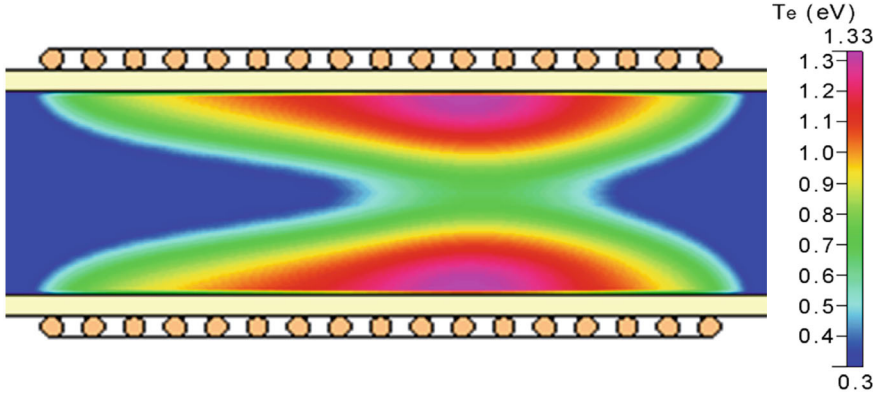


**Fig. 8.14** Electron temperature distribution inside the reactor [28]

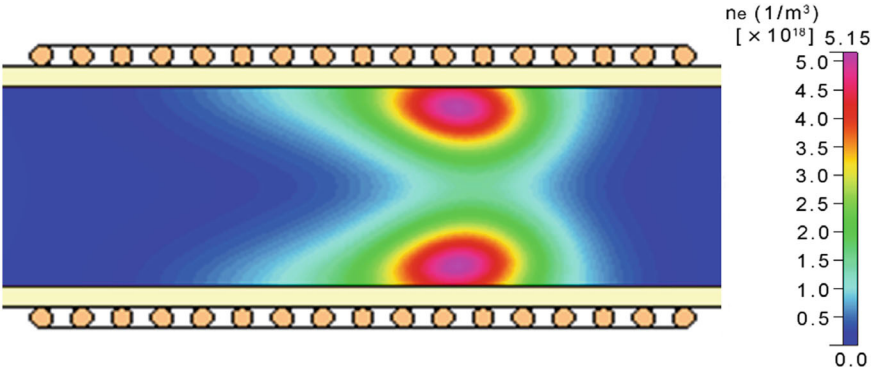


**Fig. 8.15** Electron number density distribution inside the reactor [28]

strong nonequilibrium state. One possible explanation for this discrepancy is the cooling effect near the reactor tube wall, which reduces the gas temperature locally.

Figure 8.16 presents the distribution of $CF_4$ number density throughout the reactor. The results show that $CF_4$ undergoes decomposition in the downstream region; however, partial recombination occurs near the reactor exit. Due to the complexity of the system under investigation, fully quantifying the advantages of the methods employed remains challenging. For a more in-depth discussion of the results, please refer to the original study [28].

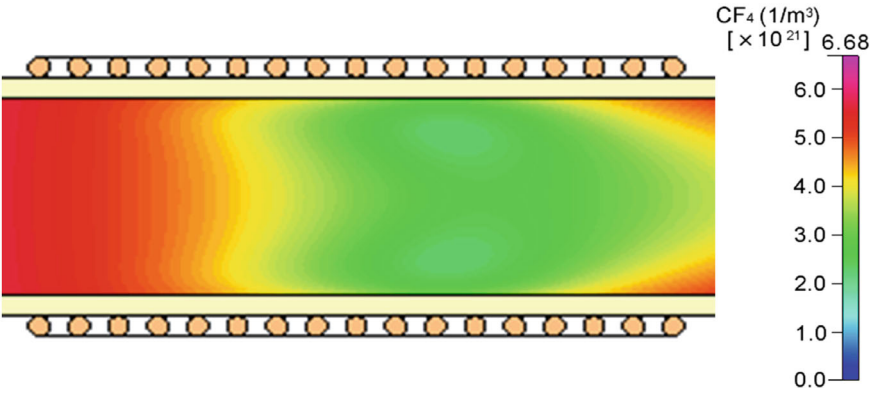


**Fig. 8.16** Distribution of $CF_4$ number density inside the reactor [28]

### 8.4.4 *Thermo-Fluid Analysis in Nonequilibrium Plasma MHD Generator*

As another example of heat conduction and convective heat transfer through plasmas, the analysis of a disk-shaped MHD generator plasma driven by a shock tube is considered [29]. Argon heated to a high temperature (approximately 2350 K) by a shock tube is passed as a supersonic flow through the flow path of a disk-type MHD generator. A small amount of cesium, which is easily ionized in the flow path, is added as a seed to form a cesium–argon plasma. A strong magnetic field is applied perpendicular to the flow, and a resistance load is connected to the electrodes installed in the flow direction of the flow channel to extract Hall current and generate power.

#### 8.4.4.1 Model for Analysis

Figure 8.17 shows an analytical model of a disk-type MHD generator. This model is a simulation of the experimental device used in the authors' experiments. The generator is divided into three parts: the nozzle section up to $r = 110$ mm, the MHD channel from $r = 110$ mm to $r = 270$ mm, and the diffuser beyond $r = 270$ mm. The inflowing high-temperature gas (approx. 2350 K) passes through the throat at the position of radius $r = 75$ mm and becomes supersonic, and Hall current and Faraday current are induced by the magnetic field (2.7 T) applied in the $z$-direction, and the current rapidly ionizes the gas in the nozzle, resulting in a nonequilibrium state. Power is generated in the MHD channel section by the nonequilibrium plasma with high electrical conductivity. The electromotive force is extracted by the load

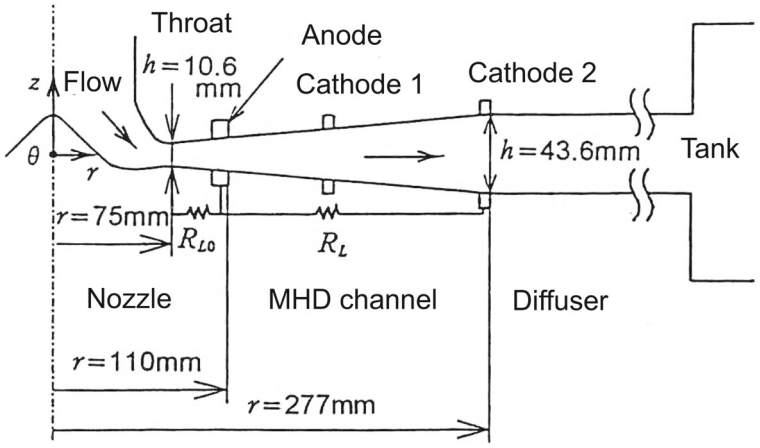


**Fig. 8.17** Model for numerical calculation. A heat transfer from a power-source combustor to Ar gas with Cs seeding to obtain higher ionization degree induces nonequilibrium plasma. Direct power generation without a turbine is realized [29]

resistance $R_L$ connected between the anode and the second cathode. The analysis area was set from the throat ($r = 75$ mm) to the MHD channel exit ($r = 277$ mm). With a heat input of approximately 2000 kW, an output of approximately 300 kW can be obtained. It is noted that the term "MHD" corresponds to direct electrical power generation by rare gas plasma.

#### 8.4.4.2 Calculation Procedure

To solve the conservation equations, we adopted the more accurate Total variation diminishing (TVD)-MacCormack method instead of the MacCormack method that includes an explicit artificial viscosity term, which has been widely used in the field of MHD. In general, it is difficult to formulate MHD conservation equations in TVD, but this was relatively easy for this system of equations. Due to the high stability and accuracy of TVD, stable solutions were obtained over a wide range of operating conditions that were previously difficult to calculate using explicit artificial viscosity terms.

#### 8.4.4.3 Initial and Boundary Conditions

The calculation conditions were mainly based on the authors' experiments and are shown in Table 8.2. As initial conditions, the fluid system was assumed to be an isentropic flow. The initial conditions for the electron temperature were a uniform distribution of 2350 K at the throat and 4000 K inside the MHD channel, and a linear distribution that changed from 2350 to 4000 K at the nozzle. The initial conditions for the number density of electrons and each ion were given as the Saha equilibrium solution corresponding to this electron temperature. The spatial increment was divided into 405 parts from the throat to the second cathode, and the time increment was set to $\triangle t = 0.1$ μs to be longer than the relaxation time of the electron temperature and shorter than the relaxation time of the electron number density. This value is sufficiently smaller than the value obtained from the Courant–Friedrichs–Lewy (CFL) condition, which is a limiting condition for the explicit method. Calculations were performed up to 60,000 steps with this time increment. As will be described later, except for the case of low load, about 20,000 steps were sufficient to obtain a steady-state convergence solution.

As for the boundary conditions, the velocity, density, and total energy of the heavy particle fluid system were fixed at the inlet (throat) based on the condition of a Mach number of 1. Furthermore, assuming that the electron concentration at the stagnation point is in equilibrium with the working gas temperature, the number densities of electrons and ions were calculated from the Saha equilibrium condition, and then the reaction-frozen condition was assumed from the stagnation point to the throat, and the number densities of electrons and ions at the throat were calculated from the adiabatic expansion relationship and fixed at these values. In addition, when the flow becomes subsonic at the exit of the MHD channel, the condition that the

**Table 8.2** Calculation conditions [29]

| | |
|---|---|
| Working gas | Ar + Cs |
| Stagnation temperature (K) | 2350 |
| Stagnation pressure (MPa) | 0.18–0.36 |
| Seed fraction | $(8.8–9.0) \times 10^{-4}$ |
| Ext. load resistance $R_{L0}$ (Ω) | 0.03–0.06 |
| Ext. load resistance $R_L$ (Ω) | 0.038–1.0 |
| Area ratio of channel | 4.2 |
| Maximum magnetic flux density (T) | 2.7 |

radial gradient of the conservative variables is 0 was imposed as the exit boundary condition.

#### 8.4.4.4 Calculated Results and Comparison with Experiments

Figure 8.18 shows the distribution of the ionization degree of cesium and argon. Cesium ionization progresses rapidly at the nozzle, and is almost completely ionized in the MHD channel, generating a uniform plasma in the radial direction. The electron concentration is around 6000 K in the MHD channel, and the ionization degree of argon is almost 0.

Figures 8.19 and 8.20 show the calculation results of the radial distribution of static pressure and Mach number. In Fig. 8.19, the experimental values are shown with

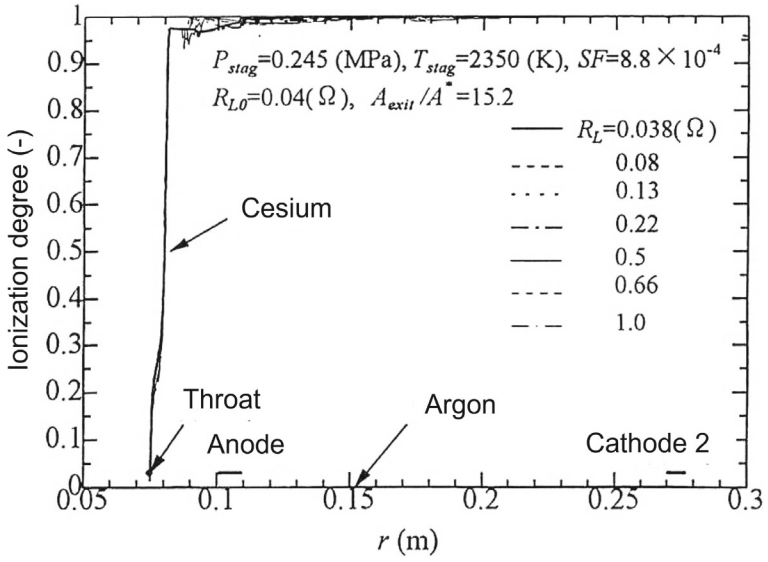


**Fig. 8.18** Distributions of ionization degree of cesium and argon [29]

white circles. Although they were not captured in the experiment because there is no static pressure hole in the nozzle, in the calculation, a shock wave is generated in the nozzle where ionization progresses rapidly. Also, as can be seen from Fig. 8.20, the flow is rapidly decelerated before entering the MHD channel and becomes subsonic at the channel (anode) entrance ($r = 0.1$ m). Figure 8.19 shows that the experimental and calculated values for the static pressure gradient are almost consistent, but there is a slight difference in the values. This is considered to be due to the difference in the conditions of the outlet boundary from the experiment.

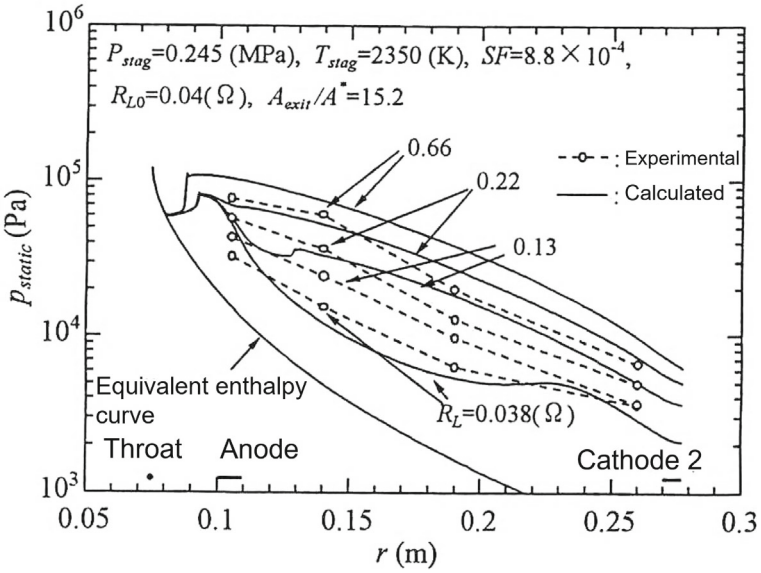


**Fig. 8.19** Calculated and measured distributions of static pressure [29]

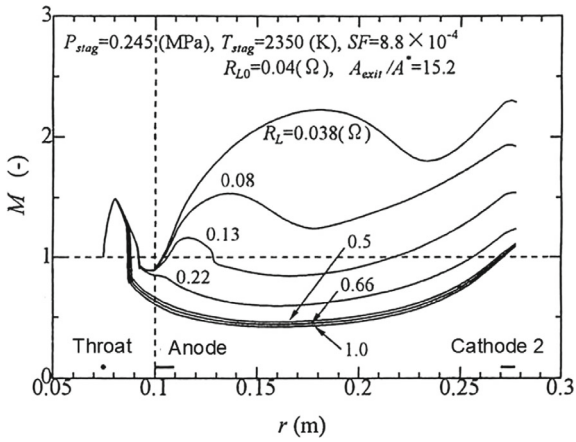


**Fig. 8.20** Calculated distributions of Mach number [29]

Figure 8.21 shows a comparison of the calculated and experimental values for the relationship between the enthalpy extraction rate *E.E.* and the load resistance $R_L$. In previous results, there was a discrepancy between the experimental and calculated values under high and low load conditions. In the present calculation results, the agreement between the experimental and calculated values is good, except for one experimental value under low load conditions. Figure 8.22 shows the calculated and experimental values for the relationship between the output voltage $V_h$ and the output current $I_h$. As with Fig. 8.21, the agreement between the experimental and calculated values is good, except for one point under low load conditions.

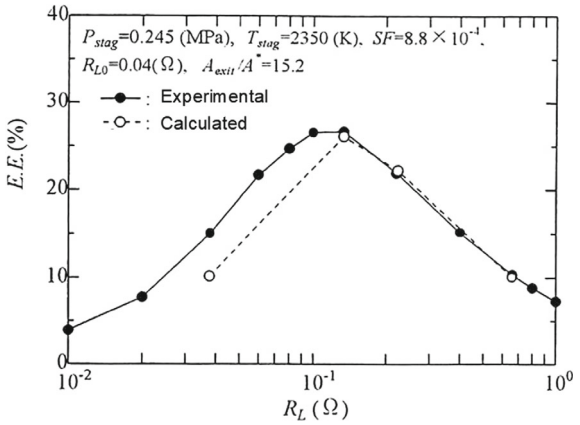


**Fig. 8.21** Calculated and measured relations between enthalpy extraction and external load resistance [29]

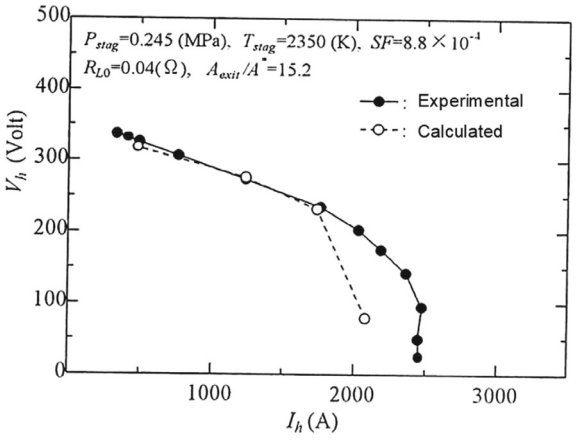


**Fig. 8.22** Calculated and measured relations between output voltage and current [29]

## 8.5 Conclusions

The heat transfer mechanisms of equilibrium and nonequilibrium plasmas are explained with reference to the basic equation system and concrete examples of analyses. Heat transfer phenomena in plasma are extremely complex and intricately related to chemical reactions, electromagnetic fields, changes in physical properties, and fluid flow. There are difficulties modeling this type of plasma in connection with the existence of spatial and temporal multiscale, therefore, the author turns to fluid modeling. However, some aspects and results presented in the paper also suggest the importance of kinetic effects, especially in the modeling of electron dynamics. It is noted that, with the increasing power of supercomputers today, some kinetic codes have now been used for several years to model this type of plasma, and especially for heat transfer processes in plasmas. In writing this chapter, the author specifically used the following books [1–8, 10–23].

### Chapter 8 Exercises

**Problem 1**: Plasma fundamentals in energy systems

(1) Derive the expression for the electron energy distribution function $f(v)$ in a plasma, assuming a Maxwellian distribution, and calculate the most probable speed $v_p$ for electrons at $T_e = 10{,}000$ K. (Mass of electron $m_e = 9.11 \times 10^{-31}$ kg, Boltzmann constant $k_B = 1.38 \times 10^{-23}$ J/K).
(2) Compute the Debye length $\lambda_D$ for a plasma with $n_e = 10^{18}$ m$^{-3}$ and $T_e = 10{,}000$ K. (Electron charge $e = 1.6 \times 10^{-19}$ C, Vacuum permittivity $\varepsilon_0 = 8.85 \times 10^{-12}$ F/m).
(3) If the plasma frequency is $\omega_p$, calculate $\omega_p$ for the same plasma conditions.

**Problem 2**: Plasma heat transfer in energy applications

(1) Derive the energy balance equation for a plasma reactor considering convective heat transfer, radiative heat transfer, and Joule heating ($q_j = \sigma E^2$).
(2) A plasma reactor operates with electrical conductivity $\sigma = 10^3$ S/m, electric field $E = 100$ V/m, and plasma temperature $T_p = 8000$ K. If the radiative heat loss is $q_r = \varepsilon\sigma {T_p}^4$ with $\varepsilon = 0.8$ and $\sigma = 5.67 \times 10^{-8}$ W/m$^2$, calculate the net heat gain per unit volume.
(3) Compute the Nusselt number $Nu$ for a plasma flow with characteristic length $L = 0.05$ m, thermal conductivity $\lambda = 0.1$ W/m K, and heat transfer coefficient $h = 500$ W/m$^2$ K.

**Problem 3**: Magnetohydrodynamic (MHD) power generation

(1) Derive the relationship between Hall parameter $\beta$ and the electrical conductivity tensor in MHD flows.
(2) An MHD generator operates with a magnetic field strength $B = 2$ T, velocity $u = 500$ m/s, and number density of ions $n_i = 10^{20}$ m$^{-3}$. Calculate the electric field induced ($E = uB$).

(3) If the MHD generator extracts 5 MW of power and operates at 40% efficiency, calculate the input thermal energy required.

**Problem 4**: $CO_2$ Plasma conversion for synthetic fuels

(1) Derive the rate of $CO_2$ dissociation in a plasma reactor using Arrhenius kinetics, $r = A \exp(-E_a/k_B T_e)$, where $A = 10^{12}$ s$^{-1}$, $E_a = 3.5$ eV, and $T_e = 20{,}000$ K.
(2) A reactor processes 10 mol/s of $CO_2$ with an energy input of 500 kJ/mol. Calculate the total power consumption.
(3) If 60% of the $CO_2$ is converted into CO, calculate the amount of CO produced per second.

**Problem 5**: Environmental contributions of plasma technology

(1) A plasma waste-to-energy reactor processes 1000 kg of waste per hour with an energy yield of 3 MJ/kg. Calculate the total energy produced in one day.
(2) If a hydrogen production reactor consumes 1500 W of power and operates at 85% efficiency, calculate the actual power converted into hydrogen production.
(3) Estimate the greenhouse gas reduction if a plasma reactor reduces emissions by 80% in a system emitting 50 tons/year of $CO_2$.

## References


1. N.G. Van Kampen, B.U. Felderhof, *Theoretical Methods in Plasma Physics* (North-Holland Publishing Company, 1967), pp. 217
2. M. Mitchner, M.C.H. Kruger, Jr., *Partially Ionized Gases* (A Wiley-Interscience Publication, 1973), pp. 518
3. A.B. Cambel, *Plasma Physics and Magnetofluidmechanics* (McGraw-Hill Inc., 1963), pp. 246
4. R.J. Rosa, *Magnetohydrodynamic Energy Conversion* (McGraw-Hill Inc., 1968), pp. 234
5. J.A. Shercliff, *A Textbook of Magnetohydrodynamics* (Pergamon Press, 1965), pp. 265
6. E.M. Lifshitz, L.P. Pitaevskii, *Physical Kinetics*, in Course of Theoretical Physics Volume 10 (Pergamon Press, 1981), pp. 452
7. L.D. Landau, E.M. Lifshitz, *The Classical Theory of Fields*, in Course of Theoretical Physics Volume 2 (Pergamon Press, 1975), pp. 402
8. J. Kanzawa, *Purazuma Dennetsu* (English translated title: *Plasma Heat Transfer*) (Shinzansha Saitech Co., Ltd., 1992), pp. 142 (in Japanese)
9. E.A. Bogdanov, A.A. Kudryavtsev, L.D. Tsendin, R.R. Arslanbekov, V.I. Kolobov, V.V. Kudryavtsev, Substantiation of the two-temperature kinetic model by comparing calculations within the kinetic and fluid models of the positive column plasma of a dc oxygen discharge. Tech. Phys. **48**, 983–994 (2003) (translated from Zh. Tekhn. Fiz. 73–78, 45–55 (2003))
10. Y. Tomita, *Ryutai Rikigaku Jyosetsu* (English translated title: *Introduction to Fluid Mechanics*) (Yokendo Co. Ltd., Tokyo, Japan, 1981), pp. 378 (in Japanese)
11. T. Tatsumi, *Ryutai Rikigaku* (English translated title: *Fluid Mechanics*) (Baifukan Co., Ltd., Tokyo, Japan, 1982), pp. 453 (in Japanese)
12. F.M. White, *Viscous Fluid Flow*, 1st edn. (McGraw-Hill, 1974), pp. 725
13. L.D. Landau, E.M. Lifschitz, *Fluid Mechanics* (Pergamon Press, 1959), pp. 536
14. M. Katsuki, A. Nakayama, *Netsuryutai no Suichi Simulation, Kiso kara Puroguramu made* (English translated title: *Numerical Simulation of Thermal Flow—From Basics to Programming*) (Morikita Publishing Co., Ltd., Tokyo, Japan, 1990), pp. 120 (in Japanese)

15. N. Kadotani, *Renzokutai Rikigaku* (English translated title: *Mechanics of Continuous Media*) (Kyoritsu Shuppan Co., Ltd., Tokyo, Japan, 1969), pp. 206 (in Japanese)
16. A. Shimizu, *Renzokutai Rikigaku no Waho* (English translated title: *Discourse of Continuous Media Mechanics*) (Morikita Publishing Co., Ltd., Tokyo, Japan, 2012), pp. 309 (in Japanese)
17. R.E. Rosensweig, *Ferrohydrodynamics* (Cambridge University Press, 1985), pp. 344
18. L.D. Landau, E.M. Lifschitz, *Theory of Elasticity*, 3rd English edn., in Course of Theoretical Physics, 3rd English edn. (Pergamon Press, 1986), pp. 187
19. C. Adachi, *Bekutoru to Tensoru* (English translated title: *Vectors and Tensors*) (Baifukan Co., Ltd., Tokyo, Japan, 1957), pp. 159 (in Japanese)
20. H. Fujita, *Denjikigaku Note (Kaiteiban) and Zoku Denjikigaku Note* (English translated title: *Notes on Electromagnetism* (revised edn.) and *Note on Electromagnetism 2*) (Corona Publishing Co., Ltd., Tokyo, Japan, 1971), pp. 228 and pp. 277 (in Japanese)
21. W.H. Giedt, *Principles of Engineering Heat Transfer*, 1st edn. (D. Van Nostrand Co., Inc., 1957), pp.372
22. T. Takeyama, S. Ohtani, T. Aihara, *Dennetsu Kogaku* (English translated title: *Heat Transfer Engineering*) (Maruzen Co., Ltd., Tokyo, Japan, 1983), pp. 254 (in Japanese)
23. T. Yamamoto, M. Okubo, Y.T. Hung, R. Zhang, *Advanced Air and Noise Pollution Control*, ed. by L.K. Wang, N.C. Pereira, Y.T. Hung (Humana Press, Springer, Berlin/Heidelberg, Germany, 2004), pp. 526
24. H. Yamasaki, H. Yamamoto, Y. Koizumi, Y. Fukuda, T. Kuroki, M. Okubo, Dry emission control technology for glass melting furnace by plasma-chemical hybrid processing. IEEE Trans. Ind. Appl. **59**, 2421–2429 (2023)
25. M. Okubo, K. Yoshida, T. Yamamoto, Numerical and experimental analysis of nanosecond pulse dielectric barrier discharge-induced nonthermal plasma for pollution control. IEEE Trans. Ind. Appl. **44**, 1410–1417 (2008)
26. M. Okubo, Evolution of streamer groups in nonthermal plasma. Phys. Plasmas **22**, 123515 (2015). https://doi.org/10.1063/1.4937776
27. T. Shimada, H. Yamasaki, M. Okubo, Evolution of streamer groups and radical generation in high-voltage multiple-pulse-induced nonthermal plasma. Phys. Plasmas **30**, 103508 (2023). https://doi.org/10.1063/5.015345130
28. T. Kuroki, S. Tanaka, M. Okubo, T. Yamamoto, Numerical investigations for $CF_4$ decomposition using RF low pressure plasma. IEEE Trans. Ind. Appl. **43**, 1075–1083 (2007)
29. M. Okubo, H. Yamasaki, Numerical prediction on performance of disk plasma MHD generator. IEE Japan Trans Power Energy **117-B**, 122–129 (1997) (in Japanese)
30. *CFD-ACE-GUI Modules Manuals (Flow, Heat Transfer, Chemistry, Electric, Plasma Modules)* (CFD Res. Corp., Huntsville, AL, USA, 2004)
31. P. Ségur, F. Massines, The role of numerical modelling to understand the behaviour and to predict the existence of an atmospheric pressure glow discharge controlled by a dielectric barrier, in *Proceedings of the 13th International Conference on Gas Discharges and their Applications*, Glasgow, UK, 3–8 Sept 2000, pp. 15–24
32. NIST (National Institute of Standards and Technology), *Atomic Spectra Database*. Available online: http://physics.nist.gov/cgi-bin/AtData/main_asd. Accessed 24 Jan 2023
33. M.-L. Zhang, C.W. Li, Y.-M. Shen, A 3D non-linear $k$–$\varepsilon$ turbulent model for prediction of flow and mass transport in channel with vegetation. Appl. Math. Model. **34**, 1021–1031 (2010)
34. V.I. Kolobov, R.R. Arslanbekov, Towards adaptive kinetic-fluid simulations of weakly ionized plasmas. J. Comput. Phys. **231**, 839–869 (2012)
35. G.J.J. Winands, Z. Liu, A.J.M. Pemen, E.J.M. van Heesch, K. Yan, E.M. van Veldhuizen, Temporal development and chemical efficiency of positive streamers in a large scale wire-plate reactor as a function of voltage waveform parameters. J. Phys. D Appl. Phys. **39**, 3010–3017 (2006)

# Chapter 9
# Gas Turbine Combined Cycle (GTCC) and Renewable Energy Technologies


**Abstract** This chapter explores the integration of gas turbine combined-cycle (GTCC) power generation systems with plasma-based renewable energy technologies. In liquefied natural gas (LNG)-fueled GTCC plants, achieving zero carbon dioxide ($CO_2$) emissions is feasible if the energy efficiency of the non-thermal plasma (NTP) $CO_2$ reduction process reaches at least 49%. The chapter provides an in-depth analysis of zero-emission power plants, covering key topics such as the fundamentals of GTCC systems, carbon monoxide (CO)-based gas turbines, and NTP conversion technologies. These technologies facilitate the transformation of $CO_2$ into synthetic fuel gases, primarily consisting of CO, through the recirculation of exhaust gases. The discussion focuses on methods to achieve $CO_2$ reduction in a self-sustaining manner at ambient temperature and atmospheric pressure. Specifically, the process of converting $CO_2$ into CO via NTP-based reduction techniques is explained. Experimental evaluations were conducted to assess the $CO_2$ reduction performance using various gas mixtures. Initially, $CO_2$ is adsorbed from a nitrogen-$CO_2$ mixture (approximately 10% $CO_2$ concentration) onto an adsorbent material. Following adsorption, the desorbed $CO_2$ is processed using NTP, achieving a concentration increase to 10–22% under similar conditions. Laboratory tests have demonstrated that NTP technology can achieve an energy efficiency of 20%. These results indicate that an efficiency of 49% could be realized for GTCC applications by scaling the NTP system to an industrial level. The chapter concludes with key findings and a set of exercises for further understanding.

## 9.1 Introduction

Minimizing carbon dioxide ($CO_2$) emissions, a key greenhouse gas, is a fundamental approach to addressing global warming. Strategies for atmospheric $CO_2$ reduction can be categorized into two primary methods: reducing $CO_2$ emissions at the source and capturing $CO_2$ from the atmosphere. Emission reduction can be achieved by enhancing the efficiency of energy conversion systems and transitioning to hydrogen-rich fuels that produce lower $CO_2$ emissions. In power generation facilities, thermal



M. Okubo, *Electrical Sustainable Energy for Mechanical Engineering*,
https://doi.org/10.1007/978-981-96-5170-2_9

efficiency improvements can be realized by implementing gas turbine combined cycle (GTCC) plants equipped with advanced gas turbines. Further reduction in $CO_2$ emissions can be attained through enhancements in thermal efficiency. Therefore, advancements in $CO_2$ waste heat recovery technologies and the development of next-generation gas turbines capable of operating at elevated temperatures are essential [1].

$CO_2$ emissions from gas turbines can also be mitigated by refining combustion processes within current gas turbine systems. These reductions are influenced by fuel characteristics following conversion. Increasing interest has been directed towards methods that break down and transform $CO_2$ from combustion processes into useful fuels. One such method, methanation, which converts $CO_2$ and $H_2$ into methane ($CH_4$), has gained substantial attention from researchers and industry stakeholders. While this technology holds promise, large-scale methane production and improved energy efficiency are necessary for it to effectively contribute to the fight against global warming.

This chapter highlights a technique that converts $CO_2$ into carbon monoxide (CO) through nonthermal plasma treatment under atmospheric conditions [2–5]. A widely recognized approach to $CO_2$ processing involves the use of nonthermal plasma—also referred to as low-temperature plasma—which utilizes high-energy electrons and atmospheric discharges to facilitate $CO_2$ reduction into CO at ambient pressure and temperature. Figure 9.1 illustrates the concept of $CO_2$ emission reduction in thermal power generation through environmental plasma hybrid technology. In this system, $CO_2$ emissions from sources such as vehicles, industrial facilities, and ships are directly captured using fans, either by adsorption onto materials or through solidification into dry ice. The concentrated $CO_2$ is then released and converted into fuel using plasma technologies. Operating under atmospheric pressure and low temperature, these plasma processes enable $CO_2$ to be reused as a fuel source in gas turbines or engines for thermal power plants. This approach offers the potential to create a self-sustaining, zero $CO_2$ emission thermal power plant. However, when plasma generation for $CO_2$ processing is powered by coal-fired generation, the energy required to process a given mass of $CO_2$ often surpasses the energy gained from converting the same mass, making it difficult to establish a sustainable, emissions-free system.

As a result, the development of a hybrid $CO_2$ capture and plasma treatment technology capable of achieving the envisioned system in Fig. 9.1 is imperative. A proof of concept for a zero-emission thermal power plant has already been established [6], with prototype laboratory systems also under development [4, 5].

In recent years, natural gas-based GTCC power generation has gained widespread global recognition due to its high efficiency and lower emissions. In contrast, coal-fired power plants are increasingly being phased out due to their substantial $CO_2$ emissions. Achieving zero $CO_2$ emission power plants can be realized by incorporating GTCC systems with plasma-based $CO_2$ treatment technologies. The pursuit of higher energy efficiency can be accomplished through environmental plasma applications. If these systems are successfully implemented, they could pave the way for zero-carbon societies, helping to mitigate climate change while addressing global

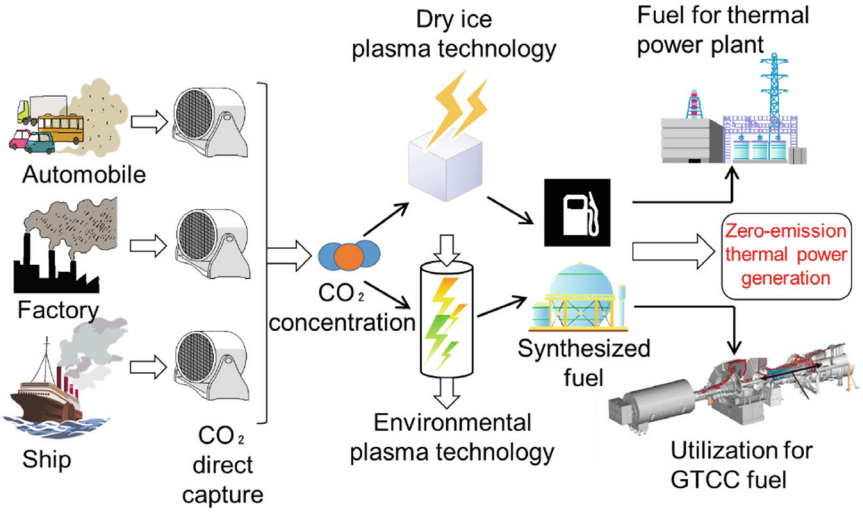


**Fig. 9.1** Concept of zero $CO_2$ emission thermal power generation using environmental plasma hybrid technology

energy demands. Additionally, the development of zero $CO_2$ emission thermal power plants using environmental plasma hybrid technology could significantly impact future research directions.

This chapter is organized as follows: Sect. 9.2 introduces the concept of natural gas combined-cycle power plants and the GTCC framework, where atmospheric and exhaust $CO_2$ are captured and converted into fuel to achieve a zero-emission system. Section 9.3 provides an overview of low-calorific gas-fired turbines utilizing hydrogen-rich gases and CO, which are crucial for fuel diversification. Section 9.4 discusses $CO_2$-to-fuel conversion through plasma treatment of exhaust gases. Finally, Sect. 9.5 summarizes the entire concept, presenting an integrated approach for heat energy recovery and low $CO_2$ emissions in natural gas combined-cycle power plants utilizing plasma technology.

## 9.2 Total $CO_2$ Reduction Power System

### *9.2.1 Natural Gas Combined Cycle Power Plant*

Figure 9.2 presents a schamatic diagram of the principles of gas turbine combined cycle (GTCC) thermal power plants, which are widely implemented across Japan due to their high efficiency. The system consists of a gas turbine capable of operating at approximately 1700 °C, power generators, a waste heat recovery boiler, an energy recovery system based on the Rankine cycle, a De-$NO_x$ catalyst for nitrogen

oxide reduction, an ammonia injection system, and a steam turbine. During power generation, the waste heat produced by the gas turbine is captured by the waste heat recovery boiler, which then drives the steam turbine through the Rankine cycle by utilizing superheated water to generate supplementary electricity. The primary pollutant emitted by gas turbines is thermal nitrogen oxides ($NO_x$). To mitigate these emissions, ammonia ($NH_3$) is introduced upstream of the De-$NO_x$ selective catalytic reduction (SCR) unit, which effectively reduces $NO_x$ and converts it into environmentally harmless compounds.

At present, $CO_2$ emissions in the exhaust gases remain untreated. To achieve significant $CO_2$ reduction, it is essential to enhance the thermal efficiency of waste heat recovery systems by developing advanced gas turbines capable of operating at higher temperatures [1].

GTCC technology integrates multiple thermodynamic cycles, including gas and steam turbines, to achieve substantial improvements in overall thermal efficiency. Among various configurations, the exhaust heat recovery system depicted in Fig. 9.2 is extensively utilized in Japan due to its operational simplicity. In this system, the high-temperature exhaust gases from the gas turbine are routed to a heat recovery boiler, where they transfer energy to heat the feed water, which subsequently drives the steam turbine.

The main features of combined cycle power generation using the exhaust heat recovery system are as follows [7].

a. High thermal efficiency (43–60%), with little efficiency loss at partial load.
b. Short start-up and stop times.

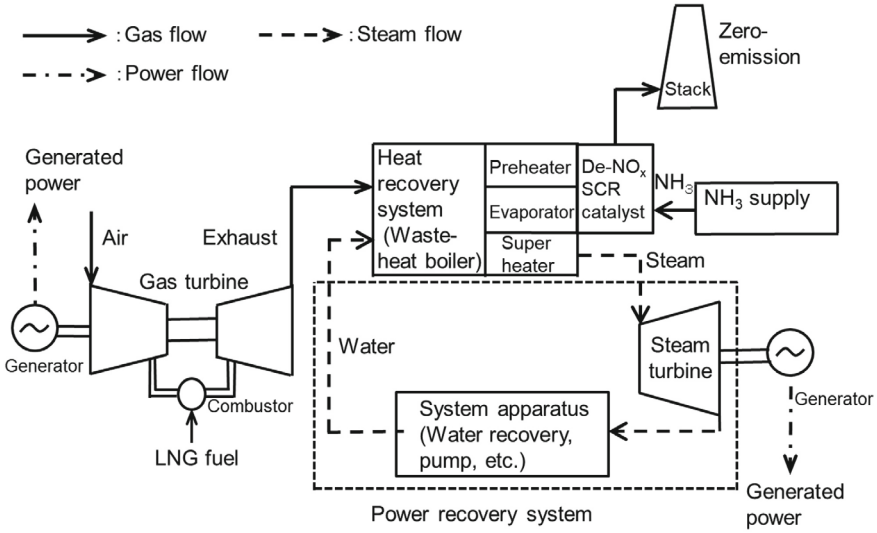


**Fig. 9.2** Schematic representation of a gas turbine combined cycle power plant

c. The amount of condenser cooling water per unit output is smaller than that for thermal power generation.
d. The output of the gas turbine is affected by the outside air temperature.
e. Gas turbines burn at high temperatures; therefore, measures against nitrogen oxides ($NO_x$) are necessary.
f. Steam turbines cannot be operated alone.
g. Noise is loud, so measures are necessary.

The basic thermal cycle of gas turbines is the Brayton cycle, whereas that of steam turbines is the Rankine cycle.

Brayton cycle (see Fig. 9.3)

1 → 2: Compressor (adiabatic compression)
2 → 3: Combustor (constant pressure heat reception, constant pressure combustion)
3 → 4: Gas turbine (adiabatic expansion)
4 → 1: Exhaust (constant pressure heat reception, constant pressure exhaust).

Rankin cycle (see Fig. 9.3)

5 → 6: Feed pump (adiabatic compression)
6 → 7: Exhaust heat recovery boiler (constant pressure heat reception, constant pressure superheat)
7 → 8: Steam turbine (adiabatic expansion)
8 → 5: Condenser (constant pressure heat reception, constant pressure condensation).

As illustrated above, the Brayton and Rankine cycles operate in conjunction to optimize power generation efficiency by utilizing both direct combustion energy and waste heat recovery.

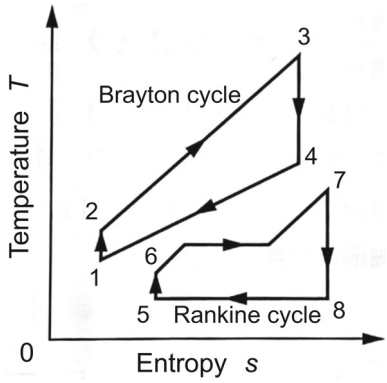


**Fig. 9.3**
*T–s* (temperature-entropy) diagram

### 9.2.2 Shaft Configuration and Thermal Efficiency of Combined Cycle

Combined cycle power generation can be categorized by shaft configuration into two types: single-shaft and multi-shaft systems [7].

In the single-shaft type, one gas turbine and one steam turbine are mechanically connected. In the multi-shaft type, the system has multi shafts or multi gas turbines and multi steam turbines. This configuration features a steam turbine are combined. The characteristics of each type are as follows:

(1) Characteristics of single-shaft type

- The steam turbine is with a large capacity and high thermal efficiency at high output, making it suitable for base supply capacity.

(2) Characteristics of multi-shaft type

- Regular inspections can be conducted on each unit, leading to a high average utilization rate.
- By adjusting the number of operating units, partial-load operation is possible, providing high partial-load efficiency and making it suitable for middle supply capacity.
- Since the smaller capacity of the steam turbine results in a shorter start-up time compared to the single-shaft type.

The thermal efficiency, $\eta$ of combined cycle power generation can be expressed as follows.

If the thermal efficiency of the gas turbine is $\eta_G$ and the thermal efficiency of the steam turbine is $\eta_S$, the total input energy is assumed to be 1. The gas turbine produces an output of $\eta_G$, while the remaining energy, $1 - \eta_G$, is utilized for steam turbine power generation. The output from the steam turbine is therefore $(1 - \eta_G)\eta_S$.

Combining these outputs, the overall thermal efficiency, $\eta$, of the combined cycle power generation is given by $\eta = \eta_G + (1 - \eta_G)\eta_S$.

Important formula: The thermal efficiency of the combined cycle power generation

$$\eta = \eta_G + (1 - \eta_G)\eta_S = \eta_G + \eta_S - \eta_G\eta_S \tag{9.1}$$

### 9.2.3 Energy Balance for a Gas Turbine Combined Cycle

Technologies aimed at converting $CO_2$ into CO offer a significant potential for reducing carbon emissions. By utilizing plasma powered by a high-efficiency gas turbine combined cycle (GTCC) system, it is possible to establish a near-zero $CO_2$ emission power generation process [6].

Figure 9.4 presents an energy balance diagram of a GTCC system, highlighting its potential to achieve carbon-neutral power generation. Conventional coal-fired power plants generally operate with a relatively low efficiency of up to 45% for supercritical plant (higher heating value base), whereas state-of-the-art GTCC plants can reach an overall efficiency of up to 64% [8]. For a GTCC system fueled by methane ($CH_4$, combustion reaction enthalpy = 891 kJ/mol = 9.23 eV/molecule) and operating at an efficiency of 64%, the resulting electrical power is calculated as 9.23 × 0.64 = 5.91 eV/molecule. If the $CO_2$ from exhaust gases is entirely converted into CO through plasma treatment, the minimum required energy would be 279.8 kJ/mol, which equals 2.90 eV/molecule. Consequently, in order to achieve net-zero $CO_2$ emissions, the energy efficiency of plasma-driven $CO_2$ reduction must surpass 2.90/5.91 × 100 = 49%. The remaining energy (5.91 − 2.90 = 3.01 eV/molecule) would then have no carbon footprint; however, the total GTCC efficiency would drop from 64 to 33%. The CO generated from the $CO_2$ conversion can be combined with hydrogen to create a synthetic fuel that can be reutilized within the GTCC system. An energy efficiency index ($\eta$) is introduced in Eq. (9.2):

$$\eta = \alpha \frac{2.90}{E_v} = \frac{2.90}{\frac{E_v}{\alpha}} \tag{9.2}$$

In this formula, $\alpha$ signifies the efficiency of $CO_2$-to-CO conversion (%), and $E_v$ represents the plasma energy needed to process a single $CO_2$ molecule (eV/molecule). Achieving zero $CO_2$ emission power generation is feasible when the plasma energy

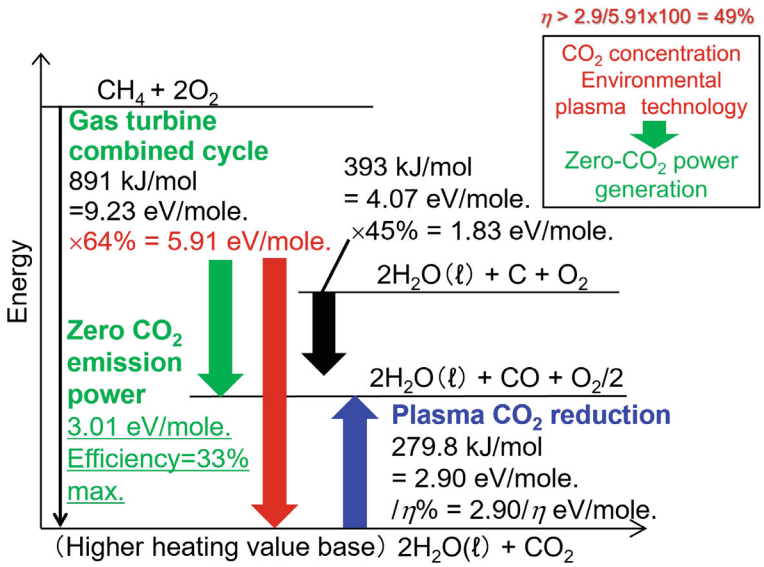


**Fig. 9.4** Energy balance diagram of a gas turbine combined cycle system illustrating the feasibility of achieving a zero $CO_2$ emission power generation system

applied per molecule ($E_v$) is less than the generated power per molecule (5.91 eV/molecule):

$$\frac{E_v}{\alpha} < \frac{5.91}{100} \tag{9.3}$$

It is not necessary to achieve a $CO_2$ conversion efficiency of 100%. For example, if $\alpha = 20\%$, then five plasma reactors (100/20 = 5) would be required to achieve complete $CO_2$ processing. Thus, $\alpha$ can achieve 100% conversion if $E_v$ is increased fivefold, maintaining the ratio $E_v/\alpha$ constant. In essence, the condition for zero emissions is $\eta > 2.90/5.91 \times 100 = 49\%$, with the surplus energy available for power generation calculated as $P = 5.91 - E_v$ (eV/molecule). The overall efficiency of the GTCC system is expressed as follows:

$$\eta_{green} = \frac{5.91 - E_v}{9.23} \times 100\ (\%) \tag{9.4}$$

If the GTCC efficiency $\eta_{gtcc}$ is 60%, then $\eta$ must exceed 52%, resulting in the total system efficiency:

$$\eta_{green} = \frac{5.54 - E_v}{9.23} \times 100\ (\%) \tag{9.5}$$

A study conducted by Spencer and Gallimore [6] at the University of Michigan demonstrated that nearly 90% of $CO_2$ could be successfully converted into CO using diluted argon plasma. While achieving almost complete $CO_2$ reduction (close to 100%) through atmospheric plasma presents challenges, it remains a feasible goal. The feasibility of this approach has been validated through laboratory-scale studies [4, 5]. Achieving a target efficiency of 49% may be possible by integrating dielectric barrier discharge (DBD) technology with direct $CO_2$ capture plasma concentration techniques. Recent experimental findings from Osaka Metropolitan University, further discussed in Sect. 9.4, provide additional insights into this approach. Note that for supercritical coal-fired power plant the resulting electrical power is calculated as 393kJ/mol = 4.07 eV/molecule of 45% = 1.83 eV/molecule. This is lower than $CO_2$ reduction enthalpy of 2.90 eV/molecule. Since coal actually contains less hydrogen than methane, the electric power is greater than 1.83 eV/molecule. However, it is difficult to significantly exceed 2.90 eV/molecule. Therefore, it is hard to realize zero-$CO_2$ emission for the carbon rich coal-fired power plants.

### 9.2.4 Targeted Values for Zero $CO_2$ Emission GTCC

The research on zero $CO_2$ emission systems focuses on three primary objectives:

1. Atmospheric $CO_2$ Capture and Concentration Enhancement

The first objective is to capture $CO_2$ directly from the atmosphere, where its concentration is approximately 400 ppm, and enhance it by 20% (up to 20,000 ppm) using just 10% of thermal energy. This method is currently under development and has demonstrated a processing speed that is ten times faster than conventional methods, such as thermal heating.

2. Achieving Energy Conversion Efficiency of 49%

The second goal is to attain an energy conversion efficiency of 49% by integrating adsorbent and plasma technologies to produce CO within an environmental plasma system. This efficiency represents the minimum requirement to realize a zero $CO_2$ emission GTCC system. Experimental studies worldwide indicate that achieving an energy efficiency of 49% or higher in a zero-emission GTCC thermal power plant is feasible. At present, laboratory tests conducted at Osaka Metropolitan University have demonstrated an energy efficiency of 34%. Enhancing plasma-to-electric energy conversion efficiency, gaining deeper insights into the high-concentration reduction process, and scaling up the plasma reactor system could make it possible to achieve an efficiency of 49% or greater.

3. Development and Deployment of a Prototype GTCC System

The third objective is the design, construction, and operation of a prototype GTCC system equipped with environmental plasma devices, small-scale gas turbines, heat exchangers, and exhaust gas treatment units. This integrated system aims to establish a completely pollution-free thermal power plant with zero $CO_2$ emissions.

### 9.2.5 Sub Research Topics

The following sections discuss key subtopics related to achieving zero $CO_2$ emission thermal power generation.

**Subtheme I**: Direct Air Capture (DAC) with Plasma Concentration

The first subtheme focuses on the implementation of a direct air capture (DAC) system enhanced by plasma concentration [9]. Figure 9.5 presents a schematic representation of the DAC system, which captures and absorbs atmospheric $CO_2$ using an adsorbent at a high flow rate. Following the capture process, air is passed through the adsorbent at a lower flow rate while being subjected to nonthermal plasma and waste heat, facilitating the desorption of $CO_2$ as a gas fuel.

This process takes place in two distinct stages. In the initial phase, atmospheric air containing approximately 400 ppm of $CO_2$ is passed through the adsorbent at a high

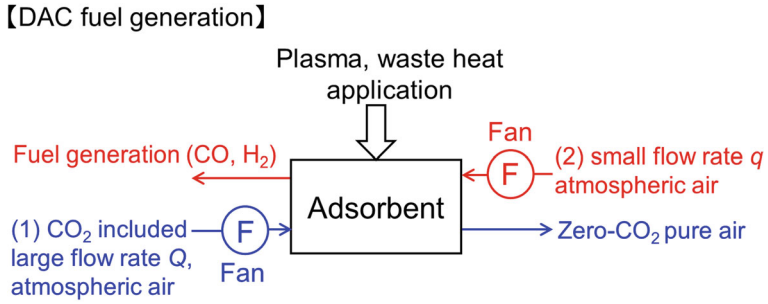


**Fig. 9.5** Operational principles of the DAC system for plasma-based fuel generation

flow rate ($Q$), which results in the concentration of $CO_2$ and the release of $CO_2$-free air. In the second phase, atmospheric air with a lower flow rate ($q < Q$) is introduced into the adsorbent containing a catalyst with the help of a fan. Concurrently, nonthermal plasma is applied to the adsorbent, leading to the desorption of $CO_2$ at a concentration up to 100 times higher than its atmospheric level. The desorbed $CO_2$ is subsequently processed into synthetic fuels such as CO, $H_2$, and $CH_4$ using plasma-enhanced chemical reactions. A prototype system capable of processing gas at a rate of $Q = 10{,}000\ Nm^3/h$ has been developed to validate the feasibility of this concept.

Figure 9.6 displays the experimental results of increasing the $CO_2$ concentration from 1000 ppm to 1.1% (11,000 ppm) using the DAC system [10]. The graph provides a time-dependent analysis of $CO_2$ and CO concentrations during the adsorption and subsequent desorption phases. The performance of $CO_2$ adsorption and desorption achieved using plasma treatment and conventional heating methods is also compared. During plasma desorption, $CO_2$ is converted into CO, with the initial inlet concentration of 1000 ppm reaching a peak of 1.12% (11,200 ppm) after the third desorption cycle. Additionally, approximately 400 ppm of CO is generated in each desorption cycle.

Figure 9.7 shows the experimental results of increasing $CO_2$ concentration from 2.75% (27,500 ppm) to 13.5% (135,000 ppm) using the DAC system [10]. The graph illustrates the process when the inlet $CO_2$ concentration is 2.75%. After the second desorption cycle, the concentration reaches approximately 14%. Plasma-based desorption yields consistently higher peak concentrations compared to conventional thermal methods.

The experimental results shown in Figs. 9.6 and 9.7 demonstrate that the two-step DAC approach is capable of enhancing $CO_2$ concentrations by nearly 100-fold. Furthermore, plasma treatment not only increases $CO_2$ concentration but also achieves fuel conversion more efficiently than conventional thermal methods. The rapid desorption observed in plasma treatment is attributed to dielectric heating and the interactions of induced ions and electrons with the adsorbent material. When compared to traditional thermal techniques, plasma processing achieves significantly greater $CO_2$ desorption performance. Further investigations were conducted to

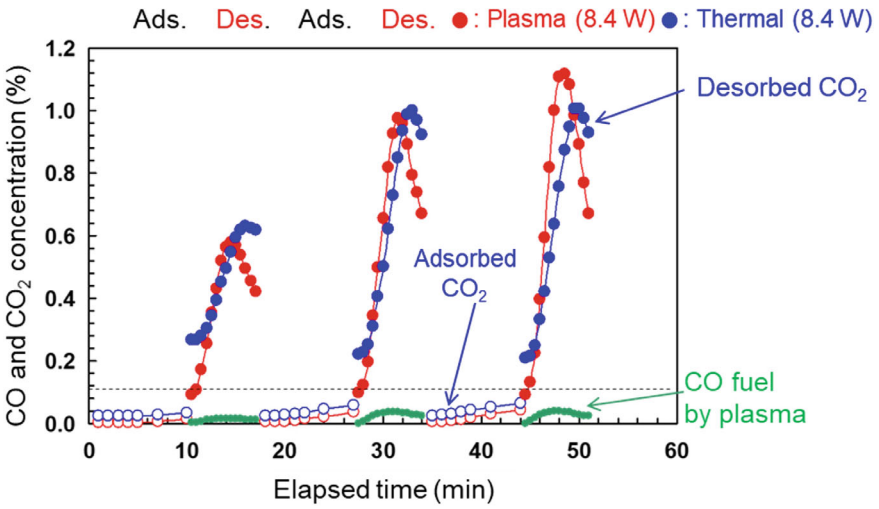


**Fig. 9.6** DAC process concentrating 1000 ppm $CO_2$ to 1.1% $CO_2$ [10]

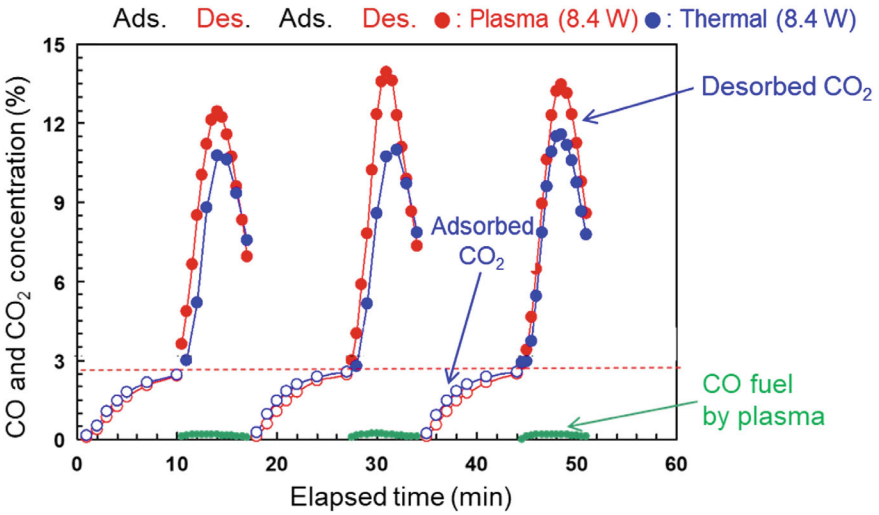


**Fig. 9.7** DAC process concentrating 2.75% $CO_2$ to 13.5% $CO_2$ [10]

assess the effectiveness of combining direct $CO_2$ capture with plasma concentration technology.

**Subtheme II**: Development of Low-Calorific Value Gas-Fired Turbines

The second subtheme shifts the focus to the advancement of low-calorific gas-fired turbines that can operate on a mixture of CO and hydrogen-rich gases, thereby promoting fuel diversification. This topic is elaborated in Sect. 9.3 of this chapter.

**Subtheme III**: Plasma-Catalyzed $CO_2$ Fuel Processing Systems

The third subtheme emphasizes the necessity for further research and development in plasma-catalyzed $CO_2$ fuel processing systems. This study explores the feasibility of achieving zero $CO_2$ emissions in GTCC power plants by leveraging plasma reduction technology. Key challenges in this domain include enhancing the efficiency of $CO_2$ reduction through nonthermal plasma operating under atmospheric pressure and ambient temperature conditions. The initial concept involves $CO_2$ adsorption onto an adsorbent, followed by plasma-induced desorption at high concentrations, and increasing the CO conversion rate to improve overall power generation efficiency.

### *9.2.6 $CO_2$ Reduction Methanation*

Methanation [11] and propanation are processes that reduce $CO_2$ in exhaust gases by adding $H_2$ to produce hydrocarbon gases such as methane $CH_4$ and propane $C_2H_6$ to form artificial fuels. Technologies that convert $CO_2$ into fuel using a catalytic reaction at high pressure and temperature have been developed. However, these technologies cannot cost effectively increase methane production. In contrast, environmental plasma technology has the potential to produce large amounts of methane at low cost.

The general methanation (Sabatier methanation) is reaction (9.6).

$$CO_2 + 4H_2 \rightarrow CH_4 + 2H_2O, \quad \Delta H = -165\,\text{kJ/mol} \tag{9.6}$$

This is the following two-step reaction.

$$CO_2 + H_2 \rightarrow CO + H_2O, \quad \Delta H = +41\,\text{kJ/mol} \tag{9.7}$$

$$CO + 3H_2 \rightarrow CH_4 + H_2O, \quad \Delta H = -206\,\text{kJ/mol} \tag{9.8}$$

Reaction (9.7) is the reverse of the water–gas shift reaction, which produces hydrogen from CO and steam, and is an endothermic reaction. By employing atmospheric pressure plasma for $CO_2$ reduction instead of reaction (9.7), a 25% reduction in hydrogen consumption is achieved under atmospheric pressure. Reaction (9.8) involves producing methane from synthesis gas. Synthesis gas can be used directly as fuel, but methanation may be applied to enhance its heating value.

To further increase the heating value of fuel, the basics of green liquefied petroleum gas (LPG) production technology are explained. Propane production and carbon deposition can occur under certain catalytic conditions.

$$CO_2 + (7/2)H_2 \rightarrow (1/2)C_2H_6\,(\text{ethane}) + 2H_2O, \quad \Delta H = +132\,\text{kJ/mol} \tag{9.9}$$

$$CO_2 + 2H_2 \rightarrow C + 2H_2O, \quad \Delta H = -90\,\text{kJ/mol} \tag{9.10}$$

$$CO_2 + H_2 \rightarrow C_3H_8, \text{ propanation, FT synthesis reaction} \tag{9.11}$$

$H_2$ is produced through the shift reaction or water electrolysis (green hydrogen), while CO is generated using plasma $CO_2$ reduction. Enhancing the performance of gas turbines that utilize CO or $CO_2 + H_2$ as fuel is crucial. This technology is exemplified by the gas turbines used in IGCC carbon gasification power generation, as explained in the next section.

## 9.3 Low-Calorie Gas-Fired Turbines

### *9.3.1 Low-Calorie Gas Fuels*

Plasma $CO_2$ reduction technology has the potential to generate carbon monoxide (CO), which can be utilized as a fuel for low-calorific gas-fired turbines that operate on a CO and hydrogen ($H_2$) mixture as their primary energy source. A notable example of this technology is the integrated coal gasification combined cycle (IGCC), which achieves an energy conversion efficiency of approximately 44–48% [12, 13], with future expectations of reaching around 50% [14]. IGCC utilizes gasified coal as fuel and incorporates key components such as a gas turbine, boiler, steam turbine, and GTCC. Currently, this technology is undergoing verification testing for potential commercialization.

The coal gasification process generates fuel by partially oxidizing coal at elevated temperatures, yielding CO and $H_2$ as the primary products. The composition of the resulting gasified fuel largely depends on the method of oxygen supply during the gasification process [15]. Typically, oxygen is introduced either in the form of atmospheric air or in highly concentrated oxygen. Using high-purity oxygen necessitates an additional production process to remove nitrogen, thereby increasing both production and operational costs. However, this method yields a high-calorific gas fuel free from nitrogen. In contrast, using air as the oxygen source is a more cost-effective approach but results in a low-calorific gas fuel containing nitrogen, which is a non-combustible component.

Figure 9.8 presents the compositions of both low- and high-calorific fuel gases [16]. In low-calorific gas fuel, combustible components account for approximately 30% of the total volume, with an energy content of 4.2 MJ/Nm$^3$—roughly one-tenth of that found in LNG. Furthermore, due to the high nitrogen content, the flame temperature is relatively low, leading to combustion instability issues. Another challenge is the presence of ammonia ($NH_3$) in the fuel, which converts into nitrogen oxides ($NO_x$) during combustion. In dry-feed gasification systems, $NH_3$ is not removed before combustion, resulting in $NO_x$ formation in the gas turbine.

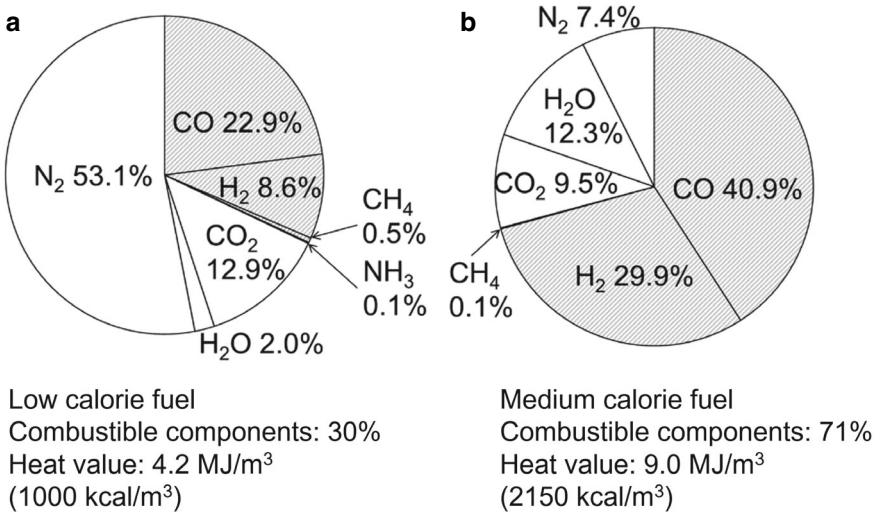


**Fig. 9.8** Composition of **a** low-calorific and **b** high-calorific coal gas fuels [15]

On the other hand, high-calorific gas fuel contains about 71% combustible components, offering a calorific value of approximately 10 MJ/Nm$^3$. However, the increased flame temperature associated with high-calorific fuel leads to greater $NO_x$ emissions. To mitigate $NO_x$ formation, nitrogen separated via an air separation unit can be injected into the combustion air of the gas turbine to dilute the reaction and suppress $NO_x$ generation. The subsequent section provides details on the development of a gas turbine specifically designed to utilize low-calorific fuels.

The potential of plasma $CO_2$ reduction technology for processing exhaust gases from gas turbines operating on low-calorific fuel is also under evaluation. Assuming a $CO_2$-to-CO conversion efficiency of 50%, the carbon content in the fuel (36.3% as shown in Fig. 9.8a) would enable the production of up to 18.2% CO. Utilizing the water–gas shift reaction ($CO + H_2O \rightleftharpoons CO_2 + H_2$) to achieve a CO/$H_2$ ratio similar to that of low-calorific gas fuels, the resulting fuel composition would consist of 13.2% CO and 5.0% $H_2$. This indicates that approximately 58% of the fuel demand could be substituted with products generated via plasma reduction technology.

### *9.3.2 Gas Turbines that Use Low-Calorie Fuels*

Gas turbines operating on low-calorific fuels, as depicted in Fig. 9.8a, encounter several challenges, including combustion instability, high $NO_x$ emissions, and a reduced cooling air supply due to the lower air-to-fuel ratio. To overcome these issues, it is essential to incorporate improvements such as enhanced flame retention capabilities, advanced $NO_x$ reduction combustion technologies, and innovative wall

cooling systems into the turbine design. A combustor specifically engineered for low-calorific fuels, capable of operating at 1773 K, has been reported in previous studies [17]. This combustor features an auxiliary combustion chamber along with distinct primary and secondary combustion zones.

In the auxiliary combustion chamber, fuel and combustion air are introduced with a swirling motion to ensure stable flame formation under rated load conditions, thereby enhancing flame retention performance. The two-stage combustion process, which spatially separates the primary and secondary combustion zones, effectively minimizes $NO_x$ emissions associated with low-calorific gas fuels. Unlike LNG-based systems, low-calorific fuels necessitate significantly lower air-to-fuel ratios, eliminating the requirement for additional air dilution. Furthermore, the tailpipe is designed with a dual-layer structure, which allows the cooling air from the tailpipe to be recirculated and utilized for cooling the secondary combustion zone.

This optimized design enables the gas turbine to efficiently produce electricity while operating on low-calorific fuels, as illustrated in Fig. 9.8a.

## 9.4 Fuel Conversion of $CO_2$ Using Plasma with Gas Recirculation

### *9.4.1 Introduction of Plasma $CO_2$ Reduction*

Under these research situations, our research group has conducted new laboratory-scale experimental trials with a novel $CO_2$ reduction treatment system combining an adsorbent and a nonthermal plasma (NTP) flow. The concept, as explained in [5], involves adsorbing $CO_2$ onto an adsorbent to enhance $CO_2$-to-CO conversion. The adsorbed $CO_2$ is desorbed at a high concentration (approximately 20%) and then reduced using a nitrogen NTP flow, an effective method for $CO_2$ reduction [4]. Previous investigations of nonthermal plasmas demonstrated that the treatment can be performed under atmospheric pressure and near room temperature. The apparent $CO_2$ conversion increases proportionally with the concentration of the reactant $CO_2$. In the current study, we developed a highly efficient $CO_2$ reduction system using an adsorbent and NTP flow at the laboratory scale, achieving a maximum reduction energy efficiency of 14%. The method is detailed in the next section.

### *9.4.2 Experimental Setup and Methods*

Owing to the $N_2$ plasma flow, the $CO_2$ adsorbed by the adsorbent is desorbed mainly by heat and reduced to CO by the plasma chemical reactions shown in [4].

$$CO_2 \rightarrow CO + O_2/2, \quad \Delta H = 2.9\,\text{eV/molecule} \tag{9.12}$$

Reaction (9.12), which is exothermic, requires energy ($\Delta H > 2.9$ eV/molecule). As no atomic carbon (C) is detected during plasma application in this experiment, the reduction of $CO_2$ to CO follows reaction (9.12). The concentrations of CO, $CO_2$, $O_2$, and $CO_3$ are measured every 10 min using gas detection tubes. At the end of the desorption period, valves B, C, and E are opened, and valve D is closed. The gas in the flow channel is discharged into the outside air through a $MnO_2$ catalyst to remove $O_3$. During both the adsorption and $N_2$ plasma desorption processes, the temperatures of the adsorbent and the upstream plasma reactor are monitored every 30 s using thermocouples. The upstream plasma reactor temperatures during adsorption and reduction processes are approximately 25 °C and 40 °C, respectively.

Figure 9.9 presents a photograph of the surface discharge NTP reactor. The plasma reactor includes twelve surface discharge elements, alternately positioned inside the channel and powered by a 10 kHz bipolar pulsed high-voltage power supply. Constructed from stainless steel, the reactor features a transparent acrylic observation window and measures 100 mm in height, 90 mm in width, and 425 mm in length. Atmospheric nonthermal plasma is generated at the surface discharge elements through surface discharge. The total power consumption is 300 W, and the electrodes are oriented toward the upstream gas flow. The $CO_2$ gas flow is primarily reduced to CO and carbon particulate matter (PM), although no PM is detected.

Figure 9.10 presents a schematic of the discharge element. The element consists of an alumina-ceramic tube with a tungsten discharge electrode on its surface and a counter electrode embedded within the ceramic tube wall. The discharge electrode is cooled using a heat-sink fin.

The energy efficiency evaluation method is described as follows. The CO and $O_2$ concentrations are measured every 10 min using an oxygen analyzer. The experiment comprises four cycles, each lasting 140 min for adsorption and 140 min for desorption. The conversion efficiency, $\alpha$, for reaction (9.12), represents the proportion of $CO_2$ reduced to CO and is defined by Eq. (9.13):

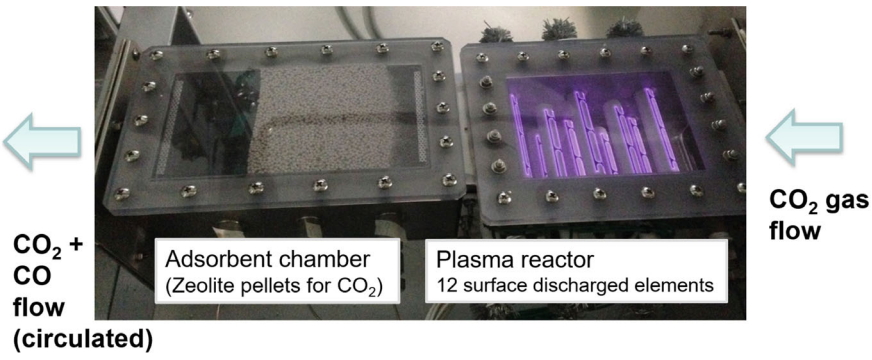


**Fig. 9.9** Photograph of surface discharge NTP reactor

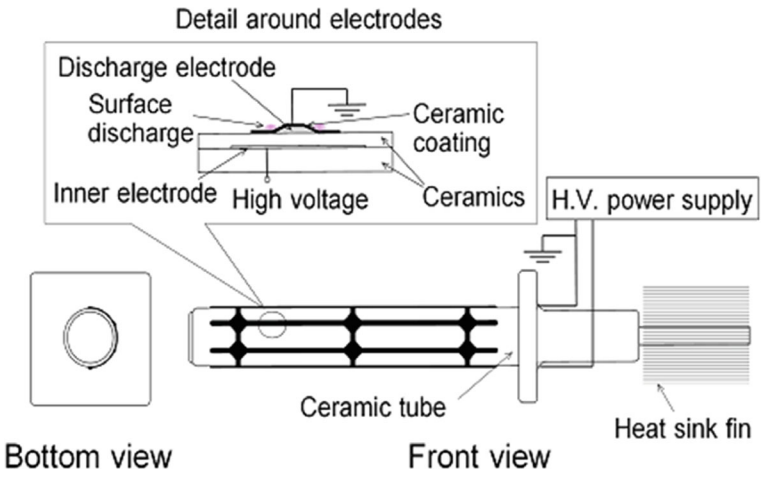


**Fig. 9.10** Schematic of discharge element

$$\alpha = \frac{\mathrm{CO}}{\mathrm{CO_2 + CO}} \times 100 \tag{9.13}$$

The energy efficiency, $\eta$, indicates the ratio of input power used for $CO_2$ reduction and is defined by Eq. (9.2). In this system, $E_v$ represents the specific input energy of the plasma (eV/molecule) [6], which is calculated using Eq. (9.14):

$$E_v = \frac{\frac{P\,(\mathrm{W})}{1.602\times10^{-19}\,(\mathrm{J/eV})}}{\frac{Q\,(\mathrm{L/min})}{60\,(\mathrm{s/min})} \times \frac{1}{22.4\,(\mathrm{L/mol})} \times 6.02 \times 10^{23}\,(\mathrm{molecule/mol}) \times \frac{273.15\,(\mathrm{K})}{T\,(\mathrm{K})}} \tag{9.14}$$

where $P$ (W) is the input energy, $Q$ (L/min) is the $CO_2$ flow rate during adsorption, and $T$ (K) is the ambient temperature. In this study, the input energy is $P = 300$ W, the $CO_2$ flow rate during the adsorption process is $Q = 1.0$ L/min, and the environmental temperature is $T = 20\ ^\circ\mathrm{C} = 293.15$ K, which yields a specific input energy of $E_v = 4.49$ eV/molecule. Notably, the experiment is conducted such that the CO concentration remains below 12.5% of the lower explosive limit.

### *9.4.3 Experimental Results and Discussion*

Figure 9.11 shows the time-dependent $CO_2$ and CO concentrations for various $Q_d$. For $Q_d = 0.54$ m$^3$/min, the maximum $CO_2$ desorption concentration is approximately 16% and the maximum CO concentration is about 4%. For 0.18 m$^3$/min, the maximum concentration of $CO_2$ desorption concentration increases to approximately 19 and the maximum concentration of CO is approximately 5%. For 0.09 m$^3$/min, the maximum $CO_2$ desorption concentration reaches approximately 20%, while the

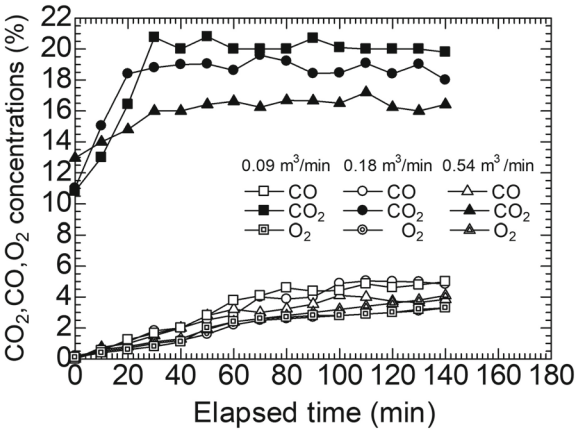


**Fig. 9.11** Effect of circulation flow rate $Q_d$ on time-dependent $CO_2$ and CO concentrations during the desorption processes: $Q_d$ = 0.09, 0.18, and 0.54 $m^3$/min [5]

maximum CO concentration remains about 5%. The results indicate that $CO_2$ desorption to increase with decrease in $Q_d$. Formation of achieve a high CO concentration of 5%.

Figure 9.12 shows the time-dependent temperature during the desorption processes for various $Q_d$. The temperature in the chamber increases with decrease in $Q_d$. It is considered that $CO_2$ desorption and CO production increase with higher temperatures due to the thermal energy generated by the plasma. The time-dependent conversion efficiency, defined as $\alpha = CO/CO_2 \times 100\%$ is shown in Fig. 9.13. It increases monotonically and reaches a maximum of approximately 22% after 120 min for $Q_d = 0.18$ $m^3$/min. The energy efficiency calculated using Eq. (9.2) for the conversion $\eta$ becomes 14%.

Figure 9.14 shows a comparison of the conversion efficiency ($\alpha$) and energy efficiency ($\eta$) obtained in this study with previously reported results. This graph, referenced from Li et al. [18] and other reports [5, 18–32], indicates that while the

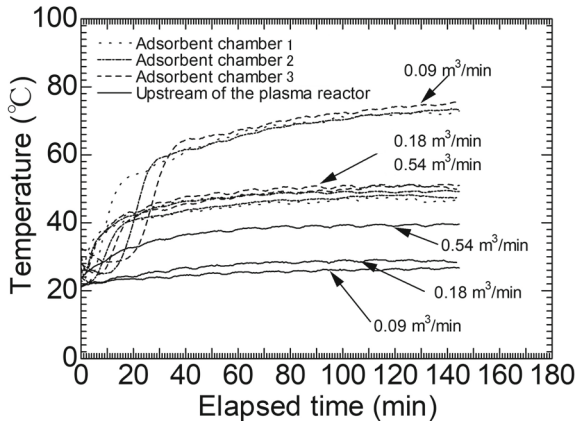


**Fig. 9.12** Time-dependent temperature of the desorption processes (adsorbent volume = 1.84 L, $Q_d$ = 0.09, 0.18, and 0.54 $m^3$/min) [5]

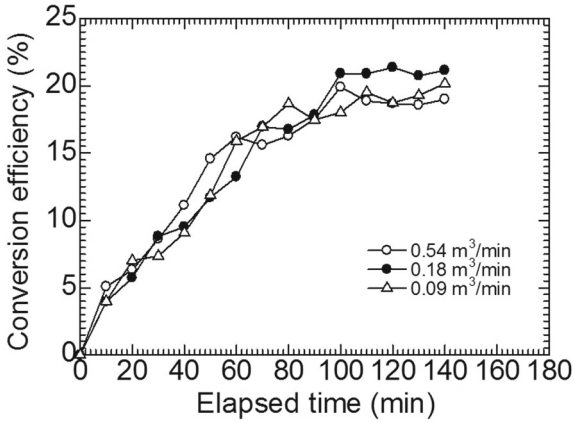


**Fig. 9.13** Time-dependent conversion defined as CO/$CO_2$ (adsorbent volume = 1.84 L, $Q_d = 0.09$, 0.18, and 0.54 $m^3$/min) [5]

surface discharge plasma (SDP) used in this study achieves comparable $\alpha$ and $\eta$ values, gliding arc discharge (GD) treatments demonstrate superior performance. Consequently, GD is gaining increased attention. In experiments conducted at the Osaka Metropolitan University (OMU) laboratory, an $\alpha$ of 21% is achieved with a twofold concentration. If results can be achieved at a fourfold concentration, the target value of 49% is expected to be attained.

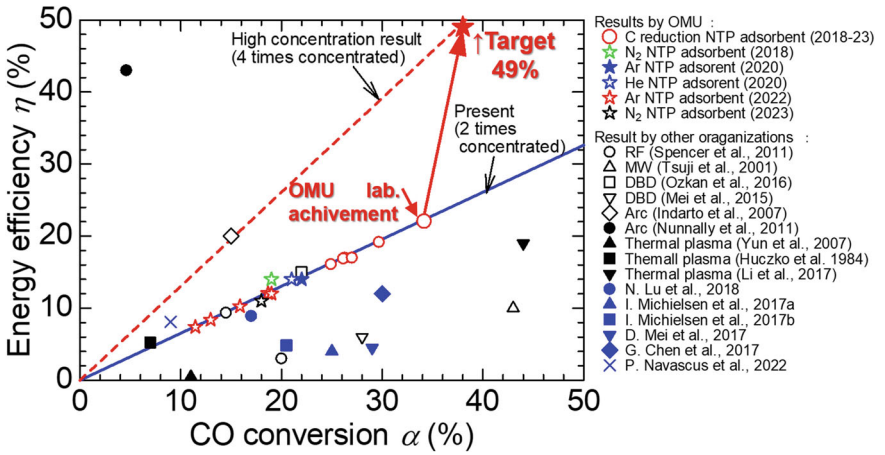


**Fig. 9.14** CO conversion efficiency $\alpha$ versus energy efficiency $\eta$. Toward zero-$CO_2$ thermal power generation with plasma $CO_2$ treatment. $\eta > 49\%$ leads to zero $CO_2$ emission in $CO_2$ reduction reaction (9.12)

## 9.5 Conclusions

Part of this project's research and development comprises a grand plan that aims to address and prevent future global warming by facilitating the achievement of the zero $CO_2$ emissions targets. In this context, the development of gas turbine combined cycle (GTCC) natural gas power generation systems using $CO_2$ plasma-catalyzed fuel processing technologies is highly significant. Compared to thermal processes, non-thermal plasma achieves higher $CO_2$ desorption and more efficient conversion into fuel. Achieving zero $CO_2$ emissions requires comprehensive research and development, in parallel with basic experiments, analyses, performance tests, and advancements in plasma reactors, adsorption systems, and $CO_2$ concentration technologies. The technologies explored in this study have been tested on a laboratory scale. Future research will involve testing on bench-scale machines to refine the processes and evaluate the new technologies.

We plan to integrate this technology into Japanese industries and expand its application to research facilities. Companies at the forefront of high-temperature gas turbine development have already adopted $CO_2$ capture technologies based on physical adsorption, providing a solid foundation for this innovation.

The findings of this study suggest that zero $CO_2$ emissions in GTCC thermal power plants may be achievable using plasma reduction technologies. Despite significant technical challenges, the development of innovative techniques has the potential to revolutionize efforts toward realizing a zero-carbon society with sustainable energy, addressing the urgent issue of global warming.

### Chapter 9 Exercises

**Problem 1**: About zero carbon thermal power generation

Explain Fig. 9.4 and explain whether it can be realized zero-$CO_2$ emission in the GTCC system.

**Problem 2**: Thermal efficiency and improvement measures I

There is a heavy-oil-burning thermal power plant with a rated output of 10,000 kW. This power plant has been operating continuously for 30 days, during which the amount of heavy oil used is 1100 tons, and the sending end power output was 5000 MWh. Calculate the value (%) for the boiler efficiency of this thermal power plant. Note that the calorific value of heavy oil is 44,000 kJ/kg, the turbine room efficiency is 47%, the generator efficiency is 98%, and the in-house efficiency is 5%.

**Problem 3**: Thermal efficiency and improvement measures II

Which of the following is incorrect for improving the thermal efficiency of a thermal power plant?

(1) High-temperature, high-pressure steam is used as the steam at the turbine inlet.
(2) The steam expands sufficiently inside the turbine by lowering the vacuum in the condenser, thereby providing a large torque to the turbine impeller.

(3) A coal economizer is installed to recover exhaust gas energy.
(4) The wet saturated steam from the high-pressure turbine is reheated in a boiler and used again as high-temperature dry saturated steam for the low-pressure turbine.
(5) The steam is taken from the high- and low-pressure turbines and directed to a feed water heater to heat the feed water.

**Problem 4**: Combined-cycle power generation

In a combined-cycle power plant using exhaust heat recovery, the thermal efficiency of combined-cycle power generation is 48%. What is the closest value to the thermal efficiency (%) of steam-turbine power generation relative to the amount of heat contained in the exhaust gas from gas-turbine power generation? Note that all exhaust gases from gas turbine power generation are supplied to steam turbine power generation.

**Problem 5**: $CO_2$ treatment cost calculation

Perform overall cost estimation of the plasma energy and spent adsorbent. The typical price of zeolite 13X per mass is US $6/kg-zeolite 13X. The zeolite 13X can be reused over thousands of regeneration or adsorption–desorption cycles to make it a possible cost-effective adsorbent. It is assumed that the cost of adsorbent 13X per mass of captured $CO_2$ is 19 $/ton-$CO_2$. This chapter explains that a specific energy for $CO_2$ plasma reduction of 3.38 eV/molecule is at least necessary for a consistent power generation system. Please calculate the following values.

(1) Calculate the energy per unit of $CO_2$ mass treatment (unit is kWh/ton-$CO_2$).
(2) Calculate the cost of electricity (unit is $/kWh), assuming the cost of 1 kWh is 0.14$.
(3) Calculate the ratio of the adsorbent cost to the total energy cost (%).

## References

1. T. Komori, S. Shiozaki, N. Yamagami, Y. Kitauchi, W. Akizuki, $CO_2$ emission reduction method through various gas turbine fuel applications. Mitsubishi Heavy Ind. Techn. Rev. **44**(1), 1–5 (2007)
2. M. Okubo, Recent development of technology in scale-up of plasma reactors for environmental and energy applications. Plasma Chem. Plasma Process. **42**, 3–31 (2021). https://doi.org/10.1007/s11090-021-10201-7
3. M. Okubo, T. Kuwahara, *New Technologies for Emission Control in Marine Diesel Engines* (Elsevier, 2019), pp. 296. ISBN: 9780128123072
4. H. Yamasaki, S. Kamei, T. Kuroki, M. Okubo, Adsorbed $CO_2$ dissociation using argon and helium nonthermal plasma flows. IEEE Trans. Ind. Appl. **56**, 6983–6989 (2020)
5. M. Okubo, K. Takahashi, S. Kamiya, T. Kuroki, High-efficiency carbon dioxide reduction using nonthermal plasma desorption. IEEE Trans. Ind. Appl. **54**, 6422–6429 (2018)
6. L.F. Spencer, A.D. Gallimore, Efficiency of $CO_2$ dissociation in a radio-frequency discharge. Plasma Chem. Plasma Process. **31**, 79–89 (2011)

7. Yukyan Denken Sanshu Shiken Kenkyukai, *Yukyan no Denken Sanshu Dokugaku no Denryoku Gokaku Tekisuto & Mondaishu* (Hinshutsu Kako Mon 100-dai Shuroku) (English translated title: *U-CAN's Electrical Engineering Third Class Self-Study Power Pass Text & Problem Book* [Contains 100 Frequently Asked Past Questions]) (U-CAN, Inc., Tokyo, Japan, 2021), pp. 592. ISBN-10: 4426612993, ISBN-13: 978-4426612993
8. K. Morimoto, Y. Matsumura, T. Iijima, S. Wakazono, M. Kataoka, M. Yuri, Validation results of 1650 °C class JAC gas turbine at T-point 2 demonstration plant. Mitsubishi Heavy Ind. Techn. Rev. **58**(1), 1–12 (2021)
9. R. Hanna, A. Abdulla, Y. Xu, D.G. Victor, Emergency deployment of direct air capture as a response to the climate crisis. Nat. Commun. **12**, 368 (2021). https://doi.org/10.1038/s41467-020-20437-0
10. M. Okubo, T. Kuroki, H. Yamada, K. Yoshida, T. Kuwahara, $CO_2$ concentration using adsorption and nonthermal plasma desorption. IEEE Trans. Ind. Appl. **53**, 2432–2439 (2017)
11. K. Akimoto, T. Kikkawa, The Japan Research Institute, Limited, Japan Gas Association, *Methanation* (Energy Forum Inc., Tokyo, Japan, 2022), pp. 278. ISBN-10: 4885555280, ISBN-13: 978-4885555282 (in Japanese)
12. Y. Oki, H. Hamada, M. Kobayashi, Y. Nakao, S. Hara, Development of high-efficiency oxy-fuel IGCC system. Mech. Eng. J. **3**, 5, 16-00351, 6 pp. (2016)
13. Mitsubishi Power Ltd., Press Release. https://power.mhi.com/news/20210419.html. Accessed 2024.12.01
14. T. Hashimoto, K. Sakamoto, H. Ishii, T. Fuji, Y. Koyama, Commercialization of clean technology with $CO_2$ recovery. Mitsubishi Heavy Ind. Techn. Rev. **47**(1), 9–14 (2010)
15. A. Giuffrida, M.C. Romano, F. Lozza, Thermodynamic analysis of air-blown gasification for IGCC applications. Appl. Energy **88**, 3949–3958 (2011)
16. M. Sato, T. Hasegawa, Development of gas turbine combustors technology. Denchuken Rev. **44**, 74–81, chap. 5 (2001) (in Japanese)
17. T. Hasegawa, Development of gas turbine combustor for utilizing various gasified fuels with high-efficiency and minimal pollutant emissions. J. Combust. Soc. Jpn. **48**(146), 46–61 (2006). ((in Japanese))
18. M. Tsuji, T. Tanoue, K. Nakano, Y. Nishimura, Decomposition of $CO_2$ into CO and O in a microwave-excited discharge flow of $CO_2$/He or $CO_2$/Ar mixtures. Chem. Lett. **30**(1), 22–23 (2001)
19. J. Li, X. Zhang, J. Shen, T. Ran, P. Chen, Y. Yin, Dissociation of $CO_2$ by thermal plasma with contracting nozzle quenching. J. $CO_2$ Util. **21**, 72–76 (2017)
20. D.H. Mei, X.B. Zhu, Y.L. He, Plasma-assisted conversion of $CO_2$ in a dielectric barrier discharge reactor: understanding the effect of packing materials. Plasma Sources Sci. Technol. **24**, 015011 (2015)
21. A. Indarto, D.R. Yang, J. Choi, H. Lee, H.K. Song, Gliding arc plasma processing of $CO_2$ conversion. J. Hazard. Mater. **146**, 309–315 (2007)
22. S.H. Yun, G.J. Kim, D.W. Park, Decomposition and conversion of carbon dioxide into synthesis gas using thermal plasma. J. Ind. Eng. Chem. **4**, 293–297 (1997)
23. A. Huczko, A. Szymanski, Thermal decomposition of carbon dioxide in an argon plasma jet. Plasma Chem. Plasma Process. **1**, 59–72 (1984)
24. A. Ozkan, T. Dufour, T. Sliva, N. Britun, R. Snyders, A. Bogaerts, The influence of power and frequency on the filamentary behavior of a flowing DBD—application to the splitting of $CO_2$. Plasma Sources Sci. Technol. **25**, 025013 (2016)
25. T. Nunnally, K. Gutsol, A. Rabinovich, Dissociation of $CO_2$ in a low current gliding arc plasmatron. J. Phys. D Appl. Phys. **44**, 274009 (2011)
26. H. Wakimoto, H. Yamasaki, T. Kuroki, M. Okubo, Effect of argon and helium concentrations on adsorbed $CO_2$ dissociation using nonthermal plasma flow. Int. J. Plasma Environ. Sci. Technol. **16**, e01006, 14 pp. (2022)
27. H. Wakimoto, H. Yamasaki, T. Kuroki, M. Okubo, High-efficiency carbon dioxide reduction using catalytic nonthermal plasma desorption. Mech. Eng. J. **10**(2), 22–00191, 13 pp. (2023)

28. N. Lu, D. Sun, C. Zhang, N. Jiang, K. Shang, X. Bao, J. Li, Y. Wu, $CO_2$ conversion in nonthermal plasma and plasma/g-$C_3N_4$ catalyst hybrid processes. J. Phys. D Appl. Phys. **51**, 094001 (2018)
29. I. Michielsen, Y. Uytdenhouwen, J. Pype, B. Michielsen, J. Mertens, F. Reniers, V. Meyen, A. Bogaerts, $CO_2$ dissociation in a packed bed DBD reactor: first steps towards a better understanding of plasma catalysis. Chem. Eng. J. **326**, 477–488 (2017)
30. D. Mei, X. Tu, Atmospheric pressure non-thermal plasma activation of $CO_2$ in a packed-bed dielectric barrier discharge reactor. ChemPhysChem **18**(22), 3253–3259 (2017)
31. G. Chen, N. Britun, T. Godfroid, V. Georgieva, R. Snyders, M.P. Delplancke-Ogletree, An overview of $CO_2$ conversion in a microwave discharge: the role of plasma-catalysis. J. Phys. D Appl. Phys. **50**(8), 084001, 11 pp. (2017)
32. P. Navascués, J. Cotrino, A.R. González-Elipe, A. Gómez-Ramírez, Plasma assisted $CO_2$ dissociation in pure and gas mixture streams with a ferroelectric packed-bed reactor in ambient conditions. Chem. Eng. J. **430**, 133066, 10 pp. (2022)

# Concluding Remarks

In conclusion, the book *Electrical Sustainable Energy for Mechanical Engineers* provides a comprehensive overview of key concepts and practical applications relevant to the field of electrical engineering, with a focus on optimizing power transfer and energy conversion across various systems. Each chapter builds upon the previous, starting from basic principles of direct and alternating current circuits in Chap. 1, progressing through detailed analyses of impedance matching using Smith charts and complex number calculations in Chaps. 2 through 6, and culminating in sophisticated discussions on energy system principle, heat transfer flow in plasmas and $CO_2$ emission reduction technologies in Chap. 7 through 9.

- Chapters 1–3 focus on fundamental electrical circuit analysis, including DC and AC circuits, transient phenomena, and series resonant circuits, equipping readers with the necessary tools to understand and manipulate electrical systems effectively.
- Chapter 4 treats the computation of averages in periodic complex signals, setting the stage for advanced topics in impedance matching and circuit design discussed in subsequent chapters.
- Chapters 5 and 6 thoroughly explore impedance matching, emphasizing the practical application of Smith charts and series and parallel connections, which are vital for optimizing the power transfer in electrical circuits. These chapters also include real-world problem-solving examples related to transformers and induction motors, enhancing the readers' ability to tackle complex engineering challenges.
- Chapters 7 and 8 transition into the basic and advanced topics of energy system principle, heat transfer flow in plasma and the intricate interactions of plasma with electromagnetic fields, fluid flow, and chemical reactions, reflecting the latest advances in modeling techniques.



M. Okubo, *Electrical Sustainable Energy for Mechanical Engineering*,
https://doi.org/10.1007/978-981-96-5170-2

- Chapter 9 discusses the application of nonthermal plasma technology in gas turbine systems and its significance in achieving zero $CO_2$ emissions, emphasizing the role of plasma-catalyzed fuel processing technologies in mitigating global warming.

Throughout the book, the blend of theoretical insights and practical exercises ensures a balanced approach, making it accessible and valuable for both students and professionals in the field of electrical engineering. The chapters provide a robust understanding of how theoretical concepts are applied in real-world scenarios, particularly in energy-efficient design and sustainable energy solutions. This comprehensive treatment of electrical sustainable energy not only enhances technological efficiency but also contributes significantly to global efforts towards a zero-carbon society.

# Appendix

## A.1 Historical Image of Sakai City

Humans settled in the region of present-day Sakai City, Osaka Prefecture, Japan, approximately 10,000 years ago. During the fourth and fifth centuries, the Imperial Court was established, and more than 100 emperor tombs were constructed in Sakai City. The name "Sakai" translates to "boundary" or "border" in English, reflecting its location at the intersection of three small prefectures established at the time.

Between the twelfth and fourteenth centuries, Sakai developed as the main shipping base of western Japan. From the late fifteenth to the late sixteenth centuries, a period marked by frequent domestic wars in Japan, Sakai flourished as an international trade port. During this era, it became a hub for imported goods and an important international trading center. The introduction of firearms from Western countries is a notable example. Information disseminated from Sakai to the rest of Japan, making it a center of innovation and exchange. Despite Japan's limited openness to foreign countries during this time, Sakai thrived as a unique, semi-independent city known as "Saccai," forming trade relationships with nations such as China and European countries. A depiction of Sakai during its prosperous sixteenth and seventeenth centuries was included in a book by the Dutch missionary and scholar Arnoldus Montanus. This image, shown in Fig. A.1 illustrates several ocean-going international ships near Sakai Port.

Following the nineteenth century, Sakai underwent rapid modernization, characterized by the development of modern industries, population growth, urban expansion, and increased traffic, much like other major cities in Japan. Although many ruins and prehistoric sites were lost during World War II bombings, Sakai continued to develop as a leading industrial city. By the early 1900s, Sakai produced more than 80% of Japan's bicycle parts, earning an international reputation as the "town of bicycles." The bicycle industry persisted after World War II, with traditional craftsmanship passed down to modern high-tech bicycle manufacturers, including Shimano Inc.



M. Okubo, *Electrical Sustainable Energy for Mechanical Engineering*,
https://doi.org/10.1007/978-981-96-5170-2

Figure A.2 shows a photo of historical site Dotou. The Dotou (Earthen Stupa) is a culturally significant historical site located in Sakai City, near Osaka Metropolitan University. This stupa is part of Onoji Temple, one of the forty-nine temples constructed by the renowned Nara-period monk Gyoki. According to the Gyoki Chronicles, construction began in 727 (the 4th year of the Shinki era). The stupa is also illustrated in the Illustrated Biography of Bodhisattva Gyoki (a National Important Cultural Property) from the Kamakura period, depicted alongside the temple's main hall and gate as a "13-tiered earthen stupa." Excavations have revealed that the Dotou is a 13-tiered structure with a square base measuring approximately 153 m (503 ft.) on each side and a height exceeding 8.6 m (28.2 ft.). Each tier was originally covered with tiles, as confirmed by findings during the survey. Eaves tiles inscribed with "Shinki Year 4" were discovered, supporting the historical record in the Gyoki Chronicles. Today, the site is preserved with an earthen mound covering the entire structure, and 12 tiers have been restored. Approximately 160 m northwest of the Dotou, two kilns used to fire the tiles were unearthed. About 460 m to the north lies Komo-e-ike (Komo-e pond), a reservoir believed to be Komo-ike (Komo pond), constructed by Gyoki before 741 (the 13th year of the Tenpyo era).

This site, located in proximity to Osaka Metropolitan University, serves as a vital cultural and educational resource for both the local community and visitors. Visitors can deepen their understanding of ancient Buddhist culture and architecture while exploring the surrounding area. Photo of Fig. A.2 included here provide a visual

**Fig. A.1** Historical illustration at Sakai Port

**Fig. A.2** Dotou's grandeur and its serene environment

glimpse of the Dotou's grandeur and its serene environment. These images capture the site's historical significance and its integration into the urban and cultural fabric of Sakai City.

## A.2 Vector and Tensor Notation

In this book, the notation for vectors and tensors follows the conventions established in Ref. [1]. We adopt the Gibbs notation, where vectors are represented by italic bold Roman or Greek letters, such as $\boldsymbol{u}$, $\boldsymbol{H}$, or $\boldsymbol{\xi}$. Second-order tensors are indicated using italic bold sans-serif letters, such as $\boldsymbol{T}$ or $\boldsymbol{D}$.

The unit vectors along Cartesian coordinates are denoted as $\boldsymbol{i}$, $\boldsymbol{j}$, and $\boldsymbol{k}$, or alternatively as $\boldsymbol{e}_1$, $\boldsymbol{e}_2$, and $\boldsymbol{e}_3$. A unit normal vector to a surface is denoted by $\boldsymbol{n}$, and, for closed surfaces, it is conventionally taken to point outward. A unit tangent vector is denoted by $t$.

The scalar (or dot) product between two vectors is represented by $\boldsymbol{a} \cdot \boldsymbol{b}$, while their vector (or cross) product is denoted as $\boldsymbol{a} \times \boldsymbol{b}$. The cross product produces a pseudovector, whose direction reverses under mirror reflection. In contrast, vectors like velocity that retain their orientation under mirror reflection are called polar vectors.

A dyad, or the indeterminate product of two vectors $\boldsymbol{a}$ and $\boldsymbol{b}$, is expressed simply by juxtaposing them: $\boldsymbol{ab}$. If the vectors are expanded in Cartesian components as $\boldsymbol{a} = a_x\boldsymbol{i} + a_y\boldsymbol{j} + a_z\boldsymbol{k}$ and $\boldsymbol{b} = b_x\boldsymbol{i} + b_y\boldsymbol{j} + b_z\boldsymbol{k}$, then their dyadic product results in $\boldsymbol{ab} = a_xb_x\boldsymbol{ii} + a_xb_y\boldsymbol{ij} + \ldots$. In general, the dyadic product is noncommutative; that is, $\boldsymbol{ab}$ and $\boldsymbol{ba}$ are not necessarily equal.

Thus, three distinct types of products can be formed between two vectors: the scalar product $\boldsymbol{a} \cdot \boldsymbol{b}$, the vector product $\boldsymbol{a} \times \boldsymbol{b}$, and the dyadic (indeterminate) product $\boldsymbol{ab}$.

A general dyadic $\boldsymbol{D}$ can be expressed as a finite sum of dyads: $\boldsymbol{D} = \boldsymbol{a}_1\boldsymbol{b}_1 + \boldsymbol{a}_2\boldsymbol{b}_2 + \cdots + \boldsymbol{a}_n\boldsymbol{b}_n$.

The transpose (or conjugate) of a dyadic is denoted as $\boldsymbol{D}^T = \boldsymbol{b}_1\boldsymbol{a}_1 + \boldsymbol{b}_2\boldsymbol{a}_2 + \ldots + \boldsymbol{b}_n\boldsymbol{a}_n$. A dyadic is said to be symmetric if $\boldsymbol{D} = \boldsymbol{D}^T$, and antisymmetric if $\boldsymbol{D} = -\boldsymbol{D}^T$.

Any dyadic $\boldsymbol{D}$ can be uniquely decomposed into its symmetric and antisymmetric parts as: $\boldsymbol{D} = \boldsymbol{D}_s + \boldsymbol{D}_a$, where $\boldsymbol{D}_s = (\boldsymbol{D} + \boldsymbol{D}^T)/2$ and $\boldsymbol{D}_s = (\boldsymbol{D} - \boldsymbol{D}^T)/2$.

Several operations are also defined for dyadics. The scalar of the dyadic $\boldsymbol{D}$ is: sca $\boldsymbol{D} = \boldsymbol{a}_1 \cdot \boldsymbol{b}_1 + \boldsymbol{a}_2 \cdot \boldsymbol{b}_2 + \cdots$, while the vector of the dyadic $\boldsymbol{D}$ is: vec $\boldsymbol{D} = \boldsymbol{a}_1 \times \boldsymbol{b}_1 + \boldsymbol{a}_2 \times \boldsymbol{b}_2 + \cdots$.

The dot product of a vector $\boldsymbol{u}$ with a dyadic $\boldsymbol{D}$ is defined in two forms: $\boldsymbol{u} \cdot \boldsymbol{D} = (\boldsymbol{u} \cdot \boldsymbol{a}_1)\boldsymbol{b}_1 + (\boldsymbol{u} \cdot \boldsymbol{a}_2)\boldsymbol{b}_2 + \cdots$, and $\boldsymbol{D} \cdot \boldsymbol{u} = \boldsymbol{a}_1(\boldsymbol{b}_1 \cdot \boldsymbol{u}) + \boldsymbol{a}_2(\boldsymbol{b}_2 \cdot \boldsymbol{u}) + \cdots$. Similarly, cross products $\boldsymbol{u} \times \boldsymbol{D}$ and $\boldsymbol{D} \times \boldsymbol{u}$ are defined analogously.

The unit dyadic $\boldsymbol{I}$ is given by: $\boldsymbol{I} = \boldsymbol{ii} + \boldsymbol{jj} + \boldsymbol{kk}$. This dyadic acts analogously to the number 1 in scalar algebra, satisfying the properties: $\boldsymbol{I} \cdot \boldsymbol{u} = \boldsymbol{u} \cdot \boldsymbol{I} = \boldsymbol{u}$ for any vector $\boldsymbol{u}$.

When taking products between dyadics, we follow the nesting convention. For instance, the dot product between dyads $\boldsymbol{ab}$ and $\boldsymbol{cd}$ is: $\boldsymbol{ab} \cdot \boldsymbol{cd} = (\boldsymbol{b} \cdot \boldsymbol{c})(\boldsymbol{ad})$. Similarly, the cross product between dyads under the nesting convention becomes: $(\boldsymbol{ab}) \times (\boldsymbol{cd}) = (\boldsymbol{a} \cdot \boldsymbol{d})(\boldsymbol{b} \times \boldsymbol{c})$.

The trace of a second-order tensor $\boldsymbol{T}$, written as tr $\boldsymbol{T}$, is the sum of its diagonal components: tr $\boldsymbol{T} = \boldsymbol{T}_{ii} = \boldsymbol{T}_{11} + \boldsymbol{T}_{22} + \boldsymbol{T}_{33}$. Importantly, the trace remains invariant under coordinate system rotations. Powers of tensors are indicated as $\boldsymbol{T}^2 = \boldsymbol{T} \cdot \boldsymbol{T}$, $\boldsymbol{T}^3 = \boldsymbol{T} \cdot \boldsymbol{T}^2$, and so on. In addition to the trace tr $\boldsymbol{T}$, the invariants tr $\boldsymbol{T}^2$, and tr $\boldsymbol{T}^3$ are also defined. The magnitude of a tensor $\boldsymbol{T}$ is

$$|\boldsymbol{T}| = \sqrt{\frac{1}{2}\boldsymbol{T} : \boldsymbol{T}^T}$$

The magnitude of a tensor, particularly if it is symmetric, can be constructed using its invariants $\sqrt{\text{tr}\boldsymbol{T}^2/2}$.

Finally, the alternator is a special third-order tensor denoted by $\boldsymbol{\varepsilon}$, defined as: $\boldsymbol{\varepsilon} = \mathbf{e}_i\mathbf{e}_j\mathbf{e}_k\varepsilon_{ijk}$, where $\varepsilon_{ijk}$ is the Levi-Civita symbol introduced in Sect. 8.6 of Ref. [1]. The alternator facilitates the definition of dual operations. For a vector $\boldsymbol{A}$, its dual is: dual $\boldsymbol{A} \equiv \boldsymbol{\varepsilon} \cdot \boldsymbol{A} = -\boldsymbol{I} \times \boldsymbol{A}$. For a tensor $\boldsymbol{D}$, the dual is defined by: dual $\boldsymbol{D} \equiv -\boldsymbol{\varepsilon} : \boldsymbol{D}/2 = \boldsymbol{I} \times \boldsymbol{D}/2$.

**Vector Identities.** Several fundamental vector identities are used throughout the text. These include relations for the gradient, divergence, curl, and Laplacian operators applied to scalar and vector fields. Familiarity with these identities is essential for manipulating equations in electromagnetism, fluid mechanics, and plasma physics:

$$(\boldsymbol{A} \times \boldsymbol{B}) \cdot \boldsymbol{C} = \boldsymbol{A} \cdot (\boldsymbol{B} \times \boldsymbol{C}) = (\boldsymbol{C} \times \boldsymbol{A}) \cdot \boldsymbol{B}$$

$$\boldsymbol{A} \times (\boldsymbol{B} \times \boldsymbol{C}) = \boldsymbol{B}(\boldsymbol{A} \cdot \boldsymbol{C}) - \boldsymbol{C}(\boldsymbol{A} \cdot \boldsymbol{B})$$

$$(\boldsymbol{A} \times \boldsymbol{B}) \cdot (\boldsymbol{C} \times \boldsymbol{D}) = (\boldsymbol{A} \cdot \boldsymbol{C})(\boldsymbol{B} \cdot \boldsymbol{D}) - (\boldsymbol{A} \cdot \boldsymbol{D})(\boldsymbol{B} \cdot \boldsymbol{C})$$

$$\nabla \times \nabla \phi = 0$$

$$\nabla \cdot (\nabla \times \boldsymbol{A}) = 0$$

$$\nabla(\phi_1 \phi_2) = \phi_1 \nabla \phi_2 + \phi_2 \nabla \phi_1$$

$$\nabla \cdot (\phi \boldsymbol{A}) = \phi \nabla \cdot \boldsymbol{A} + \boldsymbol{A} \cdot \nabla \phi$$

$$\nabla \times (\phi \boldsymbol{A}) = \phi \nabla \times \boldsymbol{A} + \nabla \phi \times \boldsymbol{A}$$

$$\nabla(\boldsymbol{A} \cdot \boldsymbol{B}) = \boldsymbol{A} \cdot \nabla \boldsymbol{B} + \boldsymbol{B} \cdot \nabla \boldsymbol{A} + \boldsymbol{A} \times (\nabla \times \boldsymbol{B}) + \boldsymbol{B} \times (\nabla \times \boldsymbol{A})$$

$$\nabla \cdot (\boldsymbol{A} \times \boldsymbol{B}) = \boldsymbol{B} \cdot (\nabla \times \boldsymbol{A}) - \boldsymbol{A} \cdot (\nabla \times \boldsymbol{B})$$

$$\nabla \times (\boldsymbol{A} \times \boldsymbol{B}) = \boldsymbol{A}(\nabla \cdot \boldsymbol{B}) - \boldsymbol{B}(\nabla \cdot \boldsymbol{A}) + \boldsymbol{B} \cdot \nabla \boldsymbol{A} - \boldsymbol{A} \cdot \nabla \boldsymbol{B}$$

$$\nabla \times (\nabla \times \boldsymbol{A}) = \nabla(\nabla \cdot \boldsymbol{A}) - \nabla^2 \boldsymbol{A}$$

$$\boldsymbol{A} \cdot \nabla \boldsymbol{A} = \frac{1}{2} \nabla(\boldsymbol{A} \cdot \boldsymbol{A}) - \boldsymbol{A} \times (\nabla \times \boldsymbol{A})$$

$$\nabla \cdot (\nabla \phi_1 \times \nabla \phi_2) = 0$$

**Tensor Identities.** Tensor operations involve identities analogous to those for vectors, but extend to higher-order derivatives and contractions. Key tensor identities relate to the properties of symmetric and antisymmetric tensors, the behavior of tensor products, and operations such as the divergence of a tensor field:

$$\boldsymbol{AB} \cdot \boldsymbol{C} = \boldsymbol{A}(\boldsymbol{B} \cdot \boldsymbol{C})$$

$$\boldsymbol{A} \cdot \boldsymbol{BC} = (\boldsymbol{A} \cdot \boldsymbol{B})\boldsymbol{C}$$

$$\nabla \cdot (\boldsymbol{AB}) = \boldsymbol{A} \cdot \nabla \boldsymbol{B} + \boldsymbol{B}(\nabla \cdot \boldsymbol{A})$$

$$\boldsymbol{A} \cdot \boldsymbol{T} = \boldsymbol{T}^T \cdot \boldsymbol{A}$$

$$\boldsymbol{I} \cdot \boldsymbol{A} = \boldsymbol{A} \cdot \boldsymbol{I} = \boldsymbol{A}$$

$$\nabla \cdot (\phi \boldsymbol{I}) = \nabla \phi$$

$$\nabla \cdot (\phi \boldsymbol{T}) = \phi \nabla \cdot \boldsymbol{T} + \nabla \phi \cdot \boldsymbol{T}$$

$$\nabla \cdot \boldsymbol{T}_a = -\frac{1}{2} \nabla \times \boldsymbol{A}, \quad \text{where } \boldsymbol{T}_a = \frac{1}{2}\left(\boldsymbol{T} - \boldsymbol{T}^T\right)$$

$$\text{and } \boldsymbol{A} = \text{vec}\, \boldsymbol{T}$$

**Integral Theorems.** Integral theorems provide a bridge between local differential properties and global integral properties. Principal theorems used include:

1. Divergence theorem: Relates the flux of a vector field across a closed surface to the divergence over the volume enclosed.
   (a) For vectors, $\int_V \nabla \cdot \boldsymbol{A} \mathrm{d}V = \oint_S \boldsymbol{A} \cdot \mathrm{d}\boldsymbol{S}$
   (b) For tensors, $\int_V \nabla \cdot \boldsymbol{T} \mathrm{d}V = \oint_S \mathrm{d}\boldsymbol{S} \cdot \boldsymbol{T}$
   (c) For vectors, $\int_V \nabla \psi \mathrm{d}V = \oint_S \psi \mathrm{d}\boldsymbol{S}$, $\int_V \nabla \times \boldsymbol{A} \mathrm{d}V = \oint_S \mathrm{d}\boldsymbol{S} \times \boldsymbol{A}$
2. Stokes's theorem: Connects the circulation of a vector field around a closed loop to the curl over the surface it bounds.

$$\oint_S (\nabla \times \boldsymbol{A}) \cdot \mathrm{d}\boldsymbol{S} = \oint_L \boldsymbol{A} \cdot \mathrm{d}\boldsymbol{l}$$

3. Reynolds' transport theorem for differentiating a volume integral: Facilitates differentiation of integrals over moving volumes, crucial for control volume analysis in fluid mechanics.

$$\frac{\mathrm{D}}{\mathrm{D}t} \int_V \psi \mathrm{d}V = \int_V \frac{\partial \psi}{\partial t} \mathrm{d}V + \oint_S \psi \boldsymbol{u} \cdot \mathrm{d}\boldsymbol{S}$$

4. Transport theorem for differentiating a surface integral: Extend transport relations to surface integral.

$$\frac{\mathrm{D}}{\mathrm{D}t}\int_S \boldsymbol{A}\cdot\mathrm{d}\boldsymbol{S} = \int_S \left[\frac{\mathrm{D}\boldsymbol{A}}{\mathrm{D}t} - \boldsymbol{A}\cdot\nabla\boldsymbol{u} + \boldsymbol{A}(\nabla\cdot\boldsymbol{u})\right]\cdot\mathrm{d}\boldsymbol{S}$$
$$= \int_S \left[\frac{\partial\boldsymbol{A}}{\partial t} + \nabla\times(\boldsymbol{A}\times\boldsymbol{u}) + \boldsymbol{u}(\nabla\cdot\boldsymbol{A})\right]\cdot\mathrm{d}\boldsymbol{S}$$

5. Transport theorem for line integrals: Extend transport relations to line integrals.

$$\frac{\mathrm{D}}{\mathrm{D}t}\int_L \boldsymbol{A}\cdot\mathrm{d}\boldsymbol{l} = \int_L \left(\frac{\mathrm{D}\boldsymbol{A}}{\mathrm{D}t} + \boldsymbol{A}\cdot\nabla\boldsymbol{u}\right)\cdot\mathrm{d}\boldsymbol{l}$$

## Reference

1. R.E. Rosensweig, *Ferrohydrodynamics* (Cambridge University Press, 1985), Appendixes, App. 1, pp. 315–318

# Back Cover Text for the Book

"Discover the Convergence of Mechanical and Electrical Engineering!"

Step into a textbook designed to aspire mechanical engineers. By harnessing years of expertise, the author introduces foundational knowledge of sustainable electrical energy and energy conversion principles. This unique resource is tailored for a 15-week semester, ensuring comprehensive coverage of essential topics beneficial to mechanical engineering research related to sustainable electrical energy. However, this is not just a textbook; it is also a bridge. Recognizing the gaps in electrical engineering knowledge for students entering their final-year projects, this book is designed to fill the void. Moving beyond the confines of conventional electrical engineering texts, it addresses topics, such as electrical circuits and sustainable energy conversion, and even provides techniques related to energy principles, circuit matching, and plasma applications. Driven by the author's commitment to excellence and passion for mentoring, this book showcases in-depth research at the intersection of electrical and mechanical engineering. With its unique focus on plasma processing and electrostatic precipitation, it serves as a foundational guide and gateway for advanced applications. To ensure practicality, a treasure trove of specific problems with detailed solutions are included, all derived from the author's extensive collaborative industrial research. Whether you are a student grappling with the complexities of electromagnetism, or an engineer keen on expanding your horizons, this textbook promises a journey that blends the best of both disciplines. Transform your understanding of sustainable electrical energy.



M. Okubo, *Electrical Sustainable Energy for Mechanical Engineering*,
https://doi.org/10.1007/978-981-96-5170-2